ADDITIVE MANUFACTURING OF INCONEL 718

USING ELECTRON BEAM MELTING:

PROCESSING, POST-PROCESSING, & MECHANICAL PROPERTIES

A Dissertation

by

WILLIAM JAMES SAMES V

Submitted to the Office of Graduate and Professional Studies of
Texas A&M University
in partial fulfillment of the requirements for the degree of

DOCTOR OF PHILOSOPHY

Chair of Committee,	Sean M. McDeavitt
Committee Members,	Raymundo Arroyave
	Ryan R. Dehoff
	Delia Perez-Nunez
	Lin Shao
Head of Department,	Yassin Hassan

May 2015

Major Subject: Nuclear Engineering

ABSTRACT

Additive Manufacturing (AM) process parameters were studied for production of the high temperature alloy Inconel 718 using Electron Beam Melting (EBM) to better understand the relationship between processing, microstructure, and mechanical properties. Processing parameters were analyzed for impact on process time, process temperature, and the amount of applied energy. The applied electron beam energy was shown to be integral to the formation of swelling defects. Standard features in the microstructure were identified, including previously unidentified solidification features such as shrinkage porosity and non-equilibrium phases. The as-solidified structure does not persist in the bulk of EBM parts due to a high process hold temperature (~1000°C), which causes *in situ* homogenization. The most significant variability in as-fabricated microstructure is the formation of intragranular delta-phase needles, which can form in samples produced with lower process temperatures (< 960°C). A novel approach was developed and demonstrated for controlling the temperature of cool down, thus providing a technique for *in situ* heat treatment of material. This technique was used to produce material with hardness of 478±7 HV with no post-processing, which exceeds the hardness of peak-aged Inconel 718. Traditional post-processing methods of hot isostatic pressing (HIP) and solution treatment and aging (STA) were found to result in variability in grain growth and phase solution. Recrystallization and grain structure are identified as possible mechanisms to promote grain growth. These results led to the conclusion that the first step in thermal post-processing of EBM Inconel 718 should be an optimized solution treatment to reset phase variation in the as-fabricated microstructure without incurring significant grain growth. Such an optimized solution treatment was developed (1120°C, 2hr) for application prior to aging or HIP. The majority of as-fabricated tensile properties met ASTM AM Inconel 718 standards for yield stress and ultimate tensile strength, and STA yield stress, ultimate tensile strength, and elongation exceeded the ASTM standards for AM Inconel 718.

ACKNOWLEDGEMENTS

I have received support from many colleagues throughout this work, to which I am very thankful.

I would like to thank my graduate advisor, Sean McDeavitt, for his guidance and for giving me the freedom to perform my research at ORNL, in a unique arrangement. His guidance has been far-sighted and enabled me to think creatively in developing my degree program.

I would like to thank my ORNL mentor, Ryan Dehoff, for agreeing to host me at ORNL and provide unique mentorship. His guidance enabled me to obtain hands on experience in all aspects of metallurgy and metal additive manufacturing from metallography to microscopy to machine operation. His support along the way has been intellectually challenging and helped me to grow as a researcher.

I would like to thank a large number of colleagues that have supported me along the way: Fred List for his mentorship, hardware support, and scientific approach, Frank Medina for his mentorship, processing knowledge, and collaboration, Larry Lowe for his support of hardware and sample production, Suresh Babu for his mentorship and metallurgy knowledge, Michael Goin for his development of software tools at ORNL, Michael Pearce for his development of software tools at ORNL, Michael Kirka for his knowledge of superalloy metallurgy and collaboration, Kinga Unocic for her knowledge of microscopy and collaboration, Don Erdman for his support of mechanical testing and collaboration, Tom Geer for teaching me metallography, Eddie Schwalbach for his collaboration, Bill Peter for his support of powder metallurgy and processing, Grant Helmreich for his collaboration, Paul Menchover for his microscopy support, Tom Muth for his metallurgy expertise, Dane Wilson for his assistance in running heat treatments, Donovan Leonard for his microscopy support, Lindsay Kolbus for her collaboration, Tapasvi Lolla for his modeling support and

collaboration, Ralph Dinwiddie for his work on thermal imaging, Chad Parish for his microscopy support, Shawn Reeves for her microscopy support, Chad Duty for his support as my ORNL group leader, Craig Blue for supporting metal AM efforts at the MDF, and the rest of the great team at ORNL and TAMU that has supported me along the way. I would further like to thank my committee for their time and efforts considering my proposal, dissertation, and defense.

This research was supported by fellowship funding received from the U.S. Department of Energy, Office of Nuclear Energy, Nuclear Energy University Programs. I can truly say that this fellowship changed my life. I am thankful for the opportunities that it provided.

Portions of this research were also sponsored by the U.S. Department of Energy, Office of Energy Efficiency and Renewable Energy, Advanced Manufacturing Office, under contract DE-AC05-00OR22725 with UT-Battelle, LLC. The United States Government retains and the publisher, by accepting the article for publication, acknowledges that the United States Government retains a non-exclusive, paid-up, irrevocable, world-wide license to publish or reproduce the published form of this manuscript, or allow others to do so, for United States Government purposes.

NOMENCLATURE

XZ Plane	a cross-section of material taken parallel to the build direction with the build direction (z-axis) oriented towards the top of the image unless otherwise noted
XY Plane	a cross-section of material taken perpendicular to the build direction
AM	additive manufacturing
EBM	electron beam melting
LM	laser melting (sometimes used as SLM for selective laser melting)
DED	direct energy deposition
IN718	Inconel 718, N07718, Alloy 718
IN625	Inconel 625, N06625, Alloy 625
YS	yield strength
UTS	ultimate tensile stress
FCC	face-centered cubic
BCT	body-centered tetragonal
GB	grain boundary
δ, δ-phase	delta-phase, orthorhombic Ni_3Nb phase in IN718
δ-needle	needle-like variant of δ-phase
γ''	gamma-double-prime, BCT Ni_3Nb phase in IN718
γ'	gamma-prime, FCC Ni_3(Al, Ti) phase in IN718

γ, γ-matrix	FCC nickel matrix of IN718
DS	directionally solidified
SX	single crystal
NR	not reported (used in tables to denote unreported information)
LOM	light optical microscope
SEM	scanning electron microscope
EBSD	electron backscatter diffraction
XRD	x-ray diffraction
ISHT	*in situ* heat treatment (reference to specific technique proposed)

TABLE OF CONTENTS

Page

LIST OF FIGURES

Page

LIST OF TABLES

Page

CHAPTER I

INTRODUCTION

I.1 Additive Manufacturing

Additive Manufacturing (AM), widely known as 3D printing, is a method of manufacturing that forms parts from powder, wire, or sheets in a process that proceeds layer-by-layer. Many techniques (using many different names) have been developed to accomplish this via melting or solid-state joining. Direct energy deposition (DED) processes feed powder of wire feedstock into a melt pool to produce parts. Electron Beam Melting (EBM) and Laser Melting (LM) are both powder bed fusion (PBF) processes, that selectively melt distribute layers of metal powder to produce a part from the bottom up. PBF processes have the advantage of being able to produce more complex shapes and features (e.g. overhangs) than DED processes. All metal AM processes have advantages over casting and subtractive machining in that unique geometries can be produced, there is a low cost of retooling, and small production quantities can be more economical.

This dissertation focuses on EBM because there has been recent interest from industrial part producers in utilizing the technology. The EBM technology has faster deposition rates (§II.7) and lower amounts of residual stress (§II.3.10) than LM. The energy density of the heat source (§II.7) also enables complete melting of a wide range of alloys. Additionally, the use of a vacuum during processing reduces many issues with oxidation during processing (§II.3.2). Finally, the ability to engineer grain orientations has demonstrated significant potential for the technology to improve materials design and engineering (§II.6.1.3).

I.2 Importance for Advanced Nuclear Energy Concepts

Inconel 718 is noted for maintaining its mechanical strength at elevated operating temperatures and is used in a variety of applications (§III.1). Of specific interest (as this dissertation was the focus of a Nuclear Engineering program), is the application of Inconel 718 into power production systems. Various in-core components for nuclear reactors and components on the secondary side (tubes, heat exchangers, turbine blades) either use or have the potential to use this material. By enabling studying and improving a method of AM for IN718, this dissertation asserts that this EBM technology presents an opportunity for designers of nuclear components to produce unique designs to improve efficiency or safety of reactor systems.

I.3 Overview of Work Presented Herein

The key findings of each chapter in this dissertation can be summarized as:

- Chapter II – Reviews the whole of metal Additive Manufacturing, offering insights into the differences between various technologies and background on processing science
- Chapter III – Reviews Inconel 718, providing a concise background on the material that is the focus of this paper
- Chapter IV – Focuses on the Arcam Electron Beam Melting (EBM) hardware and provides background on the experiments run for this dissertation
- Chapter V – Explains EBM processing parameters and the impact that changes to those parameters had on the measured process time and process temperature
- Chapter VI – Characterizes the as-fabricated microstructure of EBM IN718 and presents a novel method for control phase formations *in situ*

- Chapter VII – Explores ex situ post-processing options for improving mechanical properties and rationalizes grain growth phenomena that were observed
- Chapter VIII – Reports the differences in as-fabricated tensile properties and the use of solution treatment and aging to achieve uniform tensile properties

CHAPTER II

REVIEW OF METAL ADDITIVE MANUFACTURING

This chapter has been adapted from "The Metallurgy and Processing Science of Metal Additive Manufacturing" by Sames et al., an invited review to the *International Materials Reviews*. [1]

In this chapter, AM techniques for producing metal parts are explored, with a focus on the science of metal AM: processing defects, heat transfer, solidification, solid-state precipitation, mechanical properties, and post-processing metallurgy. The various metal AM techniques are compared, with analysis of the strengths and limitations of each. Few alloys have been developed for commercial production using AM, but recent efforts are presented as a path for the ongoing development of new materials for AM processes.

II.1 Introduction & History

Additive Manufacturing (AM), or 3D printing, has grown and changed tremendously in the past 30 years since researchers in Austin, TX started development of what is arguably the first machine in the lineage of metal AM: a laser used to selectively melt layers of polymer and, later, metal. [2] The development of metal AM techniques has made great progress since then, but faces unique processing and materials development issues. Understanding the various processes used to make metal AM parts, and the issues associated with them, is critical to improving the capabilities of the hardware and the materials that are produced.

The first experiments with metal AM grew out of efforts originally targeted at forming polymer powder into 3D parts. [3-6] This research focused on powder bed laser sintering, which was patented and copyrighted as Selective Laser Sintering (SLS). One of the earliest incarnations of SLS, "Betsy", integrated the first automated powder distribution system. SLS

by similar techniques is still used today to produce metal parts (the term “sintering” is now used loosely, as many processes use complete melting) under license by EOS GmbH. Shortly after SLS was patented, a group of researchers at MIT patented a process called “three-dimensional printing”, which used inkjet printing to deposit binder. The use of “3D printing” has grown to describe all forms of AM, while the MIT method has become known as Binder Jetting (BJ). BJ can be used to create metal parts, in addition to other materials. Another class of printers known as Direct Energy Deposition (DED) deposit feedstock directly into a molten pool, as opposed to selective melting of a powder bed. Some of these machines use a wire feedstock and are very similar to welding processes. In 1995, Sandia National Laboratories developed a different approach to powder feedstock in DED with a laser heat source. This technology was first commercialized and trademarked as Laser Engineered Net Shaping (LENS), a sub-set of DED. The last major category of metal AM, sheet lamination (SL), welds together sheets of feedstock to form parts. A process that uses ultrasonic welding and computer numerical control (CNC) milling to accomplish this was originally developed and patented by Dawn White of Solidica in 1999. In 2000, research in Sweden led to the patent of another powder bed technique: Electron Beam Melting (EBM). This process was later licensed and developed by Arcam AB. This metal AM history is more concisely presented as a timeline), with significant patents highlighted in Table 1.

II.1.1 Timeline: “30 Years of 3D Metal Printing”

- 1984 – Deckard & Beaman begin work on technology to build 3D parts out of powder, using a 100W YAG laser heat source [3]
- 1986 - Deckard & Beaman start “Betsy”, continue research into “SLS” [3]
- 1986 – SLS patented by Deckard at University of Texas [7]
- 1989 - Original “3D Printing”, or inkjet binder deposition, patented by Sachs & Cima at MIT [8]
- 1995 – EOS launches EOSINT M 250 for direct metal laser sintering (DMLS) [9]

- 1995 – Sandia National Laboratories begins LENS development [10]
- 1997 – EOS licenses SLS rights from 3D Systems and focuses on powder bed technology [9]
- 1999 – Ultrasonic consolidation patented by Dawn White of Solidica [11]
- 2000 – EBM patented by Andersson & Larson [12]
- 2001 – 3D Systems acquires rights to SLS technology through acquisition of company holding original patents by Deckard [3]
- 2002 – Arcam launches first commercial machine, the S12 [13]
- 2007 – CE-certification of hip implant manufactured by EBM [13]
- 2012 – 3D Systems acquires Z-Corp, holder of original patent on inkjet binder process [3]

Table 1. Original patents for the various classifications of metal AM.

Process	Patent Number	Patent Priority Date	Inventor	Original Associated Corporation
SLS [7]	WO1988002677 A2	1986	Carl Deckard	University of Texas
"3D Printing" [8] (binder jetting)	US5204055 A	1989	Cima et al.	MIT
EBM [12]	US 7537722 B2	2000	Lars-Erik Andersson & Morgan Larsson	Arcam AB
LENS [14]	US 6046426 A	1996	Jeantette et al.	Sandia Corporation
UAM [11]	US6519500	1999	Dawn White	Solidica

Since the invention of the various metal AM processes, R&D and industry efforts have developed some niche applications. Part repairs, biomedical implants, aerospace structures, and high temperature components highlight some of the current production use of the technologies. Metal AM has received increasing attention for direct production of

end-use parts, even being highlighted by U.S. President Barack Obama in a 2014 speech on manufacturing. [15] Despite the recent attention, some big questions remain: What are the current limitations of the technology? Can those limits be overcome?

II.2 Classification of Technologies

A diverse set of processes can be used to form feedstock (powder, sheets, or wire) into 3D objects. All metal AM processes must bond together the feedstock into a dense part. The metal must be melted at some point in the process to achieve this. In order to discuss distinct classes of machines, the ASTM F42 Committee on Additive Manufacturing has issued a standard on process terminology. [16] Of the seven F42 standard categories, the following four pertain to metal AM:

- ***powder bed fusion (PBF)***
    - laser melting (LM)
    - electron beam melting (EBM)
- ***direct energy deposition (DED)***
    - laser vs. e-beam
    - wire-fed vs. powder-fed
- ***binder jetting*** **(BJ)**
    - infiltration
    - consolidation
- ***sheet lamination (SL)***
    - ultrasonic additive manufacturing (UAM)

The other three categories specified in the standard do not currently apply to metal technologies: material extrusion, material jetting, and vat photopolymerization. There are unique uses, strengths, and challenges for each process. Each category for metal AM is

explored, but more depth is given to DED and PBF due to the larger volume of recent work published on those processes.

II.2.1 Powder Bed Fusion

Powder bed fusion (PBF) includes all processes where focused energy (electron beam or laser beam) is used to selectively melt or sinter a layer of a powder bed. For metals, melting is typically used instead of sintering. The use of laser sintering has been previously reviewed, [17] but much progress has been made since this work to include the use of full melting. Re-melting of previous layers during the melting of the current layer allows for adherence of the current layer to the rest of the part. A schematic of a PBF laser melting (LM) machine is shown in Figure 1. A schematic of PBF electron beam melting (EBM) is shown in Figure 2. Although both systems use the same powder bed principle for layer-wise selective melting, there are significant differences in the hardware setup. The EBM system is essentially a high-powered scanning electron microscope (SEM), which requires a filament, magnetic coils to collimate and deflect the position of the beam, and an electron beam column. LM typically has a system of lenses and a scanning mirror or galvanometer to maneuver the position of the beam. Powder distribution is handled differently as well; LM systems use a dispersing piston and roller, while EBM systems use powder hoppers and a rake. Both EBM and LM processes require certain steps: machine setup, operation, powder recovery, and substrate removal.

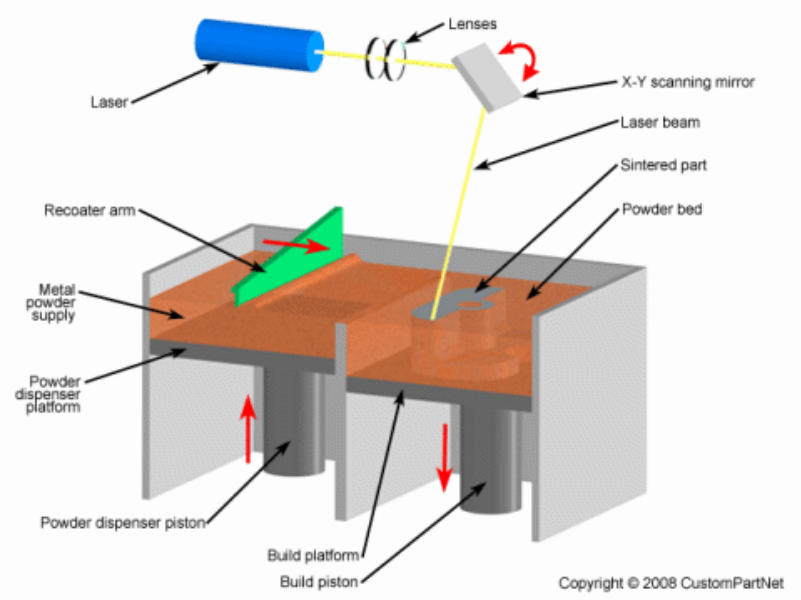

Figure 1. LM system schematic. [18]

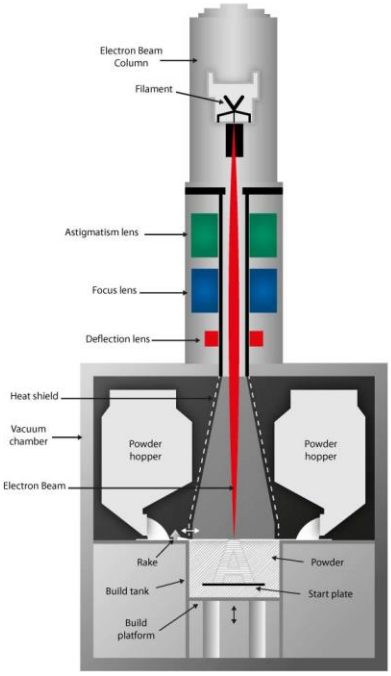

Figure 2. EBM system schematic. [19]

To setup a PBF machine, the build substrate must be positioned. The build substrate, or "start plate", is used to give mechanical and thermal support to the build material. LM processes bolt or clamp down the substrate, whereas the EBM process typically sinters powder surrounding the plate to provide stability. When successive layers of powder are distributed (rolled or raked out), existing layers of the build must not move. The substrate helps eliminate swelling and other process defects in PBF from the first layers, as building overhangs on top of loose powder can cause localized temperature fluctuations. Finally, powder containers must be loaded and a number of sensors checked and adjusted.

The operation of a PBF machine is governed by the details of the scan strategy (§II.3.6) and processing parameters (§II.4.3), which will be discussed later in more detail. After the build is complete, excess powder must be removed from the build chamber. For EBM parts, this powder is run through a powder recovery system to remove and recover sintered powder from around the parts. For LM processes, powder surrounding the parts does not sinter as much and can be sifted directly to remove any sintered clusters. Depending on the PBF process material, the build substrate may adhere to the parts. [20] The substrate must be cut off, with abrasive saws and wire EDM being common methods. For some material combinations like Ti-6Al-4V deposit and stainless steel substrate in EBM, material properties promote poor adherence; the parts fall off the substrate after the build, or can be easily removed by applied force. Parts coming directly out of the machine are considered "as-fabricated".

II.2.2 Direct Energy Deposition

Direct Energy Deposition (DED) encompasses all processes where focused energy generates a melt pool into which feedstock is deposited. This process can use a laser, arc, or e-beam heat source. The feedstock used can be either wire (Figure 3) or powder (Figure 4). The origins of this category can be traced to welding technology, which deposits material outside of a build environment by flowing a shield gas over the melt pool.

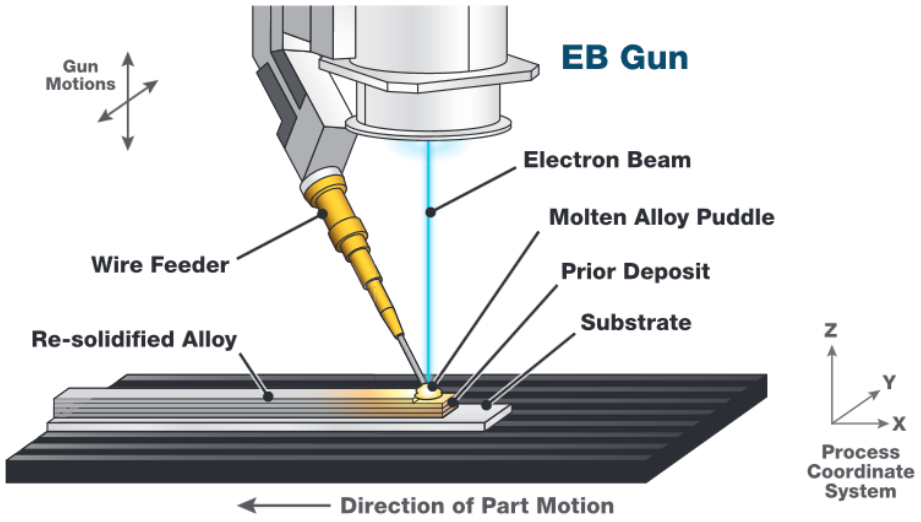

Figure 3. Electron beam, wire-fed DED system.[21]

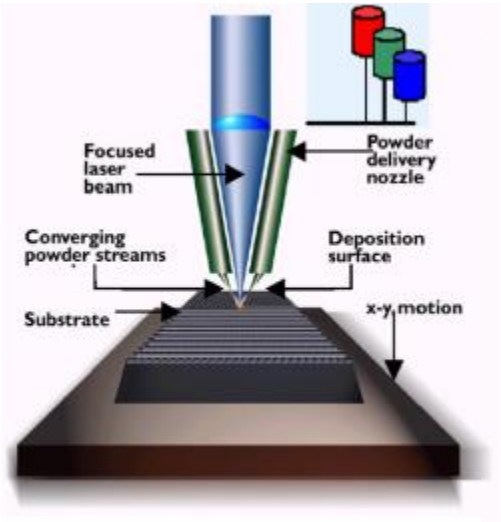

Figure 4. Laser, powder-fed DED system (LENS). [22]

One of the most studied and commercialized forms of DED is accomplished using a laser heat source to melt a stream of powder feedstock (powder-fed). This technology sub-set

has its roots in research at Sandia National Laboratories and was originally patented as the LENS process.[22, 23] Other DED processes feed wire into a molten pool (wire-fed), and are essentially extensions of welding technology. [24, 25] In fact, the use of welding machines to make parts via multi-pass welding is presently being explored. [26]

Machine setup is relatively simple; machine software automatically checks most sensors. As in PBF, powder hoppers must be filled and a build substrate positioned. The substrate can be positioned in a stationary position (3-axis systems) or on rotating axes (5+ axis systems) to increase the ability of the machine to process more complex geometries. In powder-fed systems, the feed rate of the powder must be verified regularly. If flow is impeded, nozzle cleaning or other maintenance may be performed. The build chamber is enclosed to provide laser safety, but the chamber is not necessarily filled with inert gas. For non-reactive metals, a shield gas directed at the melt pool may provide enough resistance to oxidation. For more reactive metals, like titanium, the chamber is flooded with an inert gas (argon or nitrogen). A vacuum pump and purge cycles may be used to reduce oxygen content. Cyclic purging can consume a significant amount of gas, as the build chamber is much larger than those in PBF systems.

As in PBF, a finished DED part is typically attached to the build substrate. Parts are then post-processed both thermally (to reduce residual stress and improve properties) and to achieve the desired final geometry (parts produced using DED are typically near net shapes with a rough finish). Parts may be removed from the substrate using the same processes for an adhered PBF part. Excess powder from machine operation is vacuumed to clean out the machine. Depending on the operator, this powder can may be recovered or disposed. Disposal is usually a costly option, as powder costs are typically high.

II.3 Material Processing Issues

Although PBF and DED processes have significant differences, there are some common materials processing issues that occur in both platforms. These issues are explored, noting differences between categories of equipment where appropriate. As with traditional processing methods (casting, welding, etc.), porosity is a common concern in metal AM. Other defects (residual stress, delamination, cracking, swelling, etc.) are more unique to welding or metal AM. Scan strategy, process temperature, feedstock, build chamber atmosphere, and many other inputs determine the occurrence and quantity of defects. Understanding defects, and how they arise, can help operators improve process reliability and the quality of parts produced.

In order to understand the complex relationship between basic processing science, defects, and the end product of an AM process it is useful to consider a general process flow chart (Figure 5). This process design and phenomena map links key outcomes to process selection decisions through fundamental phenomena. The process inputs are AM Software & Part Geometry, Scan Strategy, AM Hardware, Build Chamber Atmosphere, and Feedstock Quality. The process outputs are Mechanical Properties, Failed Builds, and Feature Size & Geometry Scaling. A box encloses the thermal and particle physics interaction steps: Applied Energy, Beam Interactions, Heat Transfer, and Process Temperature. These physics interactions, if properly modeled, should be able to describe dynamic process temperature, which is one of (if not the most) defining quantity of metal AM processing.

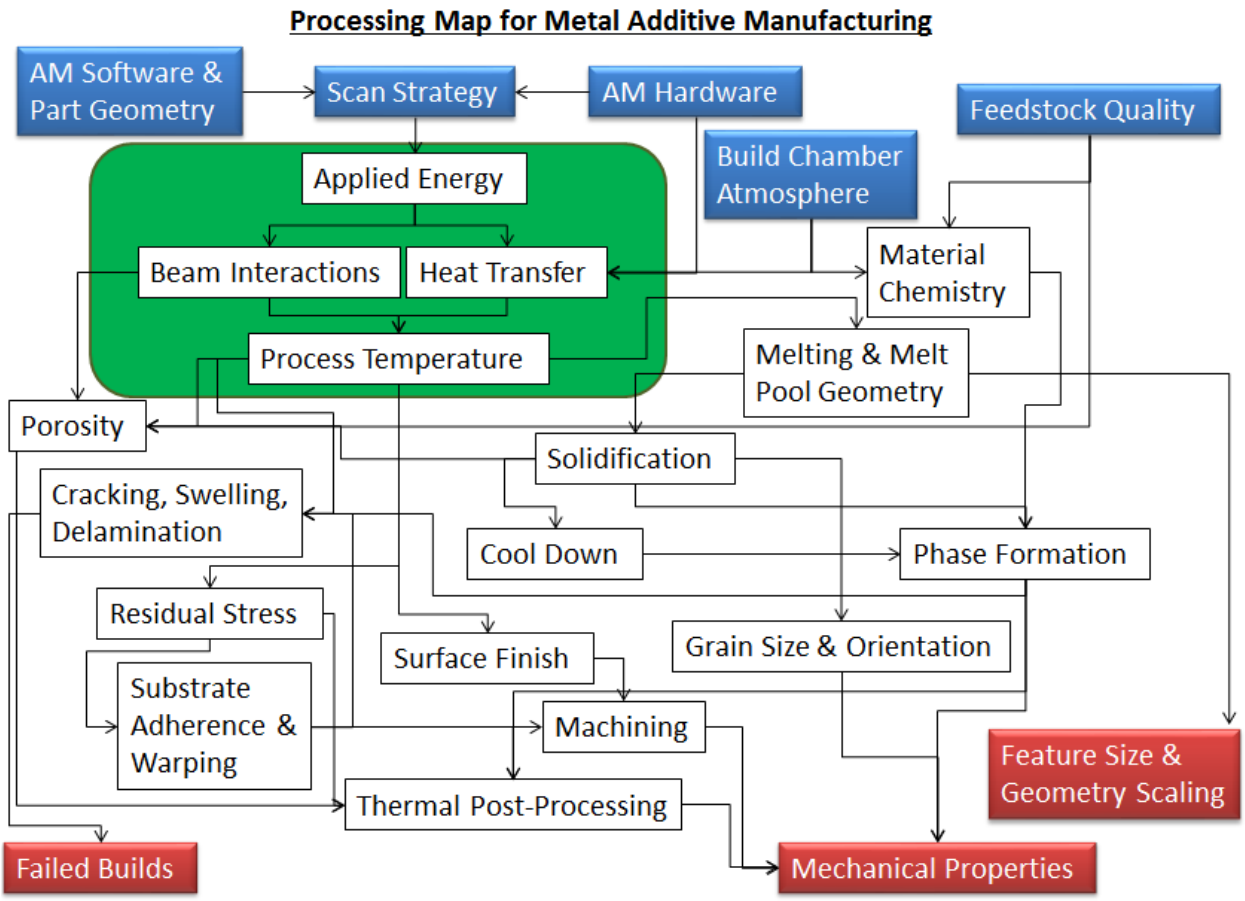

Figure 5. Process Design and Phenomena Map for metal AM.

II.3.1 Feature Size, Surface Finish, and Geometry Scaling

When printing metal parts, the minimum feature size, surface roughness, and geometrical accuracy of the part are typical concerns for equipment operators, but over-focusing on these properties is not useful for most applications because the part surface will ultimately be machined during post-processing. The minimum feature size is determined by the minimum diameter of the heat source and the size of the feedstock. This data is summarized in Table 2. It can be seen that PBF fusion typically has the best resolution, with

the resolution of LM slightly better than EBM depending on parameters used. Powder-fed DED has better resolution than wire-fed DED, which can be attributed to the use of finer feedstock (powder vs. wire). The feature size of DED systems is so large that parts made with these techniques are limited to more simple geometries than PBF techniques. Smaller feature sizes smaller layer thickness currently comes at the expense of deposition rate. The deposition rates of various technologies are explored in more detail later in this paper (§II.7). Due to small feature size and the low inertia to changing the position of the beam, PBF techniques can utilize the minimum feature size to print metal mesh or foam structures. These structures melt metal "struts", typically the size of an individual pulse of the heat source (see Table 2). Mesh parts have been well studied and reviewed elsewhere. [27, 28]

Table 2. Typcial layer thicknesses and minimum feature sizes of PBF and DED processes.

Process	Typical Layer Thickness [µm]	Minimum Feature Size or Beam Diameter [µm]
PBF – LM [29]	10-50	75-100
PBF – EBM [19]	50	100-200
DED – Powder Fed [30]	250	380
DED – Wire Fed [31]	3,000	16,000

There are two separate contributors to surface roughness as shown in Figure 6: (1) non-flat layer edges or layer roughness and (2) the actual roughness of the metal surface. The layering effect can be reduced by using smaller layer thickness values. This usually means longer melt times; the layer thickness dictates how many layers a part is divided up into. More layers translate to longer build times. The actual roughness of a material depends upon the details of the machine producing the part. DED typically has larger layer thickness, which mostly limits this technology to near net shapes (shapes produced close to the desired part geometry, but planned for the use of machining to deliver the final geometry and details). Near net shape processing is different from traditional subtractive methods where a full block of material is machined down to a final part. PBF systems typically have

finer resolution and layer thickness, but are prone to satellite formation [32] due to the sintering of powder at the part edges. Finer powder means smaller satellites and less surface roughness. LM machines use finer powder and smaller layer thickness than EBM, which results in less surface roughness.

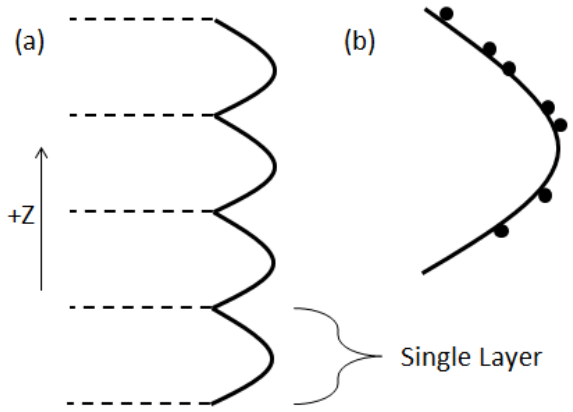

Figure 6. Sketch of the contributions to surface finish by (a) layer roughness and (b) actual surface roughness showing satellites of small powder particles incorporated onto the surface.

Geometrical accuracy can be measured by taking 3D lasers scans (or similar technique) and calculating the deviation relative to the original part file. Typical corrections are empirical modifications to scale part files in a Cartesian system. For example, an x-axis might be smaller than intended by some scaling factor. The scaling factor is then used to increase the x-axis length in the part file, before printing. This is typically accounted for during machine calibration. Post-fabrication machining is typically needed for LM, EBM, and DED parts, as even the best achievable surface finish is still not as good as a machined finish. If machining is used, the actual part tolerance, surface finish, and minimum feature size of AM parts is dictated by any machining. For this reason, work to refine surface finish using smaller powder particles and smaller layer thicknesses may just add process time and cost (the

smaller the layer, the more layers must be processed) without improving the quality of the final part.

II.3.2 Build Chamber Atmosphere

The atmosphere under which metal is processed strongly affects chemistry, processability, and heat transfer. Inert gas and vacuum systems are typically used, and each has unique processing concerns. Metal powders have a tendency to oxidize and collect moisture when exposed to air. At higher temperatures, this oxidation can be accelerated. For this reason, welding machines use inert shield gases. AM processes have the same need. As discussed previously, DED typically operates with a shield gas flowing over the melt surface and may operate under inert atmosphere. LM processes are typically run in an inert environment, with an atmosphere of Argon or Nitrogen filling or flowing over the build surface. The flow rate of the fill gas and the pathway of the flow have been shown to be important in porosity reduction in LM Ti-6Al-4V. [33] Small features may lead to heat concentration in LM, which can cause localized oxidation.

The EBM process uses a heated filament (usually made of tungsten) to generate electrons, which requires a vacuum-capable build chamber to operate the machine ($<5x10^{-2}$ Pa chamber pressure, $<5x10^{-4}$ Pa column pressure). During beam operation, a small quantity of helium is injected to reduce electrical charging of the build volume. This raises the pressure of the build chamber to ~0.3 Pa during beam operation. Operating in a near-vacuum environment leads to increased melt vaporization and unique heat transfer considerations.

II.3.3 Feedstock Quality

The quality of the feedstock that is used in the AM process is important to the quality of the final part. The quality of the powder is determined by size, shape, surface morphology,

composition, and amount of internal porosity. The quality of powder determines physical variables, such as flowability and apparent density. There are a variety of atomization techniques for producing metal powder, each producing distinct variations in powder quality. There are several unique quality issues related to wire feedstock for DED as well. By understanding feedstock quality, an operator can select the optimal material for processing in a given system. Further information on the standards associated with quantifying powder characteristics and the details of powder science are well described elsewhere. [34]

The quality of powder is directly related to the production technique. A variety of techniques are used: gas atomization (GA), rotary atomization (RA), plasma rotating electrode process (PREP), plasma atomization (PA), and others. Some atomization techniques yield irregular shapes (like RA), others have a large amount of satellites (like GA), and some are highly spherical and smooth (like PREP and PA). Figure 7 shows powder surface morphology and shape, as well as cross-sections to analyze internal porosity. Porosity in the powder feedstock is common for certain production techniques, like gas-atomization (GA), that entrap inert gas during production. This entrapped gas is transferred to the part, due to rapid solidification, and results in *powder-induced porosity* in the fabricated material. These pores are spherical, resulting from the vapor pressure of the entrapped gas. Higher quality powders produced via the plasma rotating electrode process (PREP) do not contain such pores and have been used to eliminate powder-induced porosity in DED and PBF systems. [20, 35, 36]

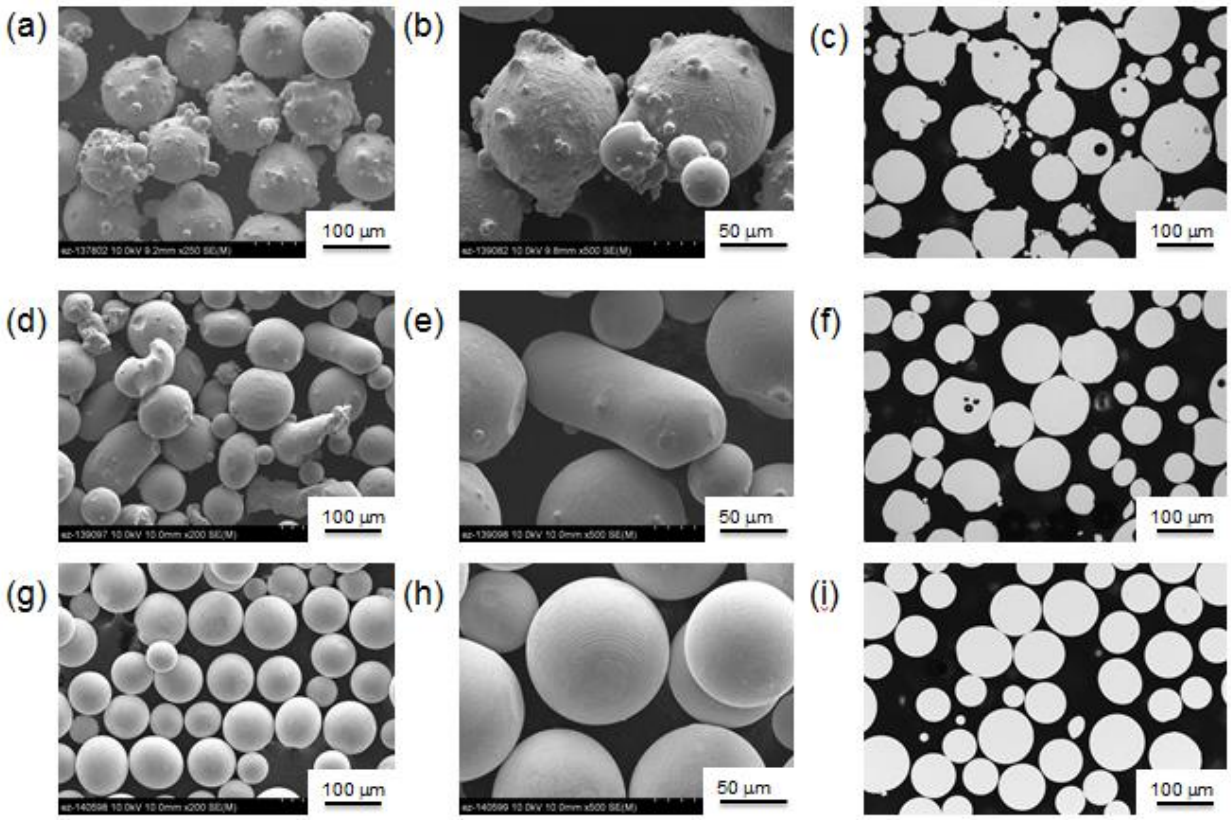

Figure 7. Comparison of powder quality before use: (a) SEM 250x of GA, (b) SEM 500x of GA, (c) LOM of GA, (d) SEM 200x of RA, (e) SEM 500x of RA, (f) LOM of RA, (g) SEM 200x of PREP, (h) SEM 500x of PREP, (i) LOM of PREP. [20]

Flowability (how well a powder flows) and apparent density (how well a powder packs) are important quantitative powder characteristics that are directly related to qualitative characteristics. A Hall Flow meter can be used to measure flow rate (flowability) [37] and apparent density [38] according to ASTM standards. Spherical particles improve flowability and apparent density. Smooth particle surfaces are better than surfaces with satellites or other defects. Fine particles, or "fines", typically improve apparent density and flowability, but can become segregated from coarser particles during use.

The nominal particle size distribution of powder used in LM is 10-45um, in EBM is 45-106um [39], and in DED is 20-200um. [40] The main tradeoff in the selection of powder size is cost versus surface finish. Smaller particles tend to improve surface finish and are normally used with smaller layer thicknesses, but smaller powder particles typically cost more as a feedstock (than a larger size range) due to lower yields for smaller particles in powder production. LM uses a fine distribution of powder to improve surface finish by enabling shorter layer thicknesses. EBM uses slightly thicker layers and a correspondingly large size distribution. EBM can use smaller size distributions, with no noticeable effect on chemistry, material properties, or microstructure. [41] The effect of powder flowability on processability using various hardware is not well published, though it is understood as an important parameter by industrial producers of AM parts. PBF systems typically have a hardware specific flowability that depends on the powder distribution method used. Very fine particles size distributions that do not have a measurable flowability may still be processable in some systems. Powder-fed DED systems must consider the effect of flowability on the ability of powder to feed into the carrier gas stream. Once in the stream, the powder flow rate has been observed to have little effect on particle speed during DED processing. [42]

Additionally, the chemical composition of the powder must remain within alloy-specific specifications. It is important to measure the elemental composition of recycled powder (wire is not recycled), as evaporative losses, contamination from powder recovery (vacuums or grit blaster used in EBM), and reaction with oxygen, nitrogen, or other gases must be considered for quality control. Depending on the feedstock material, oxidation and humidity control may be important for both wire and powder storage. A thorough survey of the many powder types used for laser processes exists [43], regarding the research available on specific powder alloys.

Wire feedstock for wire-fed DED processes is less defect prone than powder and is commonly available from welding suppliers. The diameter of wire used for wire-fed DED is typically on the order of 2.4mm. [31] Better quality wire will have less variation in wire diameter, which is similar to requirements for plastic extrusions printers that use plastic wire as a feedstock. Porosity is a common welding defect, and the quality of wire is known to affect the amount of porosity in the weld deposit. [44] For reactive metal like titanium, surface adsorption and reactions with atmosphere may also cause defects. More notably, the presence of cracks or scratches on the wire surface may translate directly to porosity formation. Unlike powder production, gas porosity is not an issue in wire production. In a study of both powder and wire feedstock, it was noted that powder had porosity, whereas the wire did not. [45]

II.3.4 Beam-Powder Interactions

The interaction of the heat source with the feedstock or melt pool impacts the amount of energy utilization and can lead to ejecta and porosity. There are four basic modes of particle ejection during beam melting processes: (1) convective transport of liquid or vaporized metal out of the melt pool (or spatter ejection), (2) electrostatic repulsion of powder particles in EBM, (3) kinetic recoil of powder in DED, and (4) enhanced convection of powder in gas streams. Lasers incur intensity losses due to reflection, whereas e-beams incur backscatter losses of electrons. E-beams systems must be designed to reduce electrical charge buildup. DED systems must also be designed to consider the effective feed rate of the feedstock, as appropriate amounts of deposit material must be delivered.

The convective transport of liquid or vapor out of the melt pool is commonly called “spatter” or “spatter ejection” and is seen in PBF, DED, and welding. This is caused by the application of a high energy beam creating localized boiling, where the energy of the ejecta must overcome surface tension forces. [46] These particles can be identified in PBF and DED

by the high temperature emission of white or other light, which is the reason that these ejecta are sometimes referred to as “fireworks”.

A laser imparts energy to the powder bed via photons. Laser techniques must therefore compensate for the reflectivity/absorptivity [47] of the metal powder, as some of the applied energy will not be absorbed. Depending on the metal, this may be a significant limitation. Higher power lasers are typically used to overcome this barrier to melting, but the higher laser power can lead to increased spatter ejection. [48] Pulse shaping, or the control of the shape of the laser power profile, has shown promise for increasing energy absorption and decreasing spatter ejection in LM. [32] Pulse shaping can be used to more slowly heat a melt area (effectively a preheat), which can cause a decrease in reflectivity associated with higher temperatures. As laser control software and hardware improves, this technique may prove useful.

In the EBM process, electrons interact with the material to transfer not just energy, but also electrical charge. If repulsive electrostatic forces are greater than the forces holding particles to the powder bed, powder particles may be ejected from the powder bed. [49] This effect can cause the bulk displacement of powder (Figure 8) within the powder bed, known as “smoking”, if sintering is not properly achieved. [50, 51] The electrostatic ejection of powder particles can be reduced in EBM by using a rapidly-scanned, diffuse beam to slightly sinter the melt surface prior to melting. Small quantities of helium gas are also injected during melting to dissipate charge from the melt surface. The ratio of the bulk density to the electrical resistivity of the powder has been identified as important for the reduction of powder ejection in EBM. [49] Pre-sintering in LM systems is not necessary, as photons do not cause charge buildup.

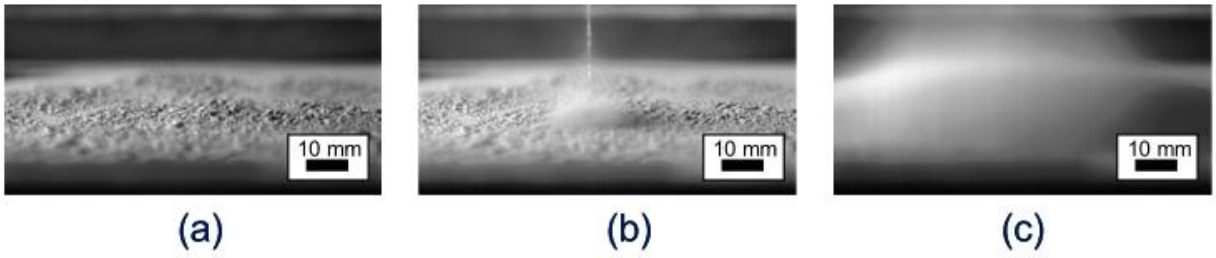

Figure 8. An event of "smoking" caused by electrostatic repulsion: (a) distributed powder bed, (b) applied beam, and (c) "smoking" or a cloud of charged powder particles. [51]

Powder may also be removed by kinetic recoil (powder-fed DED) and convection of powder in the fill or shield gas steam (LM or powder-fed DED). As the stream of powder particles is sprayed into the melt pool during DED, some particles will recoil and avoid deposition. This loss is typically adjusted for experimentally, but can be a significant loss of powder (if not recovered). Small traces of powder may appear as "dust" present in the fill gas of inert atmosphere processes. Particles lost in this way have not been quantified, though are probably not significant compared to other loss mechanisms. Both kinetic recoil and convection of powder do not directly remove particles from the melt pool, which means that these mechanisms are not of likely importance for control of porosity. Electrostatic repulsion is mostly an operational concern, but may lead to some porosity. Spatter ejection is known to result in weld defects and is an underlying mechanism for the formation of some forms of process-induced porosity.

II.3.5 Porosity

Porosity is a common defect in metal AM parts and can negatively affect mechanical properties. Porosity can be powder induced, process induced, or an artifact of solidification (compared in Figure 9). [20] As previously discussed, gas pores may form inside the powder feedstock during powder atomization. These spherical, gas pores can translate directly to

the as-fabricated parts. For most studies, porosity formation is dominated by processing technique. Process parameters must be properly tuned to avoid a range of mechanisms that can create pores.

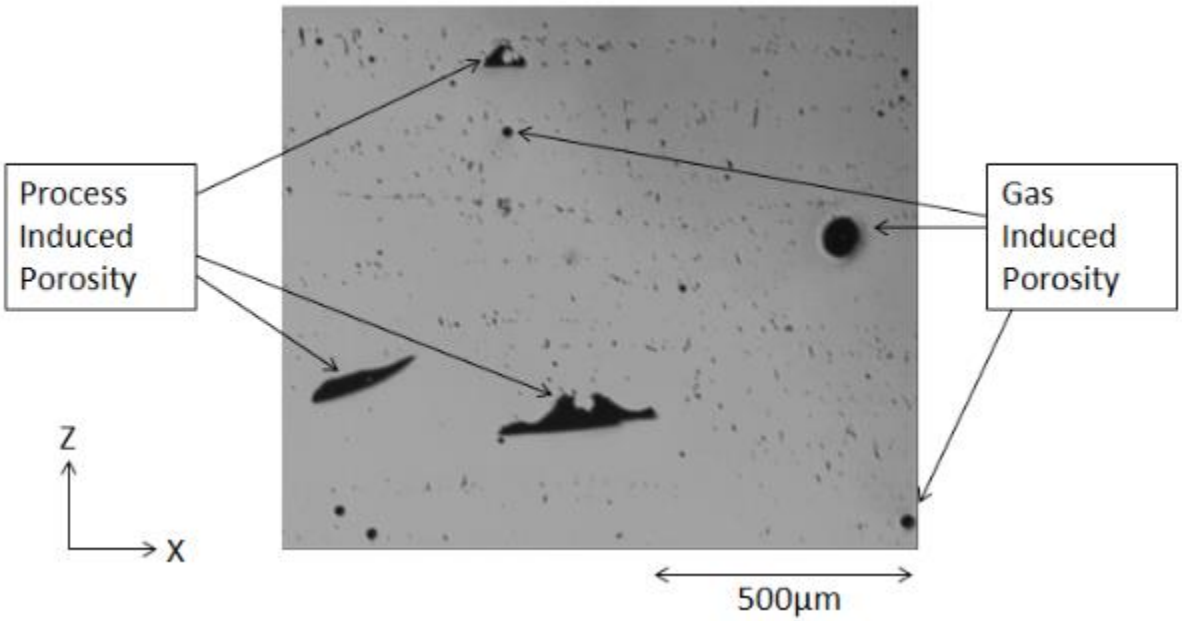

Figure 9. Light optical microscopy showing comparison of process induced, lack of fusion porosity to entrapped, gas porosity transferred from the powder feedstock. [20]

Pores formed by processing technique, known as *process induced porosity*, are formed when the applied energy is not sufficient for complete melting or spatter ejection occurs. These pores are typically non-spherical, and come in a variety of sizes (sub-micron to macroscopic). Different processing issues can create defects in the material, some of which contribute to porosity. When not enough power is supplied to a region of powder, *lack of fusion* can occur. Lack of fusion regions may be identifiable by un-melted powder particles visible in or near the pore. Another form of process-induced porosity is caused during solidification. *Shrinkage porosity* (sometimes termed “hot tearing”, explored in more detail

in §V.2.1.) is the incomplete flow of metal into the desired melt region. Spatter ejection may also lead to regions of porosity. Unlike lack of fusion regions that are created by insufficient energy application, spattering may also be caused by too much energy application. To limit spatter ejection, an operator will typically watch the process and tune parameters, while developing a new material processing strategy. Process induced porosity has other contributors, including the effect of powder consolidation from a loosely packed powder bed to a fully dense part. [52] Powder is distributed onto the processing surface and includes particles larger in diameter than the layer thickness, which upon melting are intended to consolidate into a layer of the correct height. With optimized melting parameters, process induced porosity can be reduced to very low levels in DED, LM, and EBM (greater than 99% dense). [53-55] The relationships between lack of fusion, shrinkage regions, and cracks have not been fully studied in AM material. Though, work has been done to explore the effect of process parameters (beam speed and beam power) on the formation of process-induced and gas-induced porosity. [30]

II.3.6 Scan Strategy

The tool path that the heat source follows for lasers or electron beams is classified as the *scan strategy*. Various scan strategies have been developed and are depicted in Figure 10. Scan strategies for DED tend to be relatively simple, limited by the movement of the powder or wire feeding system. Unidirectional (Figure 10(a)) and bi-directional (Figure 10(b)) fills are both standard DED processing techniques. These strategies use rectilinear infill to melt a given part layer. Both unidirectional and bidirectional fills are used in LM and EBM, though improvements have been made. In LM, island scanning (Figure 10(c)) has been used to reduce residual stress. [56] Island scanning is a checkerboard pattern of alternating unidirectional fills and reduces temperature gradients in the scan plane (x-y plane) by distributing the process heat. PBF systems tend to have lower inertia to beam movement than DED (due to no feeding mechanism) and can also melt in a pulsed, spot

mode (Figure 10(d)). This spot mode is typically used in EBM to melt contours (Figure 10(e)), which are boundaries between infill and the powder bed. Contours follow the edges of the part, melting along free surfaces of the part geometry. LM systems also used contours, though the contour melting strategy is typically linear (Figure 10(f)). Contour passes are done after melting in LM to refine surface finish [56], whereas the passes are done before melting in EBM. In EBM, the melt process heats up the build material; contours that are run after melting tend to form more satellites due to higher temperature, yielding a rougher surface finish. Most machines offer operators the choice of contour order and it is one of many parameters optimized by the machine manufacturer before releasing parameters for a material. The scan strategy for a given build may be adjusted by layer or by part. Unidirectional, bi-directional, and island scanning strategies are typically rotated at an angle between each layer.

Scan strategy has a direct impact on process parameters; heat source power and velocity must be optimized for a given scan strategy. The relationship between applied heat source power and the heat source velocity is a key parameter of PBF and DED processes and is addressed in more detail in §II.4 with heat transfer, solidification, and thermal cycles. This relationship is important for eliminating process-induced porosity and determining grain morphology.

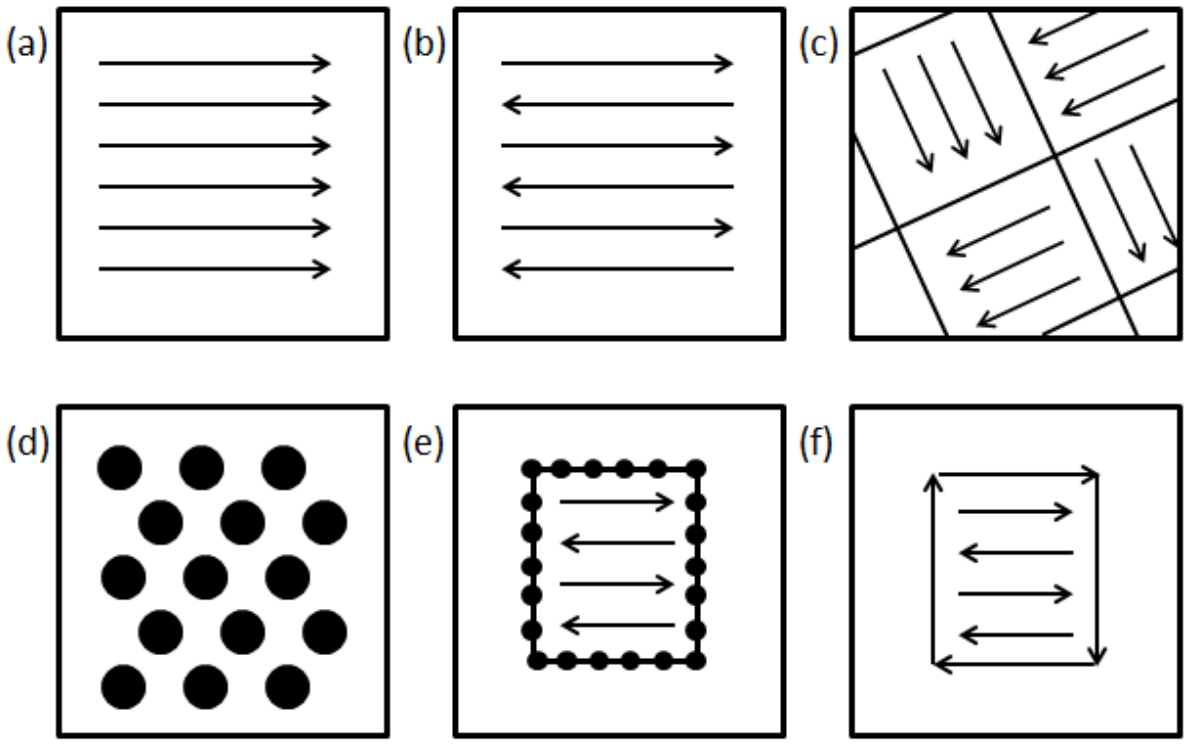

Figure 10. Scan strategies used to determine heat source path in metal AM as seen in the X-Y plane (perpendicular to the build direction): (a) unidirectional or concurrent fill, (b) bi-directional, snaking, or countercurrent fill, (c) island scanning, (d) spot melting, (e) spot melting contours with snaking fill, and (f) line melting contours with snaking fill.

II.3.7 Deposition Strategy

The way in which feedstock is delivered to the melt surface determines deposition rate and can have a strong impact on material defect and properties. In wire-fed DED, the vertical angle (α) and the horizontal angle (β) of the wire feed are related to deposition efficiency, surface roughness, incomplete melting, rippling, and other processing defects. [45] Similarly, the angle for powder spraying is important to powder-fed processes. In both powder-fed and wire-fed DED, the deposition rate is critically important. Deposition rate and the velocity of the heat source both determine how much material gets deposited in a

given pass. In DED, the build-up of material must be considered to appropriately choose the z-axis layer height, or layer thickness. In PBF, layer thickness determines how much powder is "raked" or distributed to the melt surface. In PBF, a "rake" is a metal, ceramic, or polymer-coated bar that sweeps out powder onto the build surface. The number of passes of the rake, mechanical type of rake, and the amount of powder being retrieved per pass determine the efficiency of the PBF powder delivery system.

II.3.8 Cracking, Delamination, & Swelling

The formation of defects is essentially dependent on process temperature. Cracking of the microstructure may occur during solidification or subsequent heating. Macroscopic cracks may relate to other defects, including porosity. Delamination is a lack of layer adherence due to incomplete melting (melt temperature not high enough). Delamination leading to interlayer cracking is shown in Figure 11. If the process temperature is too high, a combination of melt pool size and surface tension may lead to swelling or melt balling. If processing conditions are tightly controlled, most of these defects can be avoided. Cracking of the microstructure is material dependent as well, and there may be some processing cases where cracking is unavoidable.

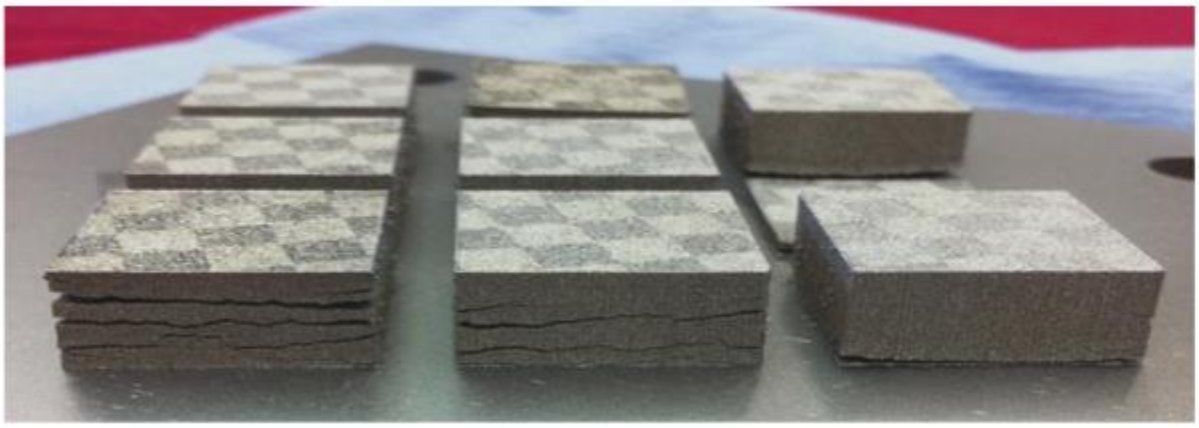

Figure 11. Layer delamination and cracking can be a problem in SLM (shown for M2 tool steel). [57]

There are different material-dependent mechanisms for which cracks form in AM material. [56] *Solidification cracking* can occur for some materials if too much energy is applied, and arises from the stress induced between solidified areas of the melt pool and areas that have yet to solidify. This type of cracking is dependent upon the solidification nature of the material (dendritic, cellular, planar). *Grain boundary cracking* is cracking that nucleates or occurs along grain boundaries of the material. The origins of this type of cracking are material dependent and depend on the formation or dissolution of precipitate phases and the grain boundary morphology. The process parameters required to minimize process induced porosity may differ from those required to minimize the formation of cracks. [56] Solidification cracking and grain boundary cracking are both phenomena that occur within the microstructure. More generally, *cracking* is sometimes used to describe macroscopic cracks in the material. These cracks may nucleate due to other macroscopic defects such as delamination that are not related to excessive energy input. [57]

Delamination is the separation of adjacent layers within parts due to incomplete melting between layers. This may occur due to incomplete melting of powder or insufficient re-melting of the underlying solid. Whereas the effects of lack-of-fusion defects may be localized within the interior of the part and mitigated with post-processing, the effects of delamination are macroscopic and cannot be repaired by post-processing. Reduction in macroscopic cracking has been demonstrated in LM by using substrate heating. [57]

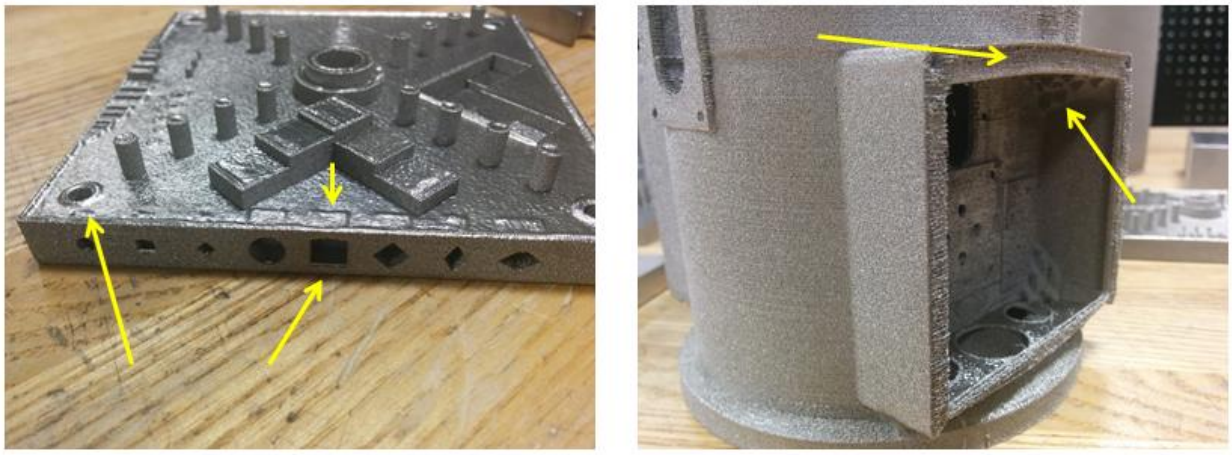

Figure 12. For EBM printed Ti-6Al-4V parts it can be seen that (Left) a NIST test artifact designed to test AM capabilities has overhangs printed in the side of the part. These are intended to test the ability of various machines to print overhangs. Minor swelling can be seen both above the overhang and near a hole on the left side on the top surface. (Right) A complex robotic part shows a slightly deformed overhang, with sintered powder and support stubs left underneath.

Excess energy input can lead to overheating of the material. This may occur due to small features or overhangs in the part geometry, as shown in Figure 12. Overhangs in PBF are typically made using support structures such as wafers. Lattice support structures have been recently explored. [58] There are two kinds of supports: mechanical support and thermal support. Mechanical supports help prevent overhangs from deformation from gravity or growth stresses. Thermal supports allow applied energy a conductive path away from the melt surface in PBF. *Swelling* is the rise of solid material above the plane of powder distribution and melting. This is similar to the humping phenomenon in welding and occurs due to surface tension effects related to the melt pool geometry. [20] *Melt ball formation* is the solidification of melted material into spheres instead of solid layers, wetted onto the underlying part. Surface tension is the physical phenomenon that drives melt balling, which is directly related to melt pool dimensions. [59] When the length over diameter ratio is great than 2.1 ($\ell/d > 2.1$), the melt pool will transition from a weld bead

(half cylinder) to a melt ball (sphere). Melt ball formation, as shown in Figure 13, is an extreme condition typically only observed during material development. It occurs with higher temperatures or alongside delamination with lower temperatures. In EBM of stainless steel, a trade-off has been noted between "balling" and delamination. [60] Wetting forces and capillary forces have been identified as contributors to both balling and swelling. [61, 62] It may be difficult to identify the cause of defects post-build, as one type of defect may change the local heat transfer conditions and lead to the compounding of defects. An example of this is the formation of porosity, which can lead to reduced thermal conductivity, causing melt ball formation or swelling on subsequent layers due to unexpected thermal resistance.

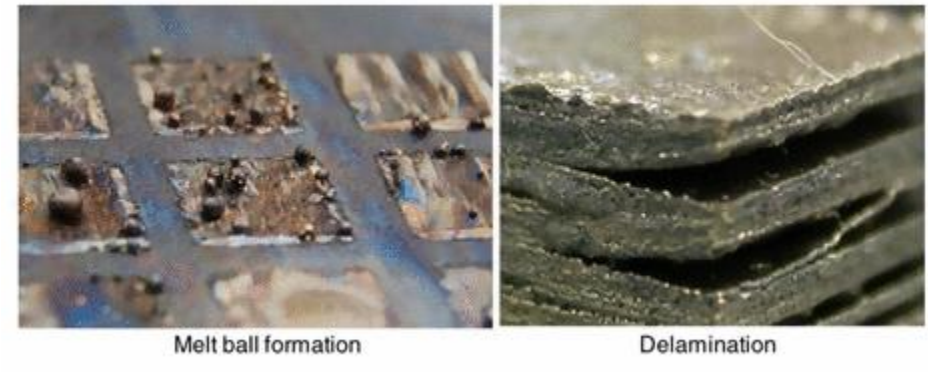

Figure 13. Melt ball formation and Delamination in EBM stainless steel. [60]

II.3.9 Substrate Adherence & Warping

The use of a substrate for the deposition of material is standard practice in DED and PBF but typically adds additional work during post-processing. Metal AM processes build on top of a metal substrate to achieve mechanical adherence of the first layers of the melted part. [20] The substrate may be left at room temperature, heated by internal heaters, or heated by an

electron beam. Most metal deposits form ductile interfaces and must be cut off of the substrate during post-processing. Ti-6Al-4V deposited on Stainless Steel 304 substrate forms a more brittle interface that can be removed by application of force, without cutting. This kind of interface is desirable for decreasing the number of post-processing steps.

Substrates may warp during use as shown in Figure 14. [63] This can be due to the operating temperature of the AM process, the heat treatment of the substrate prior to use, or due to differential coefficients of thermal expansion. Some processes use a substrate of the same material as the build, like stainless steel, to reduce this effect. The ultimate result of substrate warping is distortion of part geometry within the affected layers and possible lack-of-fusion or delamination at the transition region back to unaffected material. Substrate warping is a form of stress relief that results in permanent plastic deformation. Recent work to model substrate distortion has rationalized the progression of stresses with thermal history in EBM. [64] The same mechanisms that cause substrate warping can also lead to major issues with residual stress.

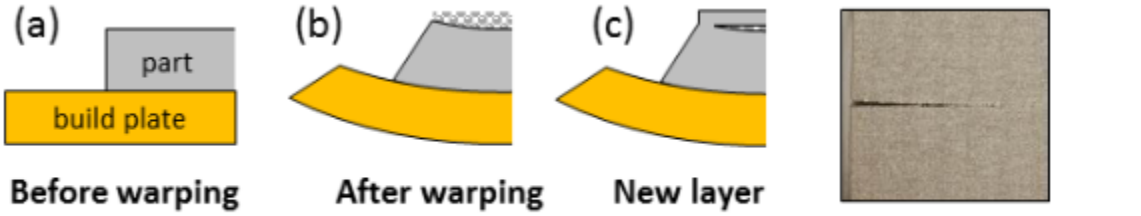

Figure 14. The effect of substrate warping can lead to lack-of-fusion or delamination. [63]

II.3.10 Residual Stress

Residual stress is common in metal AM materials due to large thermal gradients during processing, and it can negatively impact mechanical properties and act as a driving force for changes in grain structure. Residual stress is a stress within a material that persists after the removal of an applied stress. Macroscopic residual stresses can have a dramatic effect on the bulk behavior of AM parts, whereas the effects of microscopic residual stresses from precipitates or atomic dislocations are more localized. Macroscopic residual stress can be thermally introduced in metal AM by (1) differential heating of solid and (2) differential cooling during and after solidification. [65] Residual stress is a concern because it can negatively affect the mechanical properties of as-fabricated parts or lead to geometrical distortions. A number of techniques have been applied to measure residual stress in AM parts and are discussed in this section. The magnitude of residual stress and the ways to reduce it are process dependent. Residual stress may influence recrystallization, which is discussed in detail later with post-processing (§II.5.4).

Residual stress tends to be compressive in the center of DED and PBF parts, tensile at the edge, and more highly concentrated near the substrate interface. [66-69] Axially, peak tensile residual stresses were measured near the top surface and were noted to be balanced by compressive stresses in the sample interior. [66] Support structure, used to separate the build from the substrate, may slightly reduce residual stress due to having a higher initial temperature than the bare substrate. [66] Upon removal from the substrate, residual stress is relieved but may result in deformation of the part. [65] Modeling of thermal cycles for wire-fed DED using finite element methods has confirmed measurements of higher residual stress near the substrate interface. [70]

Residual stress tends to be higher in room temperature (ambient) processes (DED, LM) than those that operate at higher bulk temperature (EBM). DED residual stress measurements

using neutron diffraction have shown that residual stress in parts was 50-80% of the 0.2% yield stress. [67]

The effect of island scanning on residual stress has been studied. [63, 71] Island scanning in LM was observed to reduce porosity in parts but lead to increased residual stress. Smaller islands resulted in lower tensile residual stress than larger islands, but continuous scanning resulted in the least amount of tensile residual stress. All scan strategies studied resulted in roughly equivalent compressive residual stress. This result is unexpected, as the purpose of an island scanning strategy is nominally to reduce residual stress. It was noted, however, that significant quantities of porosity in the continuous scanning samples existed and may act to self-relieve stress, complicating analysis; the lower amounts of residual stress observed in the continuous scanning samples may be due to the presence of other defects and the comparison to island scanning samples may not be direct.

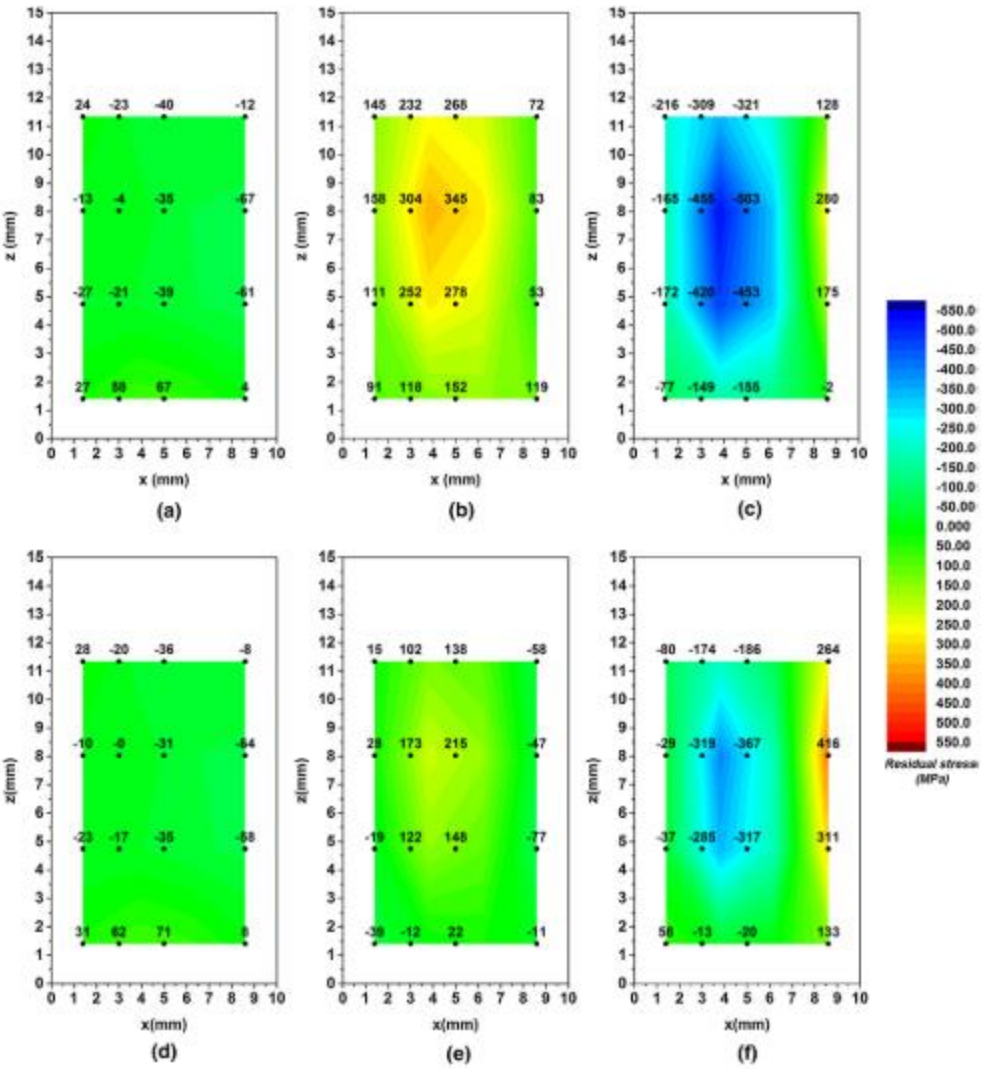

Figure 15. Work using neutron diffraction to measure residual stress in (a-c) LM and (d-f) EBM IN718 shows consistently lower residual stress in EBM samples than in LM samples. [68]

Heating of the substrate helps reduce residual stress, as does *in situ* heating of the material using the primary heat source. [65] A defocused electron beam can operate with enough speed and power to accomplish this (and does via the preheat step), but most LM and DED systems cannot. As a result, LM and DED parts generally have much more residual stress

than EBM parts due to a lower operating temperature. The lower operating temperature means that thermal gradients between the peak melting temperature and the powder bed temperature may be increased. Recent work has shown that residual stress in EBM parts is 5-10% of UTS. [68] Understanding the origins of residual stress requires a more detailed knowledge of process thermal history, while understanding methods for eliminating or reducing residual stress will be discussed in more detail with §II.5 on post-processing.

Residual stress can be measured using a variety of techniques including micro-hardness [72, 73], the contour method [74], x-ray diffraction [65], and neutron diffraction [75]. For alloys that do not have significant precipitates and are dominated by a single matrix phase, the shape of micro-hardness indents can be used to quantify the presence of residual stress. However, micro-hardness only reveals information about stress near the surface that is tested. The contour method measures the deflection of surfaces after cutting via EDM and has been shown to give comparable results to neutron diffraction. [76] Additionally, the contour method is noted to be less chemistry dependent than neutron diffraction. X-ray diffraction and neutron diffraction can both be used to measure bulk stress variation, but are more expensive and require specialized equipment. Residual stress formation may also be modeled. Finite element analysis [77] has demonstrated the ability to predict LM residual stresses. Additionally, simplified thermal cycles have been shown to qualitatively match experimental results of substrate warping. [64]

II.4 Heat Transfer, Solidification, and Thermal Cycles

The metallurgy of AM parts is determined by the feedstock chemistry and the temperatures that the material experiences, or the thermal history. There are different heat transfer mechanisms for different classifications of AM, but the use of full melting means that the metallurgical principles are the same for both DED and PBF. Solidification determines the initial phase distribution and grain morphology of the metal deposit. Heat source speed,

power, and size determine melt pool geometry, which in turn determines solidification kinetics. After solidification, thermal cycling and cool down path determine further precipitation kinetics, phase growth, and grain growth.

II.4.1 Modes of Heat Transfer

It is important to understand how the modes of heat transfer differ between AM processes. DED processes transfer heat primarily through conduction to the substrate, conduction to the build material, and convection to the shield gas. These modes of heat transfer are the same as those for welding. In LM processes, conduction may be inhibited by powder acting as a thermal insulator surrounding the part. Additionally, the fill gas in LM has a lower flow rate (Argon gas consumption of 0.035 to 0.070 m^3/hr) [78] than the shield gas in DED (0.354 m^3/hr). [40] The actual flow rate of LM cover gas may be higher than the gas consumption rate if recirculation is used (gas consumption only measures loss due to positive pressure or leakage), so it may be useful to consider local velocities across the surface (<2 m/s) as calculated in recent modeling work. [33] The higher flow rate in powder-fed DED systems is necessary, as the cover gas is also used for powder delivery (though this assumes primary gas flow for powder delivery and secondary gas flow for shielding are directly related or equal). [40] This should result in reduced convective heat transfer in LM when compared with DED.

EBM conduction mechanisms are similar to LM, but the near-vacuum environment significantly reduces convective heat transfer during the melting process. This means that, for EBM processing, radiative loss from the build surface and conductive loss to the machine are the principle modes of heat transfer. Since EBM operates at elevated temperatures (400 to 1000°C), the thermal history of EBM material must be considered with respect to solidification *and* the hold temperature during the build; the fused metal solidifies from a molten pool and then is kept at elevated temperature until all layers have finished melting. DED and LM processes may use heaters to increase the temperature of the build envelope

to 100 to 200°C. This is intended to reduce residual stress and warping but is not high enough to significantly impact the phase and grain structure of typical AM alloys.

II.4.2 Solidification

Solidification in DED and PBF is governed by the melt pool geometry, which is mostly determined by the relationship of the beam scan velocity to beam power. This relationship is extremely important and, using EBM as an example, may be defined by a function to select an appropriate scan speed based off of beam power (or current). The relationship between beam speed and beam power must be defined in some way by the user, as only certain combinations of speed and power will result in dense material. The "speed function" is such a relationship for EBM and is shown in Figure 16. [79] The slope and the translation of this relationship must position the selected speed and applied power within a certain processing window. Various combinations of speed and power allow for fully dense material (Figure 17) that is free of defects. Similar process mapping of defects using heat source power and speed has been used in welding for years to map process windows as shown in Figure 18. The relationship between speed and power is material-dependent and should be measured during new material development. LM and DED define a simple, constant relationship between speed and power, whereas the EBM parameters account for differences in part geometry and other effects by dynamically changing the speed-power relationship.

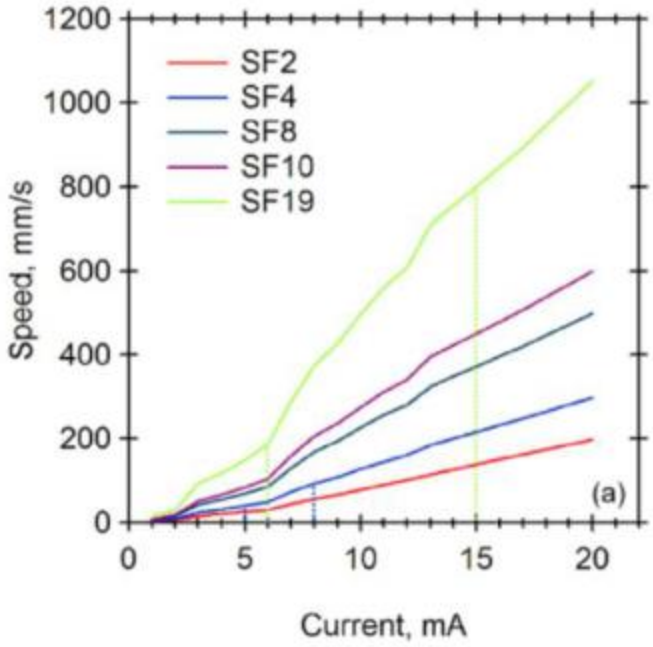

Figure 16. The relationship between speed and current is set for EBM using the "speed function" in an attempt to define successful processing space for the EBM process. [79]

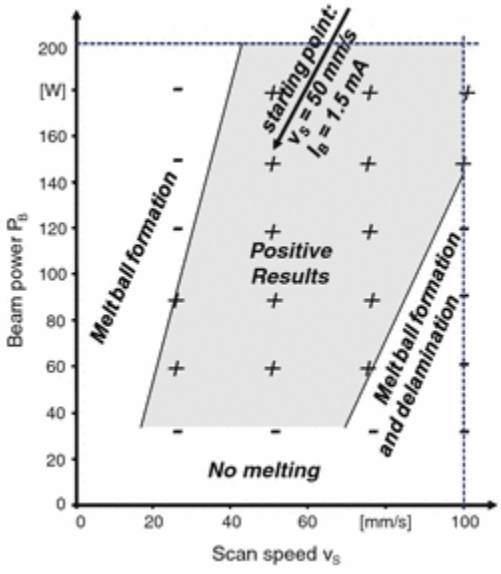

Figure 17. Process map for stainless steel EBM demonstrates importance in the relationship between applied power and beam speed. [60]

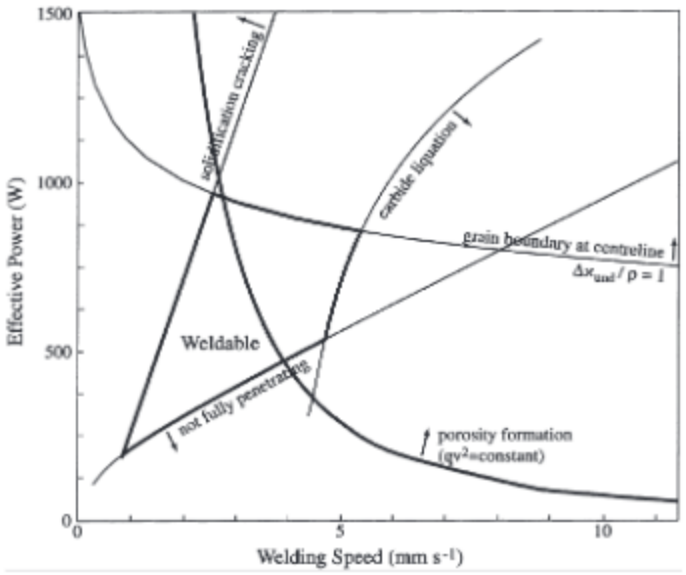

Figure 18. Relationship between effective power and speed in determining the weldability of Inconel 718. [80]

II.4.3 Speed-Power Relationship

The relationship between speed and power that is needed to avoid defects varies depending on several factors: edge effects, scan strategy, part geometry, and thickness of powder beneath the scan area. All of these factors amount to changes in the initial conditions or boundary conditions for heat transfer. After a heat source passes near an edge, it may return to the edge before the heat from the previous pass has time to dissipate. The scan strategy can have a similar impact on heat flow, depending on how the strategy allows for cool down between heat source passes. Part geometry effects include those associated with a variation in the size of the part. A small part will reach a higher peak temperature during melting than a larger part, given constant power and speed. This can lead to more defects in smaller parts or features. For PBF, the state of the material underneath the melt area (powder vs. solid) can drastically affect heat transfer. A powder

(non-sintered or sintered) has relatively poor thermal conductivity and can be considered thermally insulating compared to the solid part of the substrate. As heat is applied, it flows more slowly through the powder, which can lead to overheating of the melt surface located above the powder. The influence of all these phenomena means that applied energy density alone may not be the best indicator of porosity due to local variations. [81]

II.4.4 Columnar-to-Equiaxed Transition

The power and speed of the heat source also affect the thermal gradient (G) and liquid-solid interface velocity (R) of the melt pool. The process window of solidification can be estimated for an AM process and used to predict the nature of the grain structure as shown in Figure 19. The columnar-to-equiaxed transition (CET) can be calculated based on established methods [82] and plotted for various materials. [83] Recent work in PBF [84] has been increasingly focused on controlling the CET and is addressed in a discussion of AM microstructures later in this paper (§II.6.1.3). The CET can be transformed into a process map so that appropriate powers and velocities can be selected. [85] Further work is needed to combine the maps for defects and the CET, so that the process space can be fully understood for each material.

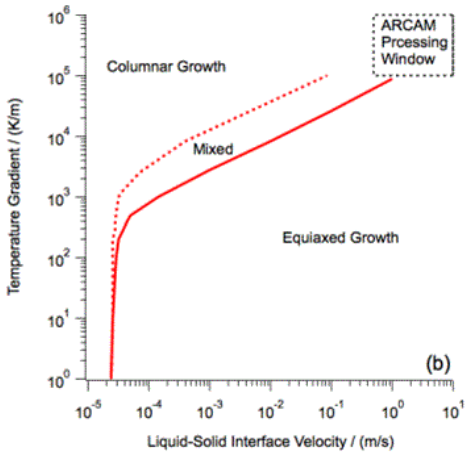

Figure 19. EBM processing window for Inconel 718 processing overlaid on G vs. R data. [86]

II.4.5 Process Thermal History

There are other consequences of melt pool geometry. Modeling has shown that poor powder thermal conductivity has a large impact on the size of the melt pool. [87] The heat sources in PBF move so fast that recent work has suggested that though the heat source is a point, a linear heat source may be a reasonable approximation. [88] Increasing beam diameter is a way to decrease the thermal gradient of the melt pool and slow down solidification, but the effect of beam diameter on grain size has not yet been reported. The effect of beam diameter, measured as “focus offset” in mA, has been related to melt pool width in EBM. [79] Such work is beneficial to the development of accurate process modeling.

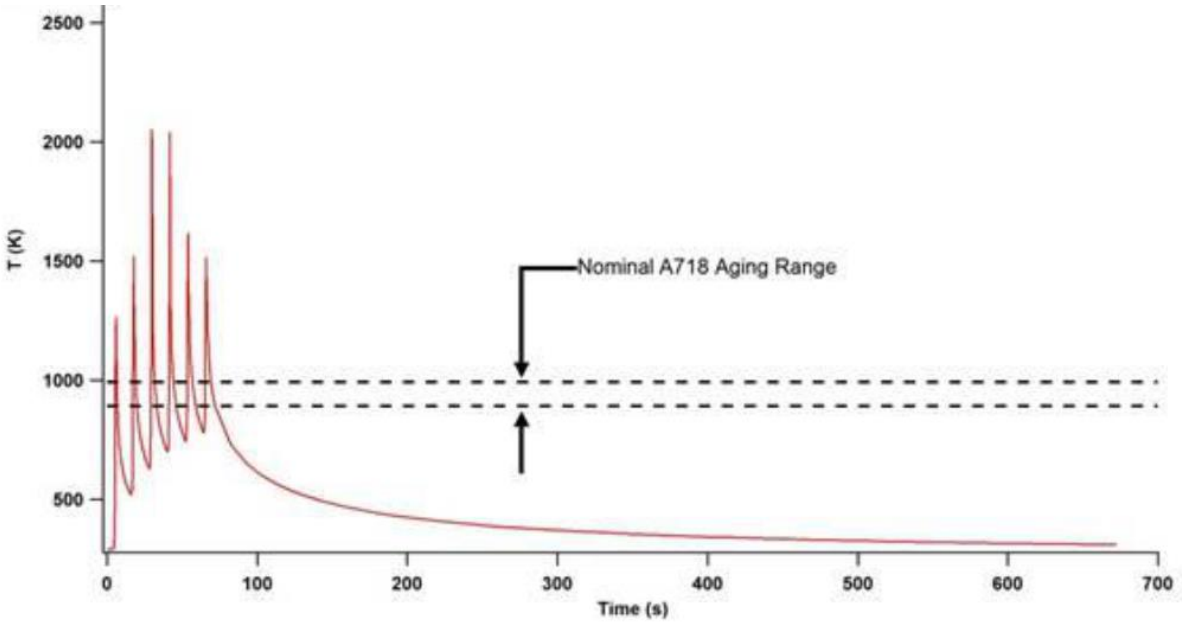

Figure 20. Thermal simulation of a point during powder-fed DED showing cyclic heating cycles. [89]

PBF and DED processes involve simultaneous melting of the top powder layer and re-melting of underlying layers. This creates thermal cycling, as the material reheats and cools. This cycling has been measured experimentally and modelled as shown in Figure 20. [89, 90] DED and LM are both typically performed at room temperature or close to it (heaters can get to 100-200°C); the material cools quickly, within seconds to minutes. In EBM, the process operates at an elevated temperature and experiences a distinct thermal history as measured by the substrate temperature in Figure 21. The EBM process can take 5-80 hours to cool below 100°C after layer melting is completed, depending on part geometry. [86] So, the effect of hold time and hold temperature on material properties must be considered for EBM. The impact on an precipitate hardened material like IN718 may be spending up to 100 hours (EBM) in the nominal aging range as opposed to ~100 seconds (DED).

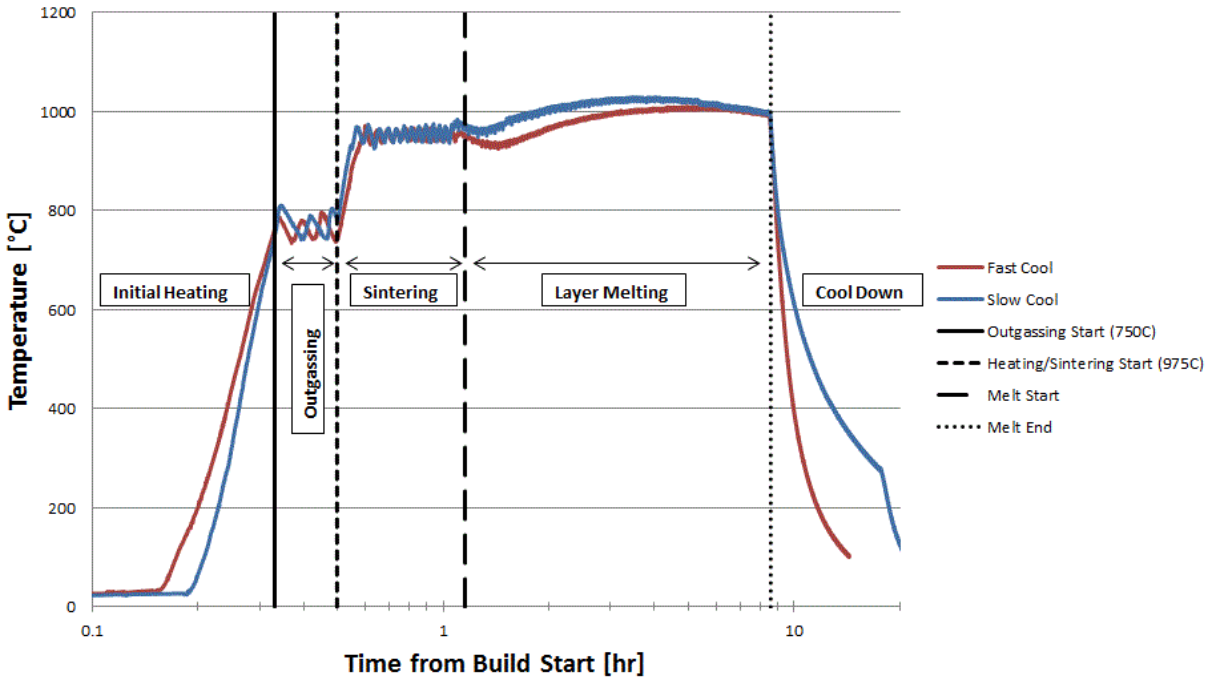

Figure 21. EBM process thermal history, as measured by the machine-standard, substrate thermocouple. [86]

II.5 Post-processing

When metal comes out of an AM process, there are many steps that are typically used to prepare an as-fabricated part into an end-use part; parts are not ready for most end-use applications directly out of a machine. Excess powder must be removed, parts must be removed from the build substrate, support structures must be removed, thermal treatments may be required to improve mechanical properties, and the surface of parts must be finished to achieve the desired surface finish and geometrical tolerance.

II.5.1 Powder, Support, & Substrate Removal

After a part is fabricated, excess powder, support structures, and substrate material must be removed. Powder-bed processes require powder to either be vacuumed from the part if loose (LM) or blasted off using loose, similar powder if sintered (EBM). DED processes may require machine clean-up, but the finished parts are not encased in feedstock. Support structures, for mechanical and thermal support, are frequently used in PBF and must be mechanically removed by application of force or cutting. The build substrate is typically adhered or joined to the finished part and must be cut off using a saw or wire electrical discharge machining. The interface of stainless steel substrate and Ti-6Al-4V is an exception in that parts may be fractured off of the substrate by application of force (typical in EBM production of Ti-6Al-4V).

II.5.2 Thermal Post-Processing

After parts are removed from the substrate and support material, thermal post-processing may be used to relieve residual stress, close pores, and/or improve the mechanical performance of the material. As-fabricated metals typically require heat treatment to achieve the desired microstructure and mechanical properties required for service. Material may be treated by hot isostatic pressing (HIP) to reduce porosity and internal cracks, furnace heating to solution treat, and/or furnace heating to age. Standard treatments for the commonly processed materials Ti-6Al-4V and IN718 are given in Table 3. The various treatment options can effect changes in grain size, grain orientation, precipitate phases, porosity, and mechanical properties. Heating AM metal in a furnace to effect changes in microstructure is the general goal of thermal post-processing. Thermal post-processing of metal affects grains through recovery, recrystallization, and growth. Phases are affected by dissolution, precipitation, and growth.

Table 3. Common post-processing procedures for Ti-6Al-4V and Inconel 718.

Treatment	Ti-6Al-4V	Inconel 718
Stress Relief	2 hours, 700-730°C [91]	0.5 hours at 982°C [29] 1065±15°C for 90 min (-5/+15min) [92]
Hot Isostatic Pressing (HIP)	2 hours, 900°C, 900MPa [91] 180±60 min, 895-955°C, >100MPa [93]	4 hours at 1120°C, 200MPa
Solution Treat (ST)	Not Typical	1 hour at 980°C [94]
Aging	Not Typical	8 hours at 720°C Cool to 620°C Hold at 620°C for 18 hours total [94]

II.5.3 Stress Relief

Stress relief involves recovery; atomic diffusion increases at elevated temperatures, and atoms in regions of high stress can move to regions of lower stress, which results in the relief of internal strain energy. LM and DED parts are typically annealed to remove residual stress (Figure 22), commonly prior to removal from the substrate. Stress relief treatments must be performed at a high enough temperature to allow atomic mobility but remain short enough in time to suppress grain recrystallization (unless desired) and growth (which is usually associated with a loss of strength). Recrystallization may be desirable in metal AM to promote the formation of equiaxed microstructure from columnar microstructure. This has been observed in LM iron, where it was theorized that thermal residual stress acts as the driving force (in the absence of cold working) for observed recrystallization. [73] Similar phenomena have been noted in wire-fed DED Ti-6Al-4V. [95, 96]

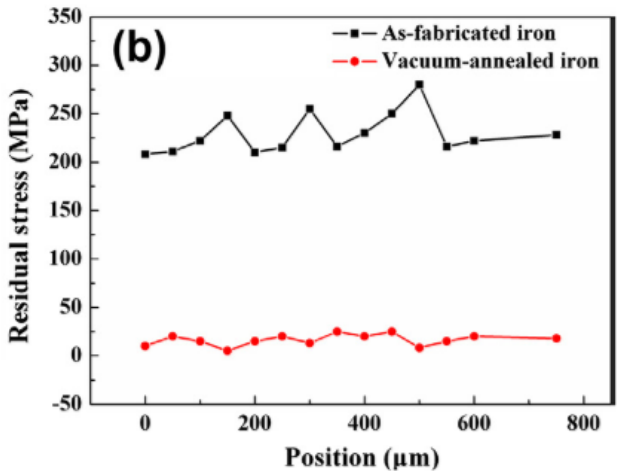

Figure 22. Stress relief through vacuum annealing can nearly eliminate residual stress present in as-fabricated material throughout the thickness of parts (shown here for LM iron). [73]

II.5.4 Recrystallization & Grain Growth

One of the most important effects of post-processing is effect on the grain structure of the processed material. As-fabricated metal AM parts typically have a columnar, oriented microstructure (especially in PBF), though heat treatments may alter this microstructure. Research on LM [73] and DED [95, 96] has noted recrystallization of as-fabricated microstructure during annealing (no HIP). In the materials in these studies (Iron and Ti-6Al-4V), residual stress is proposed as a likely driving force for this recrystallization (RX). In SLM of IN718, partial recrystallization occurred during stress relief annealing (Figure 23) and led to a very heterogeneous grain structure. [29]

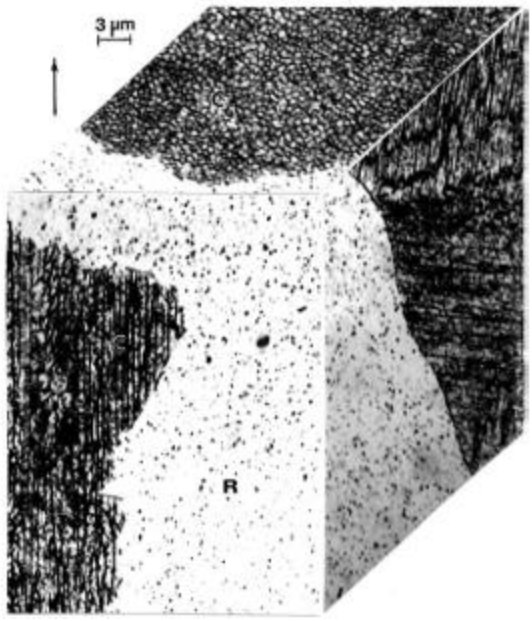

Figure 23. Recrystallization of SLM IN718 during stress relief produces an inhomogeneous grain structure. [29]

RX in direct energy deposition (DED) materials has been reported for both wire-fed and powder-fed systems, with residual stress as the likely mechanism. Brandl et al. explored solution treatment of DED Ti-6Al-4V and noted that RX occurred without hot or cold work. [95, 96] Furthermore, it was noted that the RX resulted in a grain structure change from columnar to globular, though the resulting RX grain size could not be controlled and resulted in coarse grains (300-400um). In DED of IN718, Cao et al. observed non-uniform RX with different grain morphology from the original columnar structure. [97] It was observed that overlap rate significantly influenced residual stress and the location of RX nucleation. RX grains tended to be relatively fine, though the RX process did not completely eliminate the prior columnar grains. Blackwell reported smaller amounts of grain growth from HIP of DED IN718 in deposited material than in the attached substrate of the same material. [98] The cause of this is not known, although it is speculated that carbides or oxide may not have

been dissolved by the 1160°C HIP cycle and acted to produce Zener pinning in the as-fabricated material. Zhao et al. noted recrystallization at various axial locations in DED IN718 after homogenization at 1080°C, likely due to residual stress. [35] Variance in local Niobium concentration has been observed to result in grain growth in Nb-poor regions during heat treatment of DED IN718. [36] This is due to a lower δ-solvus in regions of lower Nb concentration.

In EBM, RX is not typical during heat treatment of Ti-6Al-4V, but has been observed to occur in IN625 and IN718. Facchini et al. studied anneals on deformed and un-deformed EBM Ti-6Al-4V. [99] It was found that increasing strains led to the formation of globular RX, whereas less strained or unstrained regions retained the as-fabricated lamellar structures. The driving force in this case was shown to be deformation from mechanical testing. However, Murr et al. noted RX of EBM IN625 in un-deformed material. [100] It has been shown that residual stress is greatly reduced in EBM compared with SLM [68], so residual stress is not the likely driving force for RX. In fact, others have reported a similar phenomenon in EBM of IN718 for some solution treatments [101] and HIP. [102] Others have reported no RX and even noted that heat treated grains become even more oriented. [103] None of this work has proposed mechanisms for the RX or grain growth noted, and the cases in which this RX or grain growth occurs are not understood.

II.5.5 Hot Isostatic Pressing (HIP)

Most AM metal parts are treated by HIP to close internal pores and internal cracks. Internal pores, or "closed" pores, are surrounded by material in the center of the sample. When pores form at the surface, they are considered "open" pores. Open pores caused by surface defects are a problem for post-processing, as they allow deeper infiltration into material from air during high heat cycles, as shown in Figure 24. Internal cracks may also be closed by HIP, as has been shown in LM nickel-based superalloy parts. [56] The use of HIP may significantly alter the grain structure of AM parts. Standard HIP cycles may yield very large

grains, as published in recent work on EBM of Inconel 718. [102] There is also evidence that AM material responds differently to HIP than traditional material; LENS Inconel 718 was deposited on Inconel 718 substrate and characterized before and after HIP, and it was noted that grain growth occurred in the substrate during HIP but not the deposited material, possibly due to carbides or other high temperature phases not dissolved during HIP. [98] This means that characterization of as-built microstructure is critical to applying the correct HIP post-processing of AM parts. Alternatively, the homogenization of AM alloys prior to HIP or other post-processing could lead to standard post-processing procedures that are independent of processing conditions. Most post-processing of AM parts is currently performed this way, but the use of standard wrought or cast post-processing procedures may not be ideal for AM processed alloys.

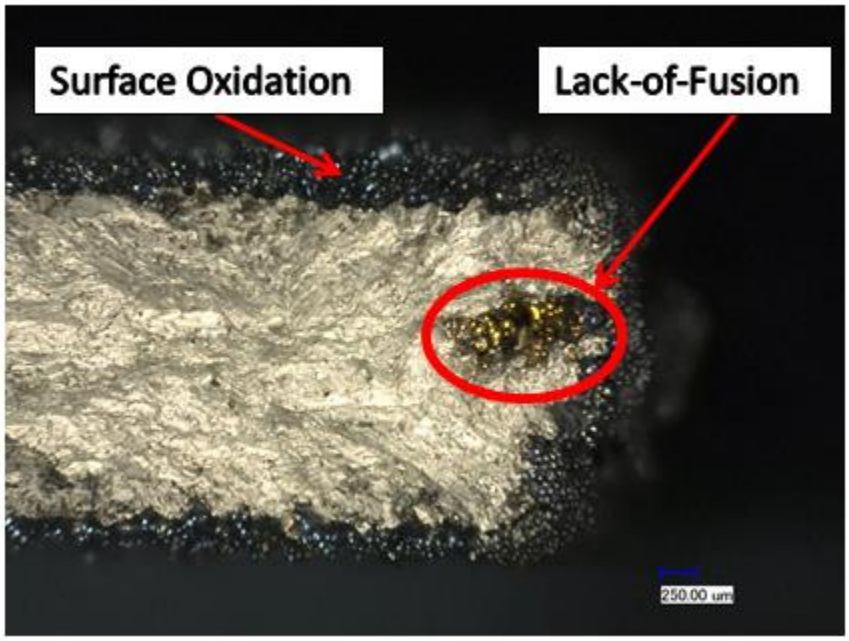

Figure 24. Thin wall EBM fracture surface of Inconel 718 from post-HIP sample with notable change in surface oxidation and oxidation of an open pore caused by lack-of-fusion near the edge. (Credit: unpublished work by the author, W. Sames)

II.5.6 Solution Treatment & Aging

For precipitate hardened materials (like Inconel 718), a solution treatment (ST) can be used to dissolve unwanted phases and aging can be used to form and grow precipitate phases. Sometimes, these processes are performed sequentially and referred to as solution treated and aged (STA). The ST temperature should be selected above the solvus temperature at which all undesired phases will dissolve. The ST time should be long enough to dissolve precipitates but short enough to limit grain growth. After a material is solutionized to form a solid solution, the matrix of the material is essentially "reset". Aging can now be done on the reset material, without the need to consider prior phase structure. The purpose of aging is to precipitate harden a material. These steps are common for cast and wrought materials, and have been performed on AM material. [29, 101, 102, 104]

II.5.7 Surface Finishing

AM parts bound for service are typically machined to achieve a smooth surface finish. As-fabricated parts typically have high surface roughness, the origins of which have been discussed previously in §II.3.1. The most common way to machine the near net shapes or parts produced using AM is to use computer numerical control (CNC) mills associated with subtractive manufacturing. Simple rotary-tool polishing or grinding with a belt sander (flat surfaces) may be adequate for some applications, but do not typically meet the standards required for high-quality parts. Chemical polishing has been explored on mesh structures and future work on electrochemical polishing is recommended. [105]

Parts to be used in service typically undergo thermal post-processing, which can oxidize the surface of the metal. Post-HIP parts are shown in Figure 25, before and after surface machining. [106] If open pores are present, oxidation can extend into the interior of the part as shown for thin-wall EBM samples in Figure 24. Defects like this can be, and must be, avoided because they may not get removed by surface machining. CNC of freeform

surfaces has been extensively reviewed in relation to tool path selection, tool orientation, and tool geometry. [107]

Figure 25. Post-HIP Ti-6Al-4V brackets, before (Top) and after (Bottom) machining. [106]

AM and CNC have been explored for operation in tandem [108], which is commonly referred to as Hybrid Manufacturing. Hybrid systems typically pair a DED process with CNC, using the same mounting position to position the CNC tools. This type of hybrid process is currently in use for part repair of aerospace components, capable of repairing compressor blades and other complex service parts. [109] Turbine blade repair using this method is shown in Figure 26.

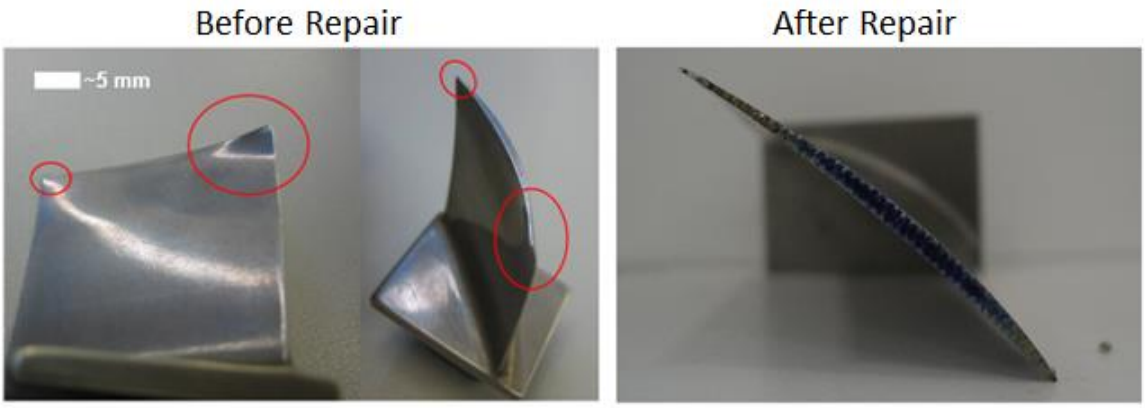

Figure 26. Airfoil repair using a hybrid DED+CNC method. [109]

II.6 Microstructure and Mechanical Properties

Characterizing the microstructure and mechanical properties of PBF and DED materials is a critical component of any AM development program. Grain morphology, grain texture, and phase identification are typically accomplished via light optical microscope (LOM), scanning electron microscope (SEM), electron backscatter diffraction (EBSD), x-ray diffraction (XRD), or some combination thereof. Tensile properties and hardness are the most commonly reported and measured mechanical properties, although some studies of fatigue life and creep have been completed. To discuss the importance of microstructure and mechanical properties, it is useful to focus on two different alloy systems, Ti-6Al-4V and Inconel 718, as there is much published research on PBF of these alloys.

II.6.1 Microstructure

The microstructure of AM produced metals has unique properties. Columnar grain structure dominates, with high amounts of grain orientation. Phase formation is process and material specific. Axial variation of grains and phases may occur due to subsequent

heating and cooling cycles of the material. Scan strategy can be used to control the microstructure in theory (G vs. R) [110, 111], and recent results show significant progress towards demonstrating control. Porosity is a concern with all processes, though < 1% porosity can be achieved using DED, LM, or EBM by optimizing process parameters.

II.6.1.1 Grain Structure

Grain structure in AM alloys is dominated by highly oriented, columnar grains. These structures are common in Ti-6Al-4V produced by EBM [112], LM [113], and DED [96, 114, 115], as well as Inconel 718 produced by EBM [20, 102], LM [29, 68, 116], and DED [117]. DED grain structure is not always as oriented or columnar as LM or EBM. In fact, DED grain structure is highly influenced by the nature of the scan strategy, as shown in Figure 27. [117] The results shown show some difference based on scan strategy, but the most pronounced difference is with higher energy melting. The resulting larger, more columnar grains should be expected; more applied energy means a larger and deeper melt pool. This will include more layers during remelting, which should promote epitaxial grain growth and a more oriented microstructure (as observed). This result can be extrapolated to other systems, given knowledge of the power per area [W/mm^2].

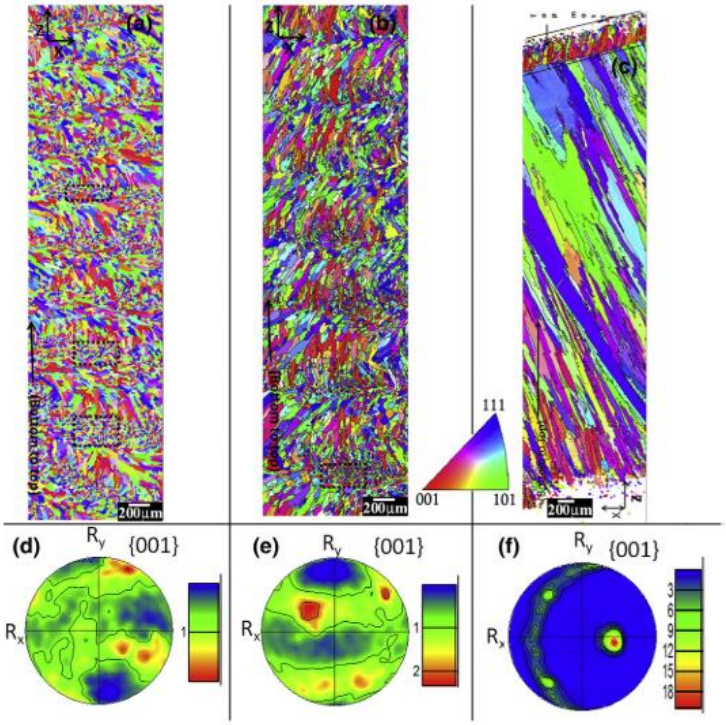

Figure 27. Grain structure in DED material is highly influenced by scan strategy. Shown is Inconel 718, produced using (a) unidirectional, (b), bi-directional, and (c) bi-directional, high power scanning. [117]

Discussed in more detail in §II.7, EBM and LM have much higher power per area capabilities than DED systems. This has a direct impact on the amount of remelting and epitaxy. The large layer thickness of DED makes finer control of microstructure difficult due to a larger minimum feature size.

In LM, the typical scan strategy used (island scanning) has evolved to reduce residual stress and cracking. The island scanning technique has recently been noted to cause repeating patterns in grain orientations. [88] This differs significantly from the oriented columnar structure seen using a rectilinear raster (no islands). Depending on the desired grain structure, this may be a limitation. In general, residual stress impacts grain structure from

the standpoint of the scan strategies used to avoid it or as a driving force for heterogeneous recrystallization.

In EBM, very high (001) orientation in the build direction is normal in both Ti-6Al-4V and Inconel 718. Work to study the origins of this texture discovered the effect of grain nucleation from powder particles. [118] Additionally, this work demonstrated a clear distinction between the fine grained, equiaxed microstructure of the contour region and the highly oriented, bulk melt. Grain size and orientation has also been noted to vary from the edge to the center of a melt pool [119], which agrees with common knowledge from welding and casting. Grain nucleation can occur at edges from powder particles in PBF (Figure 28), which can result in increased misorientation near edges or in thin walled structures.

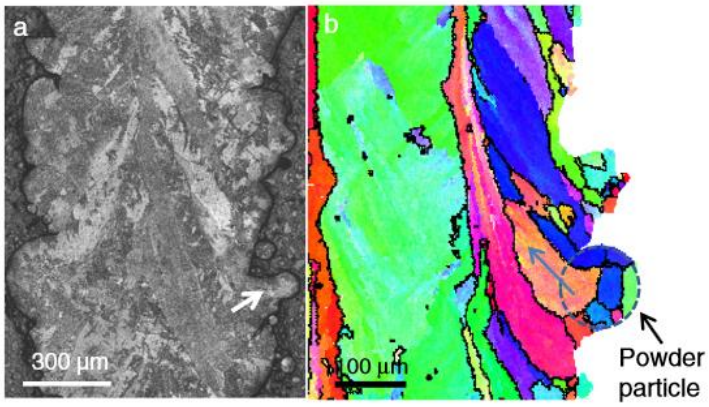

Figure 28. Effect of powder and edges on grain growth in EBM Ti-6Al-4V. [118]

II.6.1.2 Phase Formation

Phase formation during solidification and solid-state phase transformation during cyclic process heating have been studied for DED [89, 120] and EBM [86]. Phases that form during

rapid solidification of the melt material may coarsen and/or dissolve during subsequent passes of the heat source. This effect was discussed previously in §II.4.5 and is shown in Figure 20. DED of IN718 has been noted to form non-equilibrium Laves eutectic heterogeneities that transform into δ-needles during solution treatment (solution treatment should reset the phase structure). [36] Such needles are typically associated with over-aging. Such solidification Laves formations have been noted in LM but not EBM. In EBM, the powder bed temperature used for processing was shown to directly impact the width of α-phase grains, or laths, in Ti-6Al-4V and, correspondingly, tensile properties. [112] Furthermore, axial variation of lath width in Ti-6Al-4V has been noted in EBM. [121] The higher powder bed temperatures (400-1000°C) of EBM are unique, and similar effects are not noted in the lower temperatures (20-200°C) of LM or DED processing.

II.6.1.3 Microstructure Control

Local control of microstructure is possible with metal AM processes, and recent research is just beginning to demonstrate the possibilities. PBF processes have produced especially interesting results due to the accuracy and the speed of lasers and e-beams. Manipulation of G vs. R (see §II.4.4 on thermal history) has been known to modify grain structure of material during traditional processing, and applies to AM processes through manipulation of scan strategy. Control of microstructure can be discussed with respect to either grains or phases.

Control of grain morphology and size can be achieved through manipulation of G vs. R. While G vs. R curves may predict mixed grain morphology, it has been difficult to produce experimentally. It is speculated that this is due to a preference toward columnar growth once it has been established. [112] Many papers have addressed the benefits of controlled grain structure [85, 122], but demonstration has not occurred until recently in DED [117] and EBM [123, 124]. Beam modulation in wire-fed, e-beam DED has shown that beam modulation (rapid variance of the beam power) can be used to produce finer grain

structure. [125] This alternative method causes a dynamic melt pool due to a rapidly changing heat flux. The clearest demonstration of local control of grain orientation was achieved using EBM of IN718 to embed the letter D-O-E (stands for the sponsor of the research, the "Department of Energy") in misoriented grains within a highly oriented matrix (Figure 29 shows this visually using an inverse pole figure representation from EBSD). [126]

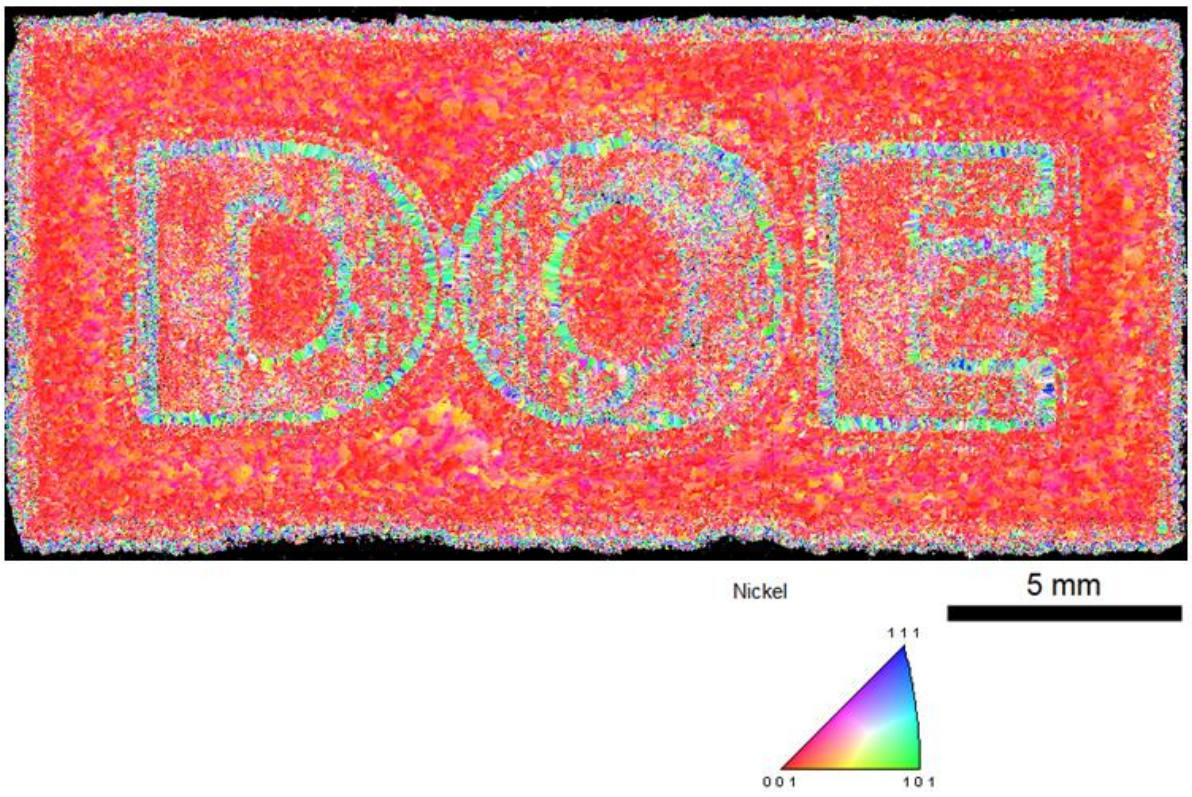

Figure 29. Local control of grain orientation in EBM of IN718. [126]

Phase control is more complex, as formation can be influenced by solidification and solid state phase transformation. Previous work in AM has investigated microstructure control of precipitate phases during fabrication by varying process parameters. For example, during Selective Laser Melting (SLM) of Ti-6Al-4V it was found that precipitation of Ti_3Al could be

controlled by varying solidification rate through scanning speed. [127] The segregation of aluminum during rapid solidification leads to periodic fluctuations of aluminum content, which is identified as a driving force for Ti_3Al precipitation. While this precipitation may not directly occur due to solidification, the non-equilibrium phase formations have a short time scale for formation during either solidification or subsequent beam passes (order of seconds to minutes in SLM). Other work on low-purity copper notes the possibility of microstructure control of Cu_2O but does not demonstrate active material control. [128] Both of these examples control phase formation through solidification control (control of the beam speed, beam power, or scan strategy). This approach, however, faces an inherent limitation in that process parameters affect both matrix solidification grain structure *and* precipitate evolution, potentially forcing the optimization of one characteristic at the expense of the other. Solidification structures are affected by subsequent heat source passes (as discussed previously). Recent work has rationalized solid state phase transformation in DED [120] and EBM [86]. Solid state phase transformation can amount to *in situ* aging of material. In DED this is done on subsequent beam passes. In EBM, subsequent passes and holding at elevated temperature cause this change. The complex thermal histories present have allowed researches to rationalize phase formations due to solid state phase transformation, but more work is needed to be able to predict microstructures. No work in metal has truly demonstrated process control of precipitate formations via solidification or solid state phase transformation to produce desirable phase structures.

II.6.2 Mechanical Properties

The mechanical properties and performance of AM material is still being measured and understood. Much of the literature on AM focuses on mechanical properties, specifically tensile behavior and hardness. Tensile tests to measure yield strength (YS), ultimate tensile strength (UTS), and elongation are the most commonly used tests to compare AM mechanical properties to traditionally processed materials (cast and wrought). The location

and orientation from which mechanical testing samples are taken from builds is important and should always be reported with results. ASTM standards exist, but are typically process and alloy specific. Defects, such as porosity, that affect mechanical properties may influence the test results of as-fabricated material but can typically be improved by post-processing.

Porosity, residual stress, test specimen orientation, and thermal history are particularly important factors to consider when discussing mechanical test results of AM materials. Unfortunately, not all reported research includes these necessary details. Orientation of the build direction relative to the test direction, quality and production method of feedstock, void fraction of porosity, thermal history during processing, and post-processing thermal history should all be included with any test results. This section focuses on mechanical properties of bulk material (as opposed to mesh or foam structures).

Porosity can negatively affect mechanical properties due to a reduction in cross sectional area. [129] Aligned pores (non-random) or pores with sharp edges are more detrimental than homogeneously dispersed spherical pores. The effect of porosity on tensile properties is most notable in the reduction of elongation. [130] Residual stress in non-stress-relieved parts can also lead to early failure. Part thermal history (*in situ* history for EBM, post-processing history for other parts) is especially important for precipitate hardened materials. The presence of columnar grains in most AM alloys means that the relationship of grain orientation to mechanical property anisotropy must be considered.

Different machines may have very different thermal histories of material, which may manifest in as-fabricated mechanical properties as variance in hardening through coarsening or aging. Similarly, the details of any post-processing heat treatments are equally important in determining mechanical properties. Data for many AM processes is only given in the stress relieved or heat treated states, which tend to have better mechanical properties. As a result, the amount of published data on as-fabricated samples (samples as they come out of the machine) is sparse. Previous work has compiled some mechanical properties, focusing on Ti-6Al-4V and Inconel 718/625. [54] A summary of tensile properties for DED, LM, and EBM is presented in Table 4 for Ti-6Al-4V and Inconel 718.

Table 4. Compilation of reported tensile results for Ti-6Al-4V and Inconel 718.

Material	0.2% YS [MPa]	UTS [MPa]	Elongation [%]	Reference
Ti-6Al-4V				
DED As-Deposited (X-Y)	976±24	1099±2	4.9±0.1	[114]
DED Stress Relieved (X-Y)	1065-1066	1109	4.9-5.5	[91]
DED Stress Relieved (Z)	832	832	0.8	[91]
DED HIP (X-Y)	946-952	1005-1007	13.0-13.1	[91]
DED HIP (Z)	899	1002	11.8	[91]
LM As-fabricated (X-Y)	910±9.9	1035±29.0	3.3±0.76	[113]
LM + HT (X-Y)	1195±19.89	1269±9.57	5±0.52	[131]
LM + HT (Z)	1143±38.34	1219±20.15	4.89±0.65	[131]
EBM As-fabricated (X-Y)	967-983	1017-1030	12.2	[132]
EBM As-fabricated (Z)	961-984	1009-1033	7.0-9.0	[132]
EBM As-fabricated (Z)	883.7-938.5	993.9-1031.9	11.6-13.6	[112]
EBM HIP (Z)	841.4-875.2	938.8-977.6	13.4-14.0	[112]
Wrought bar (annealed)	827-1000	931-1069	15-20	[133]
Cast+Anneal	889	1014	10	[133]
Cast+Anneal (peak aged)	1170	1310	-	[131, 134]
Inconel 718				
DED As-Deposited (NR)	590	845	11	[35]
DED STA (X-Y)	635-1107	958-1415	2.4-18.4	[115]
LM As-fabricated (NR)	889-907	1137-1148	19.2-25.9	[116]
LM STA (NR)	1102-1161	1280-1358	10.0-22.0	[116]
LM Stress relieved (X-Y)	830	1120	25	[29]
LM HIP+anneal (X-Y)	890	1200	28	[29]
LM HIP+anneal (Z)	850	1140	28	[29]
EBM As-fabricated (X-Y)	822 ± 25	1060 ± 26	22	[104]
EBM As-fabricated (Z)	669-744	929-1207	21-22	[102, 104]
EBM HIP+STA (X-Y)	1154 ± 46	1238 ± 22	7	[104]
EBM HIP+STA (Z)	1187 ± 27	1232 ± 16	1.1	[104]
Wrought - Bar	1190	1430	21	[134]
Wrought - Sheet	1050	1280	22	[134]

When as-fabricated samples are tested, the geometry of test specimens, surface finish, and type of measurement (global vs. extensometer) can all have a significant impact on resulting data. Comparisons of such data must therefore consider testing methodology. Sample geometry, as discussed previously, can impact local heat transfer conditions, which can

impact solidification, defects, and microstructure. It is therefore important to know how the parts were built (including what other parts they were built with) to determine the complete build geometry. For the use of as-fabricated material (not machined), surface finish is typically poor compared to well-polished test specimens. Rough surface finish can introduce stress risers or crack nucleation sites at surface defects or flaws. Using parts straight out of the machine has been observed to negatively affect mechanical performance.[113]

The reported values of UTS, YS, and elongation tend to be very similar in the X-Y versus Z directions, with the X-Y results being slightly better in some cases (see Table 4). This is unexpected, as tensile properties of directionally solidified material (columns oriented along the Z direction) should be superior to those in the X-Y direction. To understand why this is unexpected, the effect of grain orientation on mechanical properties must be considered. In nickel-based superalloys, directionally solidified material is highly oriented with the [100] direction. This high orientation is associated with an increase in primary creep, rupture life, and ductility performance. [135] The same orientation structure is seen in most metal AM parts (not just the nickel-based ones), but the increase in performance (in elongation, since orientation dependent creep data is not as common in the AM literature) is not seen. In fact, the opposite effect is seen in AM; elongation is less in the oriented [100] direction. This effect is notably seen in EBM Ti-6Al-4V, where UTS and YS remain unaffected by orientation, but elongation is 30% higher in the X-Y direction. [132] For this specific case, it was noted that the effect of "thermal mass" or *in situ* aging may have influenced results. In fact, *in situ* aging in EBM has been noted to influence mechanical properties in IN718 as well. [20, 86] Depending on the material, this effect appears to more strongly influence mechanical properties than the orientation of the material. EBM is unique in this *in situ* aging, and such an explanation cannot be applied to similar orientation variation in DED and LM processing. In fact, the underlying mechanism for the unexpected mechanical

performance due to orientation variation has not been well studied or identified for DED or LM. The mechanism is likely material and process dependent.

Post-processing can improve mechanical properties, but must be applied correctly for a given starting microstructure. The starting microstructure can vary based on process parameters (which may impact solidification kinetics), which may cause need for non-standard post-processing. Having to determine a post-processing procedure for each batch is not ideal or feasible. Work must be done to characterization the range of microstructures that may form for a given material in a given machine. If a treatment can be applied across this variance in microstructure with acceptable results, then it can be applied uniformly. If not, then processing windows must be set to insure quality control on the material coming out of the machine. For processes without *in situ* aging (LM, DED), processing parameters mostly impact solidification microstructure. For EBM, which undergoes *in situ* aging, variable amounts of aging may lead to issues in solution treatment. [86] Processing windows for EBM or precipitate hardened materials must therefore include process parameters that determine solidification kinetics and the size of the part (how long it will hold in the machine). Standard post-processing with HIP will typically change tensile properties (elongation may improve at the expense of UTS/YS in precipitate hardened materials), but can close pores (should improve fatigue life).

Recent work has focused on development of standardized testing procedures for AM processes. ASTM standards have been developed for PBF Ti-6Al-4V [93], Inconel 718 [92], and Inconel 625 [136]. The ASTM guidelines offer criteria for material, but allow for agreed upon specifications between the manufacturer and end-user. For researchers, there is no official standard for reporting test results. Work by researchers at NIST using Ti-6Al-4V began efforts to develop a standardized test procedure for EBM material to account for variation of mechanical properties within the build volume [132, 137, 138] but has yet to be written into an official standard. To improve the usefulness of published research results,

authors should be diligent to report: orientation of build direction, process thermal history (if applicable), exact conditions of any post-processing, and the nature of the mechanical test specimen (machined, etc.).

Outside of tensile test and hardness data, other mechanical properties of AM materials are less well studied. Fatigue and creep are of strong importance to industry for certain alloys, as they are often considered a limiting property of materials (whereas YS or UTS are not limiting for many applications of aerospace parts, for example). The most complete set of fatigue data exists for Ti-6Al-4V, with tests run on powder-fed DED [91], LM [113], and EBM. [99] While differences in testing (orientation, geometry, technique, etc.) make direct comparison difficult, most as-fabricated material from DED, LM, or EBM, falls in the lower range of the performance of cast parts as shown in Figure 30. Post-processing improves material to a level of performance comparable to annealed wrought or cast with HIP material.

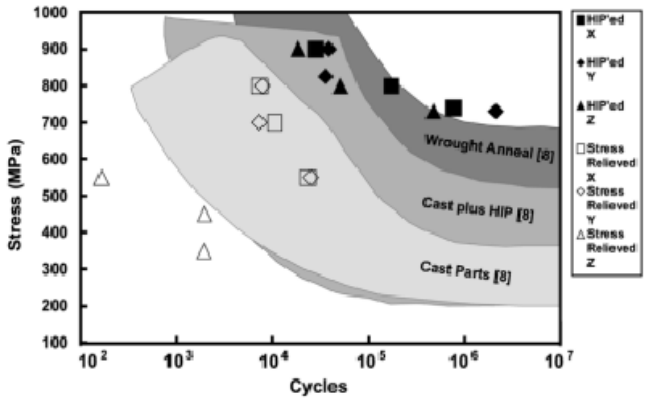

Figure 30. Fatigue test results of HIP and stress relieved DED material. [91]

Fatigue properties are highly influenced by surface finish and porosity, with samples that were processed by HIP and machined exhibiting comparable fatigue properties to wrought material. [54] Machining samples (as opposed to using the as-fabricated finish) typically improves mechanical performance, but the result can be difficult to observe if material has significant porosity and residual stress. [113] Efforts to understand underlying dislocation motion and model fatigue performance are limited, but have demonstrated accuracy compared to experimental results. [139] Other testing of crack growth, creep [140], corrosion [102], and other performance properties are also limited, making these tests a likely area of future work.

II.7 Comparison

Now that the general processing science of metal AM has been explored, this background can be used to compare the technical aspects of existing technologies. A tabulated comparison of LM, EBM, powder-fed DED, wire-fed DED, BJ, and SL is given in Table 5. Discussion will focus on just a few of the more interesting differences. For example, porosity can be kept to low levels in PBF and DED but is inherently present in BJ. BJ must address the porous nature of the material by either infiltration of consolidation. EBM and BJ are notable for low levels of residual stress induced during processing. This can be attributed to a high operating temperature for the EBM process (effectively *in situ* stress relief) and no applied temperature during BJ processing. The high operating temperature of EBM does reduce residual stress levels, but can lead to concerns with *in situ* aging of the microstructure. While BJ does have many advantages, is also has its own set of concerns associated with fragile green bodies and post-processing. PBF and BJ are more capable for producing complex geometries such as overhangs and meshes. Surface finish may be best on LM and SL systems but, as mentioned in §II.5.7, all metal AM parts should be considered net shapes; machining must be done after thermal post-processing for most uses. SL achieves a machined finish because machining is done as part of the process, after each

layer. Process clean-up is really only a concern in PBF and BJ processes. Powder must be sieved and handled appropriately. Additionally, EBM powder must be blasted away from the surface of finished parts (adds an additional step). The use of DED for deposition on top of existing structures enables its unique use for part repair. Multi-material parts can only be produced using SL (layers of different materials), BJ (infiltration), or potentially DED (multiple wire or powder feeds).

Table 5. Comparison of defects and features across platforms.

Defect or Feature	Laser Melting (LM)	Electron Beam Melting (EBM)	Direct Energy Deposition (DED) – Powder Fed	Direct Energy Deposition (DED) – Wire Fed	Binder Jetting (BJ)	Sheet Lamination (SL)
Feedstock	Powder	Powder	Powder	Wire	Powder	Sheets
Heat Source	Laser	E-Beam	Laser	Laser/E-Beam	N/A; Kiln	N/A; Ultrasound
Atmosphere	Inert	Vacuum	Inert	Inert/Vacuum	Open Air	Open Air
Part Repair	No	No	Yes	Yes	No	No
New Parts	Yes	Yes	Yes	Yes	Yes	Yes
Multi-Material	No	No	Possible	Possible	Infiltration	Yes
Porosity	Low	Low	Low	Low	Yes	At sheet interfaces
Residual Stress	Yes	Low	Yes	Yes	Unknown	Unknown
Substrate Adherence	Yes	Material Dependent	Yes	Yes	N/A	Yes
Cracking	Yes	Not Typical	Yes	Yes	Fragile Green Bodies	No
Delamination	Yes	Yes	Yes	Yes	No	Yes
Rapid Solidification	Yes	Yes	Yes	Yes	No	No
In situ Aging	No	Yes	No	No	No	No
Overhangs	Yes	Yes	Limited	Limited	Yes	Limited
Mesh Structures	Yes	Yes	No	No	Limited	No
Surface Finish	Medium -Rough	Rough	Medium - Poor	Poor but Smooth	Medium-Rough	Machined
Build Clean-Up From Process	Loose Powder	Sintered Powder	Some Loose Powder	N/A	Loose Powder	Metal Shavings

Process speed, or deposition rate, is a major limitation of current metal AM techniques. Current deposition rates are presented in Table 6. The fastest deposition rate is using BJ, which does not melt or sinter the metal. The increase in deposition speed comes at the cost of additional post-processing steps (curing, sintering, etc.). Powder-fed DED can be fast- if a larger power laser is used. The same principle is true of all processes that use a heat source; faster deposition rates can be achieved with higher power input. Higher power allows for faster scan speeds to achieve the same energy density needed for full melting. EBM is reportedly faster than LM, making it the faster PBF technique. LM deposition rate can be increased at the expense of surface finish. Depending on part requirements, LM operators should consider this to decrease build time. Unless higher power heat sources are used, wire-fed DED is reportedly about three-times faster than powder-fed DED. More efficient deposition of material can explain this, as some powder is lost during the spray process (and cooling incurred by the gas flow). For comparison to consumer polymer hardware, the RepRap deposition rate was included. All metal AM machines are on the same order of magnitude as these polymer printers, except for the high-power LENS and ExOne systems. In addition to deposition rate, the maximum power input is another usual figure of merit. This value is helpful for describing how much power can be applied to a given area. Though there is no clear relationship between max power input and deposition rate, max power input is useful for determining process efficiency and deducing the impact on microstructure (see previous section).

Table 6. Reported deposition rates for various technologies

Process	Machine	Deposition Rate [cc/hr]	Maximum Power [W]	Min. Heat Source Diameter [mm]	Max Power Input [kW/mm^2]
BJ	M-Flex [141]	1200-1800	N/A	N/A	N/A
DED – Powder Fed	LENS (2500-3000W) [22]	230	3000	1	3.8
EBM	A2 [142]	60	3500	0.2	110
DED – Wire Fed	EBFFF [24]	47	408	0.38	3.6
Material Extrusion	RepRap, Polymer [143]	33	N/A	N/A	N/A
LM	Renishaw AM 250 [144]	5-20	400	0.135	28
DED – Powder Fed	LENS (400-500W) [22]	16	500	1	0.64

II.8 Applications & Economics

Metal AM has found a range of applications within the aerospace, biomedical, automotive, robotics, and many other industries. Applications in part repair are mostly limited to the aerospace industry, whereas all industries mentioned are beginning to use metal AM for end-use part production. However, limited build volumes, slow deposition rates, and high machine costs limit the current use of the technology. With these constraints, AM technologies are limited to uses in low-volume production, material use reduction, and cases of necessity. Process improvements and quality controls may help to lower the costs associated with AM production in the future.

Market analysts predict the overall market for AM (metal and polymer) parts will grow by 18% a year until 2025, reaching a market size of $8.4 billion. [145, 146] The largest growth areas are projected to be aerospace, biomedical, and automotive. Due to the nature of the parts needed by these industries, a significant portion of that growth can be expected to come from metal AM processes. In fact, the aerospace and medical industries have been

early adopters and users of metal AM parts for end-use. The material of choice for these industries has been Ti-6Al-4V, for use as a light-weight structural material and as a bio-compatible material. Case studies for aerospace parts have demonstrated AM brackets [106] and landing gears. [147] Case studies for biomedical parts have demonstrated AM bone replacements for jaws [148], hips, and other parts. The application of mesh structures is attractive for biomedical parts [27] and also has applications for other uses, such as lithium ion batteries. [149] The use of light-weight Ti-6Al-4V has been demonstrated for use in robotics (Figure 31), as the use of AM can enable additional degrees of freedom and allow for internal routing of hydraulic and electrical lines. [150]

Figure 31. Joint of a robotic arm that embeds hydraulic lines, eliminating external lines for hydraulic fluid and wiring. [150]

The development of Inconel 718 and other superalloys has been sponsored for use in aerospace components, but could be used in any industry that has the need for high

temperatures or superalloy components. GE Aviation, a large company in the aerospace field, has committed to production of fuel injectors for the LEAP engine [151] and γ-TiAl turbine blades for the GEnX engine. [152] The aerospace industry has also found use for DED systems in turbine blade repair [109], including repair of single crystal material. [153] The use for part repair is limited to cases of high-cost parts, where the cost of repair is lower than the cost of replacement. For this reason, most AM research focuses on the production of end-use parts, fabricated without an existing component.

To analyze the economics of AM, a comparison to traditional methods and subtractive manufacturing is necessary. Cost models for LM have been developed and can calculate costs for multiple parts in a batch. [154] When comparing LM to die casting, AM is more economical only for low volumes (less than 31 parts for the geometry studied). [155] Compared to subtractive manufacturing, AM also only makes sense for small volumes or where the "buy-to-fly" ratio (amount of material consumed compared to the amount that is actually used in the final product) is high. [156] Figure 32 shows a comparison of additive manufacturing to subtractive manufacturing (where parts are machined from a block of starting material). According to this model, the cost of labor/design and the failure rate are extremely important to the viability of AM. Increasing deposition rate can also dramatically increase the range of cases where AM is viable.

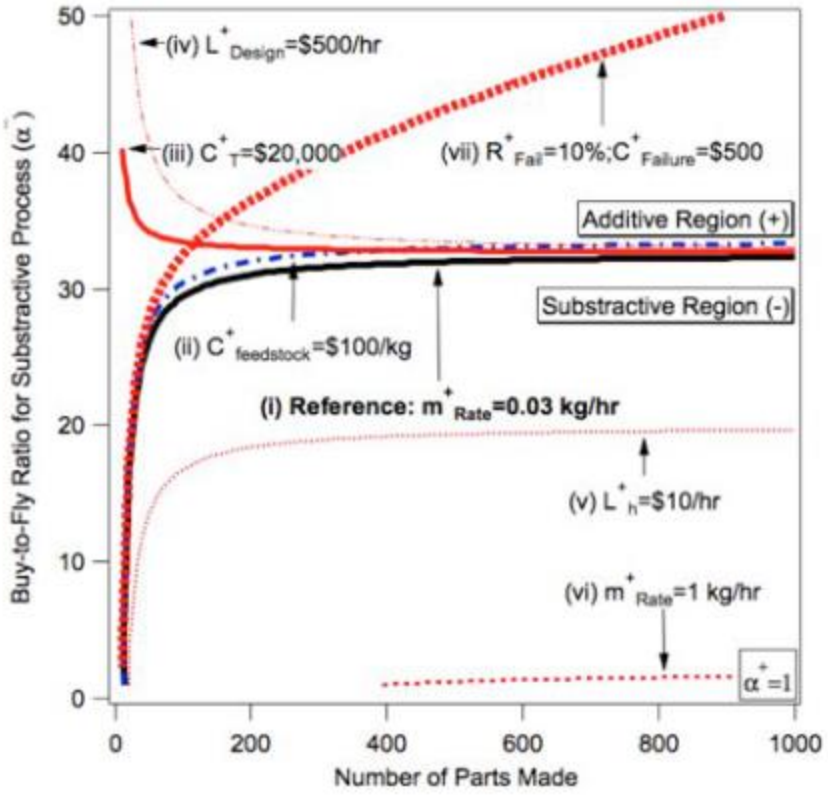

Figure 32. Comparative analysis of additive and subtractive manufacturing. [156]

These analyses mean that AM is currently economically limited for end-use parts, for small quantities of parts or parts that require large billets to be used during machining. For the remaining uses, the viability of AM comes down to economy versus necessity (which is not completely unrelated). By enabling new geometries that reduce the number of components in a part (like the GE LEAP nozzle) or mesh structures that promote body acceptance of implants (for medical implants), metal AM has the potential to make economic sense by displacing parts with inferior performance. This nuance (that AM then becomes a necessity to make the new, more efficient part design) is lost in some analyses of manufacturing economics (only looking at volumes, raw material costs, and manufacturing

efficiency). This means that the key for the growth of metal AM is to find more design improvements that are enabled by AM and/or finding ways to reduce the driving costs of using metal AM for production.

Of paramount importance is the reduction of failure rates in AM processes, which are held as proprietary information and not typically published or quoted. It has been shown that a failure rate of just 10% can make AM processes un-economical. [156] Better quality control and improved hardware/software designs will surely help. For those familiar with equipment from the last decade, there is a "Rule of 4" that has been used to describe the success rate of AM; it can take up to three iterations to produce a successful outcome, but after that the desired parts can be produced reliably. While this is viable for a standardized batch of parts, the trial and error associated with delivering new geometries must be eliminated to make AM viable for one-off parts. Hardware reliability must improve across all systems. For example, the result of selective powder fetching (only fetching powder from one hopper) in EBM is shown in Figure 33. For this build, powder distribution sensors failed to recognize powder as present in both hoppers. The machine then fetched powder from only one hopper, leaving the other completely full. The build then failed due to running out of powder (the left side of the build can be seen a depressed). There are many other machine reliability problems across platforms, and this example should be taken to highlight the kind of problems that must be overcome. Developments in technology continue to improve success rates, as does the development of a workforce skilled in AM. A skilled operator can boost success rates tremendously for most metal AM processes.

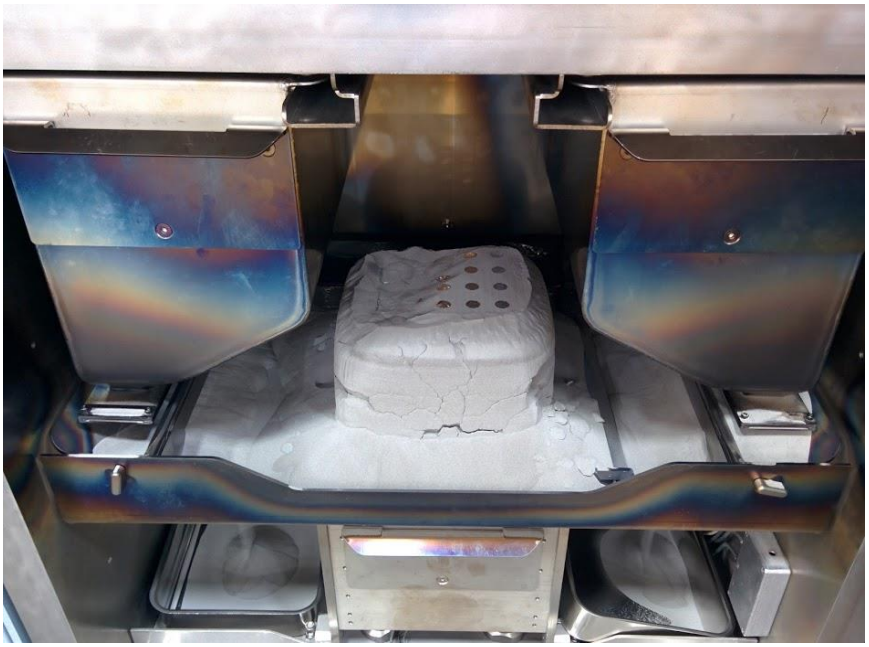

Figure 33. Failed build due to selective powder fetching in EBM. Hardware/software advances are needed to eliminate such problems.

The application area is not just limited by cost, but also by capabilities of AM machines. Small build volumes mean that parts of or greater than the meter-scale are not possible with the current technology (some thin walled samples are the exception, using DED processing). Slow deposition rates are a limiting feature in some processes from the standpoint that there are hardware limitations on extremely long build times. For example, EBM processing is limited in the maximum time possible by filament lifetime (typically replaced every 100 hours of burn time). Similarly optics in laser based systems must not get dirty or heat up during long build operations. From this viewpoint, extremely long build times (>100 hours) are not just uneconomical but also not possible due to hardware constraints. Very small parts cannot be made due to limitations on machine resolution based on material feedstock and heat source size. Overhangs and complex geometries

continue to be a limitation; though PBF and BJ have mostly enabled parts with this feature (supports are typically necessary in PBF).

Input costs (hardware, feedstock, maintenance, etc.) are high for metal AM and significantly limit the current metal AM market to researchers and large industrial users. Machine costs are not widely reported and vary based on model type. Some available hardware cost information has reported the following values: ExOne models range from $145,000-950,000 [157, 158], the EOS M270/M280 is $800,000 [142], Arcam models range from $0.6-1.3 Million [159], and the Renishaw AM250 is $750,000. [160] Based on these reported prices, hardware costs appear pretty similar across platforms. Costs for DED and SL systems remain unreported, but are expected to be similar to LM, EBM, and BJ. At a price of $0.5-1 Million, metal AM hardware is a significant capital investment for most companies. Hardware is not the only major cost in operating a system; feedstock costs can be a significant investment as well. Powder feedstock costs are typically higher than wire costs, and are a significant investment for powder-base processes. The powder used in EOS metal machines has been reported to vary from $120/kg for stainless steel to $735/kg for Ti-6Al-4V ELI. [161] LM processes require a smaller particle size distribution, which tends to cost a premium due to the yields of current powder production techniques. EBM powder is less expensive due to a large particle size distribution, though exact costs are not reported. Cost is highly dependent upon atomization technique, which can determine powder quality. Typical techniques used for AM powders are gas atomization ($165-330/kg), plasma atomization, and plasma rotating electrode ($407-1210/kg). [162] BJ particle size distributions are not well known and costs are not reported. Based on similar particle size requirements to EBM, powder-fed DED powder is expected to have similar costs.

This review details processing defects, thermal histories, post-processing, microstructure, and mechanical properties associated with DED and PBF techniques. The various metal AM techniques were described, with a focus on comparison of processing strengths and

weaknesses. Previous work identified future directions for metal AM within specific areas: limited deposition rate, surface finish, residual stress, and microstructural variations. [163] It is useful to consider the progress that has been made in these areas since the publication of the report in 2007 and identify new directions that the technology may take.

Higher power lasers have increased the deposition rate of some DED hardware. Currently, surface finish and deposition rate are inversely related, which is an undesirable trade-off. Many experiments try to improve surface finish, despite the fact that most-end use parts will be post-processed (thermally and mechanically) and surface finish will be determined by the polishing or machining techniques used. If this is the intended use, surface finish almost does not matter.

Residual stress continues to be a defining problem for DED and LM, but new technologies like EBM (and potentially BJ) have succeeded in producing parts with low amounts of residual stress. Residual stress can impact post-processing and mechanical properties. Acting as a driving force for recrystallization, residual stress in DED and LM parts may limit the ability to engineer grain structures using those approaches. Conversely, residual stress may be able to be used to help promote recrystallization and the formation of equiaxed microstructures.

The understanding of the microstructure, mechanical properties, and processability of new alloys has been the main advance in metal AM in the past five years. While microstructural heterogeneities are still observed, characterization work has shown certain features (columnar grains, high orientation, amount of porosity, etc.) to persist across technologies and materials. Improved process control and processing experience have allowed for the reduction of process-induce porosity to levels of frequently >99% dense parts.

Two current mindsets for metal AM material exist: (1) as-fabricated properties matter because there are customers who intend to use them without post-processing and (2) as-

fabricated properties are not important because material will be post-processed to eliminate pores and cracks, change the grain structure, and change phase fractions. Both of these schools of thought are relevant, but it is important to note that as-fabricated microstructure is still important to characterize even if post-processing is to be used; post-processing needs to consider the as-fabricated properties in order to achieve the desired final material. For this reason, work to characterize as-fabricated material will continue to be important to both schools of thought. As processes improve, the process metallurgy is likely to change the condition of as-fabricated material (even for those materials previously characterized).

Niche product applications (hip replacements, GE LEAP nozzles, GE turbine blades) have found recent success for the use of PBF parts. Previous success was mostly in the DED repair of traditional parts for the aerospace industry. (REF blades) Applications to the robotics industry are promising, as metal AM has been shown to enable performance characteristics, like increasing the degrees of freedom of rotating parts. All of these developments suggest that metal AM may really be about "giant engineering firms turning out sophisticated parts". [164]

II.8.1 Future Directions

The future of the technology is bright. Improvements on the high end will enable the production of higher quality AM parts, while the expiration of patents and falling costs of heat sources will help to lower the cost of the technology. New materials will be processed, offering a wider range of available alloys. Recent work on the control of grain structure and phase formation suggests that improvements in processing controls will enable metal AM to achieve microstructural engineering on a scale not previously possible.

Having explored the current state of metal AM, it is useful to look back on where limitations exist. The authors have identified the following areas as being of general importance for the continued improvement of metal AM:

- Faster Deposition rates
- Quality Control
    - NIST roadmap almost entirely falls within this category
- Machine Reliability
- Cost Reduction
- New Capabilities/Materials

Faster deposition rates are directly related to costs and feasibility. Faster rates mean more parts can be produced per machine per unit time; each machine can be made more efficient with faster deposition rates. Any decrease in process time is impactful, but jumps of orders of magnitude are needed to truly revolutionize metal AM production. To achieve faster deposition rates, limitations on the amount of power input available for the process must increase. This is possible by increasing the power or number of heat sources available. Faster deposition must not incur too much residual stress, or significant warping issues may occur. Some increase in the amount of defects (like porosity) may be tolerated, if post-processing can be done.

Quality control is a significant concern and problem for industry in suing metal AM processes. Metal AM processes are new (compared to traditional processes) and are just beginning to enter the time-frame for qualification for many aerospace companies, though biomedical qualification may offer a shorter timeline. Quality control must understand the details of the AM process to be qualified. For this reason, advances in process technology may not get incorporated as fast (as industry is likely to qualify certain machines and older software versions). A NIST roadmap for metal AM focuses entirely on quality control

concerns: standards and protocols, measurement and monitoring techniques for data, fully characterized material properties, modeling systems that couple design and manufacturing, and closed loop control systems for AM. [165] These are all extremely important efforts, but quality control is only one piece of the big picture. Developing quality control, and keeping it up-to-date, is likely to remain a focus of metal AM.

Machine reliability of all metal AM systems must improve, and the operator burden should be reduced. High failure rates are common in many systems, though these rates are hardware, operator, and design dependent. Though improvement of machine reliability must come from hardware manufacturers, researchers and operators should come together to present best practices to reduce the effect of operator error on failure rates. Improved software simulation could also play an important role in determining optimal build orientations for successful builds. As more technicians learn how to use existing hardware, operator errors will also be reduced.

The impact of cost cannot be understated. It can be argued that faster deposition rates, quality control, and machine reliability are really just sub-sets of cost. Cost is considered separately here, as reduction in hardware and feedstock costs can open up the metal AM market to completely new customers. While consumer metal printers are not likely to happen anytime soon (though open source efforts are making progress), a significant drop in hardware cost could open up the machine shop market; machine shops are a significant player in local manufacturing and have more resources to support hardware than typical consumers. Continued costs reductions should be expected to open up metal AM to more users, while increasing the number of uses considered economical.

New hardware and new materials development have the most direct impact to the research community. Development of new ways of processing metal into parts could potentially dramatically increase deposition rates and lower costs of metal AM (in the way in which large-scale polymer systems have changed what is possible with polymer printing). New

materials development is research intensive but necessary to increase the number of uses for metal AM. New alloys will have uses for new industries and new parts. AM specific alloys may be able to increase performance beyond what is capable with traditional wrought or cast alloys. The ability to manipulate grain and phase structures offers the potential for microstructural engineering and will likely see continued efforts. Fundamental processing science is important to all of these development efforts.

CHAPTER III

INCONEL 718 REVIEW

In this chapter, the microstructure, mechanical properties, post-processing, and traditional processing strategies (cast, wrought) of IN718 will be reviewed. Most recent reviews and books on nickel-based superalloys focus on gamma prime strengthened alloys or new, modern compositions (not entirely relevant to IN718), so a full review of IN718 is provided herein. In addition to a survey of historical work, a significant number of papers have been published on IN718 since the year 2000. These new works offer insight into a specific area of importance to EBM of IN718: delta phase formation.

III.1 Uses & History

The first corrosion-resistant nickel alloy, MONEL, was developed in 1906. The first development of Inconel alloys for use in jet engines was in the 1940's by Wiggin Alloys in Hereford, England. [166] In 1962, the development of IN718 was a major success due to its good weldability. [167] Specifically, IN718 is relatively insensitive to strain-age cracking. IN718 has been adopted by many industries, but aerospace companies, like Pratt & Whitney, were early adopters and applied IN718 in gas turbines and rocket engine components. [168] IN718 comprises more than half of the weight of some commercial jet engines. IN718 also enjoys widespread use in the power industry [169, 170], including in reactor internals for nuclear power plants. [171] Significant cost savings in part production have been demonstrated in the aerospace industry by using investment casting to replace wrought assemblies of parts. In the example of an IN718 diffuser case, a 38 part assembly was reduced into a single component (Figure 34). [168]

Figure 34. Investment casting was used to reduce the number of parts in a diffuser case from 38 to one. [168]

III.2 Chemistry

IN718 is known by the UNS identifier N07718, which corresponds to an alloy chemistry as shown in Table 7. The term "superalloy" typically refers to the enhanced performance of the alloy, with nickel-based superalloys being high-temperature materials that also exhibit good resistance to corrosion. Each alloying element has a purpose determined by its properties as shown in the periodic table in Figure 35. Ni, Co, Fe, Cr, Ru, Mo, Rh, and W all have similar atomic radii to Ni and, therefore, act as γ-matrix stabilizers. Al, Ti, Nb, and Ta promote ordered phase formations and tend to have larger atomic radii (though Al is smaller than some stabilizers). Both much smaller (B and C) and much larger (Zr) atoms tend to segregate to grain boundaries. Creep resistance is improved by the low interdiffusion coefficients of Ir, Re, Ru, Pt, W, Rh, and Mo. [172] During solidification, Nb, Mo, and Ti segregate to the interdendritic regions. [173] Cr adds corrosion resistance, and Co increases the solubility temperature of γ', which increases the maximum service temperature. [174] IN718 has a nominal density of 8.19g/cc, specific heat of 435 J/(kg*°C), elastic modulus of 200GPa, and thermal conductivity of 11 W/(m*K). [175]

Table 7. ASTM Standard on IN718 chemistry. [176]

Element	Composition,%
Carbon	0.08 max
Manganese	0.35 max
Silicon	0.35 max
Phosphorus	0.015 max
Sulfur	0.015 max
Chromium	17.0 to 21.0
Cobalt[A]	1.0 max
Molybdenum	2.80 to 3.30
Columbium (Nb) + tantalum	4.75 to 5.50
Titanium	0.65 to 1.15
Aluminum	0.20 to 0.80
Iron[B]	remainder
Copper	0.30 max
Nickel	50.0 to 55.0
Boron	0.006 max

[A] If determined.
[B] Iron shall be determined arithmetically by difference.

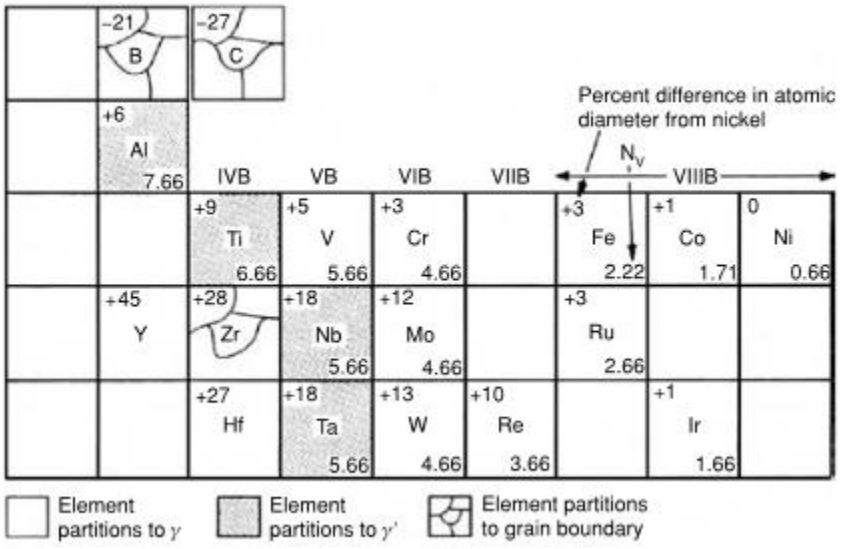

Figure 35. Various alloying elements of superalloys. [177]

Table 8. Standard vs. Historical Terminology for IN718.

Standard Terminology (Used in this Paper)	Historical Terminology (Used in Some Older References)
Niobium (Nb)	Columbium (Cb)
δ	β
γ''	γ^*
$\gamma'' \; or \; \delta$ (explicit)	Ni_3Nb (no distinction made)

III.3 Phase Formation

The γ-phase of IN718 is the Ni matrix, with alloying elements in solid solution. Precipitate phases are extremely important in determining IN718 properties, where the possible phases are listed in Table 9. Of the possible phases, γ'' is the primary strengthening phase. [173] Its formation is strongly dependent on the local Nb concentration. As Nb segregates during solidification, it creates interdendritic regions rich in Nb. If not properly homogenized, these regions can form Laves phase, which is detrimental to mechanical properties. Depending on processing thermodynamics, various phases may form in IN718.

Table 9. Possible phases in IN718 with reference lattice parameters and solvus temperatures. [178]

Phase	Crystal Structure	Formula	Lattice Parameter [nm]	Solvus Temperature [°C]
γ	FCC	N/A	a_0=0.3604 [179]	1227-1320 (solidus) [180, 181] 1260-1364 (liquidus)
γ'	FCC, ordered $L1_2$	Ni_3(Al, Ti)	a_0=0.3561-0.3568 [182]	850-910 [94, 183]
γ''	BCT, ordered $D0_{22}$	Ni_3Nb	a_0=0.3624 c_0=0.7406 [184]	910-940 [182, 185]
δ	Orthorhombic, ordered $D0_a$, ordered Cu_3Ti	Ni_3Nb	a=0.5114 b=0.4244 c=0.453 [186]	1020 [94, 182]
MC	Cubic, B_1	NbC	a_0=0.43-0.470 [182, 184]	1260-1305 [181]
$Laves$	Hexagonal, C_{14}	Fe_2Nb Fe_2Ti Fe_2Mo	a_0=0.475-0.495 c_0=0.770-0.815 [182]	1163 [173]
σ	Tetragonal	FeCr FeCrMo CrFeMoNi CrCo CrNiMo	a_0=0.880-0.910 c_0=0.450-0.480 [182]	-
$\alpha - Cr$	A_2	N/A	-	-

III.3.1 Origins of γ''

The typical structure of γ'' precipitates is shown using transmission electron microscope (TEM) in Figure 36. Recent work on a variant of IN718 has noted that clustering of Al/Ti and Nb atoms and the volume fraction of γ''/γ' suggests that γ'' nucleation occurs prior to γ' nucleation at 706°C. [187] This contrasts to previous work suggesting the co-precipitation or precipitation of γ' first [188] and experimental work that has shown the apparent precipitation of γ' before γ'' at 680°C. [189] The potential explanation for these differences in nucleation order lies in Al + Ni/Nb ratio. Alloys with a ratio >0.8 nucleate γ' first, whereas alloys with a ratio ~0.7 nucleate γ'' first. Atom probe results indicating clustering prior to

nucleation suggest that Nb clusters prior to Al/Ti, leading to the conclusion that γ'' nucleates first in some alloys. Formation of γ'' [190] and NbC [191] at GBs has been studied, which points towards the influence of Niobium segregation. It has been observed that the formation of γ'' takes place in a first stage, precipitating high density, small cubes, and a second stage, precipitating ellipsoidal discs. [192] Measurement of volume fractions of γ''/γ' using image analysis is difficult, but electrochemical extraction or precipitates can be used to produce more reliable results. [193] With this technique, the matrix is dissolved away, leaving the precipitates behind. Error may be introduced due to presence of other precipitates, and the fractions of γ'' and γ' cannot be separated. To estimate individual volume fractions, it can be assumed that the ratio is 3.0.

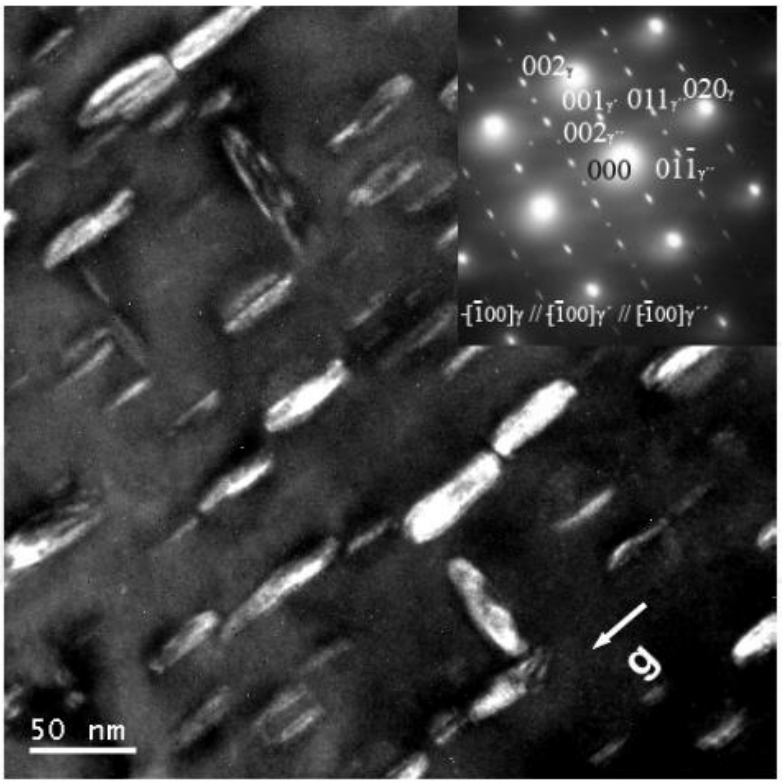

Figure 36. Dark Field TEM image and diffraction pattern showing γ'' precipitates in IN718. [194]

III.3.2 Pathways to δ-Phase Formation

The formation of δ-phase may follow a number of pathways, dependent on temperature and time (Figure 37). At low temperatures (<700°C), there is cellular precipitation of δ-phase at GBs. [195] At medium temperatures (750-800°C), there is transformation of $\gamma'' \rightarrow \delta + \gamma'$, in addition to cellular precipitation of δ-phase. This can lead to γ''-free, denuded regions of 100nm surrounding δ-phase particles. [192] At high temperatures (~960°C), there is direct precipitation of δ-phase from the supersaturated matrix. [179] The highest delta growth rate has been observed to occur at 960-980°C, for short aging times of as-forged and solution treated material. [196] The temperature and material condition (as-forged vs. solution treated) are very impactful on the quantities and morphologies of delta phase present.

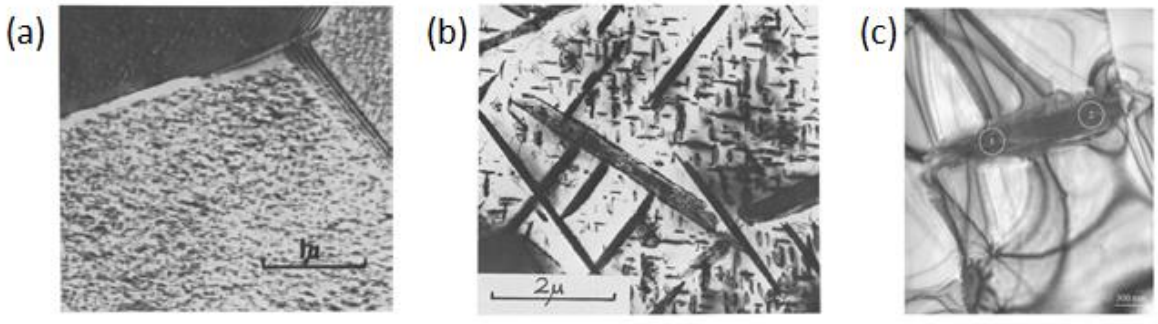

Figure 37. Formation of δ-phase in IN718 by (a) cellular precipitation at <700°C, (b) cellular precipitation and transformation from γ'' at 750-800°C, and (c) direct precipitation from the γ-matrix at 960°C. [179, 195]

For IN718, intragranular precipitation of δ was noted at 800°C. [197] The δ precipitation and growth was noted to form signicant amounts of dislocations, which may act as positive feedback to produce more stacking faults in γ'' (which may promote δ formation). At 900°C, the γ'' was completely replaced by δ. At 950°C, δ precipitates directly from the

supersaturated matrix. In some instances, δ of different variants was observed to interact by shearing. Previous work has also noted the importance of stacking faults to γ'' precipitation and the interaction with δ. [195]

The precipitation order of γ'' and δ-phase is summarized in Figure 38. In Figure 38(a), a GB is shown with respect to the supersaturated γ-matrix. No precipitate phases are present in this step. As the material is aged in Figure 38(b), δ-phase will form along the GBs and γ'' will nucleate (in addition to γ', which is not shown). The aging process continues in Figure 38(c), where γ'' coarsen and grow in different variants of the $\{100\}$ direction in the matrix. This will typically be evident as GBs, where adjacent grains have noticeable misorientation (as in high angle GBs). As the aging process continues in Figure 38(d), continued growth of γ'' may result in overaging or growth of the γ'' to sizes larger than optimal for strengthening. Additionally, δ-phase may begin to form needles on the GBs. The movement of GBs may occur, as shown in Figure 38(e), to produce jagged edges on the GBs caused by pinning by the δ-needles. As the aging process continues in Figure 38(f), γ'' may transform to intragranular δ-needles and/or δ-needles may grow from the GBs into the matrix. Denuded zones, free of γ'', will surround GBs and δ-phase. The δ-needles will form on different planes, on $\{111\}$ matrix variants. Depending on the temperature of the heat treatment, δ-phase may form directly from the super saturated matrix, though this process is not depicted in this sketch.

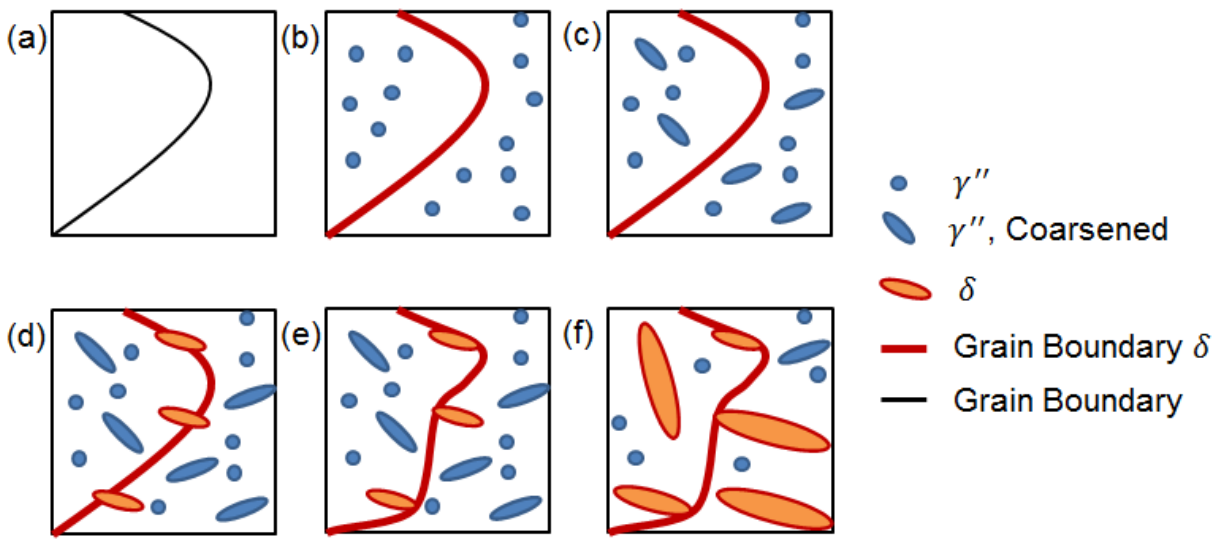

Figure 38. Sketch of the typical precipitation order of γ'' and δ-phase in IN718.

III.3.3 Misfit & Coherency

For most precipitates, there is a preferred orientation relationship with the FCC γ-matrix. For γ'', it prefers to reside on $\{100\}$ planes. Intragranular δ-phase laths form on $\{111\}$ planes. [195] Both γ'' and γ' are coherent with the matrix, giving rise to coherency strains. δ-phase is incoherent with the matrix, and has a much larger matrix misfit than γ''/γ'. [197] In fact, the incoherency has been noted to lead to the punching out of dislocations during precipitation and growth of δ-phase. The amount of coherency strain can be related to the misfit parameter, calculated by Equation 1. [177]

$$\boldsymbol{misfit = \delta = 2 * \frac{a_{\gamma'} - a_{\gamma}}{a_{\gamma'} + a_{\gamma}}} \qquad \textbf{(Eq. 1)}$$

Phase composition influences lattice parameter, which determines misfit. [172] Measured phase compositions are given in Table 10. Misfit is related to internal stresses in the

precipitate, and has a resulting influence on the phase morphology, or shape. For a γ'-strengthened alloy, misfit is related to particle radius and particle morphology in Figure 39. As misfit increases, particle morphology changes from spheres to cubes, and then rods. For a γ'' precipitate in IN718, the lattice misfit and coherency strain has been experimentally confirmed [198] to match previous theoretical calculations. [188] Coherency strains have been used to explain an intriguing feature of IN718, "compact" γ''/γ'. [188] In this structure, γ'' precipitates on the 6 faces of a γ' cube. The thermal stability of this "sandwich" structure is improved compared to normal γ' precipitates. In addition to a diffusion barrier formed by the γ'' shell, coherency strains restrict the morphology.

Table 10. Measured composition of IN718 phases. [199]

Phase	Structure	Analysis, at. %						
		Nb	Al	Ti	Fe	Cr	Mo	Si
γ	A1	1.97	0.74	0.52	23.8	22.0	2.41	0.64
γ′	L12	10.2	8.00	9.40	2.15	0.50	0.490	0.35
γ″	DO22	25.1	0.44	4.92	0.86	0.76	1.05	0.01
δ	DOa	20.4	0.80	3.00	5.30	3.40	2.20	0.10
Laves	C14	18.8	0.10	0.60	15.0	15.3	10.2	4.50
MC*	B1	14.6	0.10	80.0	0.90	1.90	0.50	1.90

*May contain nitrogen, also a high niobium form has been identified with 84 at.% Nb, 7 at.% Ti and small amounts of Fe, Ni and Cr.

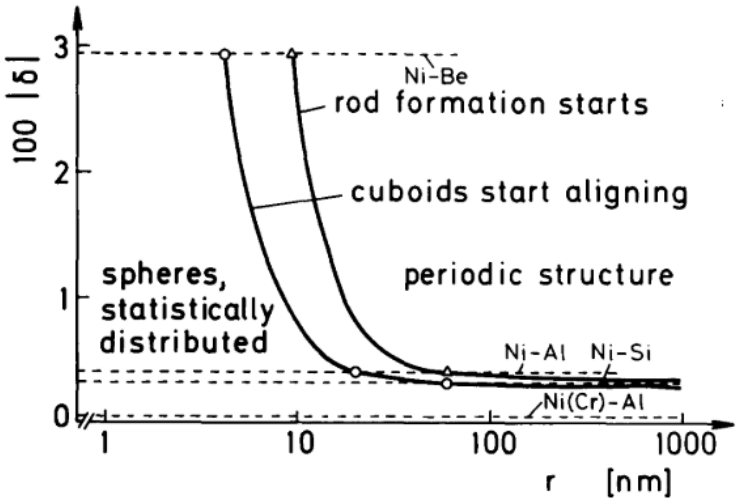

Figure 39. Lattice misfit and radius of γ' precipitates determine morphology (shown for a γ'-strengthened alloy). [200]

In nickel-based superalloys, topologically close-packed (TCP) phases are noted as a class of phases that are characterized by close-packed layers in the crystal structure. [172] TCP phases may become crack initiation sites, while also depleting the matrix of refractory elements necessary for strengthening. In IN718, the σ-phase is a TCP phase. The σ-phase and M_6C are not typically found in modern IN718 due to lower Si content and homogenization temperatures lower than 1200°C. [173] However, long annealing times (>25,000hr) were studied for the precipitation of minor phases (σ, α-Cr, Laves, δ) in IN718. [201] The stability of IN718 was noted for temperatures of 532°C, 621°C was favorable for α-Cr formation, 676°C precipitated σ, α-Cr, and Laves as shown in Figure 40, and 732°C included some σ-phase associated with large quantities of δ-phase. In the 718Plus alloy variant, the formation of an η-Ni_6AlNb phase was a unique and predominant phase formation. [202] This type of η-phase is otherwise not typical of IN718 material.

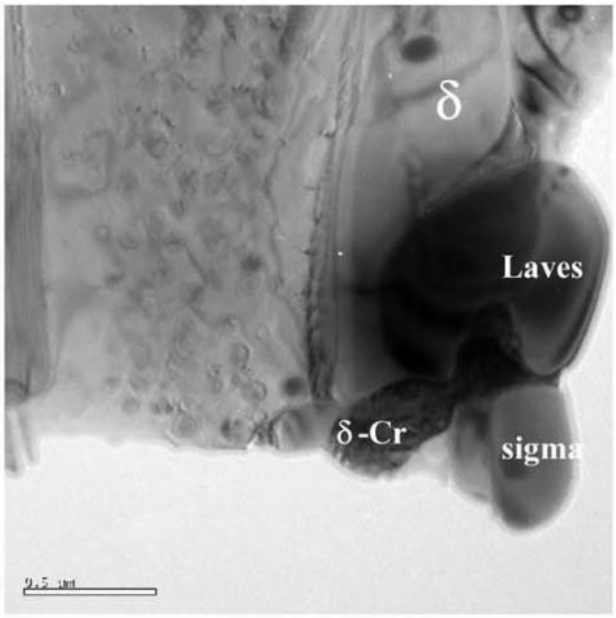

Figure 40. Formation of δ-phase, α-Cr, σ-phase, and Laves phase in a sample aged for 25,000hr at 676°C. [201]

III.3.4 Applied Stress

Previous discussions of phase formation have focused on un-stressed material without applied work. The application of stress and the introduction of dislocations can significantly impact the behavior of the material. Recent modeling efforts have studied the effect of stress on phase precipitation in IN718. [203] With no applied stress during aging, the three different $\{100\}$ variants of γ''precipitate almost equally. If stress is applied preferentially during aging, then preferential variant precipitation occurs. During coarsening, γ'' aspect ratios increase instead of uniform growth. Separate work has shown that the precipitation of δ-phase increases with strain. [204] The morphology also undergoes a change, with the quantity of needle δ decreasing and blocky/globular δ increasing with strain. Cold work introduced by shot-peening of IN718 accelerates the precipitation rate of γ''. [205] In other research on cold worked material, the nucleation and coarsening of δ-phase increased with

deformation. [206] The nucleation sites for δ-phase were found to be on dislocations above 950°C, on dislocations and GBs at 900 to 950°C, and from γ'' transformation below 900°C.

III.4 Solidification

As an alloy transforms from liquid to solid, the details of solidification are important in understanding the resulting microstructure. Dendritic solidification is the most common type of solidification, but cellular or planar front solidification is also possible. [207] The type of solidification is dependent the liquid-solid interface velocity (R), thermal gradient (G), and physical boundary conditions of the melt pool. During casting and welding solidification, IN718 tends to exhibit dendritic behavior. [208] Depending on solidification kinetics, the spacings of the dendrites will vary. The primary dendrite arm spacing (PDAS) is the spacing between the primary cores of the dendrites, whereas the secondary dendrite arm spacing (SDAS) is the spacing between the branches off of the core. As solid is formed, Nb, Mo, Ti, and other alloying elements tend to segregate to interdendritic regions. This segregation leads to local variation in the matrix composition that can promote localized phase formations in the interdendritic regions.

Cooling rate is formulated as equal to G*R and the quantity G/R may be useful in predicting the stability of a planar front. [111] The cooling rate influences diffusion rate, partition coefficient, and solidification type. [209] As cooling rate increases, the sequence changes from dendritic to cellular and then diffusionless. Cooling rates have been studied from 0.25 to 20,000°C/s. During rapid solidification, it was observed that interdendritic regions contained less Nb and no Laves phase (whereas slower solidification had more segregation and Laves). Diffusion rate and partition function both increase with cooling rate. The number of lattice defects increases with increasing solidification rate and this is proposed as a possible explanation for the observed diffusion rate and partition coefficient increases.

[209] Nucleation sites for rapid solidification were noted to be diffusionless in nature, and cell-like solidification fanning out from the site.

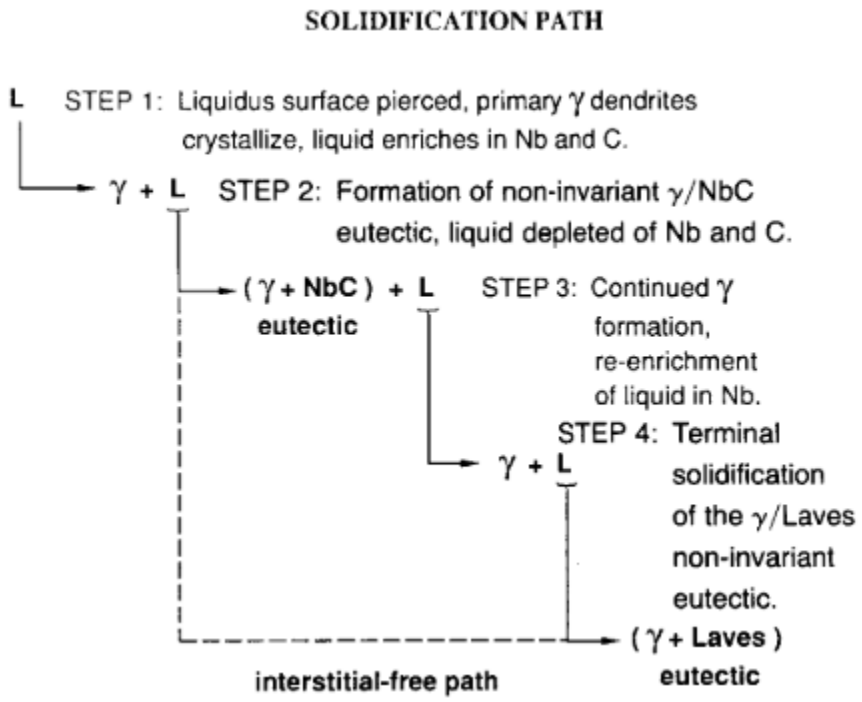

Figure 41. Solidification path for IN718, as determined in work on non-equilibrium, welding solidification. [210]

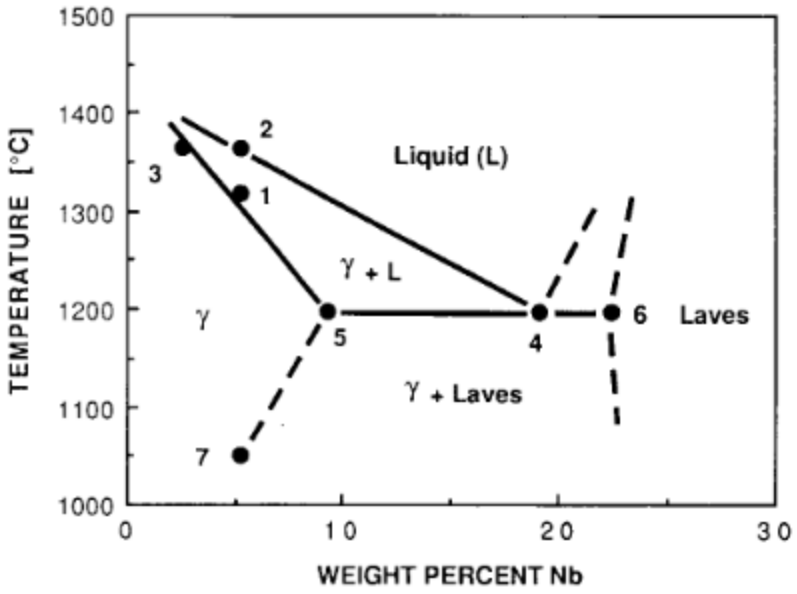

Figure 42. Solidification diagram based on welding research. [210] This diagram does not allow for suppression of Laves formation at higher weight percentages of niobium.

It has been observed that Laves phase and NbC are commonly formed during solidification (Figure 41) by enhanced segregation of Nb and C to interdendritic regions. [210] This work was done for an average cooling rate of <500°C/s. In fact, Nb-segregation during solidification can be used to form a pseudo-phase diagram to predict Laves phase formation (Figure 42) for certain solidification conditions. Phases formed during solidification are typically termed “primary” phases, whereas phases formed during solid state heating and cooling are termed “secondary” phases. Primary carbides can be correlated to cooling rate, as shown in Figure 43. [211] The relationship was developed for remelt ingots, for a limited range of cooling rates. The relationship shows an increase in carbide size with a decrease in cooling rate. Coarsening of primary carbides, or misidentification of secondary carbides, may contribute to error in these calculations. During rapid solidification of IN718, carbides were found to form between dendritic arms. [212] The dimensions of microsegregation and grain size can be reduced by process modification, which can lead to improvement in

mechanical properties. TiN from nitrogen contamination during processing can act as nucleation sites for NbC, significantly effecting precipitation kinetics. [213] Post-processing of such material, with nitride inclusions, will remain impacted due to the change in chemistry. [214] The effects of microsegregation [215] and solidification rate [216] have been studied for DS IN718. Microstructures show segregation of Nb and Mo, in addition to visible primary and secondary dendrite arms. Increased superheating was observed to reduce segregation.

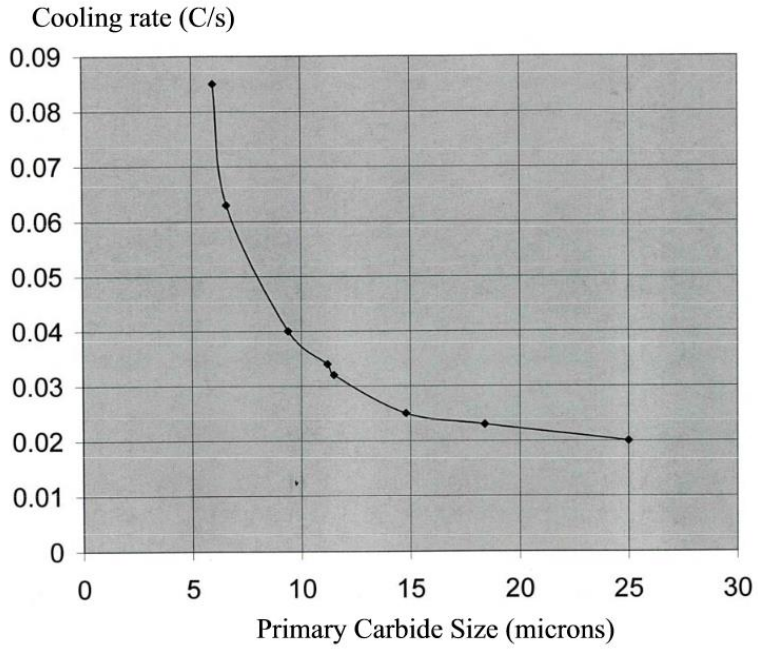

Figure 43. Relationship of primary carbide size to cooling rate for IN718. [211]

In addition to influencing phase formation and solidification type, G and R also determine the nature of the grain structure, based on the columnar-to-equiaxed transition (CET). The CET for IN718 is shown by plotting G vs. R in Figure 44. [83] Equiaxed grains are favored as R increases and G decreases. Columnar grains are favored as R decreases and G increases.

Rapid solidification of IN718, with rates faster than 10^4°C/s, are not well studied with respect to the CET.

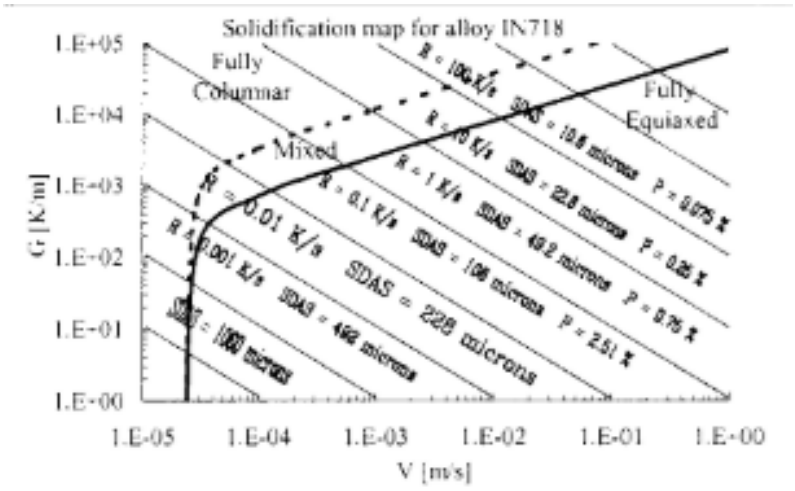

Figure 44. Solidification map for IN718. [83]

III.5 Common Post-Processing Techniques

After metals are solidified, the phases and phase fractions present may be altered without re-melting through solid-state phase transformation. These transformations form the basis for the thermal post-processing of IN718. The goal of IN718 post-processing is to produce a homogenous, precipitate hardened microstructure. Internal porosity may be removed by Hot Isostatic Pressing (HIP). Homogenization is used to reset compositional segregation incurred during solidification. Solution treatment is used to reset previous phase precipitations. Aging results in the precipitation of γ'' and γ', which strengthen the material.

During thermal treatment, the recovery, recrystallization (RX), and growth of grains must be considered. Dislocations induced during deformation (hot or cold work) can provide a driving force for RX. [217] Grain growth is impeded by GB δ-phase and carbides, as these phases act by Zener pinning. [218] The use of δ-phase to restrict grain growth during aging is well known and utilized. [173, 182, 219] RX can be used to refine the grain size during processing of wrought material. [220]

III.5.1 Homogenization & Solution Treatment

After IN718 is cast or solidified, Niobium is one of the most segregated alloying elements. Homogenization is typically the first step in post-processing of castings, seeking to reset Nb segregation by thermally activated diffusion. Homogenization of ingots has shown that Laves can be solutionized and Nb homogenized. [221] The presence of Laves phase and NbC may complicate post-processing, resulting in incipient melting at the GBs and aiding intergranular liquation cracking. [222]

Homogenization of deformed cast ingots has been observed to lead to RX. [223] It was observed that delta phase limited growth below 1010°C, but also that NbC acted as a nucleation site for RX (Figure 45). Delta phase and new nucleation of grains were related to prior GBs, which were Nb rich regions. It has also been reported that δ-phase needles can contribute to particle stimulate nucleation (PSN) during dynamic RX of high temperature tensile tests of wrought IN718. [224, 225] Recent work noted unexplainable recrystallization in IN718, [226] possibly due to high solution treatment temperature and a “higher amount of stored energy observed in the microstructure”. Ragged edges, large amounts of twinning, and a “ghost” microstructure of delta characterize the recrystallized regions of the sample processed via Gleeble. High angle GBs are greatly reduced in the recrystallized region following heat treatment. Detailed, etched SEM images of precipitate structure in the deformed state, prior to HT, are not presented, but could provide clues as to the variance in resulting recrystallization regions. For cold-rolled material, δ-phase, γ', and γ''

are all found to inhibit recovery and RX. [227] Newly RX grains show persistence of δ-phase on GBs and intragranularly (anneals were carried out below 900°C). There must be a minimum dislocation density present to initiate RX, where dislocation density has also been modeled for forgings to predict yield stress. [228]

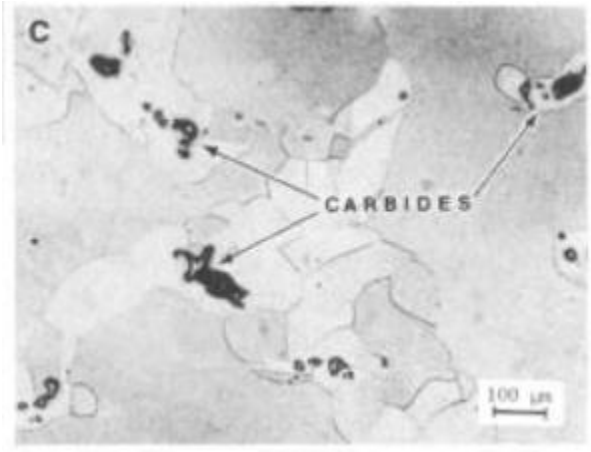

Figure 45. Nucleation sites shown to occur near carbides in deformed IN718. [223]

Solution treatment relies on annealing above the solvus temperature of any precipitates that are to be solutionized. For IN718, the solvus temperatures of various phases are given in Table 9. Solution treatment to reset γ'' and γ' is common as a standard aging procedure can then be followed to obtain peak aged material, without overaging. As NbC solutionizes at 1260-1297°C in as-cast material and 1267-1305°C in homogenized, wrought material, [181] solution treatment to reset carbide formations from solidification is likely to result in significant grain growth. Banding of fine grains in IN718 forgings was eliminated using the multi-step homogenization process. [229] With higher homogenization temperature, carbides in the forgings grew in size due to Ostwald Ripening and also became more dispersed than clustered. Homogenization and solution treatments must therefore be balanced with the effect on carbide or grain growth.

III.5.2 Hot Isostatic Pressing (HIP)

Hot isostatic pressing (HIP) may be performed to remove internal porosity from material. This step subjects material to high temperatures and high pressures, which causes voids to collapse. HIP of cast material [230, 231] has explored the impact of pressure and temperature on microstructure and mechanical properties. Porosity was observed to be reduced 64% by HIP in the castings studied. The optimal HIP parameters were found to be 100MPa, 1180°C, and a 2-hour hold time. NbC phases are still present after HIP.

III.5.3 Aging

After a material is homogenized, it may be HIP'd or aged according to standard procedures. "Direct aged" material is aged directly following receipt or a processing step. "Peak aged" material has an optimal amount of aging defined by achieving a peak in hardness, as shown in Figure 46. Solution treatment can be used to "reset" any precipitate phases that have formed and typically precedes aging. The term "STA" may refer to either "solution treated and aged" or "solution treatment anneal".

Aging in IN718 is a specific heat treatment designed to promote the formation γ'' and γ' strengthening phases. The standard aging process is to hold at 720°C for 8 hours, furnace cool to 620°C, hold for total furnace time to reach 18 hours, and then air cool. [94] This aging treatment starts in the γ''/γ' precipitation region (720°C) to precipitate hardening phases, then holds below the precipitation range (620°C) to coarsen the hardening phases. Cooling rate from solution treatment can have a significant impact on mechanical properties, as aging can occur during slow cool downs. [232]

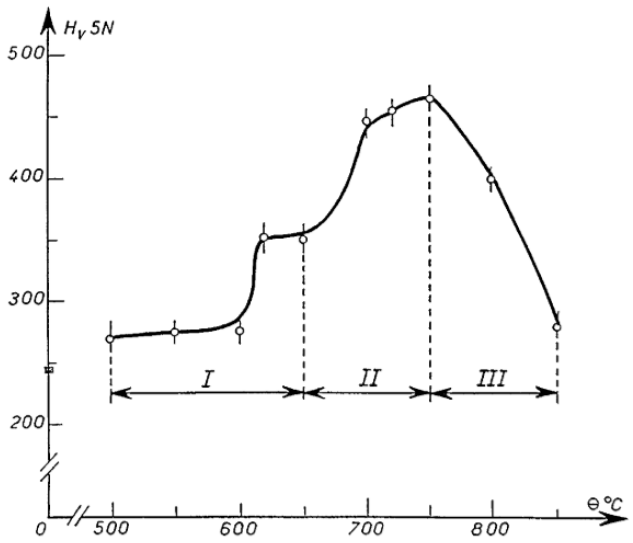

Figure 46. Hardness of IN718 as a function of temperature. Note that peak aged material is 466HV. [198]

III.5.4 Coarsening

As discussed earlier in §III.5.1, carbides may grow by Ostwald Ripening. Lifshitz-Slyozov-Wagner (LSW) Theory is a method for quantifying coarsening by Ostwald Ripening. [233] Original formulations point to a particle size proportionality, $\alpha\, t^{\frac{1}{3}}$, for particles forming directly from super saturated solution. [234] The theory for calculating growth of existing particles is more complex, and is still the subject of ongoing research. The time law for LSW theory was found to apply to the coarsening kinetics of γ'' and γ' in IN718, but not to the particle size distribution of the phases. [235] Interactions between growing particles or strains from matrix misfit were suggested in this work as reasons for the difference in size distribution. The same work on application of LSW theory calculated the activation energy for coarsening of γ'' to be 298±41 kJ/mol and that for γ' to be 271±49 kJ/mol.

Since the δ-phase is incoherent with the matrix, the surface energy of the interface is expectedly higher than for the coherent γ''/γ' interfaces. Additionally, the incoherent interface is expected to produce the most growth for a set diffusion coefficient. Since the diffusion of Nb is key to both δ and γ'' precipitation and coarsening, the role of prior grain boundaries in non-uniform precipitation, as shown in Figure 47, is important to consider; Nb rich zones left behind by prior grain boundaries or precipitates may create preferred precipitation sites. The kinetics of δ-phase and γ'' growth are not typically compared directly, however, due to the differences in precipitation kinetics.

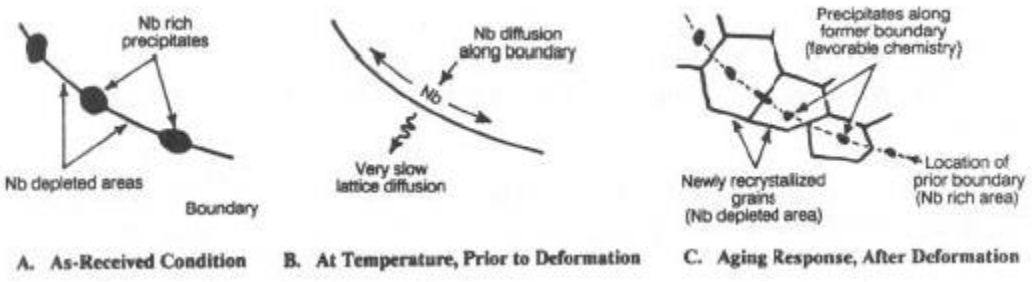

Figure 47. Mechanisms for non-uniform precipitation in IN718. [223]

III.5.5 Overaging

Overaging results from the growth of γ'' to sizes that are larger than is optimal for strengthening. Additionally, overaging can result in the transformation of γ'' to δ-phase. This is associated with a loss of strength, as the growth of intragranular δ-phase consumes γ'' that would otherwise be contributing to the high temperature strength of the material. In the case of extremely long hold times (~50,000 hrs at 538-704°C), the formation of α-Cr and σ-phase was found to occur near large delta phase particles. [178] This occurs because the growth of the δ-phase rejects Cr and Mo to the matrix (which is needed for formation).

III.5.6 Alternative Post-Processing Methods

Alternative methods for post processing IN718 exist, but are mostly held as trade secrets or proprietary standards. Patents offer clues to some methods; a patented post-processing procedure claims the ability to produce IN718 with γ' as the primary strengthening phase. [236] While it is unclear that the claims of this patented alternative method could be produced (given the typical co-precipitation of γ'' with γ'), it does show that industrial work has attempted to explore and optimize processing techniques.

For powder metallurgy (PM) of IN718, powders can be compacted into dense material by HIP. Oxides and carbides may form on prior particle boundaries (PPBs), reducing ductility of HIP material. The standard HT (980°C 1hr / 720°C 8hr / 620°C 8 hr) was found to not be suitable for PM IN718. [237] Modification of the post-processing of PM IN718 showed improvement in tensile and stress rupture properties. [238] This was accomplished by a high temperature initial solution treatment (1270°C 1hr) preceding HIP to breakup PPBs and dissolution of metal carbides MCs. The quantity of PPBs was found to be influenced by the oxygen content of the powder feedstock, but the oxygen content did not influence formation of γ',γ'', or δ-phase. [239]

III.6 Mechanical Properties

IN718 must maintain mechanical properties under high-temperature operating conditions, for long life-times. To meet performance requirements, mechanical testing of test batched of material is standard. This section will explore the tensile, fatigue, hardness, and other mechanical properties that are relevant. Mechanical properties are determined by the microstructure of the material, which impacts the deformation mechanism of choice. The impacts of grain size, grain morphology, segregation, porosity, phase fraction, and phase morphology are all discussed.

III.6.1 Grain Size & Grain Morphology

In solution treated forged bar, the difference between 40um (ASTM 6) and 59um (ASTM 5) grain size showed no notable difference in YS, UTS, or elongation, but did have an observed variation in hardness of 261.7±7.2HV (ASTM 6) compared to 222.8±10.8HV (ASTM 5). [240] Upon aging, there was no notable difference in YS, UTS, elongation, or hardness. This data supports the claim that IN718 is relatively insensitive to grain size, though the limits of this claim are not well defined for very large or small grains.

The relationship of grain size to hardness is not very strong, according to data from Schirra et al. (though there is some loss of hardness associated with very large grains as seen in Figure 48) [241] This points towards precipitate hardening, the main strengthening mechanism, as the most important consideration. The shape of grains (columnar vs. equiaxed) and the orientation are important in materials that display anisotropic material properties. [242] For example, elastic modulus is known to vary with crystallographic orientation in nickel based superalloys.

In FCC Cu, it has been shown that grain boundary strengthening has a greater effect in columnar grains than in equiaxed grains due to relatively more grain boundary in a unit volume. [243] Work hardening is discussed to be of more impact in larger grains, whereas grain boundary strengthening is more important to smaller grains. However, this analysis was done with dissimilar grain volumes (columnar grain smaller in volume than cubic grain). This of course implies that more GBs will be present within a unit volume. So, this may not be universally true. Also, the “grain size” was measured by a parameter “a”, which does not take into account variation in height of columnar grains vs. equiaxed. If the premise of this work is extrapolated to AM material, it may be useful to measure the ratio of GB length to grain area for both XY and XZ faces. This may give a method for quantifying variance in columnar grain size.

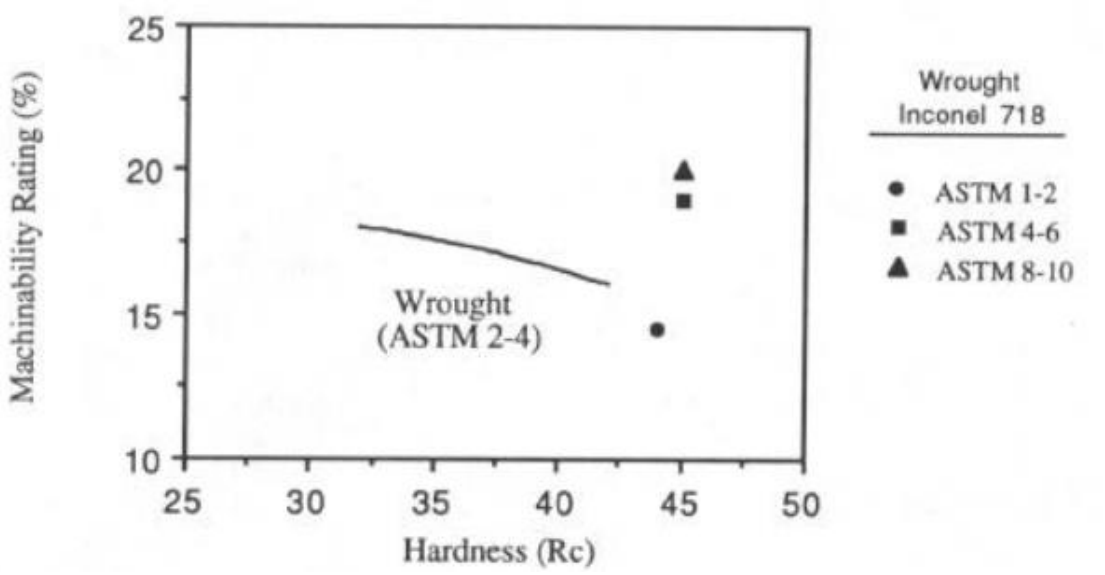

Figure 48. Relationship of machinability, grain size, and hardness. Larger grains are less machinable, due to increases in work hardening from the machining process. [241]

III.6.2 Segregation

The effects of segregation of refractory elements to the inderdendritic regions of SX and γ'-strengthened alloys is well studied. IN718 homogenizes more readily than many other nickel-based superalloys, as it is not dependent on the sluggish diffusion of Mo, W, or Rh. [244] Due to this property of IN718, homogenization treatments are typically used to eliminate (or greatly reduce) the impact of segregation on mechanical properties. As previously discussed with post-processing, the main impact of segregation is during homogenization treatments, and the possible introduction of GB liquation cracking from NbC or Laves phase formations.

III.6.3 Porosity

The influence of porosity on mechanical properties has been generally noted to negatively impact properties from a reduction in area at the failure site. [129] This can impact tensile properties and fatigue life. If pores align or are otherwise non-random, the site can become a plane of weakness. The size distribution of pores is also noted to be unimportant; only the summation of the area reduction determines the impact. For pores with sharp corners (non-spherical), these statements may no longer hold.

III.6.4 Phase Fraction & Phase Morphology

As the dominant hardening mechanism in IN718 is precipitate hardening from γ'', the first consideration for mechanical properties should be thermal history of the material and the phase fraction of γ''. HIP material tested without aging should, and does, have a lower YS/UTS than aged material, but it also has much improved elongation. The same is true for solution treated or homogenized material. Precipitate hardening increases YS and UTS, but reduces elongation.

As Laves phase is more brittle in nature than the matrix, it can act as a preferred fatigue crack initiation site. [245] Continuous GB networks of Laves can accelerate the fatigue crack propagation rate. This can reduce tensile and stress rupture properties as well. GB δ-phase can have a similarly negative impact on mechanical properties. Notch sensitivity in IN718 can be reduced through the precipitation of small amounts of GB δ-phase. [246] Nb-depleted regions are created near the GB δ-phase, which can allow stress concentration to be partly relieved by this micro-plastic-zone. The Nb-depleted region will be less hard and more ductile due to lack of Nb for forming γ''.

The presence of GB δ-phase was shown to significantly reduce stress rupture life and creep elongation to failure. [247] Samples without GB δ-phase were found to deform by grain

boundary sliding, twinning, and dislocation mechanisms. This led to ductile fracture, initiated at the incoherent interface between carbide and matrix. Samples with GB δ-phase only deform by twinning and dislocation mechanisms. The result of this difference in deformation mechanism was to promote intergranular fracture in samples with GB δ-phase. For samples with GB δ-phase, precipitate alignment in two directions showed minor improvement in creep properties over alignment in one direction. At room temperature, the presence of 0.30-1.38% by volume of δ-phase near GBs has been shown to not influence YS, UTS, or hardness. [240] A slight influence on elongation was noted. This work does not address significantly overaged IN718, with large quantities of intragranular δ-needle formation.

Hardness is an effective predictor of mechanical properties in IN718. [232] Hardness increases with γ'' particle size until peak hardness is reached, as shown in Figure 49. As previously noted, peak hardness (peak-aged) has been measured at 466HV, under-aged at 350HV, and un-aged at 275HV. [198]

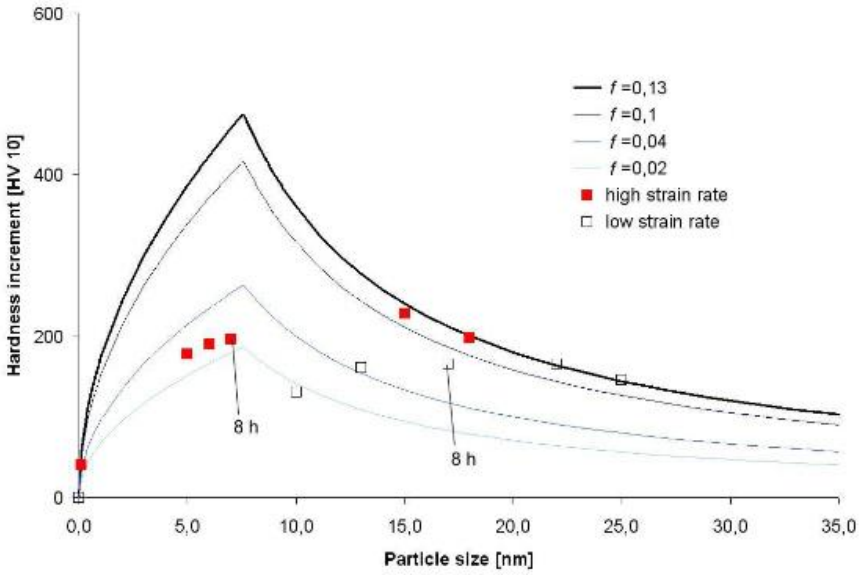

Figure 49. Relationship of hardness, γ'' size, and γ'' volume fraction. [248]

III.6.5 Tensile Properties

Tensile tests to measure yield strength (YS), ultimate tensile strength (UTS), and elongation are frequently performed and reported to compare processing techniques. Tensile data of cast and wrought IN718 is summarized in Table 11 for both room temperature (RT) and high temperature (HT). As with hardness, the tensile strength on IN718 is primarily determined by γ'' precipitation and coarsening. The initial hardening response from γ'' has been observed to result from dislocation cutting/shearing of coherent γ''. [184] Resulting stacking faults were observed on $\{110\}$ planes.

Standards set by AMS 5663 and ASTM B670-07 typically must be met or exceeded for wrought material. While as-cast material has been reported to fall short of YS and UTS requirements, HIP treatment can improve properties significantly (but not to the standards of wrought material). HIP is known to improve mechanical properties from the closure of pores, which can occur frequently during solidification in castings. Reported values for wrought material have been shown to meet and exceed AMS/ASTM standards for both RT and HT testing. HT testing is important, as the typical operating temperature range for IN718 goes up to 650°C. [184] Primary Dendrite Arm Spacing (PDAS) and Secondary Dendrite Arm Spacing (SDAS) can be related to tensile properties (see Figure 50), and PDAS and SDAS can be related to each other. The relationship between SDAS and yield strength is not well defined though; a SDAS of ~25um corresponds to a range of measured yield stress between 900-1100MPa.

Table 11. Tensile properties of cast and wrought IN718.

Material	Temperature [°C]	YS [MPa]	UTS [MPa]	Elongation [%]
As-Cast (no-post processing) [249]	RT	352-477	607-752	33.8-39.4
Wrought [232]	20	1048-1103.9	1296.3-1296.9	17-18
Wrought [232]	649	882.6-916.3	1051.9-1055.6	19.8-20.8
Wrought, AMS 5663 Minimum	RT	1034	1276	12
Wrought, AMS 5663 Minimum	649	862	1000	12
ASTM B670-07 Plate, Sheet, Strip [176]	RT	1034	1241	10-12
Conventional Cast+HIP [250]	RT	831-891	970-1017	16.3-16.7
Microcast-X [250]	RT	942	1146	15.1

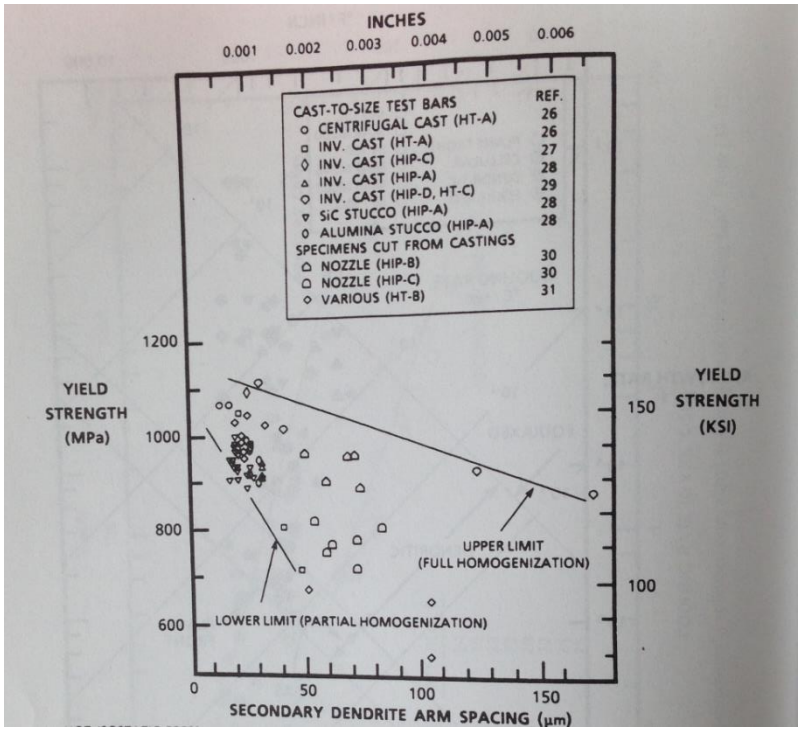

Figure 50. Relationship of SDAS to Yield Strength in IN718. [251]

III.6.6 Fatigue, Creep, & Other Tests

While tensile tests are a useful check on the condition of a material, IN718 is more typically subjected to high temperatures and loads below the UTS or YS of the material. For this reasons, fatigue and creep tests are both important to understanding the true performance of the material. For instance, the common modes of failure in gas turbine blades are LCF, HCF, and creep rupture. [252] Creep strength, LCF, and fracture toughness are important to rotors for steam power plants. [253] Fatigue tests measure the ability of the material to hold up under cyclic loading, whereas creep tests measure the ability of a material to hold up under a static load (that is less than the YS of the material). [254] Low cycle fatigue (LCF) is done to characterize fatigue life in a region where plastic deformation does occur (above YS, below UTS). The relevant quantity to measure is strain. High cycle fatigue (HCF) is done to characterize the fatigue life below YS, and the relevant quantity is stress. Creep tests and stress rupture tests both use constant loading below the YS, but stress rupture tests use higher stress and run until failure. To study the resistance of a material to the propagation of a nucleated crack, the fatigue crack growth rate (FCGR) is measured. These various tests may be run with either notched or smooth surfaces, where the notched surface tests the impact of pre-existing material defects on the mechanical property of interest.

Stress rupture data for HT is compiled in Table 12. Non-rupture creep data has been observed as well; the time to 0.2% elongation with applied stress of 250MPa and temperature of 705°C can vary from 40-161 hours. [255] Data for smooth HCF and LCF is combined in an S-N plot in Figure 51. Based on this data, the fatigue performance of forged material significantly exceeds that of cast (even with appropriate HIP and heat treatment). For all high cycle fatigue tests (RT & HT, smooth & notch), smaller grain size increases fatigue life, and the amount of GB δ-phase has no influence. [256] Below a certain frequency, the HCF failure mode is intergranular at 650°C, which means that GB δ-phase would be important. Finer grain size decreases creep resistance (while improving fatigue

life), [255] which causes a tradeoff when optimizing grain size. The self-diffusion of Nickel has been noted to govern creep deformation, and the creep deformation mechanisms are controlled by glide and climb (in cases without dynamic precipitation). [257]

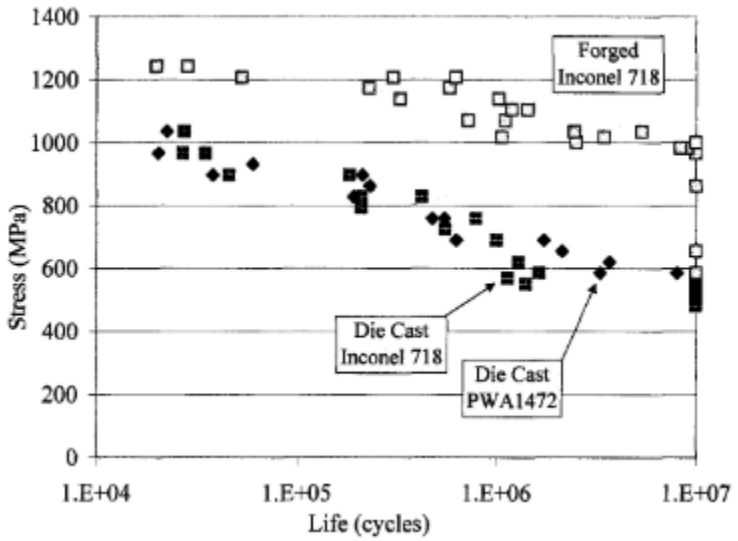

Figure 51. Smooth fatigue data for IN718 and derivative (PWA1472). [258]

Table 12. Stress rupture data for IN718.

Sample	Temperature [°C]	Stress [MPa]	Life [hr]	Elongation [%]
Wrought [232]	649	689.5	136.8-184.7	7.3-10.4
Forged [255]	650	730	50-220	NR
Round Bar [247]	650	625	159.74-331.18	1.1542-5.3565
Die Cast [258]	650	724	29.8	6.3

III.7 Welding

The study of the welding literature on IN718 is important to understand the behavior of melt pool solidification, HAZ, and cracking. As PBF and DED processes are essentially millimeter-scale welding, welding literature is particularly relevant to AM processes. When

a weld is made, there is a melt zone and a region that is not melted but with microstructural changes due to the applied heat. The region that is not melted is known as the Heat Affected Zone (HAZ).

Post-weld structures are commonly post-processed to change the microstructures formed during welding. [259] In direct-aged material, Laves phase resulted in a brittle material. Laves was partially dissolved during a 980°C solution treat + aging, but δ-phase formed near the remaining Laves. A 1080°C solution treat and aging dissolved all Laves, but resulted in significant grain growth due to lack of δ-phase to pin GBs. The 1080°C weld material led to a higher elongation and lower UTS/YS than the 980°C treatment. The base material had lower UTS/YS and lower elongation in the 1080°C case. In e-beam welding, beam oscillation can modify the formation of Laves and other phases. [260] Solution treatment of pre-weld material, with consideration for weldability, was studied and found that δ-phase increased weldability due to grain boundary pinning. [261] Following 960°C post-weld solution treatment, large quantities of δ-phase precipitated in the interdendritic regions of the melt zone. [262] The γ/NbC eutectic was suppressed by rapid solidification, but NbC and Laves were present in the fusion zone.

IN718 was a major advance in superalloy development, as it had good weldability due to insensitivity to strain-age cracking. [167] Strain-age cracking occurs when a γ'-strengthened alloyed is heated through the γ' aging range, causing the precipitation of γ'. [263] The precipitation of γ' cause a volume reduction related to misfit and can produce tensile stress. If high enough, this stress can causes cracks. Welds can be especially sensitive to this type of cracking due to residual stress, GB liquation, grain growth, and stress concentration. The precipitation of γ'' is more sluggish in IN718, which is responsible for the insensitivity.

Microfissures and liquation cracking are significant concerns, however. [264] During welding, constitutional liquation of NbC or Laves along GBs can lead to crack formation

upon thermal contraction stresses. [222] This intergranular hot cracking is known as liquation cracking, and the micro-cracks formed may be referred to as microfissures. This phenomenon is known to occur in the HAZ of some IN718 welding processes. [265] In recent work, microfissuring has been avoided in laser welding for the parameters studied. [266] Other work on e-beam welding has shown that the end of full penetration zones have increased solidification porosity that is associated with fatigue failure initiation sites. [267]

III.8 Conclusion

This background on IN718 is necessary to understand the metallurgy of the material as it is used in Additive Manufacturing. IN718 has enjoyed widespread use as a high-temperature alloy in gas turbines, steam turbines, heat exchangers, oil and gas applications, and many other uses. The primary hardening mechanism is precipitate strengthening due to coherency strengthening of γ'' precipitates. Minor variance in grain size is of less importance to tensile properties, though there is a tradeoff in grain size between creep and fatigue performance. Grain size can be controlled during post-processing through the use of δ-phase to pin GBs. However, the presence of δ-phase at the GBs can reduce creep performance and, in cases of significant overaging, can result in a loss of strength due to loss of γ''. Wrought is typically the highest standard for mechanical properties, with better performance than cast in most reported work. IN718 is insensitive to strain-age cracking and has good weldability, though liquation cracking in the HAZ must be avoided.

CHAPTER IV

ELECTRON BEAM MELTING BACKGROUND, EQUIPMENT, & METHODOLOGY

IV.1 EBM Hardware

In order to discuss the EBM process, it is necessary to describe the EBM hardware (Arcam is the only producer of such hardware as the holder of key patents on the technology, so discussion is limited to Arcam models). There are various hardware models (S12, A2, A2X, A2XX, Q10, Q20) and each has unique features (Table 13). An Arcam A2 is pictured and labeled in Figure 52. The build chamber is the vacuum chamber that encloses the process. Within the build chamber, powder is distributed onto the top of the build table from the powder hoppers. The rake is used to distribute the powder across the build envelope (processable part of the powder bed). The build envelope is the inner dimensions of the build tank, which holds excess powder and the processed part. A start plate (build substrate) is inserted into the powder bed on top of loose powder. The start plate gives the electron beam a target that will not move with charge (powder will move, or “smoke”, if not pre-sintered).

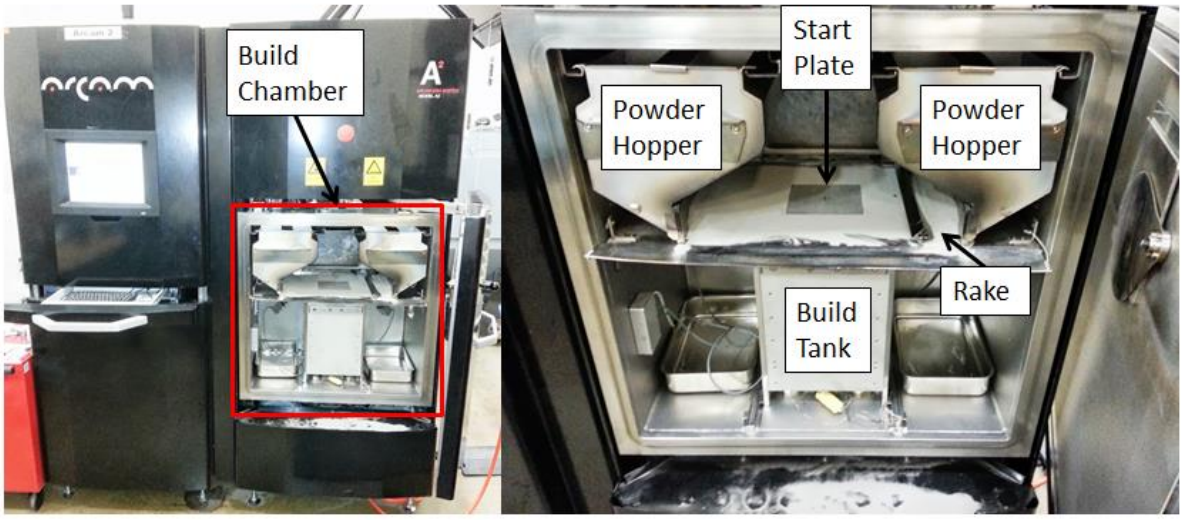

Figure 52. (Left) An Arcam A2 model showing an open build chamber and (Right) an internal view of the build chamber showing various components.

The build envelope is the processing area (powder bed) enclosed by the build tank. Most envelopes are rectangular prisms, except for cylindrical build envelopes in the A2XX and Q10 models. The beam size is measured at full-width half-max (FWHM) and is a measurement of the Gaussian width of the applied energy in the beam. The beam can be focused or defocused to manipulate the size (focus offset is used to adjust the plane of the focal point). The maximum beam speed is the hardware limitation for how fast the beam can be moved between two points. The limitation comes from inertia in the magnetic deflection coils (though EBM tends to have the least inertia to beam movement of any AM system). The deposition rate is a measure of how fast the machine can process material. This value is typically hardware and material specific (so it is given for Ti-6Al-4V, the most common EBM material). The max beam power is the maximum or range of beam power possible. All Arcam models apply a constant voltage (typically 60kV) with variable current. Both A2 and S12 models were used in the present study to produce samples.

Table 13. Hardware specifications for various Arcam models.

Feature	S12	A2	A2X	A2XX	Q10	Q20
Build Envelope (x-y-z) [mm]	200x200 x180	200x200 x350	200x200 x380	350Dx380	200x200 x180	350Dx380
Beam Size (FWHM) [mm]	NR	0.2-1.0	0.2-1.0	0.2-1.0	0.1	0.18
Max Beam Speed [mm/s]	>1000	8000	8000	8000	8000	NR
Deposition Rate (Ti-6Al-4V) [cc/hr]	60	55-80	55-80	55-80	NR	NR
Max Beam Power [W]	3500	50-3500	50-3000	50-3000	3000	3000

The A2 uses a tungsten filament (F125) to produce electrons in the beam column. The lifetime of an F125 filament is nominally 100 hours. When a filament fails or is too close to its lifetime limit, it must be replaced. This maintenance requires the vacuum to be broken, which interrupts processing; replacing a filament is not something that can be done during operation. Build time is therefore limited by filament lifetime. A failed F125 filament is shown using SEM in Figure 53. The failure surface shows material degradation at the tip. This is not present on filaments prior to use. The Q10 and Q20 units use an alternate filament with a longer lifetime.

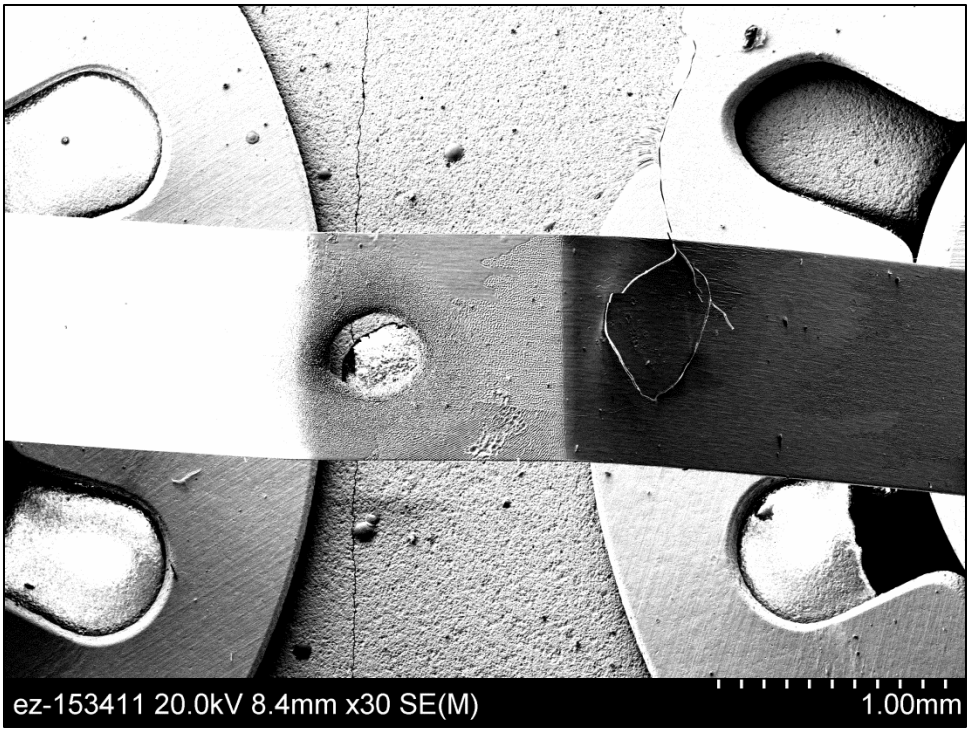

Figure 53. Failed F125 tungsten filament, used in an Arcam S12, showing a spot of material degradation on the filament tip.

IV.2 EBM Patents

It is useful to consider patents application on the EBM technology as part of a thorough technology review.[1] EBM is a form of additive manufacturing that uses an electron beam as a heat source to produce three-dimensional objects out of metal powder in a layer-wise process. The first iteration of this process was originally patented by Ralf Larsson and assigned to "Arcam Ltd" under US 5786562 A with a priority date of 1993. Though this patent expired in 2013, it covered an arc-based AM process that is significantly different

[1] This analysis is not intended as legal advice. For research purposes only.

from EBM. The first patent on the EBM process was published by Lars-Erik Andersson and Morgan Larsson with a priority date of April 2000. This patent, and other key patents, cover many of the current features used by Arcam: electron beam heat source, powder bed preheating, use of an energy balance, the use of multiple fusion zones, powder distribution, and system thermal feedback control.

IV.2.1 Expired Patents

The expired US 5786562 A patent covered a much different configuration than the any of the commercialized EBM machines. The expired process utilized a gantry to move the electrode, which is kept within a certain working distance of the powder bed. This version of the process should be thought of as the use of arc welding for powder bed fusion (PBF). In fact, the heat source is referred to as having "at least one electrode" where the electrode is used to construct an "electric arc or heat" to be used for selective melting. The use of an electrode to generate electrons, controlled by electromagnetic coils, is not addressed in this expired patent, which was addressed later in the next iteration of process patents.

IV.2.2 Current Patents

In addition to the expired patent (US 5786562 A), Arcam AB holds ten other patents related to EBM technology. Of the ten current patents, two are not currently implemented and an additional one is in the research stage. That leaves seven patents covering the critical parts of the currently implemented EBM process. An additional four patent applications on related technology exist. The patents are enumerated in Table 14. Patents appended with an "A" are patents granted prior to 2001, an "A1" denotes a post-2001 provisional patent, a "B1" is a post-2001 grant that is not associated with a previously published patent application, and a "B2" is a post-2001 grant that is associated with a previously published patent application. [268] The patent class most commonly used is Class 219 for "Electric Heating". Class 264 for "Plastic and Nonmetal Article Shaping or Treating: Processes" has

also been used. Important subclasses are 219/137R which includes processes for arc welding of metal, 219/76.12 which includes deposition welding “of multiple distinct layers”, and 264/497 which includes “using laser sintering of particulate material to build three-dimensional product”. [268] Claims on the number of patents on the technology may be higher than the 11 US patents, as each patent is typically filed in separate countries to include the United States (US), Canada (CA), China (CN), Europe (EP), WIPO (WO), and others.

Patents effectively cover these areas of the current EBM technology implemented by Arcam AB:

- Preheating
- Multispot
- Energy balance for maintaining powder bed temperature
- Powder distribution system
- System control based on temperature feedback from a camera
- General system and process (see discussion)

Table 14. Patents held on Electron Beam Melting (EBM) by Arcam AB.

Patent # [Reference #]	Covers	Currently Implemented?	Publication Date	Priority Date	Patent Expires
US 5786562 A [269]	Arc-based powder bed system	No, system improved	July 28, 1998	May 12, 1993	Expired
US 7537722 B2 [12]	Original EBM System Configuration and Process; Sensing of surface temperature and process feedback control	Yes, and Monitoring and Feedback Research at UTEP, ORNL	May 26, 2009	Apr 27, 2000	Apr 27, 2020
US 7540738 B2 [270]	Alternative method for powder distribution	No	Jun 2, 2009	Dec 13, 2002	Dec 13, 2022
US 7454262 B2 [271]	General process patent	Yes	Nov 18, 2008	Dec 19, 2002	Dec 19, 2022
US 7635825 B2 [272]	Scan strategy; island melting, spot melting, linear melting, and order optimization	Research at ORNL	Dec 22, 2009	Dec 19, 2002	Dec 19, 2022
US 7833465 B2 [272]	"Multispot" technology used to keep alive more than one fusion zone	Yes	Nov 16, 2010	Dec 19, 2002	Dec 19, 2022
US 7713454 B2 [272]	Improvements to energy balance calculation	Yes	May 11, 2010	Dec 19, 2002	Dec 19, 2022
US 7871551 B2 [273]	Current powder distribution system	Yes	Jan 18, 2011	May 11, 2005	May 11, 2025
US 8187521 B2 [274]	Layer Preheating	Yes	May 29, 2012	Jul 27, 2006	Jul 27, 2026
US 8308466 B2 [275]	Current Powder distribution system	Yes	Nov. 13, 2012	Feb 18, 2009	Feb 18, 2029
US 8570534 B1 [276]	Implementation of suction device for removing "foreign matter" during the build process	No	Oct 29, 2013	Apr 24, 2012	Apr 24, 2032

(Table 14 Continued)

Patent # [Reference #]	Covers	Currently Implemented?	Publication Date	Priority Date	Patent Expires
US 20130300286 A1 [277]	Plasma Confinement Device for Electron Generation	Unknown	Nov 14, 2013	May 9, 2012	Not Yet Granted
US 20120100031 A1 [278]	Temperature Measurement Using IR Camera	Research at UTEP, ORNL	April 26, 2012	July 15, 2009	Not Yet Granted
WO 2014090510 A1 [279]	Vacuum chamber for physical vapor deposition	Unknown	June 19, 2014	Dec 10, 2012	Not Yet Granted
US 20100310404 A1, US 20120223059 A1 [280]	Reactive gas insertion during AM	Unknown	Dec. 9, 2010 Sept. 6, 2012	Dec. 6, 2007	Not Yet Granted

The first patent on the EBM process (US 7537722 B2) as is currently implemented, with an electron beam, was awarded with a priority date of April 27, 2000. This patent covers the use of an electron beam as a heat source to produce 3D parts in a powder bed fusion process. While the system configuration was not identically implemented (the powder distribution system was not used), the system is essentially the same system currently implemented. An important concept presented in this work is the use of "interference" to make the resulting temperature of the powder bed more diffuse. What is actually being done is that the *path* of the beam is being "interfered" with; a slight oscillation is introduced to the beam motion in both the x-direction and y-direction. The position of the focal point of the beam can be described by:

$$\bar{r}(t) = (V_x t + A_x \cos(\omega t))\tilde{x} + A_y \cos(\omega t)\,\bar{y} \qquad \textbf{(Eq. 2)}$$

where V_x is the speed of the beam in the x-direction, or direction of travel. A_x and A_y are the amplitudes of the oscillation in the x and y directions, respectively. ω is the oscillation frequency, and is referenced as being defined by:

$$\boldsymbol{\omega = \frac{2\pi V_x}{A_x}} \qquad \textbf{(Eq. 3)}$$

This use of oscillations results in a "helix-like movement pattern" (Figure 54). This use of oscillatory motion is one way to make the resulting temperature distribution more diffuse (Figure 55). Another way is to adjust the focal point of the beam. The "Focus Offset", a process parameter given in units of [mA], is not addressed in the Arcam patents, but has been noted to be significantly important when determining the diameter of the beam. [79] The Focus Offset of the beam can be adjusted so that the focal point is coincident with, above, or below the build surface. While the actual implementation of the interference motion is not known, the use of focus offset to make the beam more diffuse during preheat and post-heat steps is well documented.

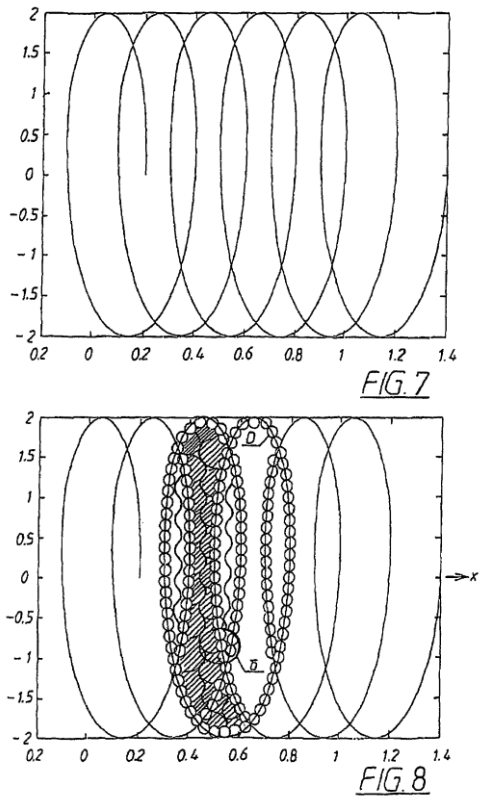

Figure 54. (Top) Movement of focal point of e-beam using oscillatory motion, and (Bottom) the larger area over which fusion takes place within beam interaction area. (US 7454262 B2) [271]

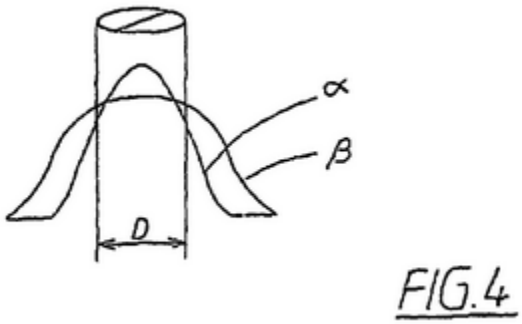

Figure 55. The resulting heat profile from the use of oscillatory motion or "interference", where α is without interference and β is with interference. D is the diameter of the focal point. (US 7454262 B2) [271]

The concept of an energy balance for a given layer is also introduced for the first time. The general concept can be summarized by the equation:

$$\boldsymbol{E_{in}(i) = E_{out}(i) + E_{heat}(i)} \quad \textbf{(Eq. 4)}$$

where E_{in} is the energy applied by the heat source, E_{out} is the energy lost due to heat transfer, and E_{heat} is the energy within the i-th layer. This concept of balancing the energy for a given layer is returned to in many of the later patents on EBM. The use of a build table, computer controller, controlled environment, viewing window, and external camera for process monitoring are also covered in US 7537722 B2. Process improvements to the calculation of the energy balance are covered in US 7713454 B2. The energy balance calculation was improved to include thermal conductivity calculations and the use of energy balances over separate areas of the powder bed.

The powder distribution system (PDS) is used to distribute a uniform layer of powder, which is an essential design feature that solves a difficult task. The original PDS as shown in Figure 56 shows a free-moving powder dispenser (label 28), which transports powder supplied from powder hoppers (label 4). Specific claims on this PDS are made in US 7540738 B2. The current raking system is claimed in US 7871551 B2 and shown in Figure 57, which is used in the commercial systems actually deployed. A powder rake (label 6) was implemented to fetch powder from powder piles (label 2b) near openings in the powder hoppers.

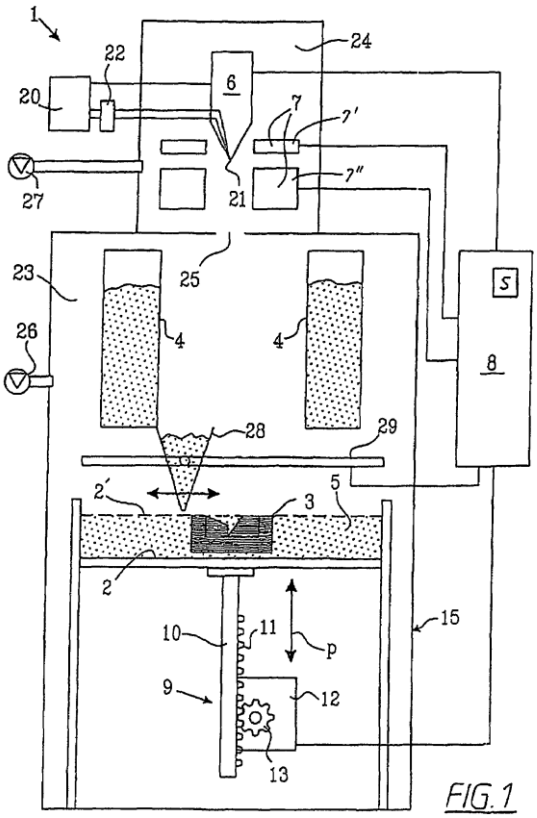

Figure 56. Originally patented configuration (US 7537722 B2). The PDS as described was never implemented on a commercial system. [12]

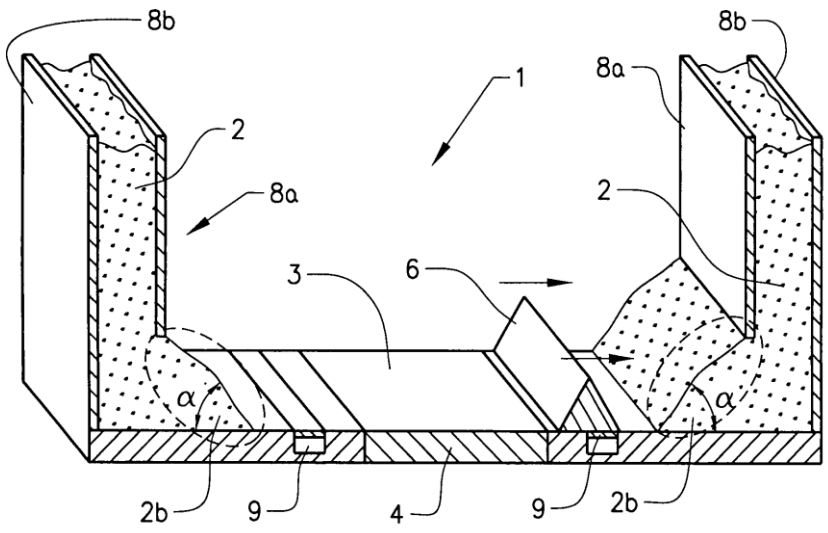

Figure 57. Currently implemented powder distribution system (PDS) in Arcam EBM systems. (US 7871551 B2) [273]

The scan strategy, or the path the beam takes to selectively melt a given layer, is a defining detail of most AM processes. Scan strategy for EBM is covered under US 7635825 B2. This patent discusses the subdivision of a melt area into subunits (standard EBM process uses one subunit), which can be melted in a random or optimized order. Rectilinear infill or spot infill can be used. The "island melting" common in laser melting processes is also defined by the described process, though island melting is not used in EBM. Scan strategies descriptions are shown in Figure 58.

The "multi-spot" technology is critical to the method for making contours, speeding up the melt process, and implementing unique scan strategies. This process is patented under US 7833465 B2. In its simplest form, multi-spot is the use of the beam to keep multiple fusion zones active at the same time. This is possible in EBM, as the electromagnetic field

controlling the beam position has less inertia to movement than does the galvanometers used in laser processes; very quick movement of the e-beam can effectively melt multiple areas at the same time. This is an important innovation, as the EBM process is essentially getting the benefit of multiple heat sources. Depending on the application of the technology, the process can be operated in unique ways.

Layer preheating is critical to the successful implementation of the EBM process. Preheating has been patented for achieving a desired energy balance, though the details of the use of preheating for sintering (the really important reason for preheating and achieving a desired temperature) are not given (US 8187521 B2).

Arcam holds a patent on a suction device (US 8570534 B1) for use in removing foreign bodies from the processing layer. While the EBM process commonly employs vacuums for removal and recovery of excess powder, this patent focuses on an entirely different use. This technology is not currently being used and no research reports exist on it.

Research is, or has been conducted, on patents or parts of patents. Specifically, *in situ* monitoring using cameras (US 7537722 B2) to collect processing data has been demonstrated at UTEP [121, 281, 282] and ORNL. [283] The UTEP work has even gone so far as to demonstrate feedback control by manipulated process parameters based on IR measurements. Additionally, work on spot melting (US 7635825 B2) has been demonstrated as an effective method for varying crystallographic orientation in EBM IN718. [123, 126]

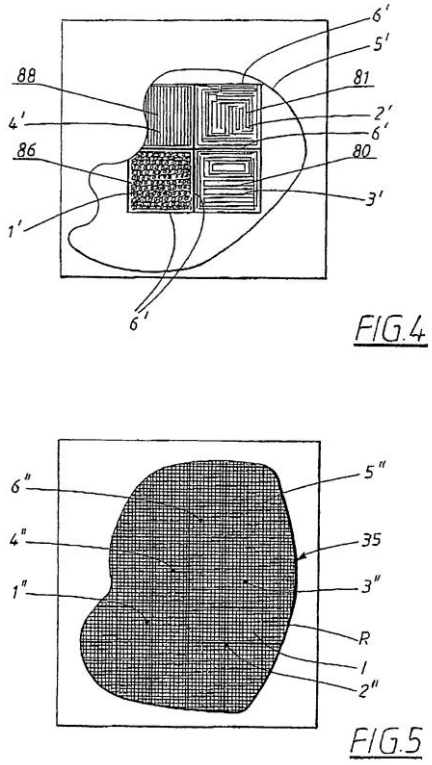

Figure 58. (Top) Description of various scan strategies and (Bottom) description of melt area sub-division into small units. [272]

In addition to the granted patents, Arcam also has published patent applications for technologies that have yet to be awarded in the United States. For temperature measurements, US 20120100031 A1 further details the use of an IR camera for measuring surface temperature and the mathematical calculation of the temperature from such data (Figure 59). The insertion of reactive gas into the EBM build chamber has also been patented (US 20120223059 A1). The insertion of reactive gases only covers chemical or physical reactions with a certain number of gases. Helium and its use for an electrical recombination effect used for charge dissipation at the build surface are not covered. Another patent focuses on the use of a plasma source for production of electrons (US 20130300286 A1), though it is not clear if this source is intended for use in EBM. The most recent, and perhaps most interesting, patent is on the physical vapor deposition (PVD), or

precipitation of metal vapors, to build up material (WO 2014090510 A1). This patent could be the first Arcam patent on new technology intended for PVD AM.

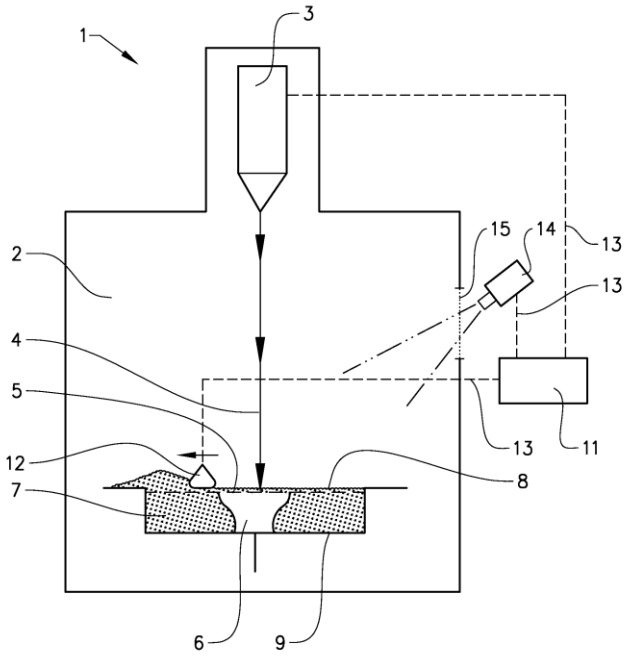

Figure 59. IR camera setup for temperature monitoring. (US 20120100031 A1) [278]

IV.2.3 Summary of Patents

Though the original patent by Arcam has expired, it only addressed arc-based AM. The critical patent on EBM technology does not expire until April 2020, and a significant cluster of other key patents will not expire until December 2022. The majority of the Arcam patents are protecting current process implementations or ongoing machine research efforts. Though these patents cover many key features, there are notable omissions from the Arcam patent portfolio (which are now prior-art due to machine documentation and implementation):

- Design patents on non-functional parts of machine
- Software patents (some of the touch screen interface may be covered by patents from other companies that supply technology)
- Outgassing
- Helium insertion and charge recombination
- Start plate sintering; the use of a free body substrate that is stabilized through sintering
- Powder Recovery System; vacuuming, sieving, removal of sintered powder through like-powder grit-blasting
- Electron gun
- Method of adjustment of focal length to supply more or less diffuse beam (details of "interference" are given with respect to this, but it is not clear how diffuse patterns are implemented in the machine)
- Method for generating and interpreting machine code
- Method for removal from start plate; pieces break off due to brittle phases, phase transformation, and/or stress relaxation

IV.3 EBM Processing

The information in the Arcam patents points to the key importance of the energy balance to achieve a desired powder bed temperature. The process currently operates with these key features decoupled; there is no feedback from the actual powder bed temperature into the melting process or energy balance. The energy balance is controlled by a complex set of process parameters that allow the operator to control the behavior of the beam. The details of this behavior are important, as they directly influence the resulting temperature (both locally within a melt pool and across the powder bed). Though the process is defined by temperature, boundary conditions and the thermal profile of a part as it is built have not been well measured (due to the difficult nature of instrumentation within the process).

The EBM processes has the following strengths when compared to other AM processes: comparatively fast build time, ability to melt overhangs (a strength of all PBF methods), and low amounts of residual stress. Of these strengths, the "fast" build time can be quantified and optimized. The process parameters that impact build time will be reviewed and a set of builds are analyzed to improve process time.

The overall EBM process proceeds through the following stages (summarized graphically with corresponding temperature data in Figure 60):

1. Start plate heating and outgassing
2. Sintering of powder under start plate
3. Layer melting
4. Cool down

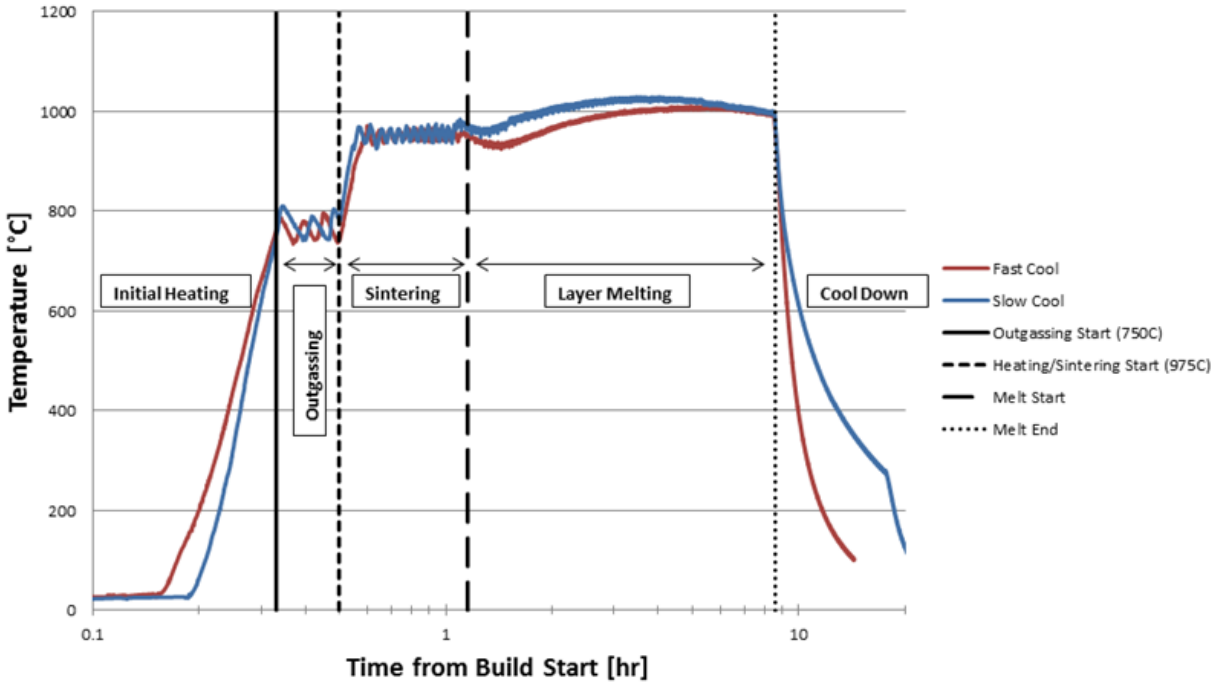

Figure 60. The change in temperature during the stages of the EBM process. [86]

The layer melting process iterates for each layer of the build through these steps:

1. Powder Raking
2. Preheat I
3. Preheat II
4. Contours
5. Post-heat (optional)
6. Bulk melting / melt hatch
7. Support melting (optional)
8. Post-heat

First, powder is distributed over the build surface by the rake. Next the e-beam is used as a diffuse planar heat source to preheat the powder to the desired sintering temperature. Preheat I is the first preheat step, which is typically performed over the entire area of the start plate (most of the powder bed). A second preheat, Preheat II, then selectively heats an area that more closely corresponds to the geometry of the slice to be melted. Preheat II typically achieves more sintering of the powder bed. After a set number of preheat passes are run, the contours are melted (this is the typical operation, contours may be melted in any order). The multi-spot technology is utilized to spot melt the edges of the desired part. These spot melts are distinctly different from the standard in-fill technique. Various parameters may be adjusted for the contours, including current, spot melt order, overlap, and number of contours. Two contours are typically run to border the bulk melt. Therefore, there is an overlap between the inner-contour and outer-contour, as well as between the inner-contour and the bulk melt. The optimization of the contour parameters is important for determining the surface finish of the as-fabricated parts.

IV.3.1 Bulk Melting Overview

Next, the bulk melt (referred to in system documentation as "Melt Hatch") is performed. The electron beam is typically moved in a rectilinear fashion, in either snaking bi-directional motion or unidirectional motion. This is similar to the scan strategy used in laser melting processes. [127] The speed of the beam is so fast that the heat source may be considered as a linear heat source. [88] Alternatively, recent work has shown that spot melting can be used to obtain differences in crystallographic orientation. [123, 126] Line melting may be controlled with a developed list of Arcam process parameters: current, speed, speed function, turning point function, thickness function, current compensation, and others. Current and speed are the most important parameters for the EBM process, as they determine the applied energy according to:

$$\boldsymbol{E_{app} = P_{app} * t = i * \forall * t} \quad \textbf{(Eq. 5)}$$

The applied current (i) and time (t) are functions of geometry, while voltage (∀) is considered constant at 60kV (the actual voltage may be slightly different). The set value for current is not the final values used by the machine; the current is modified based on the length of the line being melted (line scan length) for line melts. The applied energy can be considered over a single line scan length (ℓ):

$$\boldsymbol{E_{app}(\ell) = i(\ell) * \forall * t(\ell) = i(\ell) * \forall * \frac{\ell}{v}} \quad \textbf{(Eq. 6)}$$

The scanning speed of the beam (v) has been accounted for, but the calculation of $i(\ell)$ and v must be detailed. This calculation is complex and is addressed in more detail later along with process parameters (§V.1.3). The applied energy for a spot melt is simply based on pulse duration (t_{spot}), constant current, and constant voltage:

$$\boldsymbol{E_{spot} = i * \forall * t_{spot}} \quad \textbf{(Eq. 7)}$$

The speed is set as a function of current by the “speed function”. The “thickness function” modifies the speed based on the depth of powder or melted material beneath the current layer. The “turning point function” modifies the speed of the beam near edges, as the snaking path can result in local overheating due to continuous speeds; the edge material does not have enough time to reach the bulk temperature before the return pass. Similarly, “current compensation” accounts for length of the line being melted (line scan length).

So, the speed is based on the current, which is based on part geometry. This makes scientific testing of EBM process parameters difficult, as the current and speed both vary throughout a part. The ultimate goal of the EBM process has been to achieve geometrically accurate, fully dense parts. The effect on microstructure has been mostly treated as secondary, until recently. [123, 126] This recent work has demonstrated the ability to control the grain structure and texture of EBM parts in IN718 by manipulating microstructure to read D-O-E (as in Department of Energy). [126] Manipulation of microstructure and achieving fully dense parts both require the same EBM process knowledge covered in this chapter. Both line and spot melting will continue to be addressed for this reason.

IV.3.2 Support Structure

The optional support melting step (known as “wafer support” in the software), can be performed in any order between Preheat II and Post-heat. The support melting step is done to melt additional material for thermal and mechanical support for overhangs; the thickness function does not perfectly correct for overhangs, as melting a solid layer on top of previously sintered layers can still result in localized defects (i.e. swelling or porosity) or geometrical distortions. By building in support material, or material designed for removal during post-processing, the success rate for building overhangs can be increased.

IV.3.3 Postheating

The last step in a given iteration of layer melting is Post-heating. This step can be performed at the end of melting all parts, or after each individual part is melted (which may be done to lower the amount of temperature fluctuations). Similar to Preheat I, the area of the powder bed (a little less than the start plate area) is heated with an area heat source (really a point/line source moving very fast). The post-heat current is set according to the settings under "Heating". The post-heat time is set according to the energy balance, as determined by the Arcam software. Officially, this is calculated according to an average current, but this correlation has not been able to be confirmed.

IV.3.4 Cool Down

The cool down stage can be modified, depending on desire of operator, to use a vacuum cool, helium injection cool, or controlled cool. The vacuum cool is the standard Arcam procedure for producing parts, where the build is allowed to cool (via conduction and radiation) until a minimum temperature is reached for helium injection (100-200°C). This is referred to as "slow cool". Once a build is cooled below 100°C (as measured by the start plate thermocouple), it is considered safe to open to atmosphere. Helium can also be injected upon build completion to provide the addition of convective cooling to the top surface of the part. This has the effect of speeding up the cool down process (by at least 1 hour, depending on part size), which is why the helium injection method is also referred to as "fast cool". Alternatively, the cool down process can be deliberately controlled by using the e-beam to heat a completed build. This is done by manually adjusting the current, using the "Start Plate Heating" function that is typically used for reheating a part after starting and stopping a build. The amount of heating provided by the e-beam can thus be adjusted in stages, which effectively allows for the *in situ* heat treatment (annealing, solution treatment, aging, etc.) of the material. The impact of the cool down procedure on microstructure (§VI.3.1) and mechanical properties (§VIII.4.1) is explored in a later chapters.

IV.3.5 Melt Pool Overlap

The minimum theoretical overlap to achieve fully dense material for overlapping spot melt pools must first be considered from the XY plane (lines must at least meet at edges). This can be done by calculating the intersection of circles (assuming spot melts are circular in nature), as described in Figure 61.

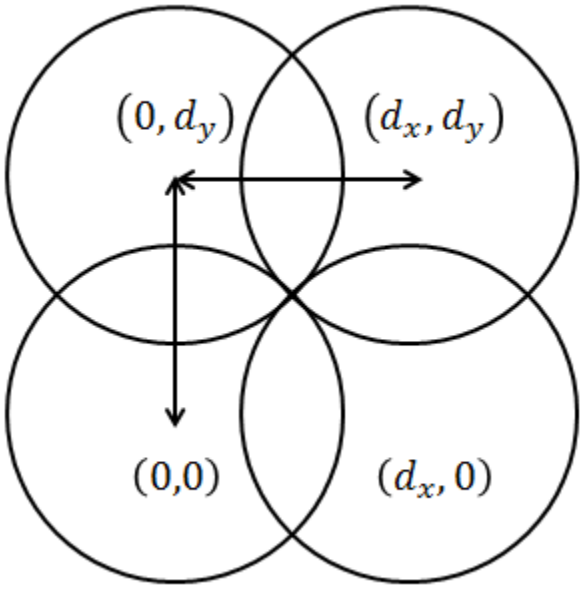

Figure 61. Four overlapping circles of radius, R, and spacing, d.

To begin, consider the areas of four overlapping circles, with the same radius, R:

$$\boldsymbol{x^2 + y^2 = R^2}$$
$$\boldsymbol{(x - d_x)^2 + y^2 = R^2}$$

$$\boldsymbol{x^2 + \left(y - d_y\right)^2 = R^2}$$

$$\boldsymbol{(x - d_x)^2 + \left(y - d_y\right)^2 = R^2} \quad \textbf{(Eq. 8)}$$

These equations can be combined to solve for position variables x and y, in terms of the spacing between circles in the x-direction (d_x) and y-direction (d_y):

$$x = \frac{d_x}{2}\ , y = \frac{d_y}{2}$$

By substituting into Equation 8, and requiring uniform overlap of $d = d_x = d_y$:

$$R^2 = \frac{d_x^2}{4} + \frac{d_y^2}{4} = \frac{d^2}{2}$$

Which yields a theoretical minimum spot melt pool overlap, based on X-Y requirements of:

$$d = \sqrt{2} * R$$

The area of the overlap can be calculated by applying the equation for the area bound by the chord of a circle:

$$\boldsymbol{A_{chord} = R^2 \cos^{-1}\left(\frac{d}{2R}\right) - \frac{1}{4} d\sqrt{(2R - d)(2R + d)}} \quad \textbf{(Eq. 9)}$$

Which for the area bound by two circles, and applying the theoretical minimum, is:

$$\boldsymbol{A_{overlap} = 2A_{chord} = \left(\frac{\pi}{2} - 1\right) R^2} \quad \textbf{(Eq. 10)}$$

And if calculated for all four overlaps is:

$$\boldsymbol{A = 4A_{overlap} = 2(\pi - 2)R^2} \quad \textbf{(Eq. 11)}$$

Which matches previous derivations. [284] This, however, does not address the fact that the limiting overlap value may be caused by the X-Z requirements. To calculate a theoretical minimum overlap for both spot and line melts in the X-Z direction, we can assume a Gaussian melt pool shape. The overlap is defined in Figure 62, where d_x is the distance between melt pool centers, "a" is the depth of the melt pool, and h is the depth as which the melt pools overlap.

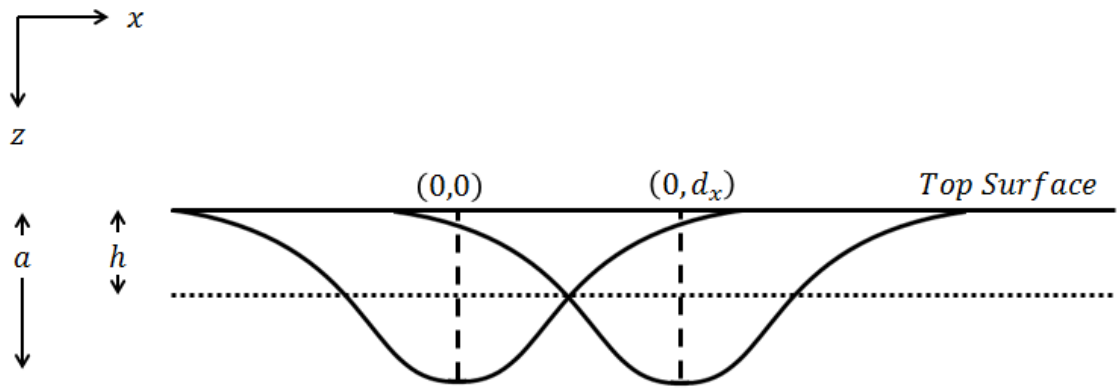

Figure 62. Two overlapping Gaussian distributions for modeling melt pool overlap in the X-Z direction.

Now the Gaussian function must be defined:

$$\boldsymbol{z = f(x) = a * \exp\left(-\frac{(x-b)^2}{2c^2}\right)} \qquad \textbf{(Eq. 12)}$$

Where "b" is the position of the center and "c" controls the width of the profile. Using this equation, profiles can be formulated for overlapping melt pools:

$$z_1(x) = a * \exp\left(-\frac{x^2}{2c^2}\right)$$
$$z_2(x) = a * \exp\left(-\frac{(x-d)^2}{2c^2}\right)$$

And the constraint for overlap may be applied as $z_1\left(\frac{d}{2}\right) = z_2\left(\frac{d}{2}\right) = h$:

$$\boldsymbol{h = a * \exp\left(-\frac{\frac{d^2}{4}}{2c^2}\right)}$$

$$\boldsymbol{d = \sqrt{8c^2 \ln\left(\frac{a}{h}\right)} = 2c\sqrt{2\ln\left(\frac{a}{h}\right)}} \qquad \textbf{(Eq. 13)}$$

So, the minimum theoretical overlap of two adjacent line or spots must meet this value of spacing, d. Depending on processing conditions, the melt pool size and shape will change. The minimum overlap to avoid porosity will then be limited by the smaller of either the X-Y limit or the X-Z limit. It is worth clarifying that as the value of d increases, overlap decreases. So, decreasing d will increase overlap until the paths are coincident. While overlap should meet the minimum value to avoid porosity, it should also be minimized to avoid unnecessary remelting. It is also important to note that theoretical overlap requirements do not account for a number of complicating factors, especially local process variability. Small fluctuations in a real system would likely lead to localized porosity formation, if minimum parameters were used. Still, the minimum theoretical overlap may be used as a check on processing conditions and processing windows.

The process steps for melting metal are designated by the terms “contours” and “bulk” (or “hatch”) melting. Contours are spot melts that melt the edge of the of a part layer (Figure 63a). The order of the spots is determined by an EBM control algorithm. After contours are made, the bulk of the part must be melted. This can be done by either rectilinear line melting (Figure 63b) or using spot melts (Figure 63c). The end result is full melting of the enclosed part slice (Figure 63d). If the speed of the beam is known (details on calculating speed are addressed in §V.1.3), the time for the bulk melt can be estimated for rectilinear infill. The number of spots and spot pulse time must be known to calculate the bulk melt time for spot melting.

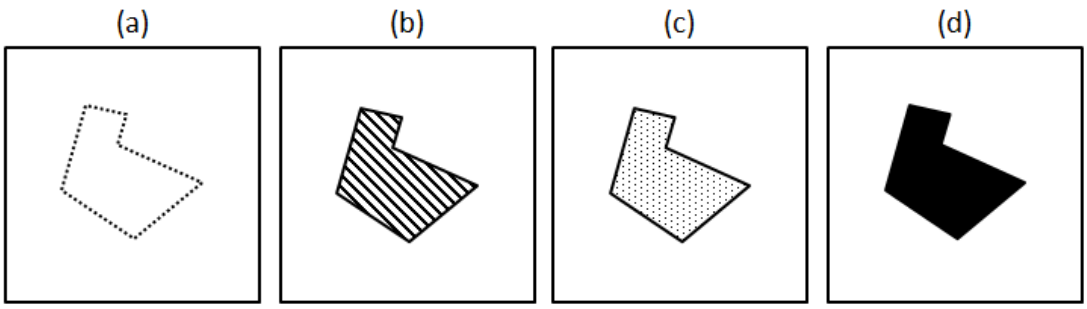

Figure 63. The steps of melting; (a) contour melting using spot melts, (b) standard linear bulk melting, (c) alternative spot bulk melting, and (d) completed melt of a part slice for example geometry.

The amount of time required to melt example geometries is shown in Figure 64 for both spot and line melting. The line melting time is dependent on the angle of melting relative to the part because of the dependence of speed on line scan length; the number and length of lines changes for various rotations. Squares and triangles show a periodic structure, whereas a more complex geometry has an optimal angle to minimize melt time. Spot melting time does not vary with angle and is constant. The equivalent time for bulk spot melting (if the layer is melted using only spot pulses) of each geometry is shown as a constant value in each graph for a point offset of 0.5mm and a pulse time of 0.5ms. While the spot time appears to always be fastest, the spot melt parameters used may have to be adjusted such that an increase in melt time is incurred; the constant value may be vertically translated, depending on parameter optimization, and may not always be fastest. Note that each pattern repeats certain symmetry; the rotation from 0-180 degrees is effectively the same as the rotation from 180-360 degrees. Melt time for line melts were calculated from average line speed for each rotation.

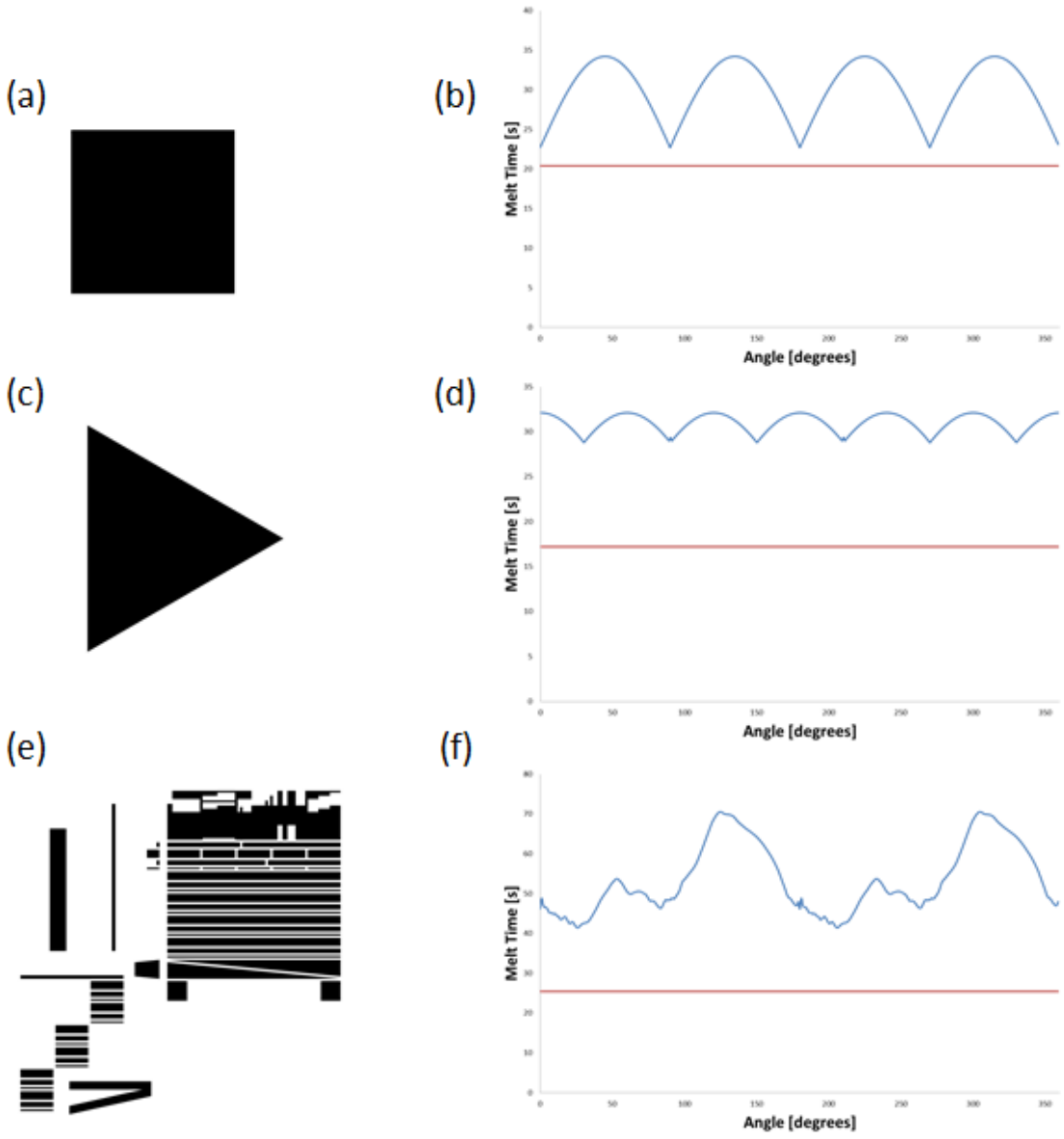

Figure 64. Melt time optimization for slices of a (a) square, (c) triangle, and (e) complex build. The standard linear melt is rotated through angles of 360 degrees to show variation for the (b) square, (d) triangle, and (f) complex build.

CHAPTER V

IMPACT OF PROCESS PARAMETERS ON DEFECTS, PROCESS TIME, & THERMAL HISTORY

V.1 EBM Software

Though temperature is a defining quantity for the EBM process, little measurement is done in the standard operating procedure. Temperatures are measured in the beam column (only used as a machine safety criterion) and from a thermocouple positioned on the underside of the center of the start plate in the powder bed. The start plate thermocouple is used for feedback during start plate heating, outgassing, and sintering. After start plate sintering (sintering of the powder surrounding the start plate) is completed, temperature feedback is no longer utilized for control for the remainder of the process. However, it is useful to monitor this temperature, as is demonstrated herein. An energy balance and various empirical process parameters are used to control melting.

V.1.1 Part Creation & Machine Code Generation

The first step in creating a part is creating the digital geometry. This is done using CAD software like *SolidWorks*, *Inventor*, *SketchUp*, or many others. The part geometry is typically exported as a .STL file, which had its origins in stereolithography. A .STL file is a representation of a geometry in the form of triangles. The next step is to prepare and fix the .STL file. This step is typically done with *Magics* (for EBM), although other hardware specific programs may be used. *Magics* can fix errors in the .STL file (intersecting triangles, overlapping triangles, etc.) that might otherwise cause errors during machine code generation. Supports (both thermal and mechanical) are also added during this step to improve the quality of the final part. After the .STL is fixed and supports are added, the .STL

is exported again. The fixed .STL file is now imported into *Arcam Build Assembler* (example shown in Figure 65) to generate the machine code that is read by the EBM Control software that runs the Arcam hardware. This machine code is an Arcam Build File (.ABF). The .ABF file contains the geometry as a set of points, sliced by each layer. The layer thickness is set during generation of the .ABF file. The .ABF is then loaded into EBM Control, process parameters are loaded, and the build process is started.

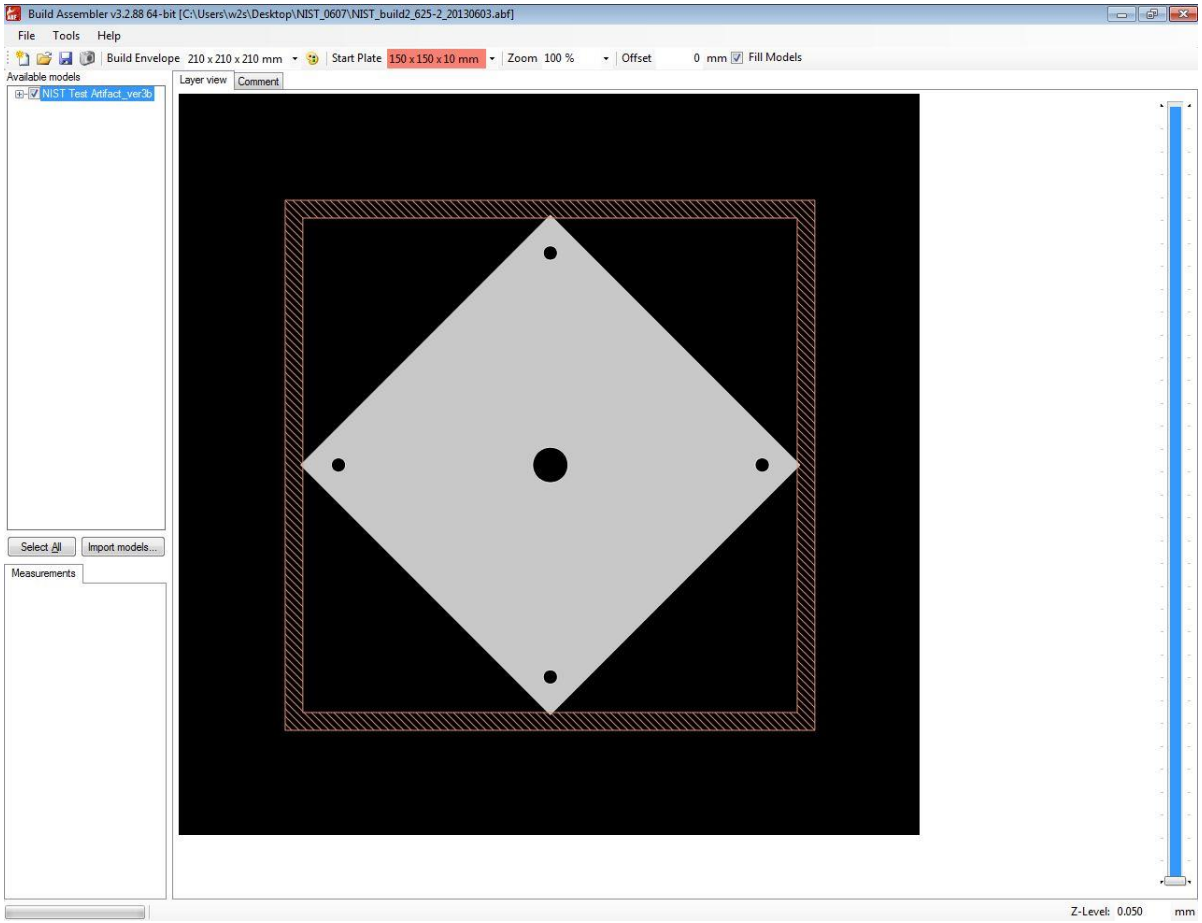

Figure 65. Build Assembler software is used to create .ABF machine code to run the Arcam systems. The bottom slice of the NIST Test Artifact is shown.

V.1.2 EBM Control Software

The Arcam process is operated using proprietary software called EBM Control. In this dissertation, versions 3.2 and 4.1 were both used to produce samples. Screen captures from EBM Control 3.2 will be used to describe the Arcam process parameters used. The EBM Control software is divided into five primary tabs: *Build*, *Process*, *Hardware*, *Center Beam*, and *Align Beam*. Once the steps in each tab have been completed (green circles in the upper right of each tab show completed steps), the build process can be started.

The *Build* tab (Figure 66) is used to load the .ABF build file to input part geometry. The start plate theme and size can be selected, powder and machine information can be logged, and all of the process parameters can be saved together with the geometry as a "Project" file. The start plate theme includes the beam parameters that are used for "Start Plate Heating" to heat the start plate for outgassing and sintering. The outgassing time, temperature, and timeout can be found in the *Start Plate theme*. The *Process* tab (Figure 67) allows the use to select a material theme. The material theme includes a lot of values (density, thermal conductivity, etc.) that are not used by the process. The important sintering quantities are the sintering temperature and sintering time that are set to determine the time and temperature at which the start plate sintering step is carried out. The *Hardware* tab (not shown) is used to control the "Powder Dispatcher" which includes both the build table and the rake. It also controls the vacuum, controls the power supply, and confirms the filament burn time (reset for replaced filaments). The *Center Beam* tab (not shown) is used to maneuver the e-beam to the center of the start plate (pre-marked with a Sharpie). The *Align Beam* tab (not shown) is used to adjust the alignment of the beam over a 3x3 grid on the start plate.

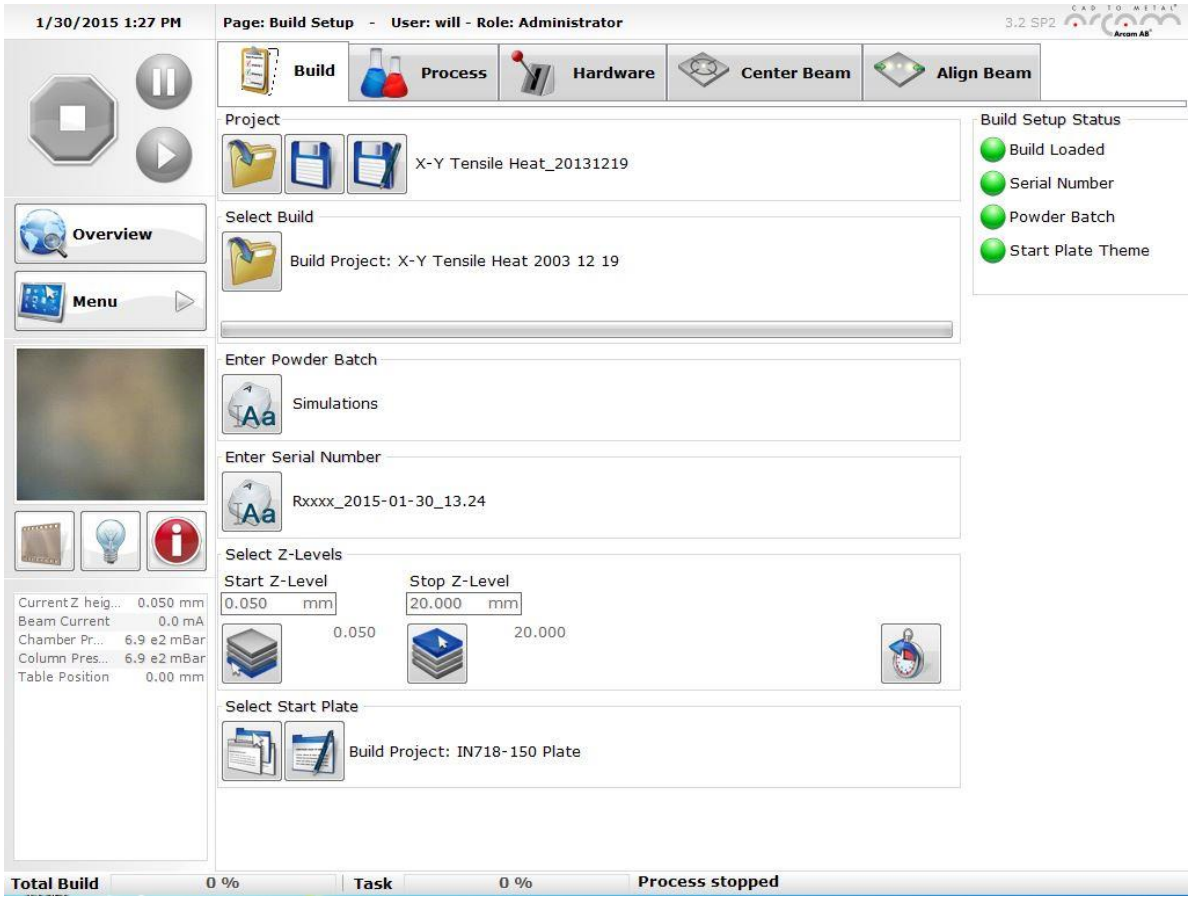

Figure 66. The "Build" tab in EBM Control is used to load geometry, select start plate parameters, and save parameter inputs as a Project.

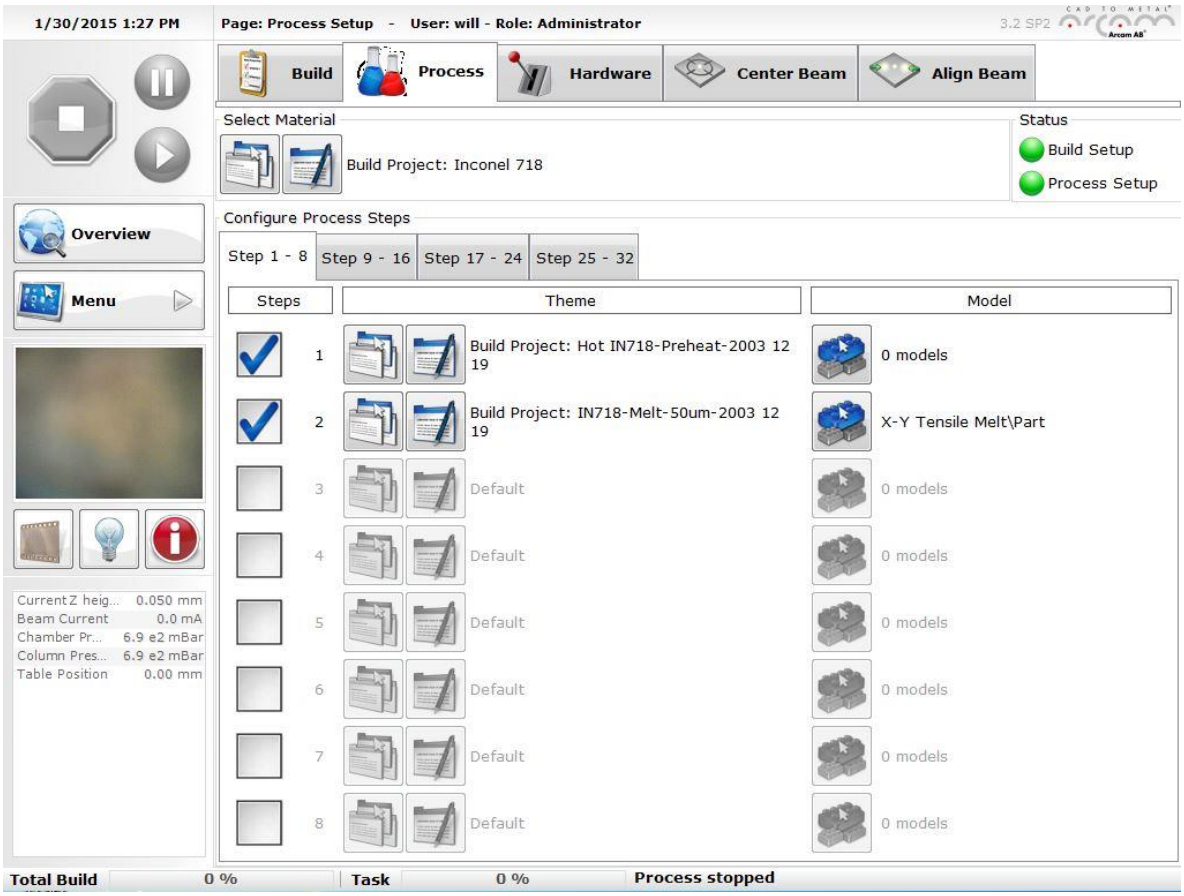

Figure 67. The "Process" tab in EBM control allows the user to load and select material sintering and processing parameters.

V.1.3 Process Parameters

The EBM Control software has a complex way of calculating the beam current, beam speed, preheat parameters, postheat parameters, and order of process steps. Features can be modified by the user, but a thorough understanding is necessary. The understanding of process parameters as presented in this section is attributed to work by I. Elfstrom. [285]

Variables in this section will be defined by level according to EBM Control parameter levels. For example, a menu item that is found under Preheat, then Square, then *Preheating 1*, then Beam Speed would be labeled as following:

preheat.square.preheating1.beamspeed

To understand the structure of parameter levels, it is useful to look at screen captures of the EBM Control Software. The first process step, Raking, occurs when the rake is engaged to distribute a layer of powder after the build table is lowered.

The next process step, Preheat, occurs in two stages defined as "Preheat 1" (Preheat I) and "Preheat 2" (Preheat II) that are defined by the parameters in Figure 68 and Figure 69. Since preheat.square.autocalculation is always enabled, the software will calculate a *Preheat 2* if *Preheat 1* is enabled (this is always the case, as using both preheats has been found to improve processing). *Preheat 1* parameters are set by either the enclosed area of the entire part. Preheat 1 is done over a square area, with the maximum size being based on the size of the start plate (146mm x 146mm for a 150mm start plate). The actual area of *Preheat 1* (A_1) is calculated by drawing a square containing all parts and adding the value of preheat.square.offsettopart to each dimension x and y. The current used is calculated according to:

$$i_{P1} = i_{ref1} * \frac{A_{P1}}{A_{ref}}$$

$$A_{ref} = (preheat.square.size)^2$$

The *Preheat 2* area (A_2) must be calculated based on a relationship between currents, the reference area, and A_1:

$$i_{avg2} = i_{avg1} * \frac{A_2 - A_1}{A_{ref}}$$

$$\boldsymbol{A_2 = \frac{i_{avg2}}{i_{avg1}} * A_{ref} + A_1} \quad \textbf{(Eq. 14)}$$

The average current across the entire preheat step can then be calculated according to:

$$\boldsymbol{i_{avgPreheat} = \frac{i_{avg1}(A_1 - A_2) + i_{avg2}A_2}{A_{ref}}} \quad \textbf{(Eq. 15)}$$

Postheating can be engaged (optionally) at the end of the preheat cycle and again after the melt is complete (although is described in general terms as coming after the melting stage). In both cases, $i_{avgPreheat}$ sets the average current that the process targets. Postheating is calculated based on the inputs on several parameters: preheat.heating.maximumheattime, melt.heating.maximumheattime, and arguably every other parameter used during processing. The fact that postheat time is calculated based on an energy balance means that any other parameter that impacts the current or time of the process will impact postheat. The parameters with the most direct effect are those associated with preheat. The Preheat 1 current (i_{P1}) and Preheat 1 area (A_1) are set as the current and area for postheating as well. The term "heating" is used in EBM Control to denote Postheating. The actual average current (measured) can be calculated if the postheating time is known:

$$i_{avgPreheat} * t_{total} = i_{avgPreheat} * \left(t_{process} + t_{postheat1}\right) = \left(i_{avg} * t_{process} + i_{P1} * t_{postheat1}\right)$$

$$\boldsymbol{i_{avgPreheat} = \frac{\left(i_{avg} * t_{process} + i_{P1} * t_{postheat1}\right)}{\left(t_{process} + t_{postheat1}\right)}} \quad \textbf{(Eq. 16)}$$

This equation can be rearranged to solve for postheating time (the time needed to bring the average current up to $i_{avgPreheat}$):

$$t_{postheat1} = \frac{\left(i_{avgPreheat} - i_{avg}\right)}{\left(i_{P1} - i_{avgPreheat}\right)} * t_{process} \qquad \textbf{(Eq. 17)}$$

The variable i_{avg} is the actual average current (not the target) across the preceding process steps (not including raking), and the variable $t_{process}$ is the time associated with the preceding process steps. This same equation applies to calculation of the time for the melt postheating step ($t_{postheat2}$), except that the values used for i_{avg} and $t_{process}$ are calculated in a different way. In melt postheating, the preceding process steps include all of the preceding steps except for the optional first postheat. Since the preheat postheating is optional, the calculation for the melt postheating is set to always include heating for previous steps. When the optional step is engaged, it is not included in the energy balance (it is unclear if this is by design). It should be noted that contours are included in the energy balance for the preheat postheating calculation, and are done prior to the preheat postheating.

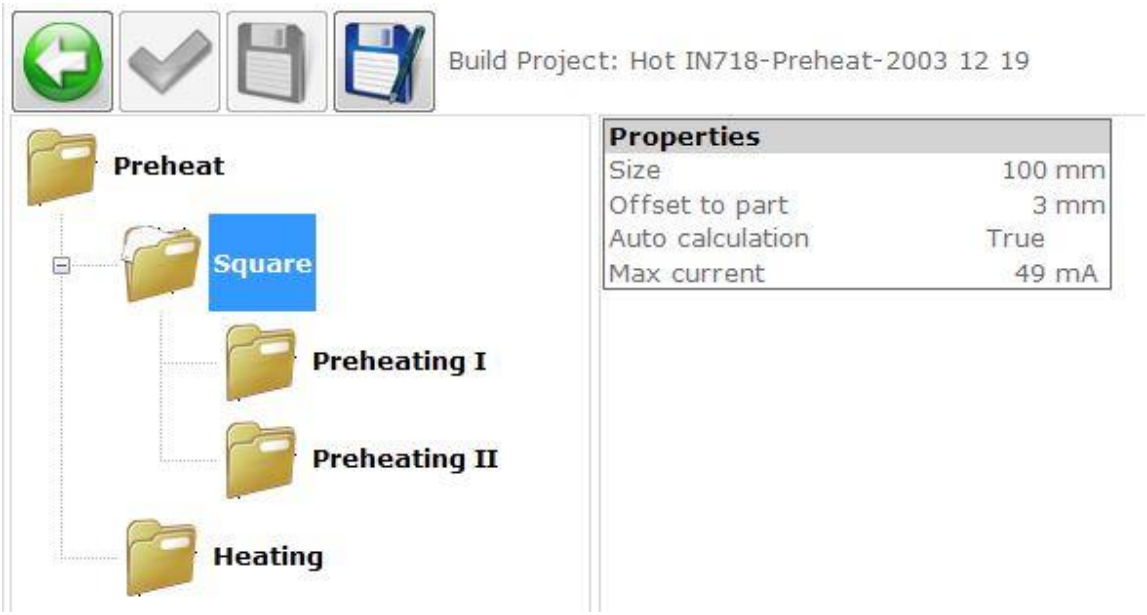

Figure 68. Parameters for the Preheat step.

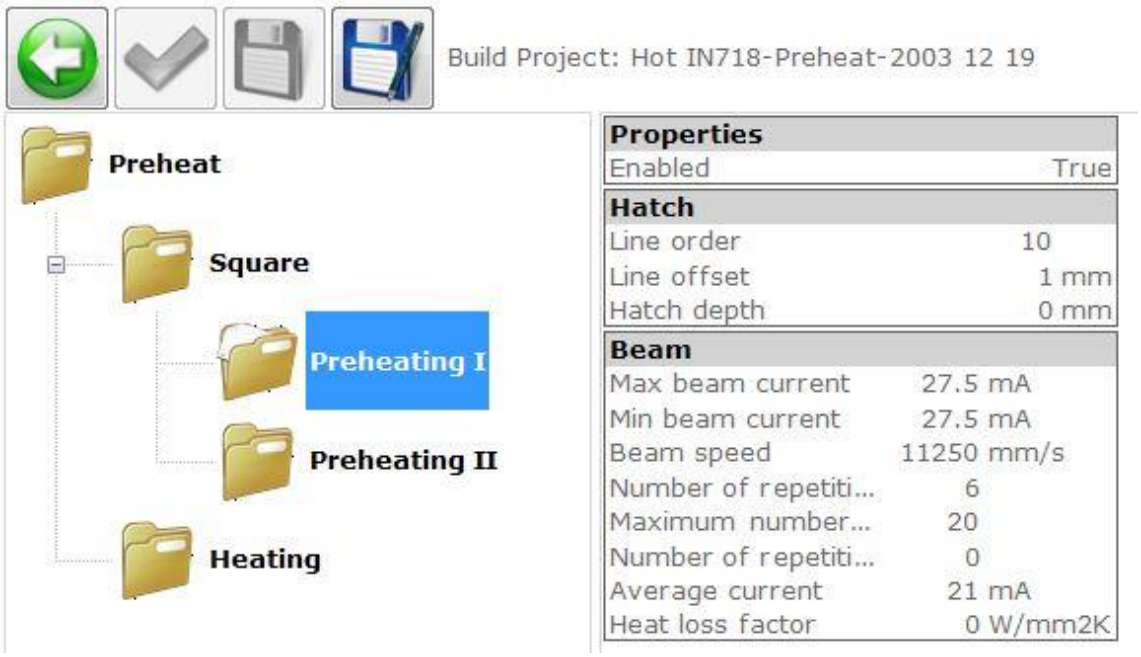

Figure 69. Parameters for the Preheat 1 (Preheat I) step.

After a layer is preheated, the next step is *Melting*. If support structures are included (Wafer Support), the order of bulk melting and support melting is not considered important. There are many parameters associated *Melting*, but the most important is melt.hatch.square (Figure 70). This menu includes the empirical inputs used to adjust the beam speed and beam current. Unlike a laser-based PBF system, neither speed nor power is constant in an EBM system. In fact, but vary almost constantly (unless the system is run in Manual Mode). First, a nominal beam current (i_{input}) and beam speed (v_{input}) are input by the user. The Focus Offset controls the focal point of the beam. [79] If melt.poweranalyse.automaticpowercalculation is not enabled, then the process will run in manual mode using constant current (i_{input}) and constant speed (v_{input}). This mode may be useful for researchers looking to control variables.

If the *Automatic Power Calculation* is enabled, then speed and current are modified according to many functions (this is the standard processing technique). The timing between beam passes changes based on geometry and location relative to the part edge, so the nominal speed and nominal current are modified. The use of the term line scan length (ℓ) is used to denote the length of a given beam pass. Line scan length varies with geometry (based on ℓ) and is used to change the power input of the beam to account for small and large regions; a small region should not be melted with the same power/speed combination as a larger region that has more time between beam passes. So, the *Current Compensation Function* is used to modify i_{input} according to:

$$\boldsymbol{i_{melt} = i_{CC}(\ell) = i_{input} * \left(1 + PropK * \frac{\ell - Scan\ Length\ Reference}{Scan\ Lenth\ Reference}\right)} \quad \textbf{(Eq. 18)}$$

This equation is bounded by setting a minimum current (some power is needed to melt even the smallest line scan lengths) and a maximum length (this sets a max current, effectively) in the process parameters. The value of i_{melt} is the current that is actually used to melt. Speed is now determined according to the value set by the *Speed Function* (the value v_{input} is not used in Automatic mode). The *Speed Function* is an empirical relationship between speed and current, which means that speed is also a function of line scan length. Values are not typically published but graphs of this relationship do exist. [79] A higher value of *Speed Function* means that the speed will be faster for a given current. This can be summarized as:

$$\boldsymbol{v_{SF} = v(i_{melt}, \ell)} \quad \textbf{(Eq. 19)}$$

Now that speed is set based on i_{melt}, other factors need to be considered. This speed is then modified based on the z-distance down to powder; for overhangs, the underlying powder can be more insulative than a solid part. The *Thickness Function* modifies speed to compensate for the lower amount of applied energy needed in overhangs based on the distance down to powder (z_{powder}). The function modifies the speed based on:

$$\boldsymbol{v_{Thickness} = v_{SF} * \left(1 + \frac{SpeedFactor}{1+\exp\left(Exponent\ Factor*\left(z_{powder}-Thickness\ Factor\right)\right)}\right)} \quad \textbf{(Eq. 20)}$$

Speed must also be modified to account for edge effects. As a snaking scan strategy is typically used, local heat build near edges can occur; the time that the melt pool has to cool near an edge is less than in the center of a part. To reduce the applied energy near edges, the *Turning Point Function* is used to increase the speed of the beam as it comes out of an edge. To do this, a Gaussian-type function is applied as:

$$v_{TP} = v_{Thickness} * (1 + (Pre\ exponential\ factor) * S)$$

$$\boldsymbol{S = \exp\left(-\left(v_{Thickness}\left((Exponential\ Factor\ I) * \ell - (Exponential\ Factor\ II) * v_{Thickness}\right)\right)^2\right)} \quad \textbf{(Eq. 21)}$$

At this point, an optional compensation for line scan length can be enabled (*Speed Compensation Function*) but is not used with typical parameters. The *Speed Compensation Function* operates the same way as *Current Compensation* but based on speed. That means that the melt speed is now known:

$$\boldsymbol{v_{melt} = v_{melt}\left(i, \ell, z_{powder}\right) = v_{TP}} \quad \textbf{(Eq. 22)}$$

The other features associated with process parameters in the *Melt* step include *Postheating* and *Contours*. It should be noted that the order of *Contours* can be changed to occur either before or after the *Hatch Melting* step. Postheating may be engaged after the melt step, as previously discussed.

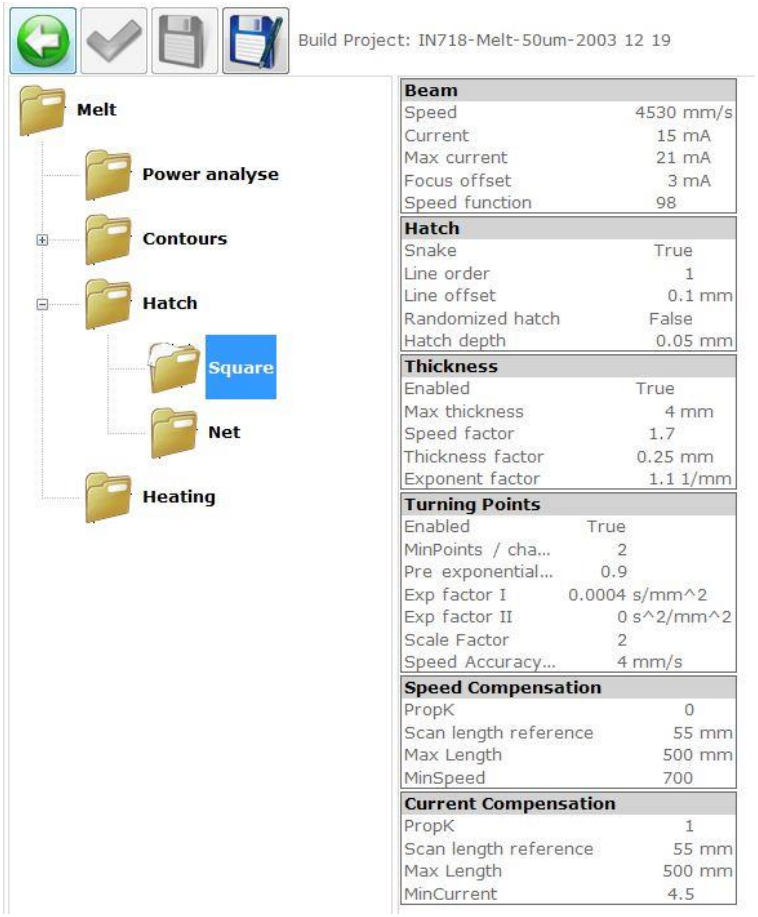

Figure 70. The melt.hatch.square menu is used to understand the values used for beam speed and beam current.

V.1.4 Example: NIST Test Artifact

It is useful to consider an example from a real part build. The log file for a NIST Test Artifact [286] as shown in Figure 71 (made from IN625 using an A2, software 3.2) was analyzed. The process parameters are given in Table 15. The real machine measured values are plotted in Figure 72. Nominal process parameter inputs are compared to measured values in Table 16. It is important to note that the nominal values input into the machine and those used in

calculations can be slightly off (usually higher in the case of current) than the actual values used and measured by the hardware.

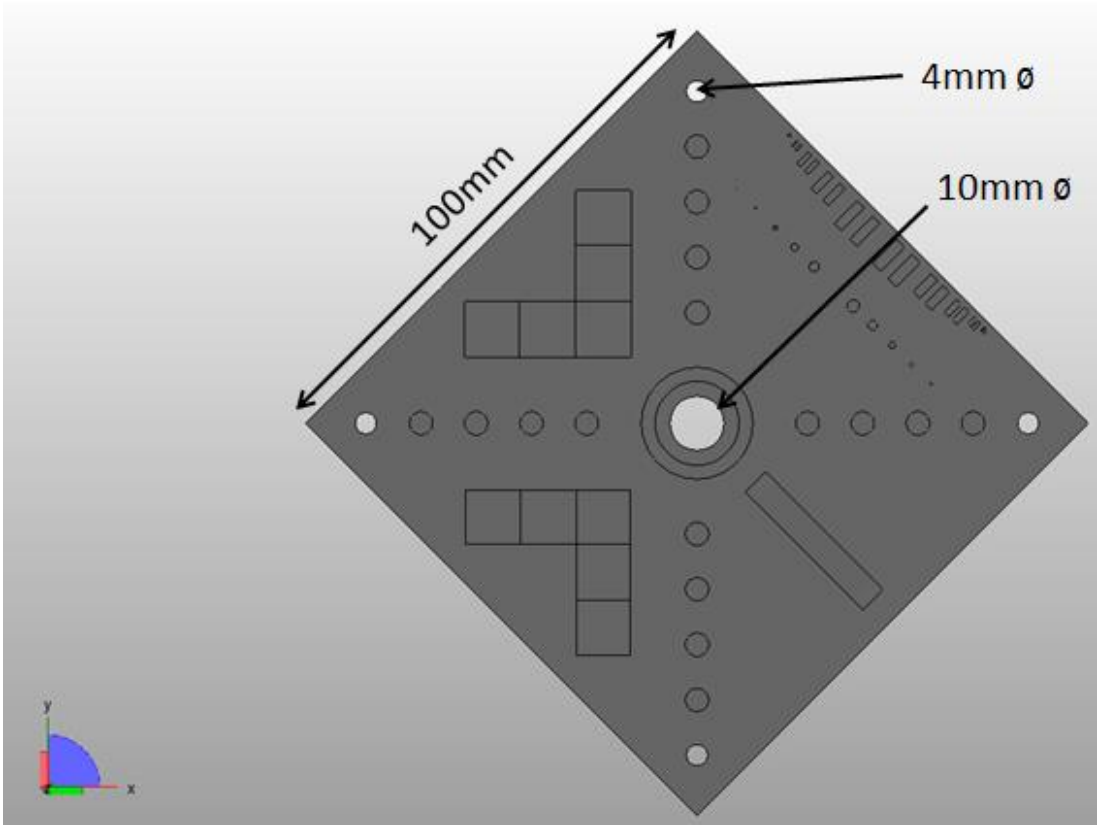

Figure 71. NIST Test Artifact with relevant dimensions.

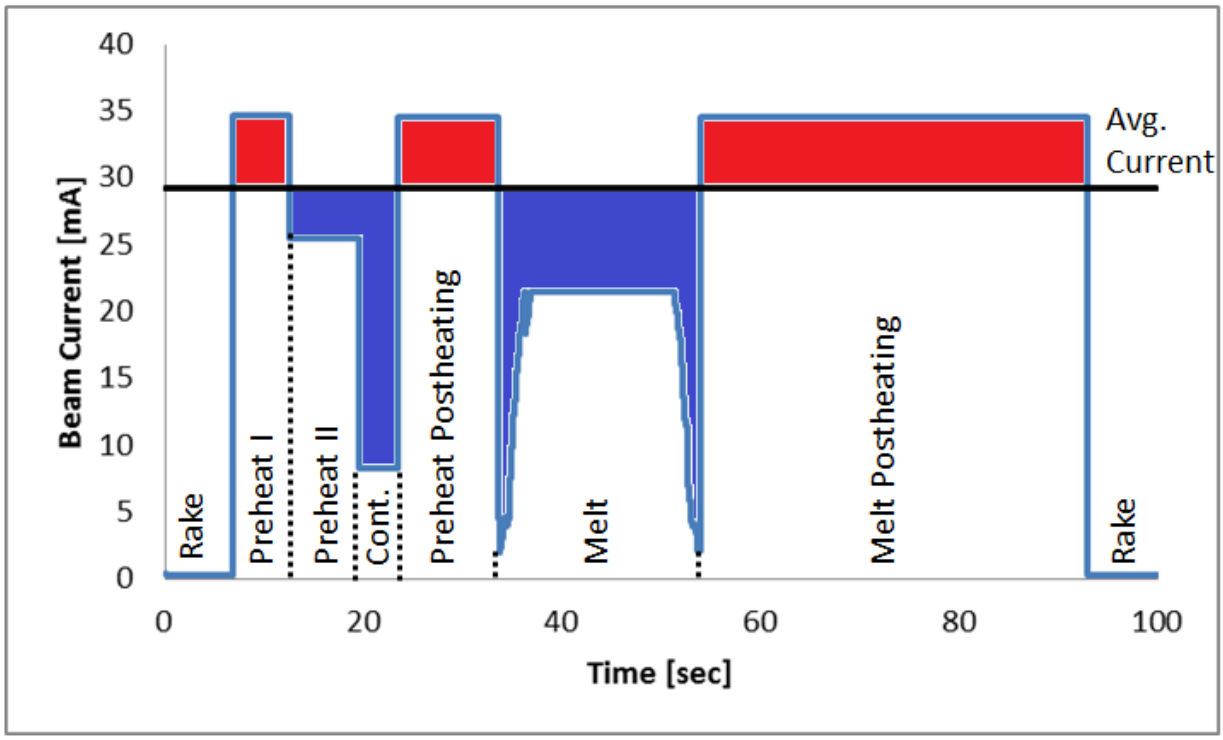

Figure 72. Measured values of beam current for a representative layer.

First, the Preheat 1 area is calculated by enclosing the entire layer to be melted in a square area in the X-Y plane (assuming base layer of this part, z=0mm) and adding offset to the dimension from the edge (3mm offset from the part in this example). The NIST artifact then has an edge of 141.4mm + 2*3mm = 147.4mm:

$$A_1 = (147.4\ mm)^2 = 21733.1\ mm^2$$

Now the Preheat 2 area is calculated by the area enclosed by the layer to be melted (not an X-Y box). The area must account for inner holes and offset:

$$A_2 = (106\ mm)^2 - \frac{\pi}{4} * (4\ mm)^2 = 11223.4\ mm^2$$

The Preheat 1 and Preheat 2 currents can then be calculated as:

$$i_{P1} = i_{ref1} * \frac{A_{P1}}{A_{ref}} = 17\ mA * \frac{21733.1\ mm^2}{(100\ mm)^2} = 36.9\ mA$$

$$i_{P2} = i_{ref2} * \frac{A_{P2}}{A_{ref}} = 24mA * \frac{A}{(100mm)^2} = 26.9\ mA$$

According to the melt parameters, a *Max Current* of 22mA is to be used for melting. This maximum current value is the limiting value for current in this case (the *Max Line Length* could also be used to limit, but is set at 500mm so does not impact the current value calculated in this case). The minimum current value used is 2.5mA, and limits how low the melting current can vary. The variation of melt current with line scan length is shown in Figure 73. The shape of the NIST Test Artifact layer being melted is a diamond with max length of 133.4mm (calculated from 141.4mm – 2*4mm); this means that the current ramps up to the maximum current quickly, holds during the center of the diamond at the maximum current, then ramps down quickly. This is reflected in the shape of the melt current profile.

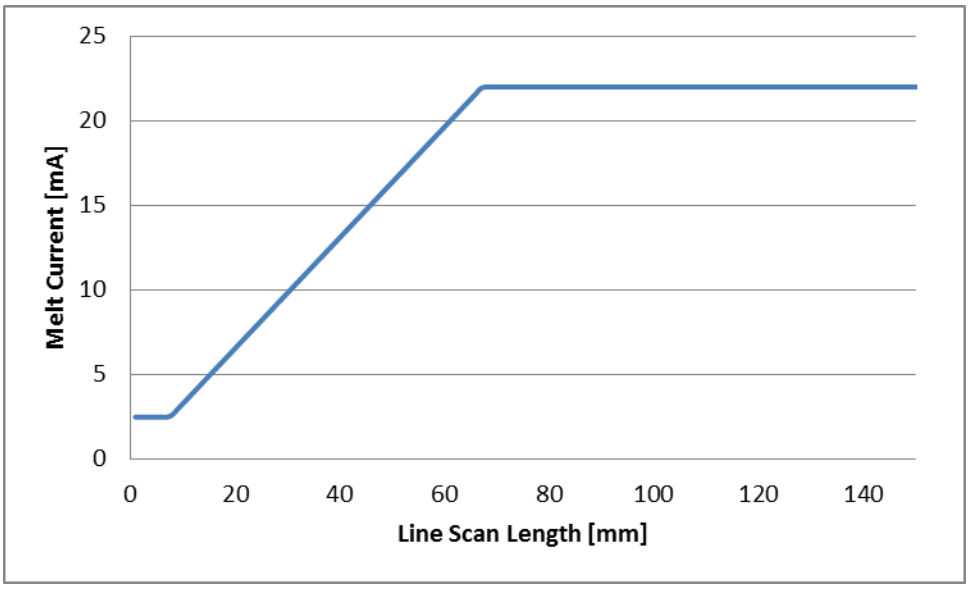

Figure 73. Variation of melt current with line scan length in an example build.

The contours are run before the preheat postheating, and included in the energy balance. The *Preheat* "average" current is calculated with respect to the reference area:

$$\boldsymbol{i_{avgPreheat}} = \frac{\boldsymbol{i_{avg1}(A_1 - A_2) + i_{avg2}A_2}}{\boldsymbol{A_{ref}}} \quad \textbf{(Eq. 23)}$$

$$= \frac{13.5mA\left(21733.1mm^2 - 11223.4mm^2\right) + 13.5mA * 11223.4mm^2}{(100\ mm)^2}$$

$$= 29.3mA$$

This value is then used in calculating the preheat postheating time (the first, optional post-heating cycle). The actual average current (measured) can be calculated if the postheating time is known:

$$\boldsymbol{i_{avgMeasured1}} = \frac{\left(\boldsymbol{i_{avg} * t_{process} + i_{P1} * t_{postheat1}}\right)}{\left(\boldsymbol{t_{process} + t_{postheat1}}\right)} \quad \textbf{(Eq. 24)}$$

$$= 28.3mA$$

The average for the melt step can be calculated in the same way:

$$\boldsymbol{i_{avgMeasured2}} = \frac{\left(\boldsymbol{i_{avg} * t_{melt} + i_{P1} * t_{postheat2}}\right)}{\left(\boldsymbol{t_{melt} + t_{postheat2}}\right)} \quad \textbf{(Eq. 25)}$$

$$= 29.1mA$$

This equation can be rearranged to solve for postheating time (the time needed to bring the average current up to $i_{avgPreheat}$):

$$\boldsymbol{t_{postheat1}} = \frac{\left(\boldsymbol{i_{avgPreheat} - i_{avg}}\right)}{\left(\boldsymbol{i_{P1} - i_{avgPreheat}}\right)} * \boldsymbol{t_{process}} \quad \textbf{(Eq. 26)}$$

$$= \frac{29.3 - 24.5}{36.9 - 29.3} * 16.6\ sec = 10.6\ sec$$

$$t_{postheat2} = \frac{(i_{avgPreheat} - i_{avg})}{(i_{P1} - i_{avgPreheat})} * t_{process}$$

$$= \frac{29.3 - 21.2}{36.9 - 29.3} * 37.0\ sec = 39.4\ sec$$

This same balance (using the same $i_{avgPreheat}$ as the target average current) will be applied to a balance between the melt and the melt postheating (second postheat). This balance to achieve the set average current can be shown visually by balancing the areas bounded above the average current line with those below it in Figure 72. The area of preheat postheating and *Preheat 1* above the average should match that below for *Preheat 2* and *Contours*. The area above melt postheating and *Preheat 1* should match the balance of all previous steps, except for the preheat postheating.

Table 15. Select Process Parameters for the NIST build example.

Beam	
Current [mA]	17
Speed Function	80
Focus [mA]	5
Max Current [mA]	22

Melt.Heating	
Enable	TRUE
MeanCurrFraction	1
MaxHeatTime [s]	60
UseProcess Power	FALSE
HeatingBetweenModels	TRUE

Current Compensation	
Min Current [mA]	2.5
PropK	1
ScanLengthRef [mm]	52
Max Length [mm]	500

Preheating	
Enabled	TRUE
FocusValue [mA]	80
UseEnergyConsumption	TRUE
AutoCalc	TRUE
OffsetToPart [mm]	3
Size [mm]	100

Preheat.Heating	
Enabled	TRUE
HeatingBetweenModels	TRUE
MaxHeatTime [s]	60
MeanCurrFraction	1
UseProcessPower	FALSE

Preheat 1	
MaxCurrent [mA]	17
MinCurrent [mA]	17
MeanPower [mA]	13.5
TotalRepetitionsOfSweep	8
Speed [mm/s]	14600
MaxNumberOfSweeps	200
HeatLossFactor	6E-06

Preheat 2	
MaxCurrent [mA]	24
MinCurrent [mA]	24
MeanPower [mA]	13.5
TotalRepetitionsOfSweep	7
Speed [mm/s]	10000
MaxNumberOfSweeps	25
HeatLossFactor	9.5E-06

Inner Contour	
Current [mA]	9
Max Current [mA]	9

Outer Contour	
Current [mA]	9
Max Current [mA]	9

Table 16. The measured process data compared to the nominal or calculated parameter inputs.

Current Value	Nominal [mA]	Measured [mA]
Min. Melt Current	2.5	2.05
Max. Melt Current	22	21.4
Preheat I	36.9	34.6
Preheat II	26.9	25.5
Contours	9	8.2
Preheat Postheating	36.9	34.6
Melt Postheating	36.9	34.6
Time Value	Calculated [s]	Measured [s]
Preheat I	-	5.69
Preheat II	-	6.89
Contours	-	3.94
Preheat Postheating	10.6	10.06
Melt	-	20.23
Melt Postheating	39.4	39.05

V.1.5 Calculating Applied Energy

Now that $i(\ell)$ (Equation 18) and $v(\ell)$ (Equation 22) can be calculated, the applied energy can be considered over a single line scan length. Recall the applied energy equation:

$$\boldsymbol{E_{app}(\ell) = i(\ell) * \forall * t(\ell) = i(\ell) * \forall * \frac{\ell}{v} = i(\ell) * \forall * \frac{\ell}{v(\ell)}} \quad \textbf{(Eq. 27)}$$

This may now be modified as a function of the *Current Compensation Function*, *Speed Function*, *Thickness Function*, and *Turning Point Function*. These functions transform applied energy such that it is now a function of position (x, y, z):

$$\boldsymbol{E_{app}(\ell, x, y, z) = i(\ell) * \forall * \frac{\ell}{v(i,\ell,x,y,z)}} \quad \textbf{(Eq. 28)}$$

Equations for $E_{app}(l,x,y,z)$, $i(\ell)$, and $v(i,\ell,x,y,z)$ have been applied to pixels of digital image slices. Each pixel can be assigned length dimensions so that pixels are used to calculate position and line scan length. This is done to calculate energy density as:

$$\boldsymbol{E_{app}}\left[\frac{J}{mm^3}\right] = \boldsymbol{i}\left[\frac{mA}{pixel^2}\right] * \forall[\boldsymbol{kV}] * \frac{\boldsymbol{t_{pixel}}}{\boldsymbol{z_{layer}}} \quad \textbf{(Eq. 29)}$$

The current is now applied as an average over the area of the pixel (this assumes uniform energy deposition across the pixel, which is an approximation). The variables for time of the beam in one pixel (t_{pixel}) and layer height (z_{layer}) must be known. The ratio of pixels to position, or R, (10 pixels/mm if using exported images from Build Assembler) must also be known. The applied energy for the NIST example build then becomes:

$$\boldsymbol{E_{app}}\left[\frac{J}{mm^3}\right] = \boldsymbol{i}\left[\frac{mA}{pixel^2}\right] * \forall[\boldsymbol{kV}] * \frac{\left(\frac{1\,[pixel]}{v\left[\frac{mm}{s}\right]}\right)}{\boldsymbol{z_{layer}}} * \boldsymbol{R} \quad \textbf{(Eq. 30)}$$

$$E_{app,\max current}\left[\frac{J}{mm^3}\right] = 22\ \left[\frac{mA}{pixel^2}\right] * 60[kV] * \frac{1}{3785.3}\left[pixel * \frac{s}{mm}\right] * \frac{1}{0.05}\left[\frac{1}{mm}\right] * 10\left[\frac{pixel}{mm}\right] = 69.7\ \left[\frac{J}{mm^3}\right] \quad \textbf{(Eq. 31)}$$

This method was applied to a software package developed at ORNL to analyze EBM process parameters. The software outputs color-coded graphs of current, speed, and applied energy for the melting step. The NIST example build was analyzed and the calculated values of current (Figure 74), speed (Figure 75), and applied energy (Figure 76) were plotted. The majority of the layer is melted with the maximum current of 22mA, which corresponds to a beam speed of 3785.3mm/s. Using the above energy calculation, the applied energy in the maximum current zone is 69.7 J/mm^3. By plotting the values of speed, current, and applied energy geometrically, useful information can be learned about the EBM process. For example, the energy applied near the corners of the NIST example is much higher than the relatively constant applied energy throughout the rest of the body. This is not desirable, as

applied energy should be kept more constant (except in overhangs or edges). It can also be seen that less energy is applied near the edges. This is due to the *Turning Point Function* to increase beam speed as the beam returns out of an edge. The higher applied energy near the corner is due to shorter line scan lengths, but the reason that this occurs is not immediately clear. The resulting build shows swelling in the regions of increased energy application (Figure 77). The build was made using EBM Control 3.2, which uses 90 degree rotations between layers. Therefore, all corners experienced the higher apply energies for every other layer.

The reason for the increase in applied energy in small line scan lengths is related to the relationship between speed and current, or the *Speed Function*. The standard *Speed Function* reads data from a set of empirical points. This data is non-linear, and results in a non-linear relationship with speed and current. A linear relationship is required for uniform applied energy. In fact, EBM Control allows for linear functions to be selected. If a linear *Speed Function* is selected, the applied energy balance does not over apply energy in corners (Figure 78). The magnitude of the applied energy of the linear *Speed Function* case can be adjusted by modifying the slope and translation of the relationship. Future work should test the use of a linear speed function to reduce swelling in smaller line scan lengths.

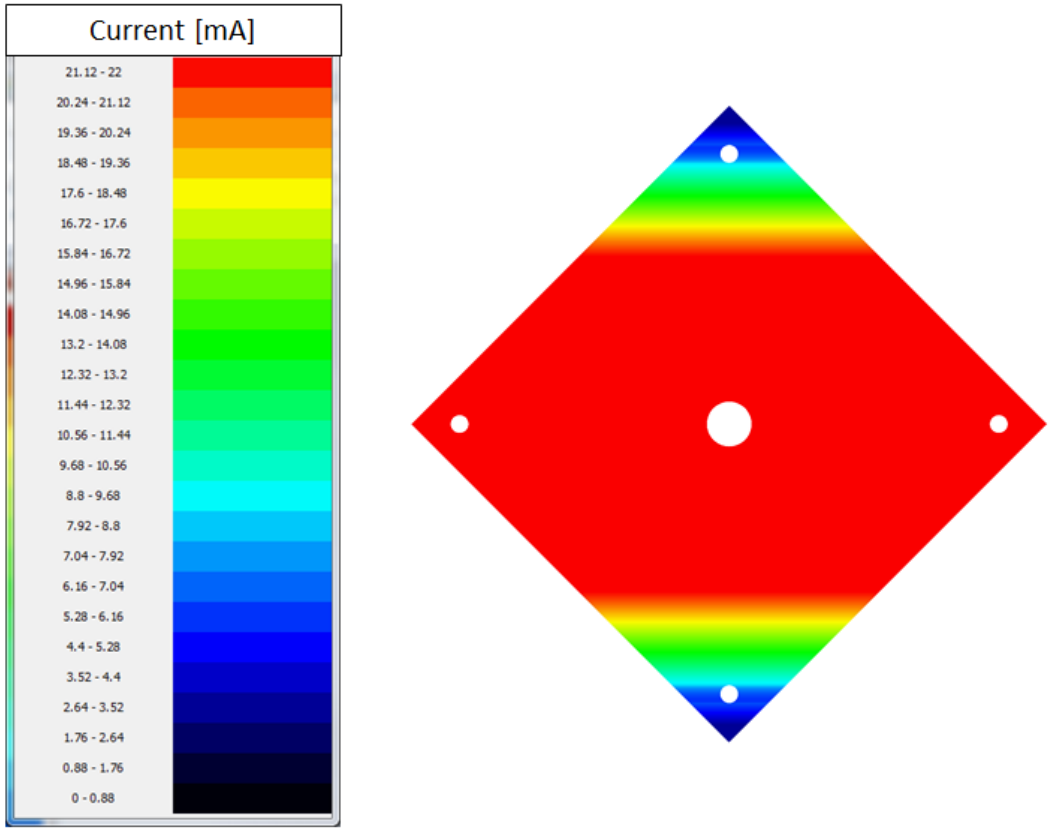

Figure 74. Melt current used during processing of the first layer of the NIST Test Artifact example.

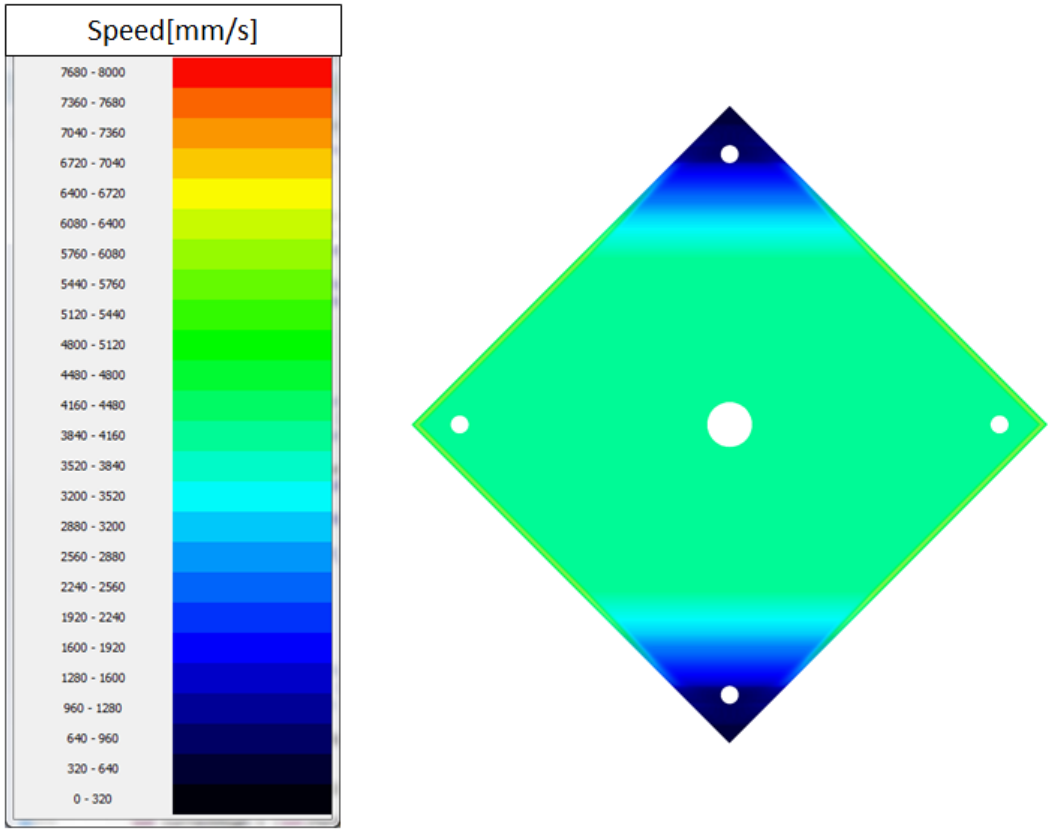

Figure 75. Beam speed used during processing of the first layer of the NIST Test Artifact example.

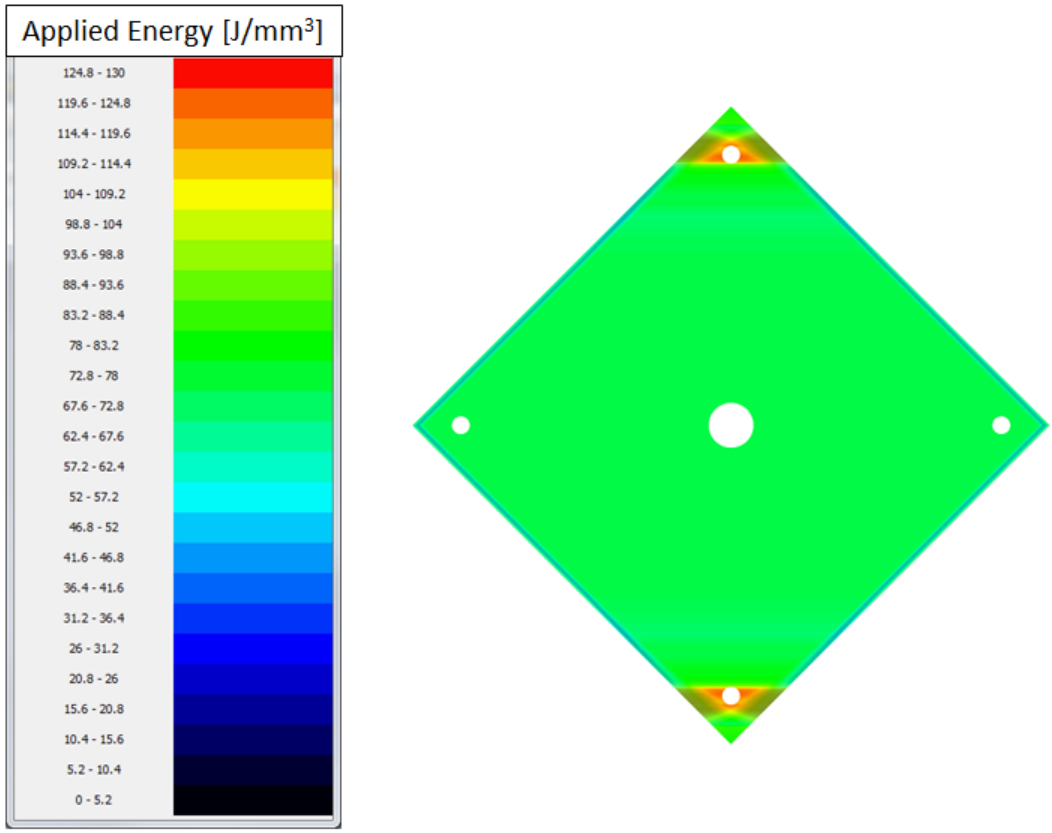

Figure 76. Applied energy density during processing of the first layer of the NIST Test Artifact example.

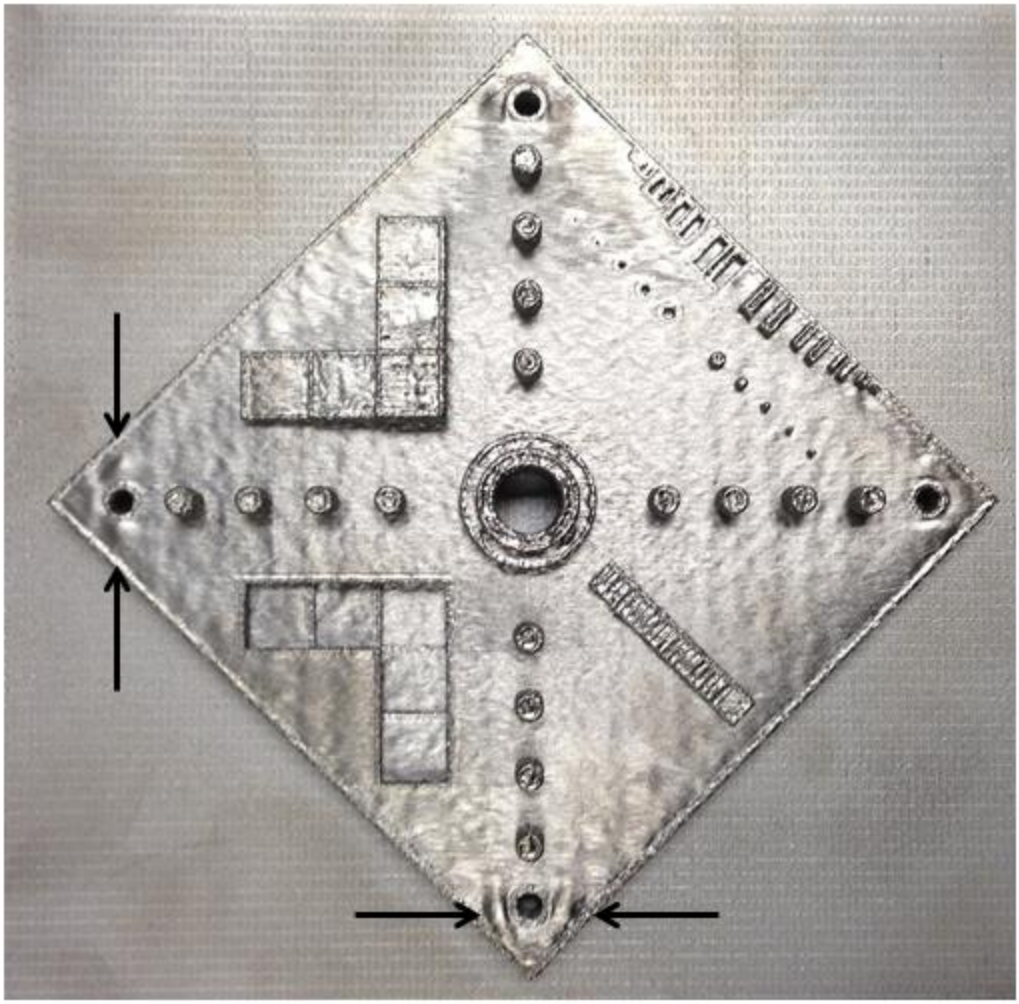

Figure 77. Deposited NIST Test Artifact in IN625 from example. Swelling is notable in the corner regions, which corresponds to areas of increased energy application.

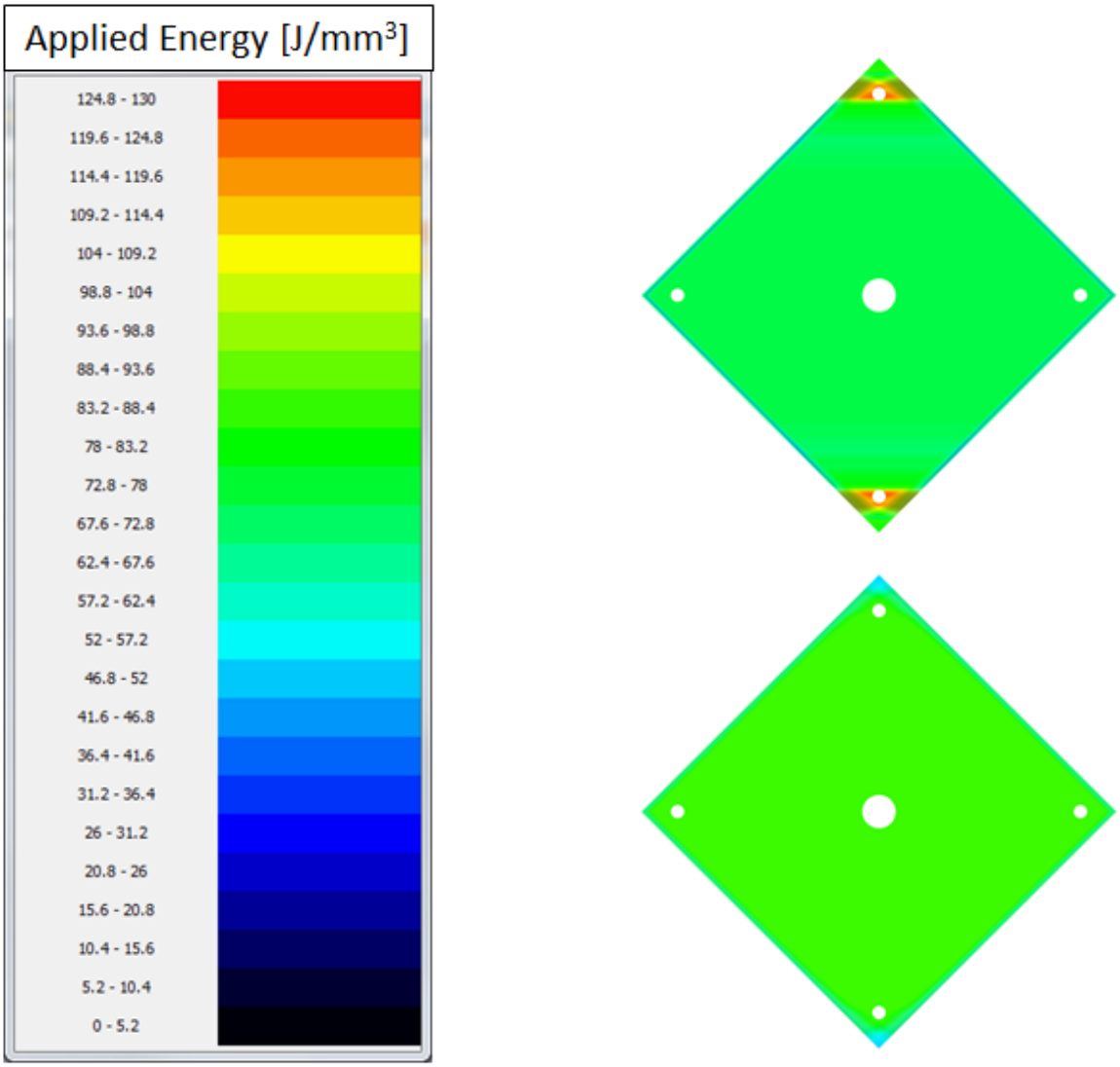

Figure 78. The amount of energy is over applied when using (Top) the standard, non-linear Speed Function and (Bottom) is uniform through corners with a linear Speed Function.

V.1.6 Process Parameter Development

Process parameter development is currently focused on powder bed temperature but controls need to be more intuitive. The typical pattern for development of a new material

is to adjust the powder bed temperature based on sintering kinetics and thermal conductivity of the material. In order to avoid the loss of powder from the build surface due to particle charging ("smoking"), the powder is sintered. Different alloys and different powder morphologies will sinter differently. The powder bed temperature, as measured from the substrate thermocouple, is typically used to gauge the processing window for a material. For IN718, a powder bed temperature of 975±25°C has been noted as optimal. [20] For temperatures <950°C, powder ejection increases (not just from electrostatic charging, but also spattering from the melt pool).

To increase the powder bed temperature, the start plate sintering temperature is increased and more energy is put in during preheating and postheating. For IN718, the start plate sintering temperature is typically 975°C for a 30 minute hold time. For Ti-6Al-4V, the start plate sintering temperature is typically 650-730°C with no hold time. This temperature for IN718 may be adjusted up to near 1000°C to accommodate extra temperature loss during the first few layers (the start plate behaves as a large radiant surface). This sets the powder bed temperature at the beginning of the build. To keep the temperature high (~1000°C) during processing, the preheating and postheating parameters must be correctly set or manually manipulated. It should be noted that the only melt parameters that should be adjusted are the value of the speed function and the input current. The melt parameters used for Ti-6Al-4V are considered standard and are not typically changed for other materials; the sintering kinetics and powder bed temperature are held to be much more important. To adjust preheating for higher temperatures, the input values of *Minimum Current* and *Maximum Current* (set to the same value) can be adjusted up to increase the current used during the preheat steps (the Preheat 1 values also increase the postheat current). Care must be taken to not use too much current during preheating, otherwise over-sintering of the powder bed will make powder recovery more difficult (Figure 79) or impossible. To avoid over-sintering, the preheat cycle time should be increased. This can be done by adjusting the *Number of Repetitions* and the *Maximum Number of Repetitions*.

The *Average Current* can be adjusted to modify the postheating time. If the maximum postheating time is reached, then the value of *Maximum Heat Time* may need to be increased. Finding the optimum balance between beam current and cycle time is critical to maintaining the powder bed temperature while avoiding over- or under-sintering.

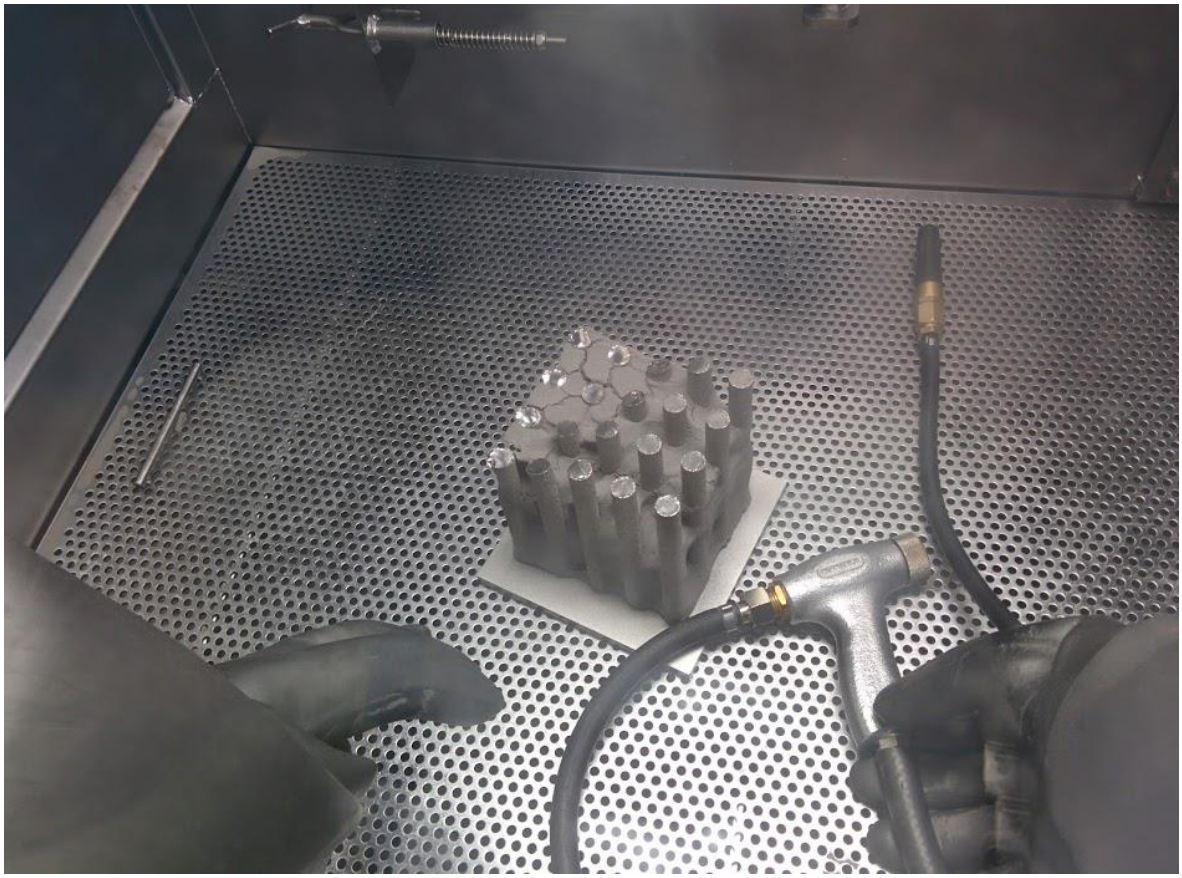

Figure 79. Over-sintering of powder in EBM IN718.

V.2 Arcam Log File Analysis

As the build is processing, EBM Control registers process data in a log file (.PLG). Upon completion of the build, the .PLG file is compressed into a .ZIP folder. The .PLG file is a text

file, with its own unique syntax for storing data. Given an understanding of the syntax of the log file, a user can pull out useful data about the process. This may be done manually, with a script, or by using the proprietary EBM Log Studio software from Arcam.

Process Themes store process parameters locally, so that a given theme can be recalled in EBM Control for running a build. These are stored locally as .XML files. However, the theme values are stored in the .PLG file, so it is not necessary to store the .XML files (but may make it easier to compare and/or re-run a specific theme). In fact, it is necessary to look at the .PLG file to check for any parameter changes made during processing (these will not be registered in the .XML file unless saved).

Each line of the .PLG file includes a piece of data. Some lines are prefaced with a date/time stamp; these lines are collected data. Other lines are prefaced with "#-IOItem:" to delimit inputs from the process themes selected.

```
#-IOItem:
Name=Themes.ProcessStep[9].Theme.Melt.Squares.StartSquare.AutoOffset.Enable|DName
=Enabled|Type=Boolean|Unit=|Format=|Axis=Linear|HiHi=0|Hi=0|Lo=0|LoLo=0
```

Most lines log either inputs from the user or data measured by the machine. An example line of standard user input is:

```
2014-07-28
13:38:46.671|Themes.ProcessStep[10].Theme.Melt.Squares.StartSquare.Beam.Current|Cor
e|44316247|12
```

Vertical bars are used to divide values. Periods are used to divide levels/classes on the list. The last value listed is the input value (in this case 12mA) for the last level (Current). The units for the value are taken from the standard IO that is shown on the user input screen.

Brackets are used to hold the value of the process step (in this case step 10). These process steps correlate to the order in which the steps were loaded in the Theme, which may not be the same order that steps are run in; the order in which steps are run and loaded may be different and cause some confusion during analysis (especially is themes are re-loaded or un-loaded).

A standard line of output data looks like:

```
2014-07-30 00:00:37.828|OPC.Temperature.BottomTemperature|SuperUser (OPC)|49110884|858
```

Again, the timestamp is the leading value. This line shows the output of the temperature from the thermocouple under the start plate reading a value of 858°C. Data is appended as it is collected, so it is ordered by time and not by category. For this reason, parsing of the log file data can be useful for data analysis.

V.2.1 Data Analysis Code Development at ORNL

Work at ORNL has started to develop a log file analysis code for the EBM process. The code is written in a set of Python modules that read .PLG files. The code works by first parsing the .PLG file into a more readable file format (.hdf5). The python module *h5py* is then used to read the .hdf5 file. *NumPy* and *Matplotlib* modules are then called and used to plot the data, as specified by the user. One of the most useful tools is the ability to calculate the average layer time, while excluding anomalous layers (Figure 80).

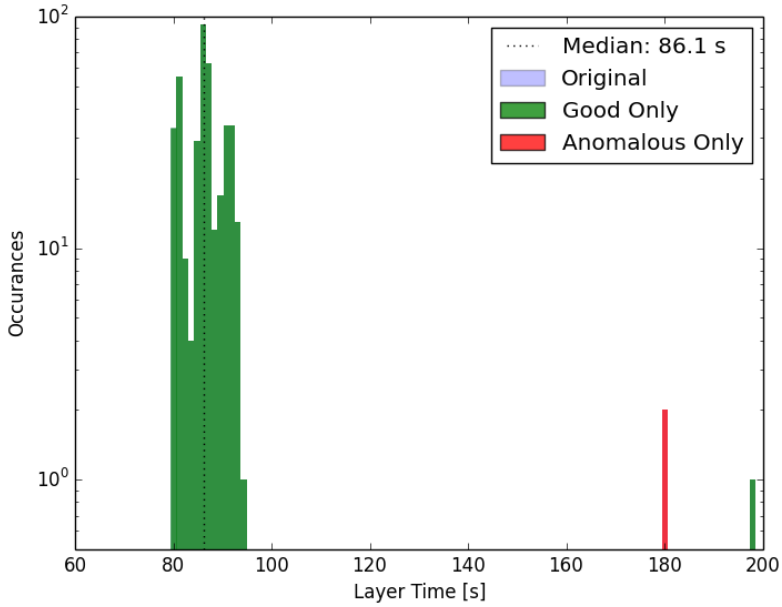

Figure 80. Average layer time as calculated by the ORNL code from log file data.

These modules were used in this dissertation to analyze builds from a variety of different materials, hardware, software versions, and layer thicknesses. Although parameter optimization was ongoing for most of these builds, useful information can still be extracted; a few parameter changes between builds is mostly assumed to not be impactful, except as noted in the text for the various builds considered. Build descriptions for samples prepared for this study are given in Table 17. Data on processing time is given in Table 18. The average layer time was calculated using the ORNL code, excluding anomalous layers. The part volumes were calculated using a function in the basic version *NetFabb*. Deposition rate was calculated by dividing either the mass or volume by the process time. This gives a deposition rate that includes the time waited for raking, preheating, and postheating (not just the melting stage) to give a more accurate account of the rate the process occurs at. Cool down time was not included in the deposition rate calculation. If cool down time was included, the calculated deposition rates would decrease relatively dramatically; the cool down time for shorter builds is sometimes larger than the process time (in cases using the

slow, vacuum cool). Cases from this data will be compared (§V.2.4 through §V.2.10), including discussion of important differences in process parameters.

Table 17. Summary of analyzed builds.

Build #	Layer Thickness	Machine	Software	Powder	Build Geometry	Material	Cooling
1	70um	A2	3.2.142	RA	X-Y Tensile	Inconel 718	Slow
2	50um	A2	3.2	GA	X-Y Tensile	Inconel 718	Slow
3	50um	A2	3.2	GA	X-Y Tensile	Inconel 718	Fast
4	50um	A2	4.1.22	PREP	X-Y Tensile	Inconel 718	Fast
5	100um	A2	4.1.22	PREP	X-Y Tensile	Inconel 718	Fast
6	75um	A2	4.1.22	PA	Ver. Build, No Box	Inconel 718	Fast
7	75um	A2	4.1.22	PA	X-Y Tensile	Inconel 718	Fast
8	50um	S12	4.1.22	GA	X-Y Tensile	Inconel 718	Fast
9	75um	S12	4.1.22	GA	X-Y Tensile	Inconel 718	Fast
10	50um	Q10	4.1.71	PREP	Ver. Build	Ti-6Al-4V	Slow
11	50um	A2	3.2.121		Ver. Build	Ti-6Al-4V	Slow
12	50um	A2	3.2		NIST Test Artifact	Inconel 625	Slow

Table 18. Summary layer time, process time, and deposition rate.

Build #	Average Layer Time [s]	Process Time [hr]	Cool Down Time [hr]	Part Volume [cc]	Density [g/cc]	Part Mass [kg]	Dep. Rate [cc/hr]	Dep. Rate [kg/hr]
1	80.1	6.33	13.28	172.8	8.19	1.42	27.3	0.223
2	67.0	7.47	11.83	172.8	8.19	1.42	23.1	0.190
3	66.7	7.40	5.35	172.8	8.19	1.42	23.4	0.191
4	86.1	9.60	5.77	172.8	8.19	1.42	18.0	0.147
5	91.0	5.27	5.22	172.8	8.19	1.42	32.8	0.269
6	93.7	37.12	11.38	1245.92	8.19	10.2	33.6	0.275
7	62.6	4.73	4.88	172.8	8.19	1.42	36.5	0.299
8	105.9	12.35	5.23	172.8	8.19	1.42	14.0	0.115
9	88.0	6.43	5.02	172.8	8.19	1.42	26.9	0.220
10	89.0	52.55	3.13	1319.9	4.43	5.85	25.1	0.111
11	56.4	33.67	6.18	1319.9	4.43	5.85	39.2	0.174
12	92.4	6.77	7.13	100.98	8.44	0.852	14.9	0.126

V.2.2 Geometry Descriptions

In addition to the NIST Test Artifact, other example geometries were run. Simple bars were designed to fit on a 150x150mm start plate and are called the “X-Y Tensile” part. These bars (Figure 81) were designed to measure tensile properties in the X- and Y-directions. Another build was designed to produce both horizontal and vertical tensile samples. This build is called the “Verification” part (Figure 82).

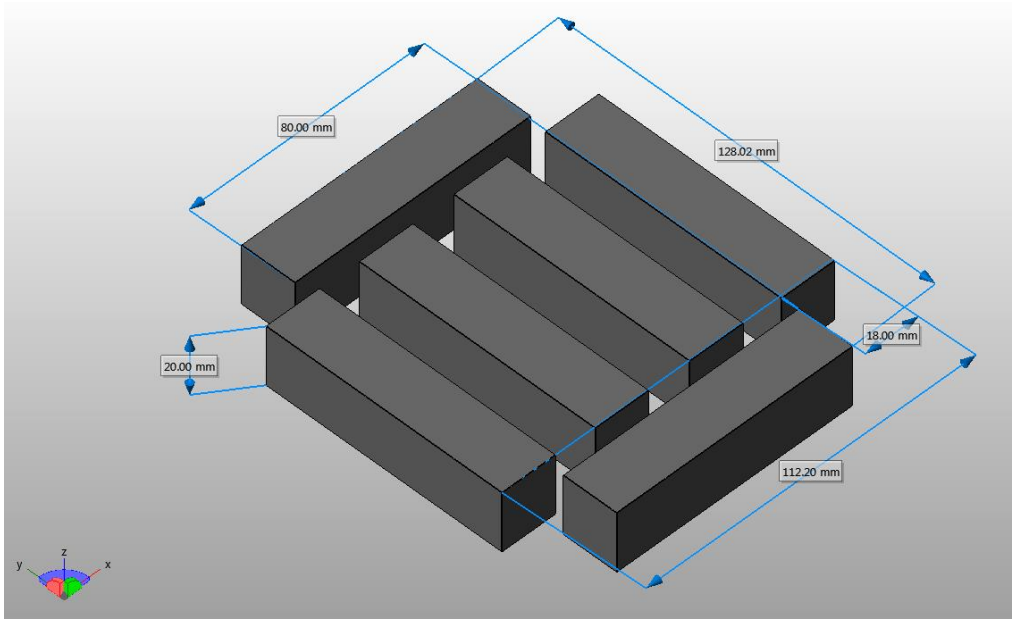

Figure 81. The "X-Y Tensile" build geometry.

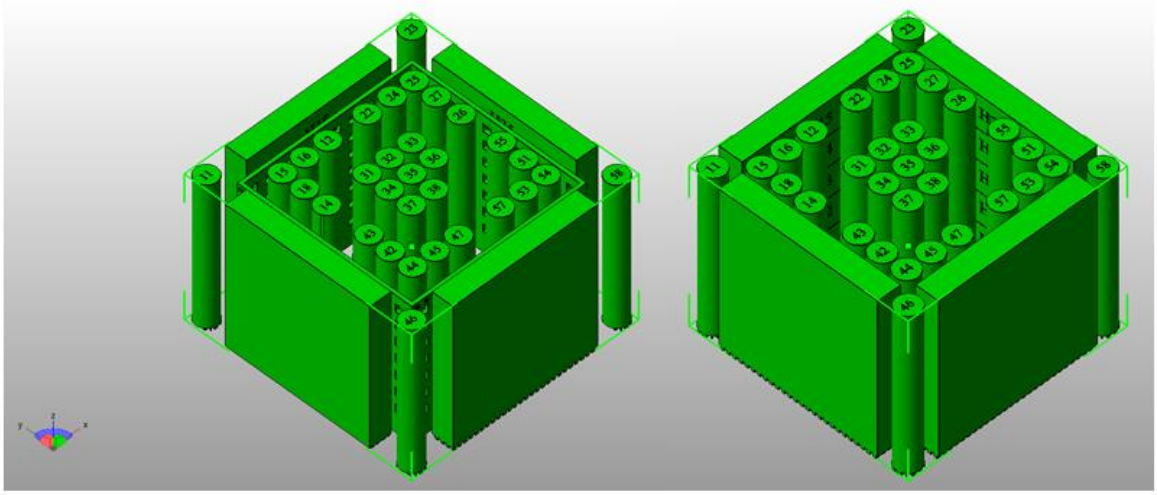

Figure 82. The "Verification" build geometry (Left) with box and (Right) without.

V.2.3 Build Analyses

The analysis of the build data presented in Table 17 and Table 18 was complicated by software changes and process parameter changes made between builds. This section is an attempt to pull useful information from builds produced during ongoing process development. An important assumption that was made for the following analysis was that powder did not influence process time through rake time or process temperature due to sintering kinetics and packing density (this assumption is known to not necessarily be true, but the analysis must be simplified). Further work should be done to adequately understand the effect of powder quality on production time. Such work should simplify analyses by using consistent layer thickness, geometry, and build parameters.

V.2.4 Impact of Software Version

The EBM Control software version was updated from 3.2 to 4.1 during the course of this work. This update was a major change that added a number of features. The most significant feature was the addition of the ability to rotate raster angle through a full 360 degrees. Additionally, a feature was added to melt multiple parts at the same time (separate feature from not engaging *Melt Modelwise*). The combination of these features makes the application of equations to model the current and speed more difficult in the 4.1 software. With the new software, the rotation angle must be known for each layer in order to calculate layer time.

V.2.5 Effect of Rotation on Layer Time

The layer times measurements for the first X-Y Tensile build using version 4.1 are compared to times from a comparable version 3.2 build in Figure 83. This initial application of the new software version actually led to longer build times; the average layer time jumped to 86.1 seconds (Build 4) from 66.7 seconds (Build 3) for the X-Y Tensile build. By adjusting process

parameters, the average layer time was able to reach 62.6 seconds (Build 7) even using a larger layer thickness of 75um. It is also notable that there was increased variation in the layer time with version 4.1 software. The builds selected (3,4, and 7) were all produced on the same hardware (A2) and were chosen to compare different sets of processing conditions during the development cycle (90 degree rotation, full 360 degree rotation). This is a predictable effect of rotation; as the melt pattern rotates, the beam speed changes with line scan length. The rotation pattern leads to periodicity in layer time, since the melt geometry is constant with height for the X-Y Tensile part. For 3.2 builds, this is repetitive of every other layer having nearly the same layer time (except for anomalies) because the rotation angle is always 90 degrees. For 4.1 builds, the periodic structure includes the number of layers until the melt angle returns to its initial value. The default rotation angle is 18 degrees, which creates symmetry every 10 layers (this is seen in Figure 83).

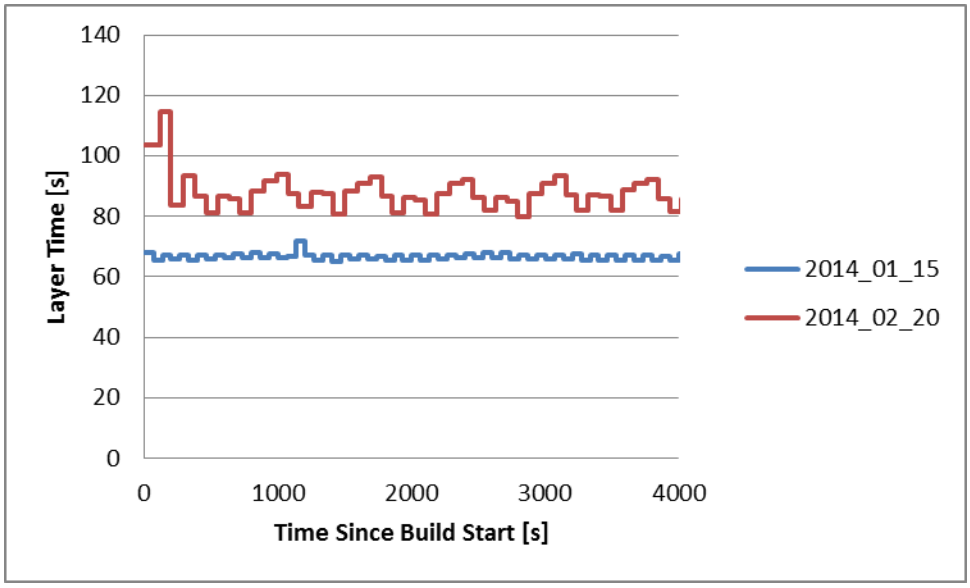

Figure 83. Comparison of the layer time between EBM Control 3.2 (Build 3, 2014_01_15) and 4.1 (Build 4, 2014_02_20) shows increased variance in layer time with version 4.1.

V.2.6 Impact of Process Steps on Layer Time

To better understand the differences in layer time, the current profile for a representative layer from each build should be examined. Considering Builds 3, 4, and 7 again, the current for the first layer has been plotted in Figure 84. The layer time for each layer can be broken down according to Table 19. The data shows that the raking and preheating times are relatively consistent between builds. The variation in process time arises from significant differences during melting and postheating (*Postheat 2*). Only Build 3 used *Postheat 1* (optional postheat after contours, but before melt), but the time contribution due to this heating is not significant. The most significant difference was that the melt current used during melting steps remained higher during Build 7. Build 4 used a low current (~10mA) for approximately half of the melting time, compared to the higher current (15-20mA) used during Build 7. Given the same melt area of each build for each layer, lower currents correspond to lower speeds. This made the melting time longer, when lower currents were used. This lowered the average current of the build, which was then accounted for by increasing *Postheat 2* time; the amount of postheating time was increased to compensate for less energy input during melting. The overall impact was that slower melt speeds with less current increased both the melting time and the time needed to postheat the build.

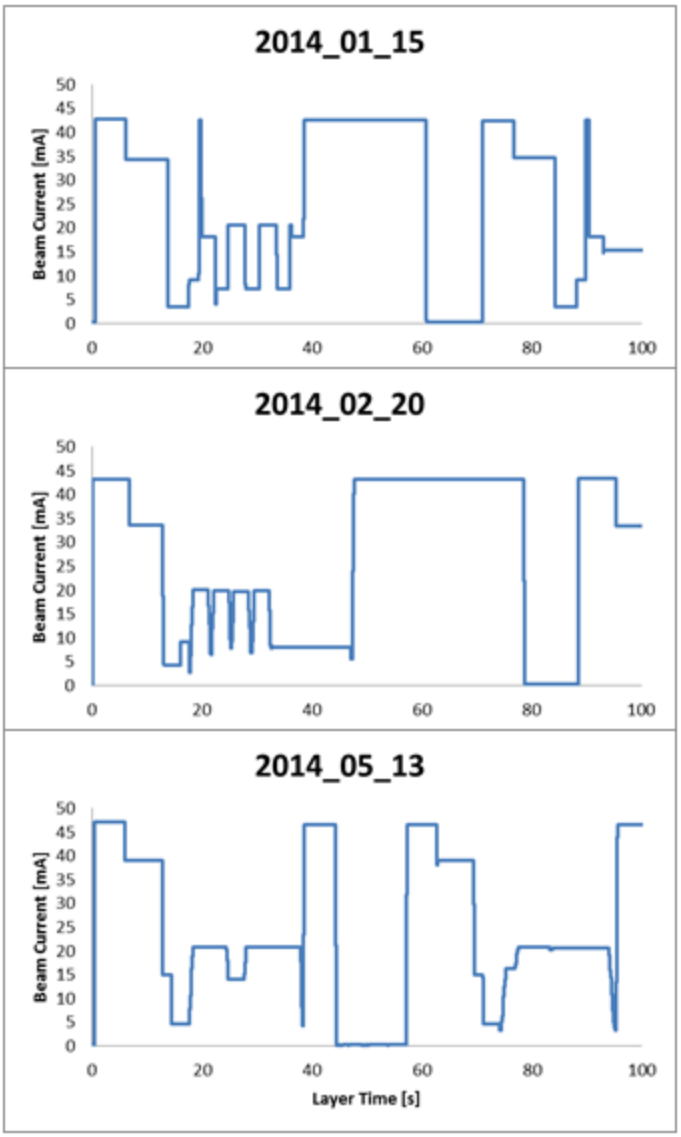

Figure 84. Beam current profiles starting with the first layer of each build for (Top) Build 3, (Center) Build 4, and (Bottom) Build 7.

Table 19. Breakdown of layer time for the first layer of select builds. Data given in both time and percentage of total layer time.

Build #	Avg. Layer Time [s]	Layer Time [s]	Raking Time [s]	Preheat Time [s]	Melt + Contours + Postheat 1 Time [s]	Postheat 2 Time [s]
3	66.7	71.1	10.3	13.8	24.8	22.2
4	86.1	88.6	9.8	12.9	34.7	31.2
7	62.6	57.2	12.7	12.8	25.8	5.9
Build #	Avg. Layer Time	Layer Time [%]	Raking [%]	Preheat [%]	Melt + Contours + Postheat 1 [%]	Postheat 2 [%]
3	-	100	14	19	35	31
4	-	100	11	15	39	35
7	-	100	22	22	45	10

V.2.7 Impact of Process Parameters on Layer Time

It is important to consider the differences in process parameters that contribute to the observed variation in layer time. Table 20 shows the process parameters that were changed between builds 3, 4, and 7. Though the preheat current and times remained relatively consistent during Builds 3, 4, and 7, the values of average current and minimum/maximum current must still be considered for the impact on postheat time.

Table 20. Changes in process parameters between Builds 3, 4, and 7.

Parameter	Units	Build 3	Build 4	Build 7
Max Current, Preheat 1	mA	27.5	27.5	31
Average Current, Preheat 1	mA	21	22	17
Min Current, Preheat 1	mA	27.5	27.5	31
Max Current, Preheat 2	mA	30	28	38
Average Current, Preheat 2	mA	18	22	16
Min Current, Preheat 2	mA	30	28	38
Focus Offset, Preheating	mA	150	150	325
Max Heating Time, Postheat 1	s	30	0	0
Max Heating Time, Postheat 2	s	25	0	0
Focus Offset, Melt	mA	3	20	15
Max Current, Melt	mA	21	21	22
Speed Function, Melt		98	55	50
Min Current, Current Comp.	mA	4.5	3.5	3.5
Scan Length Ref, Current Comp.	mm	55	45	45

The first notable difference in parameters is that the *Speed Function* is the lowest for Build 7; this means that for a given current, the beam will be traveling slowest in Build 7 during the melt. This results in an increased amount of applied energy during melting and can reduce the amount of postheat time needed. Build 7 also has the lowest preheat average current, which is used to determine the energy balance for postheating. The lower average current has the effect of increasing *Postheat 2* time (though this is not comparatively observed, as other parameters have competing impact). The *Preheat 1* and *Preheat 2* currents are also higher for Build 7, which puts more energy in during preheating and also sets a higher current for postheating; the higher current both increases energy input during preheat and reduces the time needed to balance energy during postheating (due to a higher current). It is worth noting that although the maximum *Postheat 2* time was zeroed for both Build 4 and Build 7, neither experienced any reduction in postheat time. This may be attributable to a software feature, bug, or competing parameters not examined in the analysis herein. A decrease in the reference line length for current compensation (from 55 to 45mm) means that for an input current, a higher value of current is output to use during

melting. This does not seem to have as much impact as other parameters, as there is not any notable increase in current from Build 3 to Build 4.

V.2.8 Impact of Hardware

Various hardware models (A2, S12, Q10) were used to produce the builds analyzed herein, so the differences between machines should be considered. Unfortunately, due to other changing conditions and the materials processed, no direct comparison between the A2 and Q10 is possible from this study. For 50um layer thickness, IN718 builds (X-Y Tensile Geometry) were both processed using 4.1 software on the A2 and S12 models. The A2 build (Build 4) had an average layer time of 86.1 seconds and a total process time of 9.60 hours. The S12 build (Build 8) had an average layer time of 105.9 seconds and a total process time of 12.35 hours. From this data, the A2 was 22% faster than the S12. To understand why, it is useful to look at the beam current profile for a representative layer from each case.

Table 21. Differences in process parameters between Build 4 and Build 8.

Parameter	Units	Build 4	Build 8
Max Current Preheat 2	mA	28	30
Min Current, Preheat 2	mA	28	30
Focus Offset, Preheat	mA	150	275
Angle Iterations, Melt		1	6
Region Rotation Enabled, Melt		False	True

There were no changes to the basic melt process parameters, but changes in the preheating process parameters and the melt rotation parameters are summarized in Table 21. Increasing the Preheat 2 current should put more energy in and reduce build time in Build 8,

but this effect is not observed. More important is the effect of rotation. The *Angle Iterations* number is the number of angles that the EBM Control software tests to find an optimal melt angle. The *Region Rotation* is an algorithm that splits up pieces of a layer and melts at various angles to achieve a desired "optimal" line length (this was set with a *Max Scan Length* of 90mm for Build 8). Layer time was still observed to be periodic in Build 8, so the effect of angle iteration is considered to be minimal. The *Region Rotation* feature, however, was determined to optimize based on a constant line scan length (90mm) that was smaller than could normally be melted. This means that regions were broken up to reduce the line scan length of the melt areas (no longer melted in a continuous snaking pattern, but a broken snaking pattern). Shorter line scans lengths mean lower current and lower speed. This has the effect of slowing down the build process tremendously. It can be seen (Figure 85) that the melt profile for Build 8 is relatively constant; optimizing for a single line scan length means that current will be relatively constant (exactly constant if only one length is melted). Since this parameter had significant effect on processing, the build time of the S12 cannot be compared to that of the A2. Though the implementation of the region rotation parameter was shown to cause an increase in time, work should be possible to make this feature save time; if a build is optimized to melt with the longest line scan lengths possible, build time will be reduced to the lowest possible time within a parameter set.

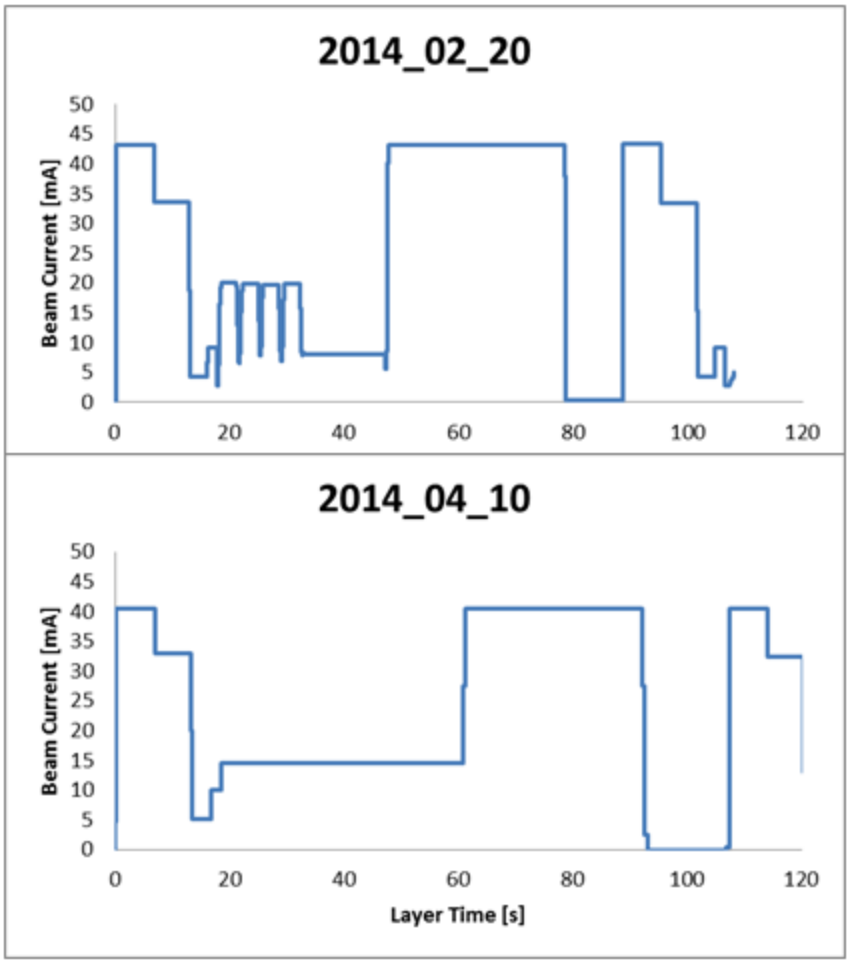

Figure 85. Beam current profiles for the first layer of (Top) Build 4 and (Bottom) Build 8.

V.2.9 IN718 vs. Ti-6Al-4V

For IN718, EBM processing time takes longer (14.0-36.5 cc/hr) than for Ti-6Al-4V (25.1-39.2 cc/hr) when considering volumetric deposition rate (see Table 18). This difference disappears when considering the mass deposition rate for IN718 (0.115-0.299 kg/hr) compared to Ti-6Al-4V (0.111-0.220 kg/hr); the mass deposition rate for both metals is roughly equivalent. Considering basic theory, equivalent amounts of mass require the same

amount of energy to melt. Material properties effect both the phase change (specific heat) and heat transfer conditions (thermal conductivity, emissivity) that modify this basic theory.

To better understand the differences in IN718 and Ti-6Al-4V EBM processing, the substrate temperatures of two standard builds can be compared (Figure 86). The most notable difference is that the process hold temperature is much higher for IN718 (900-1000°C) than for Ti-6Al-4V (~500°C). The difference in required operator temperature cannot be explained by melting temperature (IN718 has a lower melting temperature than Ti-6Al-4V). Sintering kinetics are not well characterized and quantified for the powders used. Sintering kinetics are expected to vary significantly with powder morphology as well. However, Plasma Atomized (PA) powders have been used for both IN718 and Ti-6Al-4V without noticeable difference on process temperature. Thermal conductivity is higher for IN718 (11 W/m*K) than for Ti-6Al-4V (6.7 W/m*K). This is plausible explanation for increased heat loss during IN718, which would imply that more energy would need to be input to account for this extra loss. As more energy is applied to the system, the base plate and system hardware heat up more in response to the improved conduction pathway. Powder thermal conductivities are known to be impacted by packing densities, but the impact on EBM heat transfer is not known. High temperature emissivity losses should also be considered.

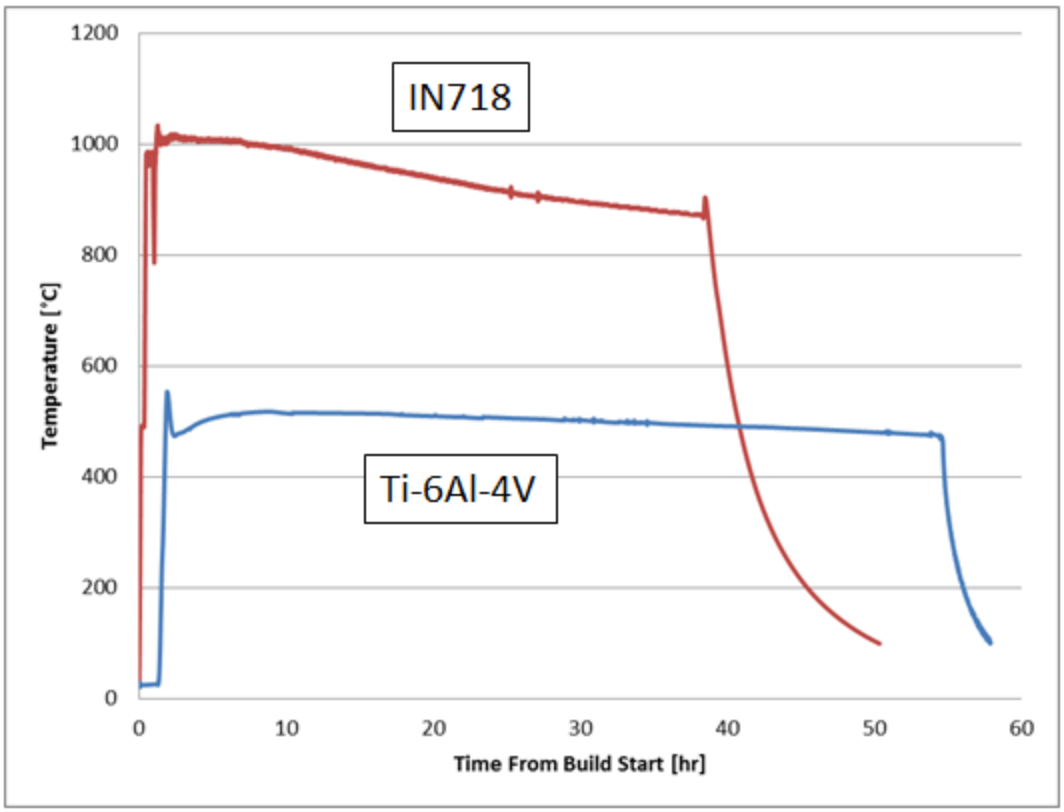

Figure 86. Temperature profiles comparing standard build processes with comparable geometries (Verification Build) for IN718 (Build 6) and Ti-6Al-4V (Build 10).

Process time has been reduced dramatically in IN718 by using increased layer thickness (75um). It can be concluded that for a set layer thickness, Ti-6Al-4V processing is faster. However, IN718 can be faster (even volumetrically) if different layer thicknesses and parameters are used. For those using EBM for near net parts that require surface finishing (e.g. aerospace parts), increasing layer thickness in Ti-6Al-4V production should be explored to speed up process time. This may not be an option for parts that require a certain as-fabricated surface finish (e.g. biomedical implants) or tight internal passageways (e.g. robotics).

V.2.10 Layer Thickness Optimization

While melting time is essentially unchanged, the amount of preheat and postheat time for IN718 is increased. Since the limit of the F125 tungsten filaments is ~100 hours, the build volume would be limited by filament life instead of actual capacity; at an average layer time of 67 seconds and layer height of 50um, the maximum height would be 268.65mm instead of the physical limit of 350mm (for an A2). In order to overcome this limitation, larger layer thicknesses were explored.

With the lowest average layer time achieved of 62.6 seconds (Build 7), a build height of 431.31mm can be melted under the 100 hour filament lifetime constraint using 75um layer thickness. Depending on part geometry, this speed will decrease as the cross sectional area of each slice is increased. Despite this, the reduction in build time afforded by increasing layer thickness should make printing the maximum build envelope possible.

As layer thickness is increased, it is expected that more energy should be input to melt more volume of material. Additionally, a larger layer thickness may be expected to increase electron backscatter and energy loss due to beam-powder interactions. To compensate, it might be hypothesized that preheat and postheat times would need to be increased to compensate for the added requirement of heating more thermal mass. As evidenced in Figure 84, this is not necessarily the case; other factors seem to be more important in determining the amount of process energy required. While there are variations in process parameters between cases, comparison is based on the assumption that each case was run with a set of “good” parameters that sought to minimize spatter ejection and ultimately produced dense parts.

For example, Build 7 used a layer thickness of 75um but also had the lowest average layer time in IN718 (even faster per layer than 50um layer builds). As discussed previously, changes to process parameters resulted in decreased melt time and decreased postheating

time; the melt current was higher, which both increased the beam speed and reduced the time of the postheat. The resulting metal was geometrically accurate and qualitatively comparable.

There appears to be a limit to how large a layer thickness can be used; the 100um layer thickness resulted in an average layer time of 91.0 seconds, which is much higher than the times for other thickness values. As layer thickness increases, there is more powder that needs to be sintered prior to melting (to prevent smoking and reduce spatter ejection). It is possible that this limit was reached at 100um (further builds would only be more difficult to process), but further experiments would be needed to confirm. The loss of geometric resolution also increases with increasing layer thickness, and a balance with process time must be made.

V.3 Summary of EBM Processing

The EBM process has been demonstrated to be complex and the details of process parameters were reviewed and shown to have a significant impact on applied energy and process time. The relationship between speed and current was shown to be immensely important, with a linear relationship being best for eliminating defects (swelling in the example shown in Figure 78). Process time can be reduced by using larger layer thickness and altering process parameters. Specifically, rotation, region rotation, and maximum melt current may all affect the melt current based on the line scan length. Optimizing line scan length to achieve melting a maximum values should reduce process time (the converse was demonstrated here). Overall, better modeling, visualization, and pre-build analysis can lead to reduction of defects and decreasing process time.

CHAPTER VI

AS-FABRICATED MICROSTRUCTURE AND *IN SITU* HEAT TREATMENT

Having previously reviewed both IN718 and EBM, the microstructure of IN718 samples fabricated using EBM can now be presented. Specific attention is given to the effect of process temperature and process time on phase formation and evolution; the amount of *in situ* aging may result in different as-fabricated microstructures. The as-solidified structure is identified, and the effect of process temperature on homogenization of solidification phases is discussed. By applying process knowledge, a controlled *in situ* heat treatment is then demonstrated. This controlled treatment was designed to produce peak-aged IN718 straight from the machine.

VI.1 Characterization Methods

Various methods were used to characterize the EBM IN718 microstructures herein. Hardness indentations were performed using a LECO LM Series micro-indenter. A JEOL-6500 scanning electron microscope (SEM) was used to perform electron backscatter diffraction (EBSD) at a total sample tilt of 70 degrees. A Hitachi-4800S SEM was used for SEM analysis of etched samples, un-etched samples, and powders. Various Light Optical Microscopes (LOM) were used, including a Zeiss Axio Scope.

The EBM fabricated IN718 samples were cold mounted in epoxy and ground using steps on piano disks, followed by polishing steps from 6um to 3um to 1um diamond suspension. Etching was performed using a 30 ml Acetic Acid, 30 ml Hydrochloric Acid (HCL), 30 ml Nitric Acid (HNO3) mix. Submersion for 30-90 seconds of a freshly polished surface was found to reveal grain boundaries and precipitates in as-fabricated, HIP, and heat treated material; the etchant preferentially removes the nickel matrix. Swabbing was also used as an etching

technique, but resulted in dark residue remaining and some carbide pullout. For this reason, submersion was selected as the preferred technique. Electro-etching techniques were tried, but abandoned in favor of the ease of submersion etching. The 1um diamond polish was followed by colloidal silica polishing prior to EBSD.

VI.2 As-Fabricated Microstructures

The microstructure of IN718 processed using EBM has been reported in both under-aged [20, 104, 287] and overaged conditions.[86, 102] The underaged material may have some δ-phase present, but may not meet the tensile properties of peak-aged material. Overaged material includes large quantities of intragranular δ-phase. The impact of the differences in as-fabricated phase formation on post-processing will be explored later in §VII.2 chapter. This chapter focuses on variations in phase formation that occur during EBM processing. The hold temperature and hold time were observed to significantly impact the final microstructure.

The increased formation of δ-phase due to stress in IN718 could contribute to the formation of intragranular δ-needles in EBM IN718. Computational analysis of the stress formation during EBM of IN718 has shown that thermal stresses evolve during various stages of processing. [64] Such thermal stresses due to large thermal gradients could very well impact phase formation. For the analysis presented herein, it is assumed that any stress assisted phase formation contributed uniformly in all of the as-fabricated samples that were analyzed.

VI.2.1 Solidification Structure

The solidification structure of EBM IN718 has not been previously reported in the current literature, but it is important to the subsequent solid state phase transformations that occur. The as-solidified structure of EBM material is difficult to examine, as the material sits

at an elevated hold temperature for multiple hours as a build processes. However, material very close to the top of a build will experience less hold time and offers insight into the solidification structure of IN718.

Solidification determines the initial grain structure and phase distribution of an alloy. Compositional segregation during solidification is especially important in nickel-based superalloys. Rapid solidification occurs during EBM processing, and the effects of segregation in IN718 are not well known.

The solidification grain structure requires conductive epoxy mounts or elimination of epoxy in order to perform EBSD at the edge of the sample. For this reason, EBSD of the top surface was not measured.

SEM and LOM images of the XY plane (Figure 87) taken near the last-fabricated portion (top) of a sample (an X-Y Tensile build, as described in a previous chapter) show a unique phase structure that is not observed in the lower portions (first-fabricated) of the material. This top surface region has the lowest hold time of the build. Paired with a fast cool down (helium injection), this is closest microstructure to as-solidified EBM IN718 that was observed in the work herein. From the XZ plane, there are distinct variations in microstructure at 5-10um from the surface and again at 30-35um from the surface (Figure 88). The region analyzed in Figure 87 is likely from the second region, though it is not known how much material was removed during metallography. If it is from the second region, then the top region has yet to be observed or characterized. In this case, the first region may have segregated Nb prior to formation of phase clusters. After a certain vertical height, the third region resembles the commonly analyzed bulk material (discussed later in §VI.2.3).

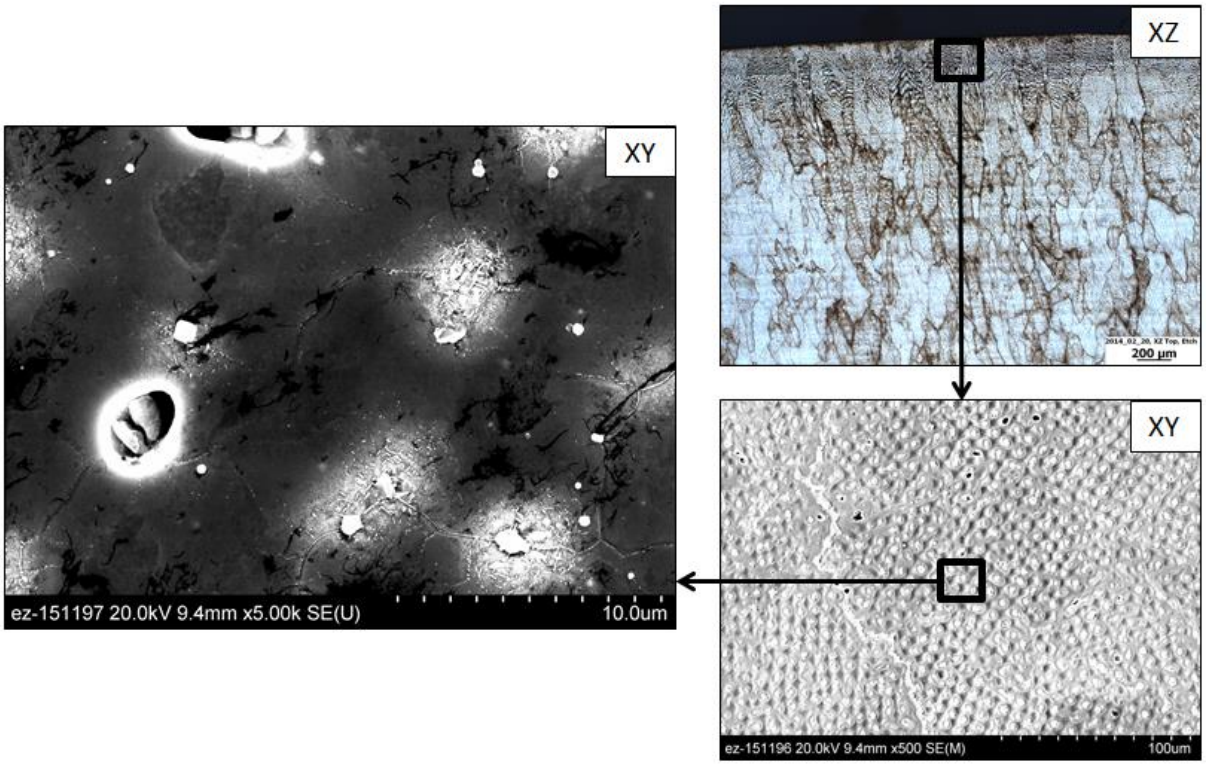

Figure 87. (Left) SEM showing clusters of precipitate phase in interdendritic regions that (Bottom Right) are characteristic of the material as observed in a larger scale SEM image. (Top Right) This microstructure occurs near of the build (XZ shown using LOM).

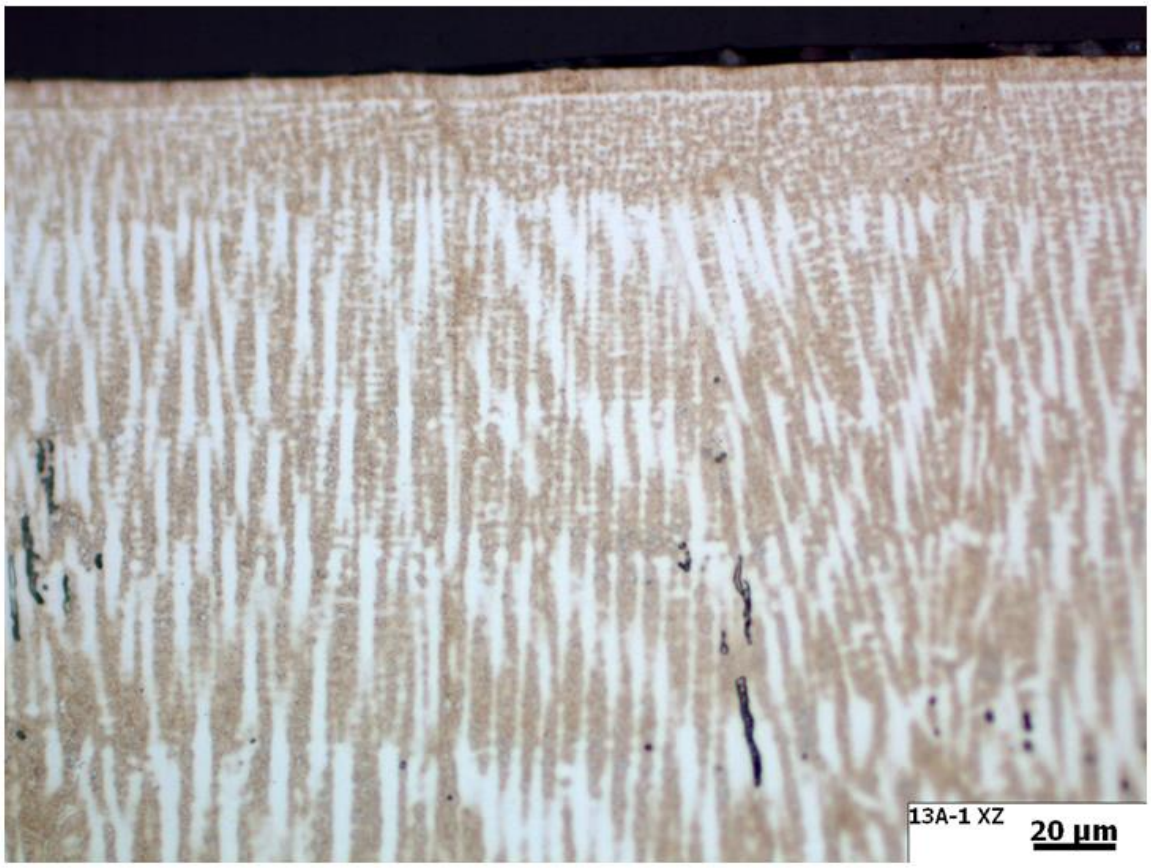

Figure 88. LOM near the top surface of EBM IN718 shows two distinct region transitions: 5-10um from the surface and 30-35um from the surface.

Given the tendency of Nb to segregate in IN718 castings, this structure is indicative of Nb segregation to interdendritic regions. The clusters show a regular pattern with a spacing of 5-10um, which could be considered the primary dendrite arm spacing (PDAS). The presence or absence of secondary dendrite arms was not confirmed. If secondary dendrite arms are not present, the argument for solidification as a cellular process may be made. Either way, the segregation of Nb is clear. The clusters of Nb-rich phases have morphology that suggests clusters of NbC, γ'', and/or δ-phase. Higher resolution SEM images of the precipitate clusters are shown in Figure 89. The irregular dark regions are artifacts of the

swab technique used during etching. In some interdendritic regions, voids are formed. These voids appear circular in the XY plane, but are the likely explanation for solidification shrinkage porosity seen in bulk EBM IN718. [104] In the XZ plane, shrinkage pores are contrasted to gas pores incorporate from GA feedstock powder in Figure 90.

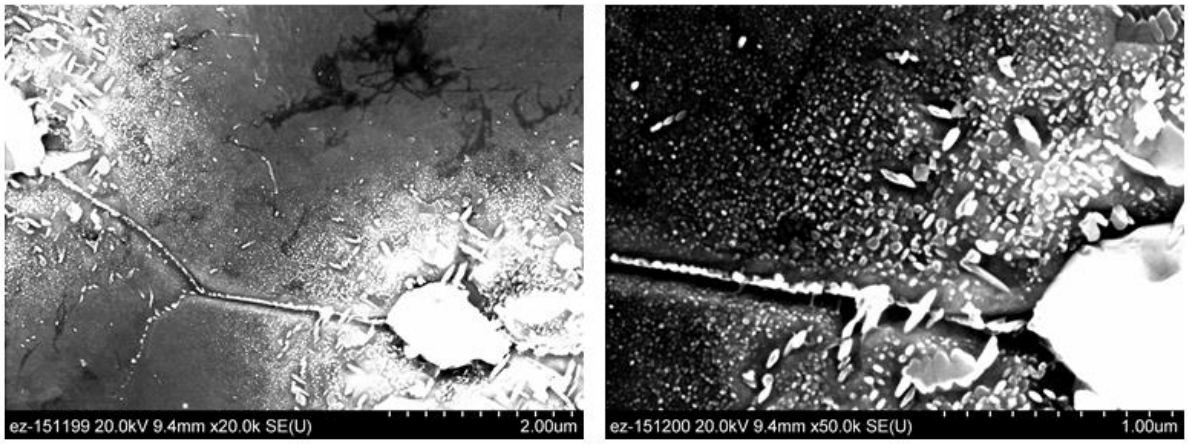

Figure 89. Higher resolution SEM of precipitate clusters near top surface in the XY plane (perpendicular to build direction).

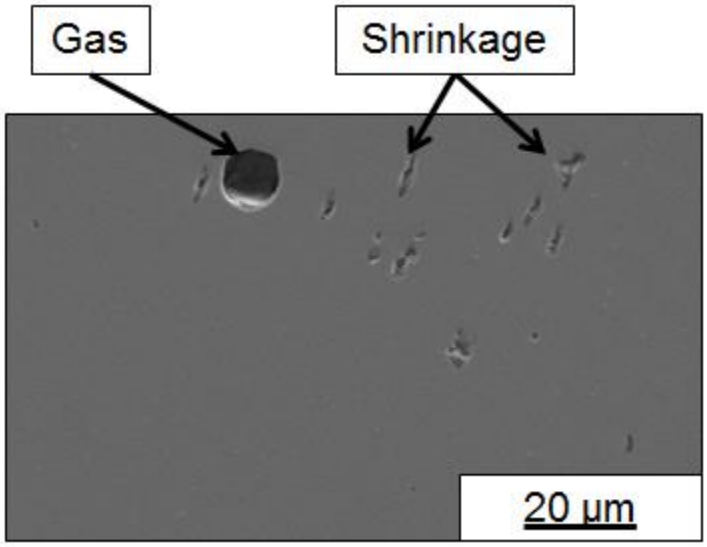

Figure 90. SEM of un-etched EBM IN718 in the XZ plane (parallel to build direction) showing the difference between spherical, gas pores and shrinkage porosity from solidification.

In some samples, shrinkage porosity is heterogeneous and can be found in clusters. In one of these cases, shrinkage pores in the XY plane near the top surface of the build were found to align with line scan angle (Figure 91). The spacing of these pores is roughly 250um apart, which is double the value of the line offset used in the process parameters (0.125mm). The line offset is the distance between line scans. This means that, if shrinkage pores align in the center of a melt pool (the last region to solidify), the pores are only present in every other pass. The turning point function presents the most likely explanation; the pores exist in regions 1700-1800um from the edge (as measured along the line scan angle). This is within the range that the turning point function effects beam speed. The turning point function increases the speed of the beam coming out of edges, which could result in melt pool instabilities or undesirable speed-power combinations in those beam passes. Since the large amount of pores found in this region is not characteristic of the bulk or of edge regions (Figure 92), it can be assumed that some unique combination of speed and power based on line scan length and turning point function led to the defects. From Figure 92, it is observed that solidification pores also are present in the spot melted contour regions closest to the part edge. These results do offer experimental evidence that the impact of process parameters is critically important to solidification and that the alignment of this type of pore is indeed related to solidification. These pores are typical features, though usually in very small, localized quantities.

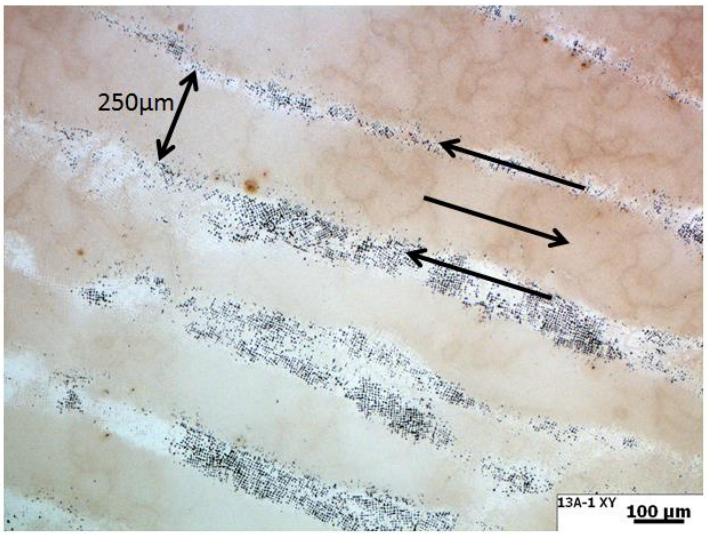

Figure 91. Solidification shrinkage pores are space ~250um apart and were found to correspond to the angle of beam scanning. LOM near the top surface of a PREP, 50um, slow cool build in the XY plane.

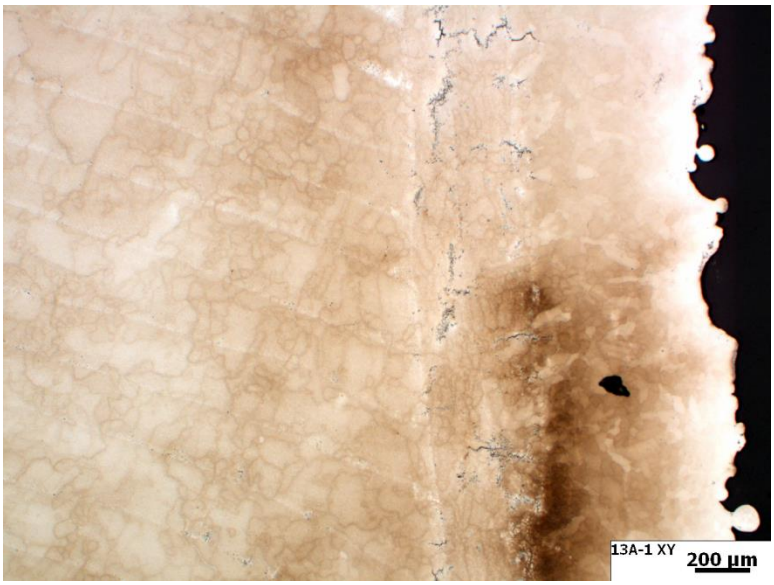

Figure 92. Characteristic LOM near an edge in the XY plane near the top surface of a PREP, 50um, slow cool build in the XY plane.

VI.2.2 Grain Structure

The grain structure of EBM IN718 has been widely reported to exist as highly-oriented, columnar grains. [86, 102, 104] This grain structure is the result of remelting, epitaxy, and melt pool solidification kinetics. The same grain structure has been confirmed in this work to be highly oriented with (001) texture in the build direction (Figure 93). The columnar grain structure can also be seen in the EBSD image of the XZ plane. Each grain contains a number of columnar dendrites or cells, as discussed previously. Identification of dendritic boundaries versus grain boundaries in SEM (EBSD represents dendrites with the same orientation as one grain) is important when discussing the bulk microstructure.

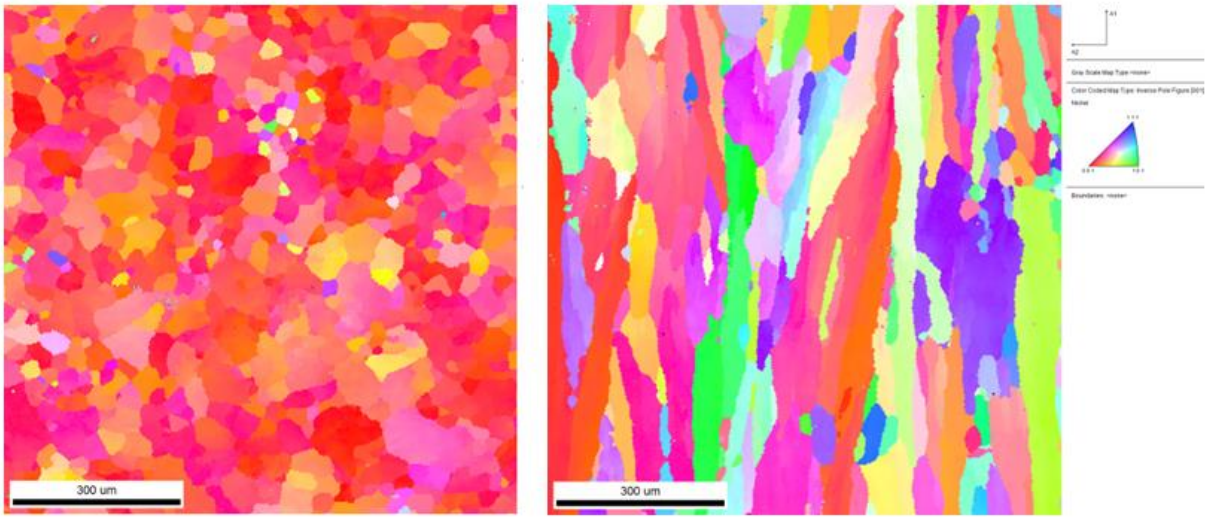

Figure 93. Typical grain orientation structure of IN718 using EBSD for (Left) the XY plane and (Right) the XZ plane for a sample prepared from the Verification Build geometry (taken from the bottom of a verification build cylinder as reported in §V.2.2).

VI.2.3 Normal *In Situ* Aging & Bulk Phase Structure

Based on bulk EBM IN718 structures, some features from solidification survive. Shrinkage pores are noted along dendritic columns in the bulk. While phase clusters mostly disappear, NbC remains ordered in columns parallel to the build direction. This effect of columnar phase architectures in bulk material has been reported before in EBM IN625. [100] Another common feature in bulk EBM IN718 is precipitate "networks" as shown in Figure 94. These networks are distinctly different from matrix phases, and tend to connect NbC phases in a "wavy" path. A denuded zone also surrounds the precipitate networks. These networks are noted in the top surface, solidification structure as well (Figure 87). The exact formation kinetics are not known but appear to occur along dendrite boundaries. These structures persist throughout the bulk material with the presence of various sizes of precipitates depending on region.

The precipitate clusters appear to be non-equilibium phases, since extended holds during processing leads to dissolution of most of the cluster phases. This can be rationalized through the diffusion of segregated Nb from interdendritic regions back into dendritic regions. This is effectively *in situ* homogenization of the solidification structure. Carbides are not dissolved during processing (or even post-processing as seen in §VII.2.7), however, and remain aligned in columnar arrays associated with solidification (§VIII.4.2).

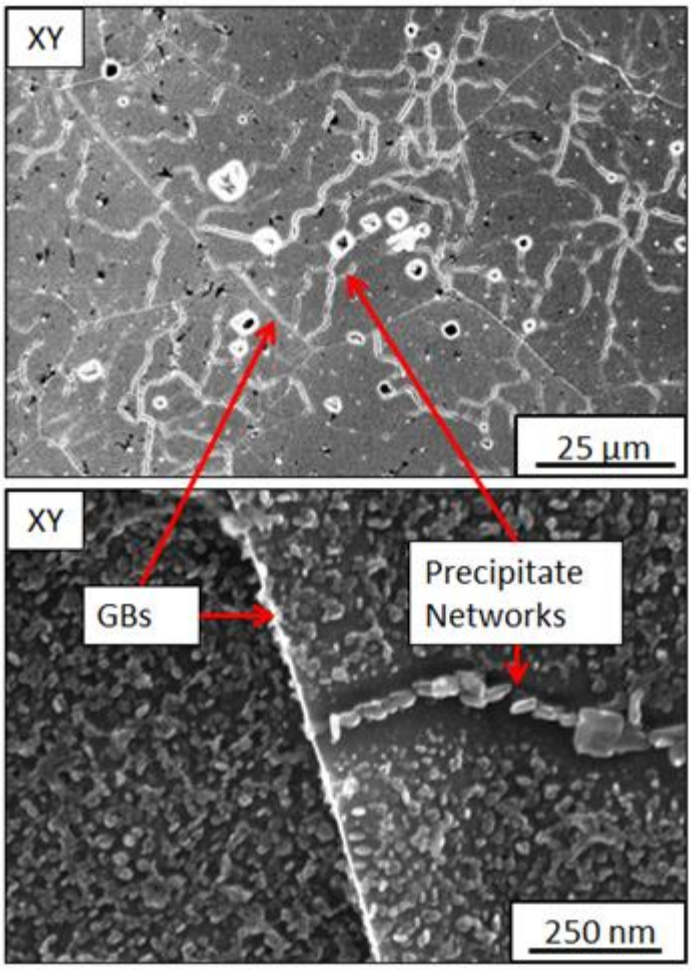

Figure 94. SEM showing precipitate networks and GBs in the XY plane.

Another distinctive feature of the microstructure of overaged samples is phase "banding" of δ-needles. This feature is shown in Figure 95. While the width of the bands does appear to vary, many of the observed bands are approximately 50um wide. This is the depth of the layer height for the build analyzed. There is likely segregation in the Z-direction (in addition to the segregation in the XY plane discussed earlier) during the solidification of an individual layer. This would result in the segregation of Nb to the top of a given melt pool (which covers more than one layer). A subsequent melt pool may then be somewhat enriched in

Nb, resulting in variable kinetics. One possible explanation for the banding is this solute "pushing". This pushing effect would appear limited to local areas and shows no signs of pushing solutes, like Nb, to the top of a part (no overabundance of Nb-rich phases at the top of a part). Another potential explanation for the banding is variation in process parameters for each layer. As identified in §V.2.5, samples (like this one) built with EBM Control 4.1 utilize a rotation pattern symmetric every 10 layers; the variation of speed and power for a given layer may account for local variations of segregation within a given layer. Regardless of the mechanism, banding does lead to regions of inhomogeneous precipitation of δ-needles in the sample shown (happens in the bottom, middle, and top). No pattern was identified in banding in the XY surface.

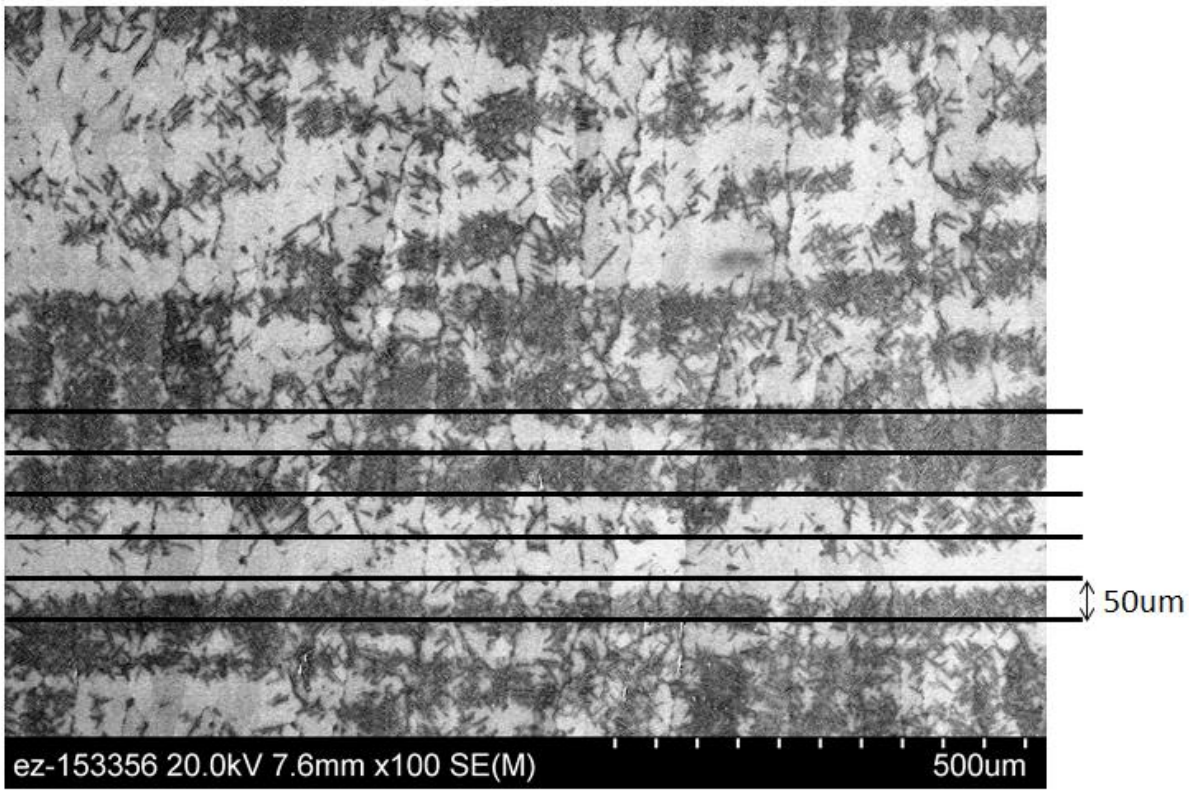

Figure 95. Phase banding of δ-needles in the XZ plane in the middle of the 50um, PREP, fast cool, vertical tensile sample (Build 6A from §VIII.4).

VI.2.4 Under- vs. Over-Aged

Depending on process hold time and temperature, the amount of *in situ* aging may lead to significant differences in the precipitate structure of as-fabricated material. Typical microstructures showing both presence and absence of intragranular δ-needles are shown in Figure 96. It is important to understand the differences in formation, as differences in as-fabricated microstructure have been noted to influence post-processing (see §VII.2). For the microstructures presented in Figure 96, the thermal profiles should be considered (Figure 97). Due to a complex thermal history (melt, remelt, and cool down included) and the addition of new material at each layer, neither TTT nor CCT diagrams can be perfectly applied within their assumptions (they may still be used for cool down or in certain cases for the melt region). For these reasons, the nominal phase formation ranges for γ'', γ', and δ-phase are plotted alongside the thermal histories to allow for better understanding of phase formation regions. It is noticeable that the overaged build holds for 8 hours longer and the process temperature falls to 935°C by the end of processing, whereas the under-aged build only falls to 978°C by the end of processing. Within this temperature range (~960°C), the likely pathway for δ-phase formation is precipitation directly from the supersaturated matrix. [179] So, the "overaged" samples are likely not actually experiencing a transition for $\gamma'' \rightarrow \delta$ but are directly precipitating the observed δ-needles. Though classifying the microstructure as "overaged" is, thus, somewhat misleading, the term is still used herein due to the classical association of this phase with overaging.

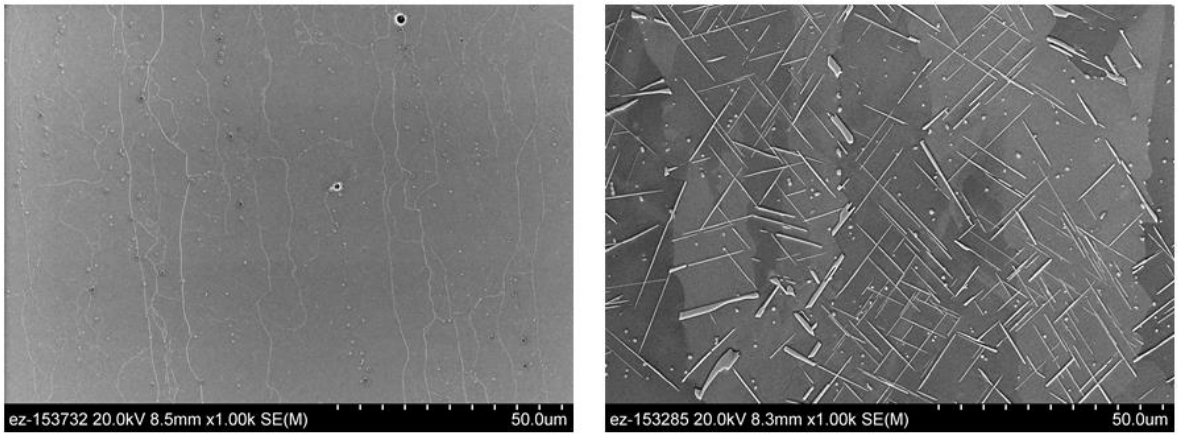

Figure 96. (Left) SEM of typical "under-aged" structure with columns of carbides and absence of δ-needles and (Right) SEM of typical "over-aged" structure showing significant quantities of intragranular δ-needles. (Left) From 50um, PREP, slow cool, XY Tensile build (Build 13A from §VIII.4) and (Right) from 50um, PREP, fast cool, vertical tensile samples (Build 6A from §VIII.4).

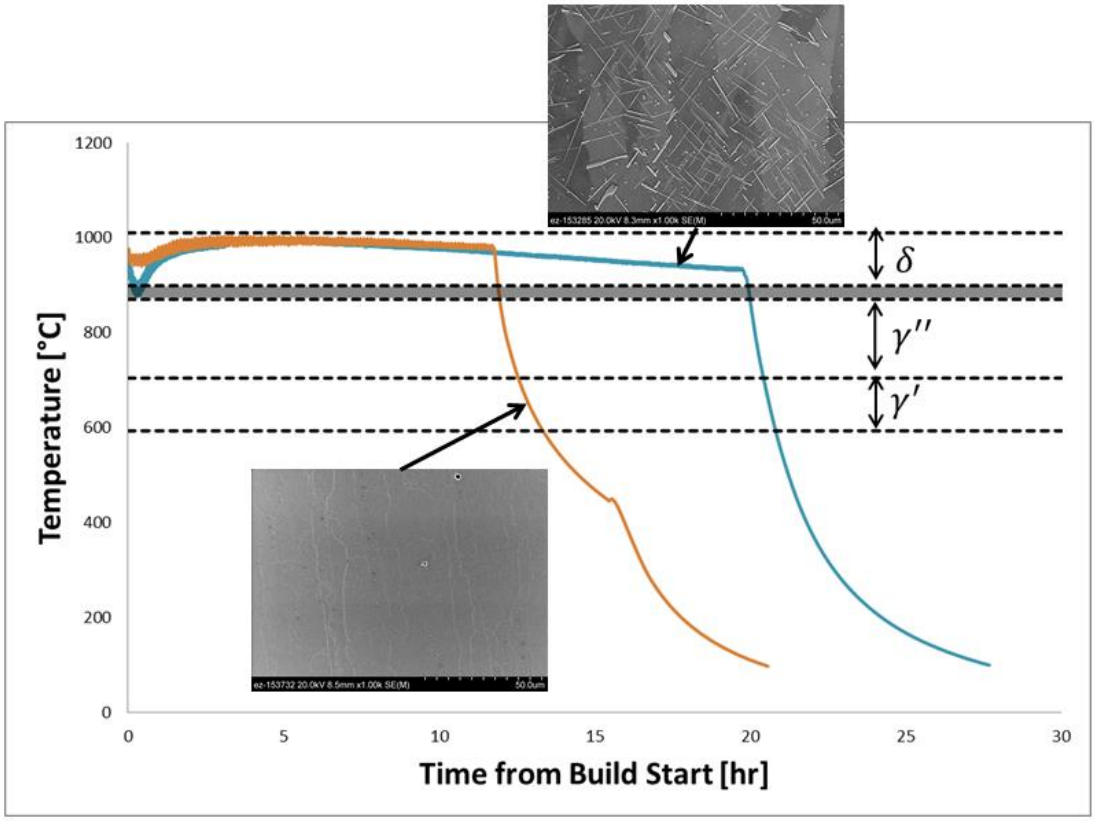

Figure 97. Thermal history of builds showing (Top) over-aged and (Bottom) under-aged microstructure.

VI.2.5 Axial Variation

In previous work the axial variation of the size of δ-needles in EBM IN718 has been noted (Figure 98). [86] In this build coarser needles were observed near the top of a part, whereas finer needles were observed near the bottom. This was not expected, as the bottom microstructure should have had more time at elevated temperature to allow for more coarsening. It was noted that the top of the part actually corresponded to the middle of the build (other, taller parts were also included in the batch). For this reason, it was noted that more information on build thermal history (including information about surface temperature) was needed to better understand the variation.

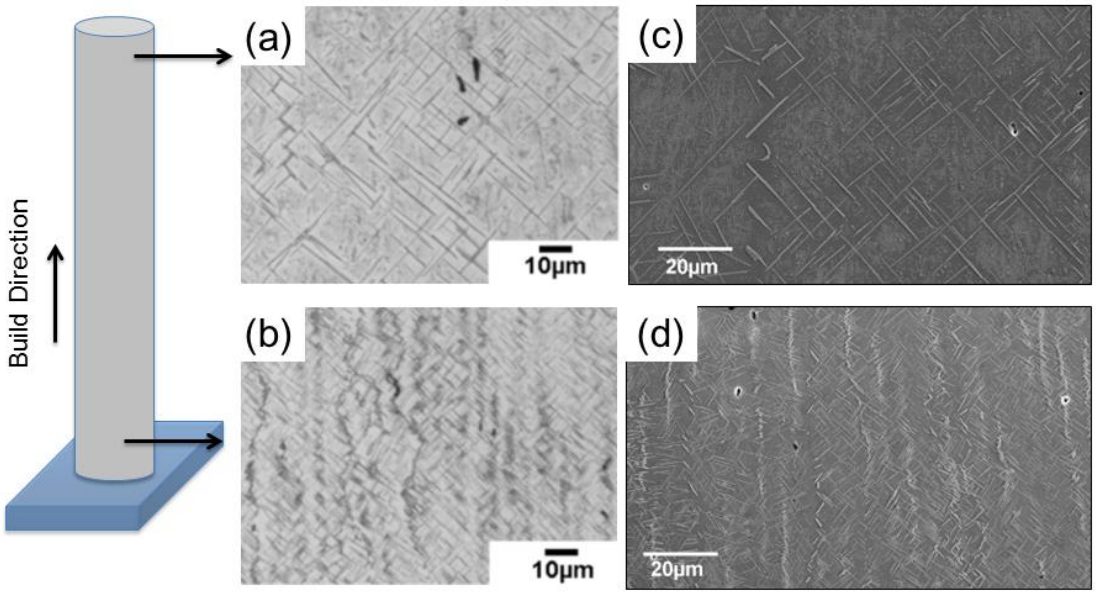

Figure 98. Axial variation of δ-phase showing (a) LOM and (c) SEM of etched microstructure in the XZ plane near the top of a part (but not the top of the build) and (b) LOM and (d) SEM of the XZ plane near the bottom of the build. [86]

Follow-up work was performed to characterize the axial variation of δ-needles in the overaged sample previously discussed (Figure 96, Figure 97). The top surface of this sample was not analyzed, as the build ultimately failed due to running out of powder. Samples near the top, however, were analyzed. The results of SEM analysis show that δ-needles were present in the top, middle, and bottom of the sample (Figure 99). The quantity of δ-needles in the top sample is noticeably less than the middle and bottom. This is expected, as the top spends less time in the δ-phase precipitation temperature range. Depending on processing conditions, the temperature range for the top, middle, and bottom of the build may also vary. It is noticeable in Figure 99(d) that the precipitate networks present in under-aged as-fabricated material are also present in samples with significant δ-needles. The regions near the δ-needles appear darker, as they are depleted of Nb and a noticeable denuding of precipitates. Visual identification of carbides becomes difficult in samples with δ-needles, as the tops of needles that correspond to a certain variant may be of similar size to carbide diameters.

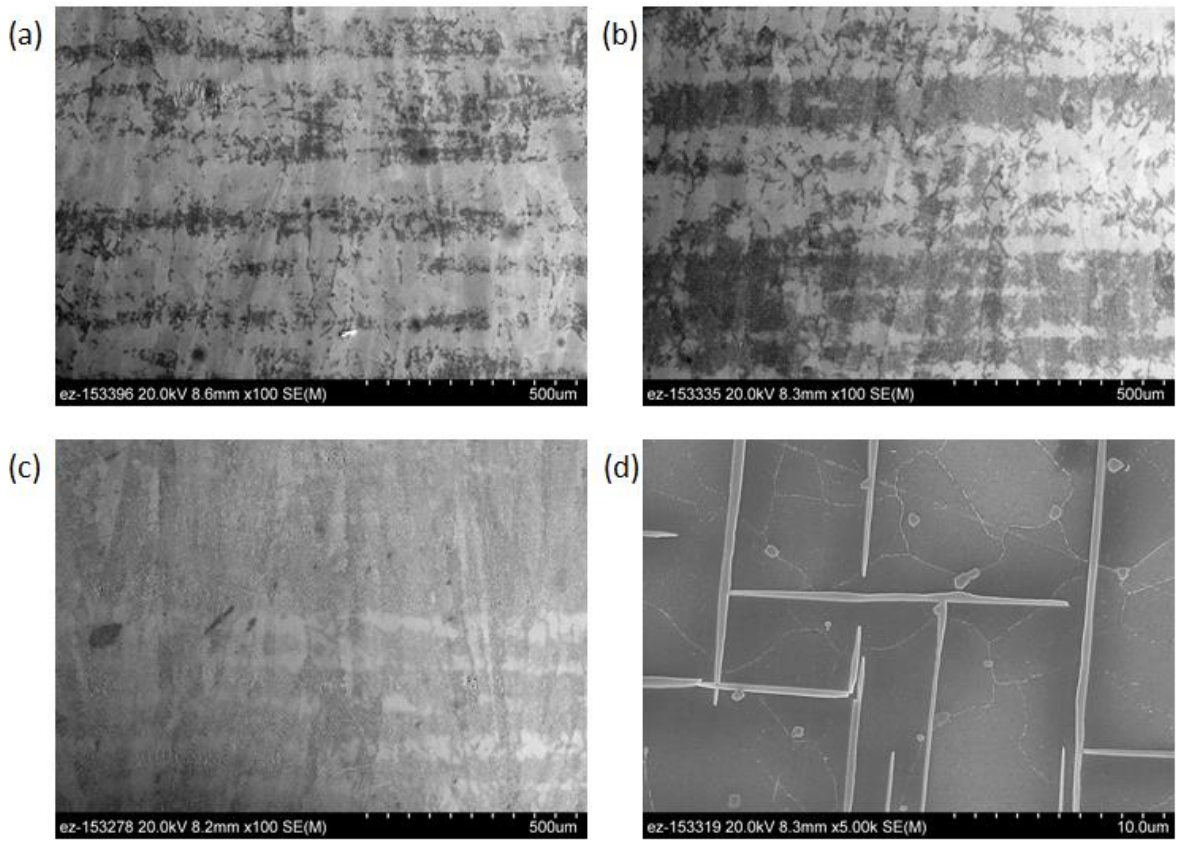

Figure 99. As-fabricated SEM of XZ planes in (a) top, (b) middle, and (c) bottom of the 50um, PREP, fast cool, vertical tensile sample (Build 6A from §VIII.4). The (d) XY plane near the bottom shows the δ-needle structure more clearly.

VI.2.6 TEM Characterization

Characterization of overaged EBM IN718 was done in previously-reported portions of this work (Figure 100). [86] This work identified the size and orientation of δ-phase, γ'', and γ' phases within the build. Some metastable "sandwich" structures of γ''/γ' were observed, where γ'' was present on the face of γ' cubes. The orientation of the build direction to grain orientation and preferred precipitate orientation still need to be noted. Additionally, TEM of a representative under-aged sample is needed to analyze the differences in phase

formation for that microstructure. Analysis of an under-aged sample should carefully analyze matrix phases, precipitate networks, and phase clusters where possible. More information about stacking faults and dislocations in the regions of δ-needles would also support efforts to better understand post-processing.

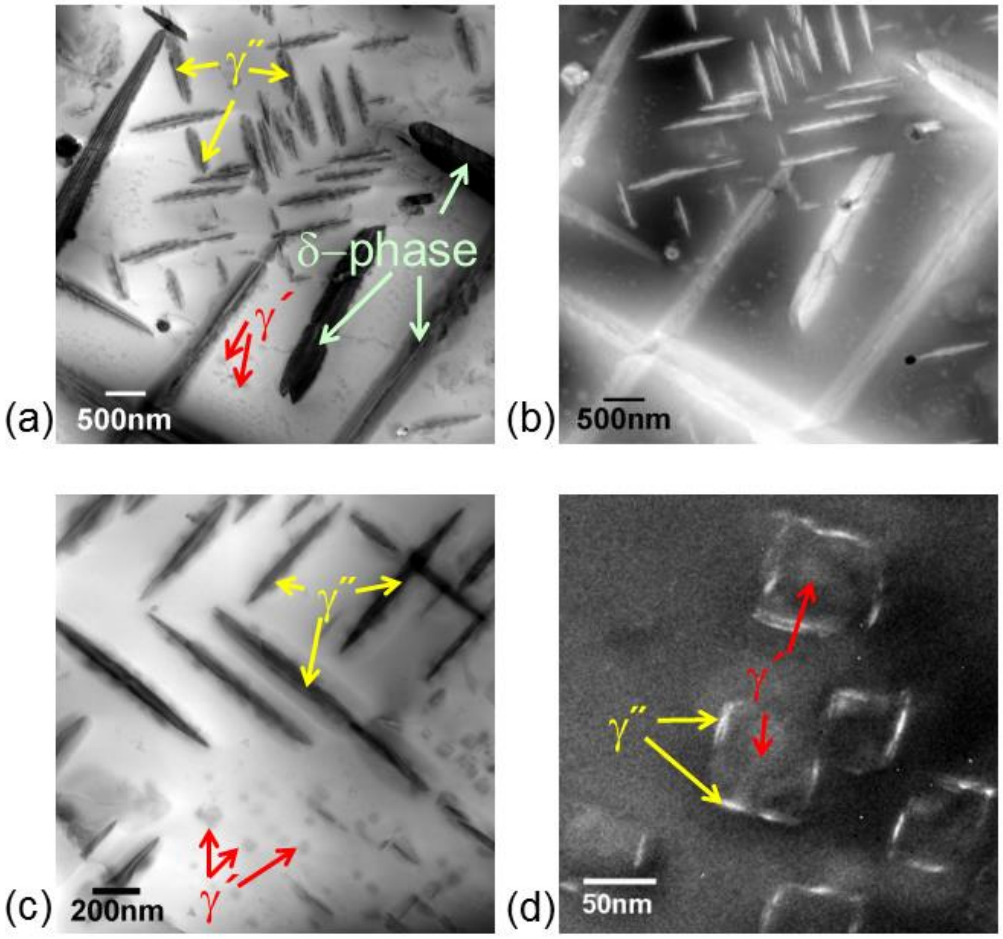

Figure 100. Analysis of as-fabricated phase structure of overaged EBM IN718 using (a) BF STEM, (b) high angle angular DF image (Z-contrast image), (c) higher magnification of BF STEM, and (d) DF image. [86]

VI.2.7 Comparison to Cast, Wrought, and Other AM Material

The as-fabricated microstructure of EBM IN718 is much different than cast or wrought material. Most metal AM processes have more in common with weld deposition than with traditional processing techniques due to the similarities in melting strategy. AM processes, like welding, cannot typically be hot or cold worked like wrought material, as the final geometric structure must be maintained and non-deformed. So, many grain refinement and processing techniques used in wrought processing are not applicable to AM material. However, thermal post-processing is commonly used in cast, wrought, weld, and AM material.

Oriented, columnar grains in EBM IN718 are more typical of directional solidified (DS) castings than of typical, equiaxed wrought IN718. This should result in anisotropic tensile properties in EBM IN718. Shrinkage porosity in equiaxed, cast IN718 has been observed to be highly irregular in shape and correspond to interdendritic regions. [288] Shrinkage porosity in EBM IN718 is more columnar in shape but still aligned with the growth of interdendritic regions.

The solidification structure of EBM IN718 is also unique, due to small melt pools and rapid solidification. AM processes in general are much different from casting in solidification phase precipitation due to rapid solidification, which can lead to non-equilibrium formations. An interesting feature of EBM IN718 is the lack of Laves phase. Laves phase has a tendency to form in interdendritic regions due to increased Nb concentration due to segregation in both cast IN718 [173] and in IN718 welds. [264] Work in LM has both reported [216] and not reported Laves formation. [29] The segregation of Nb during solidification was found to result in precipitation of Laves and carbides in interdendritic regions during powder-fed DED. [120] Subsequent re-heating was also noted to result in diffusion of Nb, resulting in increased precipitation of γ'' (Ni_3Nb) near interdendritic regions. In EBM, similar mechanisms are possible. In fact, the higher operating

temperature promotes Nb diffusion out of interdendritic regions, resulting in *in situ* homogenization. It is possible that Laves is either suppressed due to solidification kinetics or solutionized during the process hold. Based on SEM results of the "as-solidified" structure observed in the present study, there is no indication of Laves phase in the interdendritic solidifications regions. Follow-up compositional analysis using TEM techniques would provide more information on the impact of the diffusion of other elements (Fe, Mo, Ti) on phase formation in the as-solidified structure.

Precipitate networks (or "necklace" structures) have been identified along GBs and within grains in some early work in wrought IN718 [289], with the reason for formation suggested as related to NbC "film" formation followed by spheroidization during a 954°C solution treatment. These networks bear resemblance to those in the bulk of EBM IN718, though the pathway for Nb-rich network formation is likely different; EBM IN718 forms Nb-rich networks along interdendritic boundaries during or very near solidification, while Nb-rich regions have been related to prior GBs in cast IN718. [223] It is not clear what effect these networks may have on EBM IN718 mechanical properties, but work in cast IN718 suggests that the networks are preferred sites for δ-phase formation.

The formation of intragranular δ-needles can be especially pronounced in EBM IN718. While δ-needles can form in wrought or cast IN718, typical processing schedules avoid spending significant time in the high temperature precipitation range for formation of δ-phase from the supersaturated matrix (~960°C). Traditional processing uses a 980°C solution treatment, which does not appear to be long enough to cause intragranular δ-phase precipitation (but may form GB δ-phase). When δ-needles do form in traditional processing, they tend to form from overaging [195] or growth of GB δ-phase into the matrix. [240] This contrasts to formation in EBM IN718, which appears to be mostly through direct, high-temperature precipitation.

VI.3 Controlled *In Situ* Heat Treatment

In metal AM, the standard practice is to use some combination of thermal post-processing steps: stress relief, solutionizing, Hot-Isostatic Pressing (HIP), and aging before the deployment in service. [92] These steps are designed to relieve residual stress, reduce process-induced porosity, and produce the desired precipitate microstructure. Due to relatively low levels of residual stress [68] and porosity in EBM parts, it may be possible to eliminate the need for stress relief and HIP for EBM material. Nevertheless, post-processing methods including solution treatment and aging (STA) are required. This chapter demonstrates that STA may be performed *in situ*, producing parts with the desired microstructure directly from the machine.

At this point, previous work related to *in situ* heat treatment for EBM must be addressed. It is apparent that the process control proposed herein is entirely novel, with no previously published research on the topic. There is, however, a single patent that must be noted. In US 20130015609 A1, Landau proposes the use of *in situ* heat treatment during AM processing. [290] The patent claims address the use of a heat source during the melting process to produce a functionally graded microstructure. Neither the background nor the claims address the fact that this was essentially already being done in EBM; the EBM process essentially anneals or heat treats a material as it processes, with lower layers being treated for different times than higher layers. The patent also does not explore the implementation of *in situ* heat treatment at the end of the AM process (as presented herein) and does not address the scan strategy in which a heat source would be used (EBM software currently allows for planar, circular, or part areas to be used). The control of the

process step is the key novelty in the research presented herein, through use of an under-powered heat source to achieve a near-equilibrium temperature for a hold time.[2]

VI.3.1 Cool Down Rate

Mechanical testing on EBM processed IN718 has demonstrated the effects of cooling rates on as-fabricated tensile properties. [20, 86] An increase in hardening (higher UTS, lower elongation) was observed for the use of slow cool when compared to fast cool; the mechanical properties for the fast cool (Build 1A from §VIII.4) and slow cool (Build 2A from §VIII.4) were measured to be: UTS of 942±61 [MPa] and 1108±50 [MPa], YS(0.2%) of 590±40 [MPa] and 869±32 [MPa], and elongation of 34±2.6% and 22±1.8%, respectively. This difference was ascribed to age hardening due to the difference in time at temperature. These results motivated the investigation of *in situ* heat treatment of EBM fabricated IN718 to directly control as-fabricated precipitate fractions using a controlled cool down to room temperature.

The cool down rate following build completion in EBM can be controlled by modifying build chamber atmosphere, using either vacuum (slow cool: 0.07 to 0.08 °C/s) or helium injection (fast cool: 0.1 to 0.2 °C/s). These values of cooling rate assume a linear rate between the process temperature and 600°C. If it is assumed that the material is in solution (it may be solutionized during a 1000°C hold following solidification) and that the cool down is approximately linear (the actual rate shows exponential decay), then a continuous cooling transformation (CCT) diagram may be used to predict phase formation (Figure 101). The CCT diagram shows that the fast and slow cool pathways both pass through the γ'' precipitation region is essentially the same path. The differences in cool down rates only

[2] *The comments made herein represent the author's attempt to differentiate the research presented from previous patents, and are intended for research use only. These comments do not constitute legal advice.*

diverge below 800°C; it takes another ~45 minutes for the slow cool to reach 600°C than for the fast cool. This suggests that any resulting microstructure difference is due to enhanced coarsening and not different precipitation pathways.

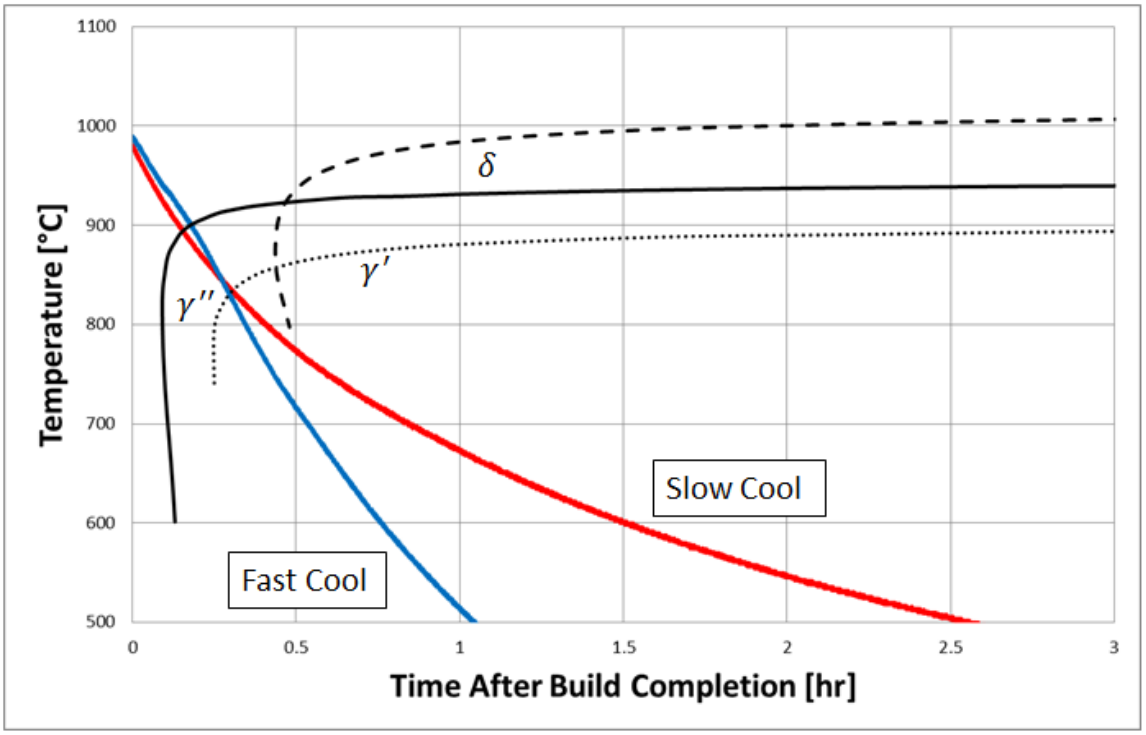

Figure 101. Cool down from process temperature plotted on a CCT diagram.

VI.3.2 Process Description of *In Situ* Heat Treatment

A third, novel cool down technique, *in situ* heat treatment (ISHT), is described in this section. An Arcam A2 EBM machine running EBM Control software version 4.1 was used to produce the ISHT sample. The samples for the ISHT were melted with a layer thickness of 75um using plasma atomized powder. The slow cool and fast cool cases used for comparison were built with previously reported machine parameters of 50um layers, gas

atomized powder, and version 3.2 software. The ISHT was accomplished by engaging planar heating over the build substrate using the "Start Plate Heating" function; after the melting process is completed, the cool down process was stopped and the heating process was restarted. The restart of processing prompts the user to engage heating (originally intended to reheat the surface temperature following process changes or machine stops). This heating was engaged and used as the heat source for the heat treatment step. The heating parameters are defined under the State Plate Theme, and use a diffuse beam (focus offset of 80mA), line offsets, and rotation in an attempt to achieve uniform, planar heating. This heating function must specify either a square of circular area. Newer software (version 4.1) functions offer the ability to heat over the area of the previous part layer (and not the powder area). The square area was used to heat over the entire part surface and enclosed powder bed area (a similar process to Preheat 1). The beam scans a single line at a time, skipping lines (usually 20 lines) to prevent the buildup of heat locally; the beam iterates scanning every 20 lines, until the entire area has been passed over. This is done for a number of iterations, and then the process is rotated 90 degrees to prevent "striping". Striping is the creation of strips or "stripes" of material that are more sintered than the rest of a part owing to the repeated pass of the beam over the same line.

The beam current is a critical parameter for this heating step. The beam will use this current value to heat to a preset temperature. If this temperature is not reached in a certain time, the process will "time out" and stop. The ISHT attempted to match the conventional, or "standard", post-processing steps as detailed in Table 22 and shown in Figure 102. [94] The currents reported for different process steps include the currents used to heat the substrate thermocouple to the desired temperature range. Isothermal hold temperatures were achieved by increasing the heating timeout (normally 1 to 4 hours) to an arbitrarily large number (>20 hours) while fixing the current to an underpowered level (values given in Table 22). The heating timeout is a value set to limit the amount of time that the machine tries to heat before a build fails. By increasing this value to >20 hours, the

entire *in situ* processing step can be run without the machine turning off and failing the build.

This caused the electron beam to heat continuously and the powder bed to reach an equilibrium temperature dependent on the fixed current. Cooling between process steps was achieved by manually stopping the electron beam and vacuum cooling until the lower temperature range was reached. It was assumed that the equilibrium temperature (as measured from the substrate) was representative of the temperature throughout the powder bed. The assumption is revisited later (§VI.3.5), through hardness indentation.

Table 22. Process current used to achieve *in situ* heat treatment.

Process Step	Desired Temperature [°C]	Desired Time of Step [hr]	Selected Current [mA]
Solution Treatment (ST)	980	1	30-31
Aging (precipitation)	720	8	11-12
Aging (coarsening)	620	10	8-11

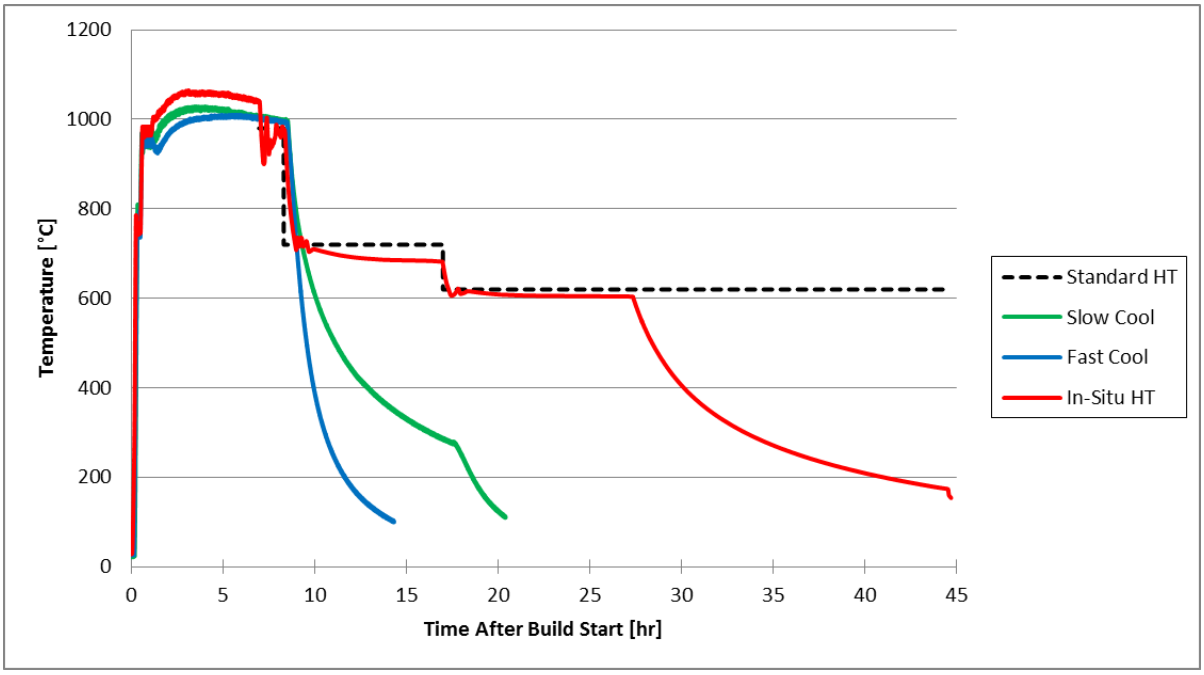

Figure 102. Thermal histories as measured from start plate thermocouple for various cool down techniques. The standard HT is graphed for comparison to the ISHT.

The resulting parts from a control build and the ISHT are shown in Figure 103. Significant amounts of powder were over-sintered during the ISHT. This was due to using a planar heat source over the entire build area to perform the heat treatment. This powder is not recoverable using the Powder Recovery System, and is a significant limitation to the implementation of an ISHT; powder waste should be limited, and over-sintered powder can be difficult to remove from complicated features. However, this test did demonstrate the concept of phase control. New EBM process controls allow for heating only on the surfaces of the last melted layer. Future work should apply this new process control to try to limit the amount of powder sintering.

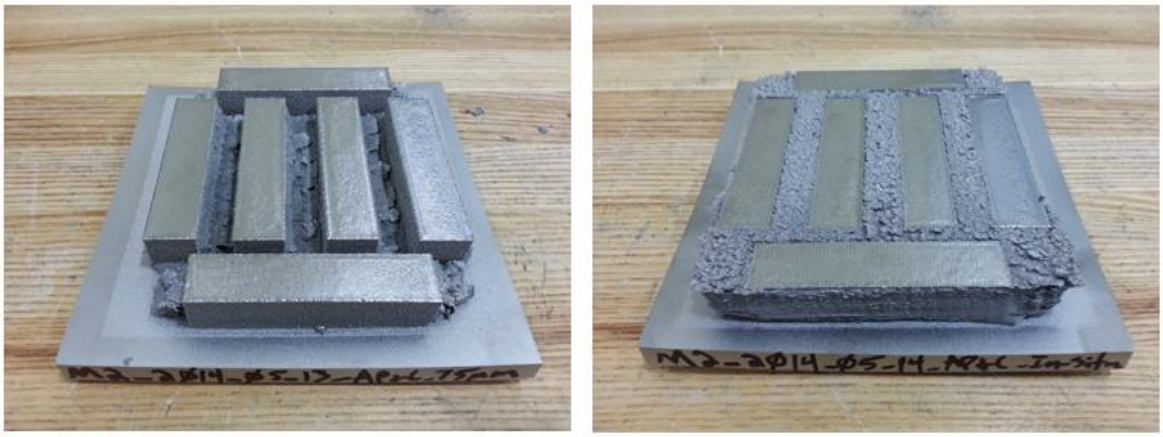

Figure 103. Builds showing (Left) a control build and (Right) the result of the *in situ* heat treatment. Due to processing conditions, significant over-sintering of powder occurred during *in situ* processing.

VI.3.3 Microstructure Analysis

The resulting microstructures of the fast cool, slow cool, and ISHT cases show variation in precipitate size and morphology that is characteristic of the age hardening of IN718. SEM analysis of characteristic precipitate phases of the matrix (Figure 104) shows that a decreasing cooling rate results in a transition from small, spherical particles (Figure 104(a)) to larger, slightly elongated disks (Figure 104(b)). This elongation and increase in precipitate size is consistent with the hardening effect seen in tensile properties. The ISHT resulted in even more coarsening of precipitates as seen in Figure 104(c). The change is precipitate size is discussed in this section, while the impact on hardness is explored in §VI.3.5 on mechanical properties.

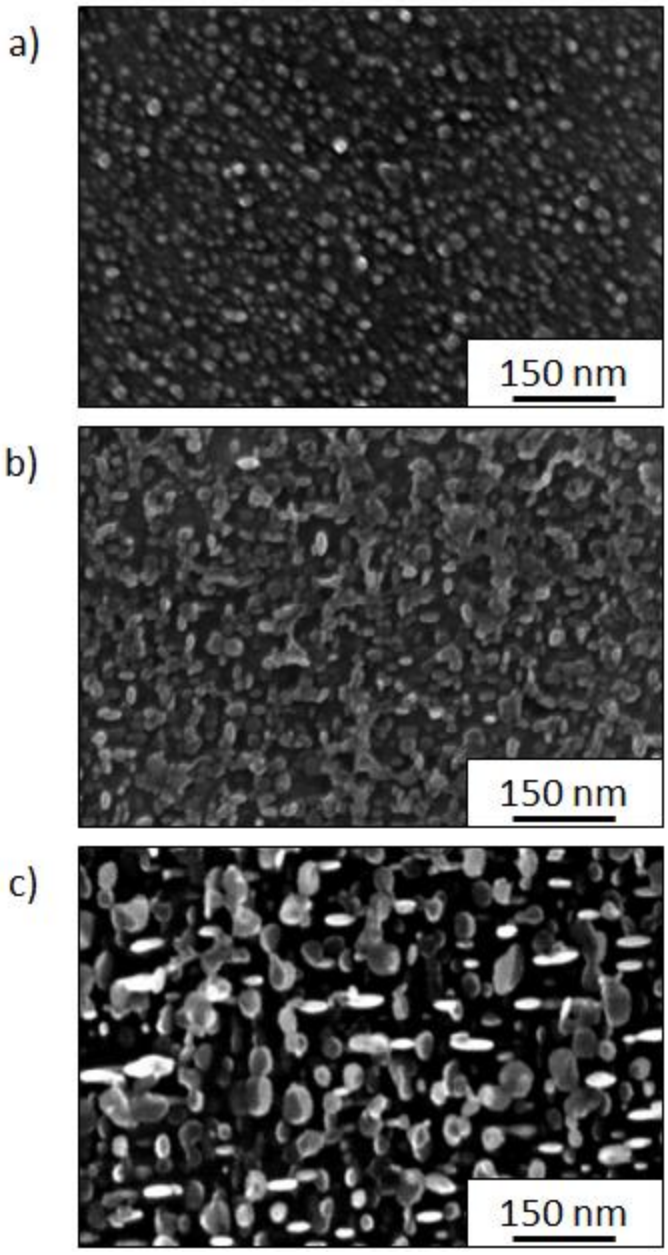

Figure 104. SEM of precipitates in the matrix for (a) fast cool, (b) slow cool, and (c) *in situ* heat treatment.

The principle strengthening phase of IN718 is known to be the γ'' phase, which is primarily associated with coherency hardening. [291] Detailed, site-specific TEM characterization of

these samples is required to confirm precipitate identification. Without TEM confirmation it may not be possible to differentiate between γ'' and γ' formations, but the precipitate sizes of matrix phases may be measured and compared against previously reported values. Previous work on TEM analysis of peak aged IN718 sheet (720°C for 8 hours, 621°C for 8 hours) found volume fractions of precipitates ($\gamma'' + \gamma'$) to be 17±3%. [292, 293] It is noted in this previous TEM that such volume fraction analysis may be highly variable in scope due to small sampling areas. Further work is needed to confirm the volume fractions of the samples presented here; image analysis of SEM images may lead to overestimation of volume fraction, as multiple layers of precipitates may be exposed.

To better understand the effect of the cooling rate on precipitate hardening, image analysis was performed on SEM images of the precipitates. It was assumed that the precipitates being measured were γ'' with disk morphology. ImageJ was used to set the scale and manual measurements were taken across the long dimension (assumed to be diameter) and short dimension (assumed to be thickness) of representative particles. The fast cool case was not analyzed due to the ambiguity of dimensions (all particles appear spherical). The slow cool case was found to have a diameter of 19±5nm and a thickness of 9±2nm. The ISHT case had a diameter of 39±13nm and a thickness of 13±3nm. The diameter of γ'' disks is expected to grow preferentially compared to the thickness, [203] as is observed here. For conventional aging of powder metallurgy material, γ'' disks are expected to be 25 to 35nm in diameter and 7 to 12nm thick. [294] The range of precipitate sizes for both cases overlap the conventional range (the fast cool case did not precipitate measureable γ'').

Caution is recommended when considering these results; multiple planes of precipitates are likely revealed during etching and the diffraction pattern of the phases from TEM has not been measured. This means that there is likely to be error in distinguishing γ'' from γ' or γ'' from δ-phase. Additionally, there are outliers in all cases due to formation in precipitate networks or at grain boundaries that were not included in this analysis. Follow-up work

with TEM is needed to truly quantitatively express this information. For these same reasons, volume fractions of precipitates cannot be reasonably calculated from image analysis of SEM images. Given these qualifications, the current data on precipitate size suggests that the slow cool material is slightly underaged, while the ISHT material was peak-aged or slightly overaged.

Notably, the ISHT did not form large quantities of the intragranular, needle δ-phase that has been observed in previous work on EBM IN718. [102, 104]. This may be attributable to the fact that the long hold for the ISHT was not in the temperature range for direct precipitation of δ-phase from the matrix; the hold temperature for the ISHT was within the range for γ''/γ' formation and coarsening. Formation of δ-phase in this temperature region is mostly limited to cellular formation on GBs (<700°C) or transformation of $\gamma'' \rightarrow \delta$ due to overaging (750-800°C). [195]

VI.3.4 Large Grains & Cracking

The ISHT resulted in large grain size and cracking parallel to the build directions (along the z-axis). EBSD shows that the columnar grains extend at least the length (>700um) of the observation distance (Figure 105), which is much larger than the grain size seen in a control sample. Though the grains are large, the grain orientation and columnar structure remains intact (no growth of misoriented or recrystallized grains was observed). Small clusters of mis-oriented grains are seen in both the control and ISHT samples. The large grain size was likely a result of an elevated processing hold temperature (peak of 1065°C). This hold temperature was far higher than typical IN718 builds (~1000°C), caused due to ongoing parameter optimization efforts. Two pathways for the formation of large grains must be considered: (1) grain growth and (2) formation during solidification.

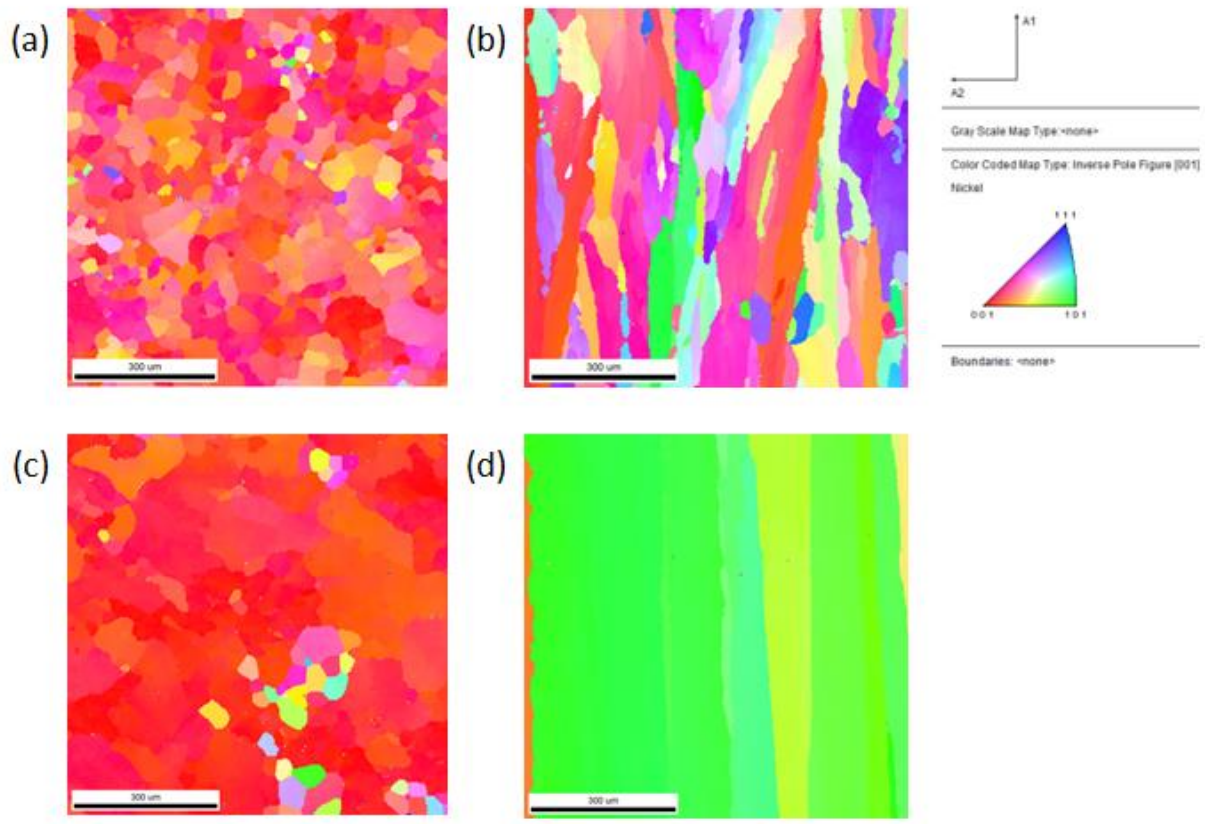

Figure 105. EBSD showing grain structure for a control case in the (a) XY plane and (b) XZ plane, and for *in situ* heat treatment in the (c) XY plane and (d) XZ plane.

The δ-solvus for IN718 is ~1010°C [173], and grain boundary δ-phase is typically used to control γ-matrix grain growth. [177] Above ~1040°C, discontinuous grain growth is typical in IN718. [219] Thus, the ISHT build temperature was high enough above the δ-solvus that grain growth likely occurred in previous layers during ongoing layer melting. In addition to the high process temperature, a 1 hour solution treatment (980°C) hold was engaged directly following the melting process. This step may have contributed to growth (if no GB δ-phase was present). After this step, a lack of GB δ-phase may have allowed grain growth

during the other aging steps of the ISHT. Grain growth during these aging steps is less likely, as the γ''/γ' aging region also allows for precipitation of GB δ-phase.

Due to the higher processing temperature, it is also possible that different solidification conditions led to increased grain size directly from solidification. Higher temperature should lead to larger melt pool size and changes in the thermal gradient of the melt pool. Since the ISHT was aged in situ, it is not possible to observe the "as-solidified" structure from this case. Follow-up work to understand grain growth in columnar, EBM material should be done. Based on work in subsequent chapters (see §VII.2.3), the grain growth seen here is not characteristic of high temperature annealing, but the effect of phase structure is still not completely characterized.

Significant cracks were present in the ISHT samples, aligned parallel to columnar grains and the build direction (z-axis). SEM shows that shrinkage porosity is common feature of both a control sample and the ISHT sample (Figure 106). It is possible that high temperature mobility of some pores enabled migration during grain growth in the ISHT sample, collecting along edges of growing grains. The cracking could also be related to solidification conditions, as grain boundary liquation could occur if high segregation led to formation of certain solidification phases (e.g. Laves). This cracking and the presence of large grains do appear to be related, as neither is a common feature in other control samples. Further work should focus on performing an ISHT on a build with more tightly controlled process temperature to better understand the limitations of this technique.

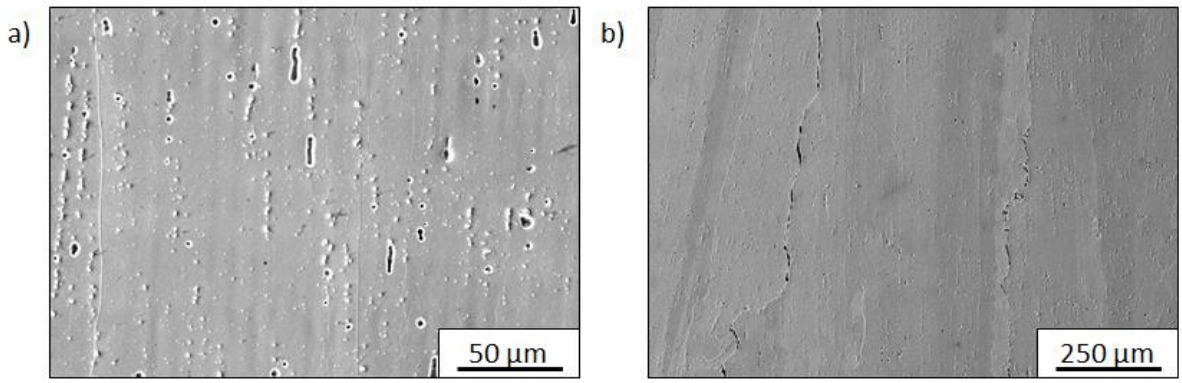

Figure 106. SEM of etched (a) control sample (Build 16A from §VIII.4) shows lines of shrinkage porosity aligned in z-direction and (b) *in situ* sample shows aligned cracks.

VI.3.5 Mechanical Testing

In the interest of completely discussing all data relevant to ISHT in this chapter, the tensile properties and hardness values measured from samples prepared for the study are reported herein (as opposed to §VIII.4 and §VIII.5 that describe the mechanical properties of as-fabricated and post-processed samples, respectively). Tensile testing was performed perpendicular to the build direction for the ISHT material; however, these tests failed during loading (Figure 107). Fractography shows no necking of the ISHT sample, while some is seen in the control case (Figure 108). Additionally, striations are evident penetrating the entire gauge diameter in the ISHT case, whereas fewer striations are present in the control case. These striations are likely an artifact of the columnar grain boundaries, pointing to the importance of these boundaries in the ISHT sample. This poor tensile performance of the ISHT samples is postulated to be a result of a combination of cracking and large grains; while the cracks present in the microstructure is the likely reason for mechanical failure, the large grain size may be related to the growth of these cracks.

Though tensile performance does not allow for useful comparison of the ISHT samples, hardness can be used as a measurement of the amount of aging that was achieved. Baselines for hardness comparisons to peak aged, unaged, and underaged material were taken from previous analysis of rolled bar by Slama et al. [198] Values of 275HV, 350HV, and 466HV were used for unaged, underaged, and peak aged, respectively. The hardness values of the fast cool, slow cool, and ISHT are compared in the z-direction (Figure 109) and the x-direction (Figure 110), and a summary of average hardness is given in Table 23. Hardness values were collected as an array, then sorted into x- and z-values. The fast cool had the lowest hardness (as expected), which is somewhere between unaged and underaged material. The slow cool was harder than the fast cool material (this confirms the tensile results) but softer than the *in situ* material. The slow cool material was harder than underaged material but not as hard as peak aged. The ISHT material had the highest hardness, which was at or above peak aged material. This confirms that the ISHT can be used to age material *in situ*. Further work is needed to better study crack formation to improve tensile results; this may be as simple as running material at the normal processing temperature during melting (~1000°C).

Since hardness was not observed to vary with z-position (Figure 109), the assumption of an isothermal build volume appears to be valid for the XY Tensile geometry. Additionally no variation is noted with hardness in the x-direction either (Figure 110). *In situ* temperature measurements of the top build surface during operation are needed, as this assumption may not hold for larger builds than the X-Y Tensile geometry (defined in §V.2.2, height of 20mm).

Table 23. Hardness values considered for all x- and z-positions.

Case	Average Hardness [HV]	Min Hardness [HV]	Max Hardness [HV]
Fast Cool	324±18	282	368
Slow Cool	392±15	355	424
In Situ HT	478±7	462	493

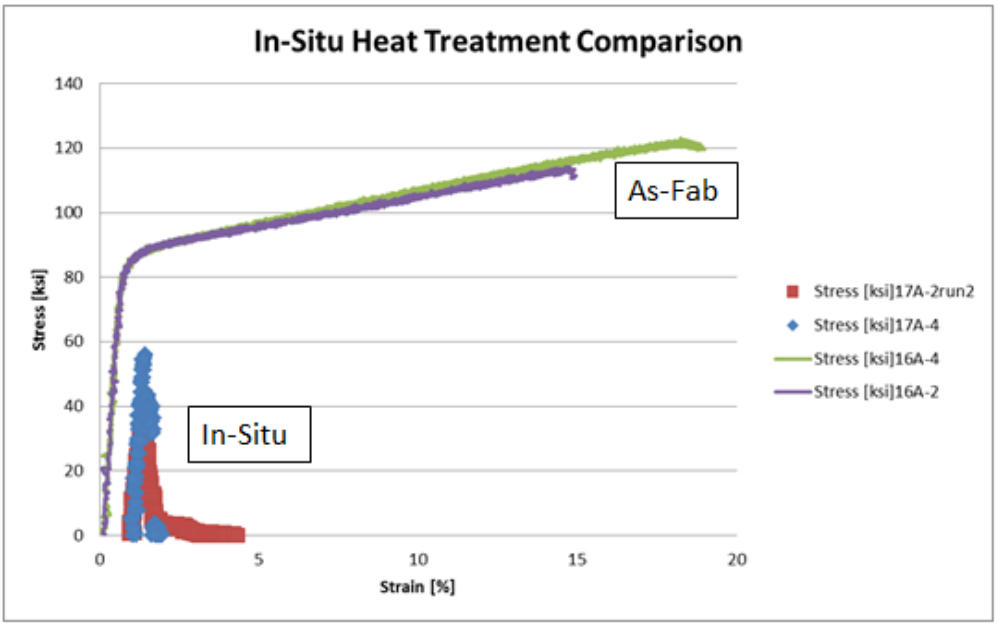

Figure 107. Mechanical testing results comparing the ISHT to a control case. Two tensile tests were completed for each case.

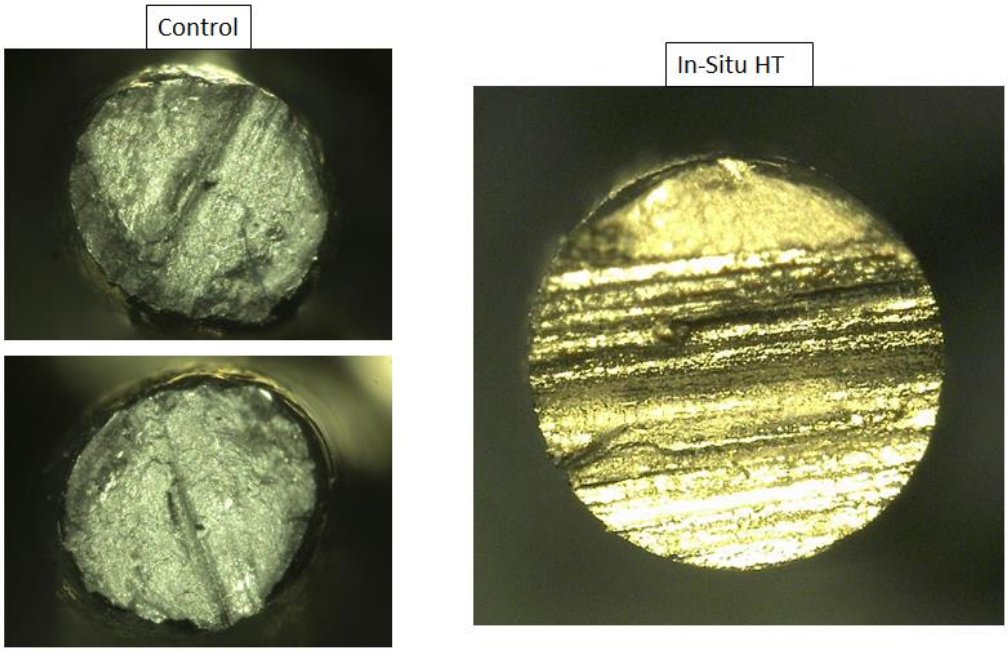

Figure 108. LOM of fracture surfaces for the (Left) control sample (Build 16A from §VIII.4) and (Right) ISHT sample.

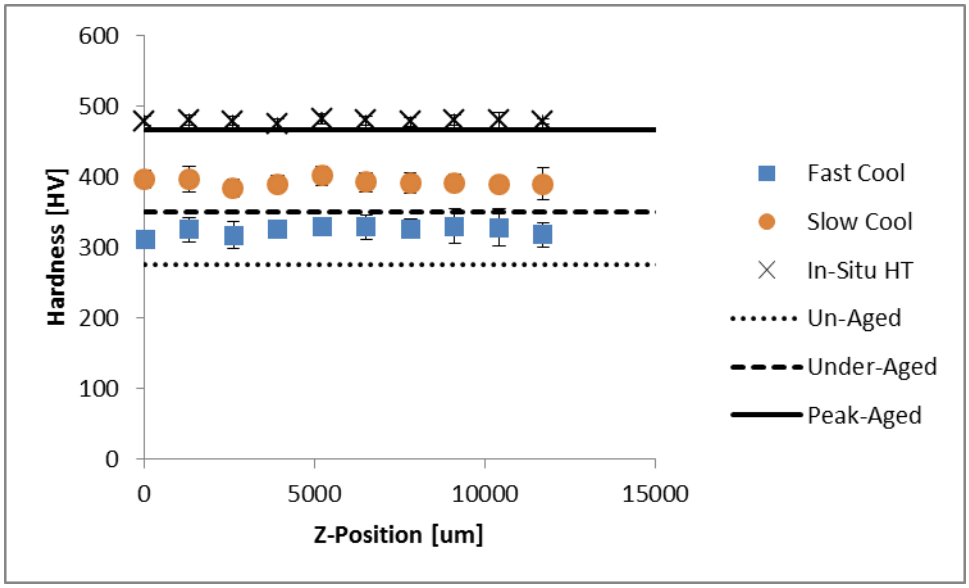

Figure 109. The hardness profile in the z-direction confirms uniform axial aging of material; the *in situ* case is at or above the hardness of peak aged material.

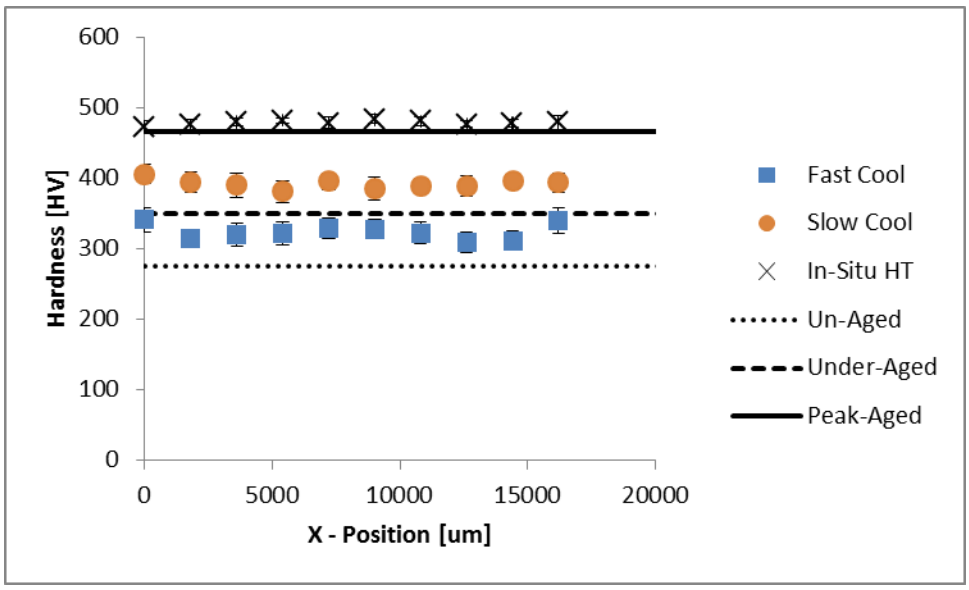

Figure 110. The hardness profile in the x-direction confirms uniform aging.

VI.4 Summary of Microstructure & *In Situ* Heat Treatment

The as-fabricated structure is defined by the EBM process hold time and hold temperature. Initial as-solidified structures show segregation effects and phase clustering, but these structures are homogenized by the elevated process temperature in the majority of the build material. If the temperature is held at or above 1000°C, then phase formation during processing may be limited; an under-aged structure can be achieved if process temperature is kept above the δ-solvus. For process temperatures below the δ-solvus with long hold times, significant quantities of intragranular δ-needles can form. This structure is characteristic of significantly overaged material, though likely precipitates directly from the supersaturate matrix. Various thermal post-processing methods for addressing microstructure variation will be addressed in the following chapter (§VII). The rest of this chapter, however, explored the development of *in situ* heat treatment of EBM IN718 to control phase formations during processing.

A novel technique was demonstrated which successfully controlled the *in situ* phase formation of EBM parts. Measured matrix-phase diameters and widths fell within the expected range for peak aged material, and Vickers hardness indentation indicated that the ISHT achieved peak aging. This work demonstrates the potential for decoupling grain structure formation and phase development by allowing the former to be controlled through solidification and the latter to be controlled through solid state phase transformation. While this technique was demonstrated as a means of post-processing by modifying phases after completion of all layers, future work could be done to apply it in stages to produce functionally graded microstructures along the build direction. Adjustments to process parameters to lower the processing temperature below the δ-solvus are needed to prevent the formation of large grains seen in the analyzed sample. Thus, this method demonstrates the potential to eliminate additional ex-situ thermal post-processing steps from AM processes.

CHAPTER VII

THERMAL POST-PROCESSING & GRAIN GROWTH

Post-processing treatments can be used to improve mechanical properties of Electron Beam Melting (EBM) Inconel 718 (IN718) by closing porosity, changing or maintaining grain structure, and changing the quantity and quality of precipitate phases. Stress relief annealing, Hot-Isostatic Pressing (HIP), solution treatment (ST), and aging are all thermal treatments that are done to achieve various effects on the microstructure. Stress relief is not necessary for EBM material, HIP can be used to close pores, ST is used to homogenize phases and reset the microstructure, and aging is used to achieve precipitate hardening. Variance in grain size and orientation during thermal post-processing was shown to be the result of grain growth during high temperature (1200°C) ST and HIP. Variability in the as-fabricated microstructure due to the presence or absence of intragranular δ-phase needles led to variation during sub-solvus (980°C) solution treatment (when present, δ-phase needles were not dissolved). It was found that a solution treatment for removing δ-needles, without incurring significant grain growth, was 1120°C for 2 hours. Potential mechanisms for grain growth in EBM IN718 are identified and rationalized.

VII.1 Experimental Procedure

An Arcam A2 and S12 were used to produce the samples described in this chapter. Post-processing was performed using furnace anneals or HIP. A tube furnace was used to obtain high temperatures (1020-1200°C) for solution treatment with temperature measured from the midpoint of the furnace. The furnace was heated to the ST temperature, and then the samples were inserted. It took ~7 minutes for the temperature to increase back to with 2°C of the ST temperature. After completion of the ST time, samples were water quenched. For a combined solution treatment and aging (STA), a box furnace was used for a lower

temperature solution treatment of 980°C, followed by steps of 720°C for 8hr and 620°C for 10hr. HIP was performed by a private firm, Avure, which provided data files to confirm the exact HIP cycle temperature and pressures (Figure 111). The process used pressurizes the treatment chamber, followed by heating to the desire temperature. This process is commonly used for IN718. Other techniques have been developed for HIP to reduce recrystallization (RX) in other nickel-based superalloys. A technique patented by Eridon and Dalal [295] explores the use of a multi-step HIP process to avoid RX in castings. Metallography and microscopy procedures were the same as previously described in the chapter on microstructure.

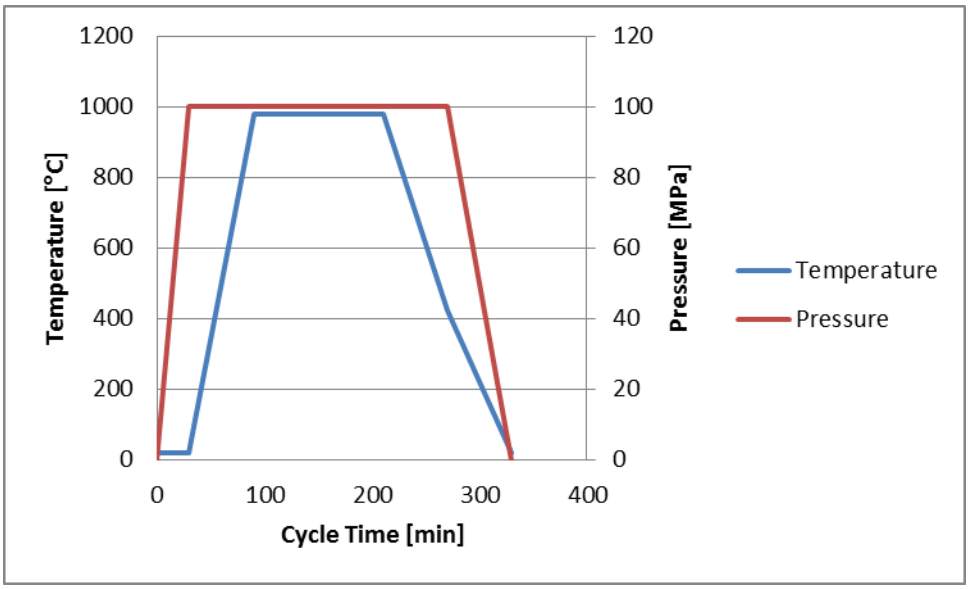

Figure 111. HIP cycle temperature and pressure for settings including start-up and cool down of 980°C, 100MPa for 2hr (other HIP cycles were tested as well).

Samples for the HIP testing were taken from Verification Build geometries (described in §V.2.2). ST samples were taken from vertical tensile bars (described as Build 8A in the

following chapter on mechanical properties). STA samples were taken from a variety of XY Tensile builds (also described in §V.2.2) and vertical tensile bars.

VII.2 Results & Analysis

To explore the thermal post-processing of EBM IN718, three treatments were tested: HIP, ST, and STA. HIP is important for closure of porosity, but was also noted to result in large grain size based on previous results in EBM material. A standard STA process was tested, which resulted in variations in final microstructure based on the presence of δ-needles in the as-fabricated microstructure. Based on the importance of the as-fabricated microstructural variance, a ST test matrix was run to optimize the ST for removal of δ-needles without incurring significant grain growth.

VII.2.1 HIP Test Matrix & Results

Based on previous results indicating grain growth from HIP of EBM IN718 at 1200°C, 100MPa for 4hr, [102] it was determined that lower temperatures and pressures would need to be tested to see if grain growth still occurred. A HIP test matrix was developed to span 800-1120°C, 100-200MPa, and 2-4hours. Upon analysis, grain growth did not occur, but porosity was also not fully closed. Follow-up EBSD of the previously published work [296] was compared to the results of the HIP test matrix (Figure 112) and shows the large grain size and disruption of columnar grains can result when the HIP temperature rises to 1200°C.

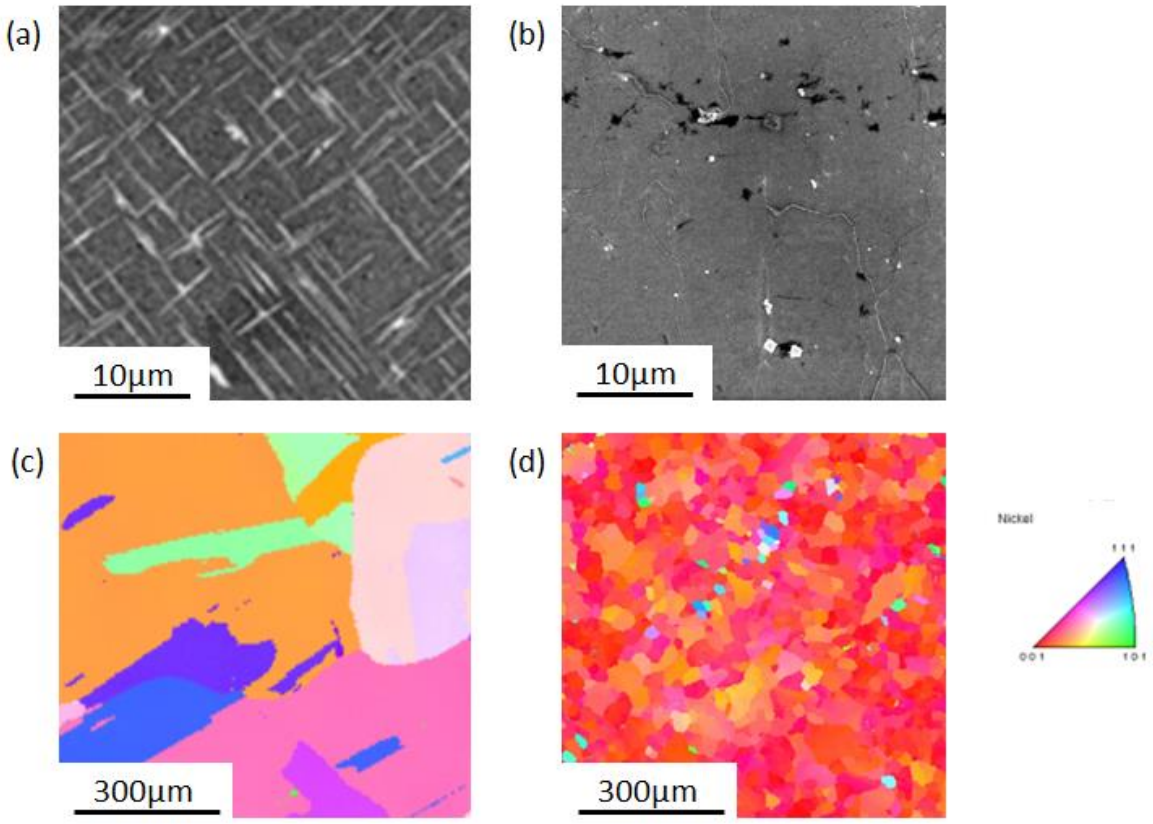

Figure 112. As-fabricated microstructure showing (a) intragranular δ-needles was processed at 1200°C, 100MPa for 2hr and (b) microstructure with no intragranular δ-needles was processed with a HIP cycle of 1120°C, 100MPa for 2hr. The results are (c) large grain growth and the disruption of the oriented, columnar structure and (d) limited coarsening and no disruption of the grain structure. Images were taken of (a) SEM of the XZ plane, (b) SEM of the XZ plane, (c) EBSD of the XY plane, and (d) EBSD of the XY plane. [296]

Analyzing the difference in resulting grain structures is complicated by variance in the as-fabricated microstructure of each sample. The sample with large quantities of δ-needles (Figure 112(a)) experienced large grain growth during HIP and the oriented, columnar grain structure was disrupted (Figure 112(c)). The sample with an "underaged" microstructure (defined in previous chapter, without δ-needles, Figure 112(b)) did not experience grain growth and maintained a highly oriented, columnar grain structure. Since the as-fabricated microstructures were very different and the HIP temperatures were different, more data

needed to be collected (inspiring the ST test matrix in §VII.2.3). This is a similar variance that has been observed before for heat treated EBM IN718 that did [101] or did not experience grain growth. [103]

Since the HIP matrix was carried out at lower temperatures and shorter times (in an attempt to avoid grain growth), full closure of porosity was not achieved in any of the tested HIP conditions (Figure 113). Shrinkage pores persisted, as should be expected given the tight window for closure of porosity in IN718. [297]

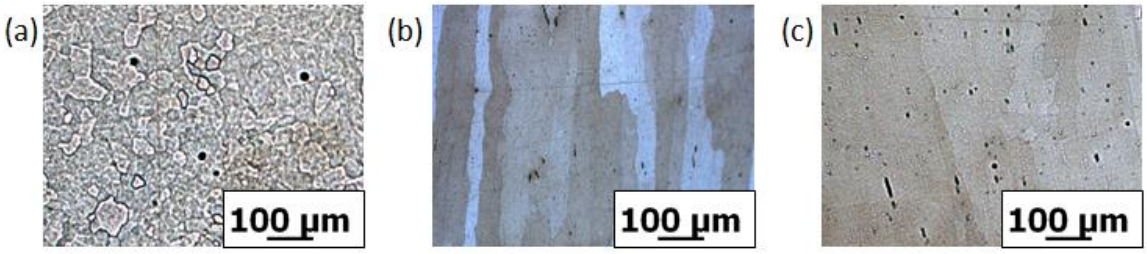

Figure 113. Etched LOM showing persistence of shrinkage pores in the (a) XY, (b) XZ, and (c) XZ planes after HIP at (a) 100MPa, 1120°C, 120min, (b) 100MPa, 800°C, 120min, and (c) 200MPa, 800°C, 120min.

VII.2.2 Standard STA

Given the variability in HIP results (grain growth occurred either based on as-fabricated microstructure or post-processing temperature), it was determined that ST was the key to understanding phase dissolution and grain growth in EBM IN718. As a baseline for understanding the effect of ST on EBM IN718, a standard STA was run on as-fabricated material with δ-needles both (1A) absent and (8A) present. A standard 980°C for 1hr ST was used prior to aging of 720°C for 8hr and 620°C for 10hr. The resulting STA samples are labeled 1B and 8B, and show the persistence of the original as-fabricated microstructure for each case (Figure 114). While one sample (1B) resulted in the expected aged structure, the other (8B) resulted in large quantities of intragranular δ-needles and possibly other plate/needle phases. The difference is attributable to differences in the as-fabricated microstructure; when intragranular δ-needles are present, the 980°C ST does not fully solution the material. During subsequent aging, the needles continue to coarsen. When the as-fabricated structure does not have intragranular δ-needles, the 980°C ST works as intended and may only form some additional δ-phase on GBs. This incomplete solution treatment of δ-phase means that the resulting microstructures are very different and that a significant difference in mechanical performance may be expected. To reduce variability in EBM IN718 microstructures following thermal post-processing, higher temperature ST must be explored.

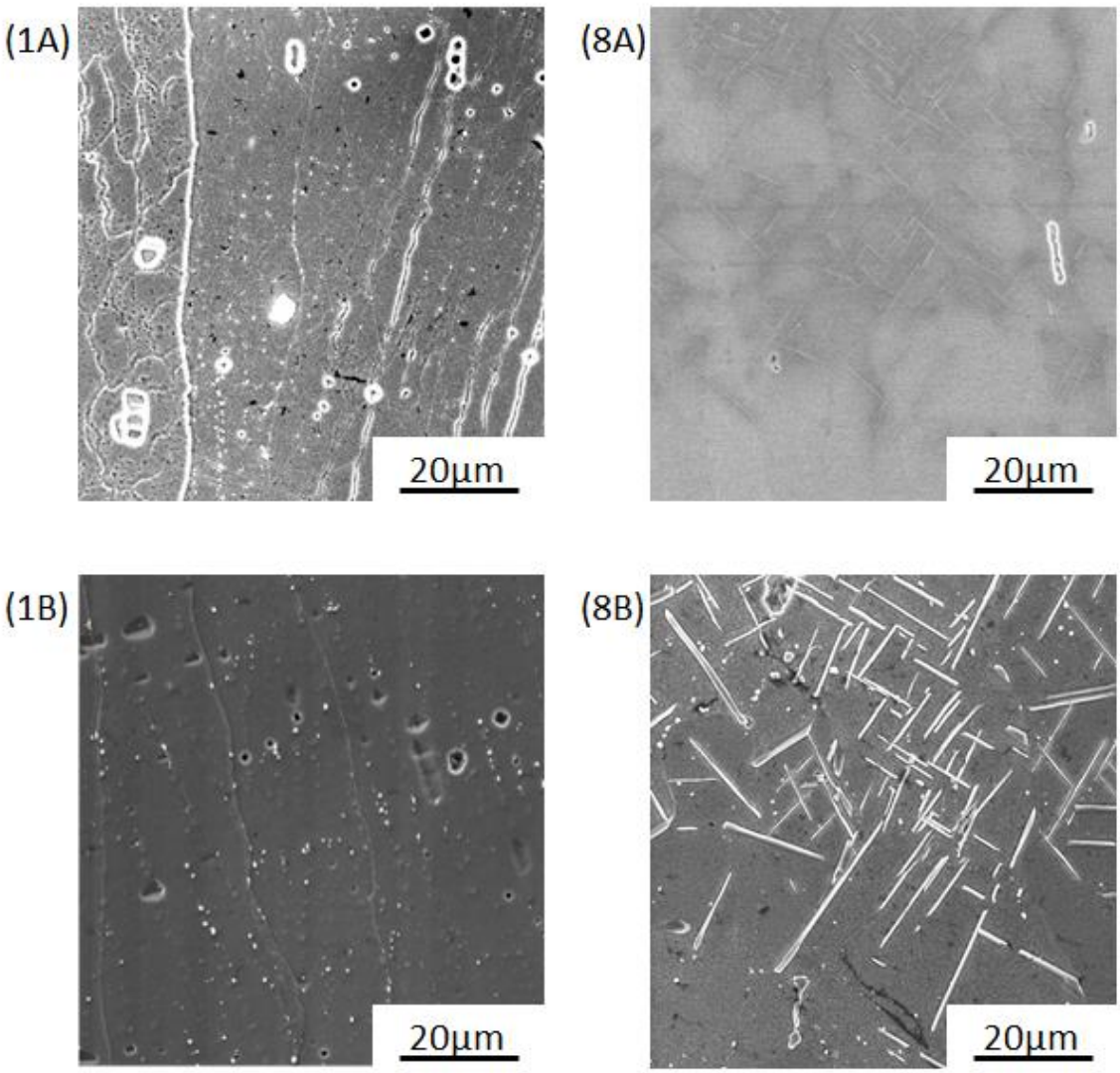

Figure 114. SEM of the XZ planes of as-fabricated microstructures (1A) without intragranular δ-needles and (8A) with needles show variation in the resulting phases present given the same solution treatment and aging of 980°C for 1hr, 720°C for 8hr, and 620°C for 10hr that shows (1B) no precipitation of δ-needles and (8B) no dissolution and possible growth of existing δ-needles.

VII.2.3 Solution Treatment Optimization

A ST test matrix was developed to determine if overaged microstructures, full of intragranular δ-needles, could be reset without incurring grain growth. Qualitative results of the test matrix are presented in Table 24. The qualitative analysis was obtained by a combination of LOM (Figure 115) and ESBD (Figure 116) analysis. For lower temperatures near the δ-solvus (8P), complete solution of δ-needles is not achieved. This is in agreement with previous work by Strondl et al. [104] to solution treat EBM IN718 with δ-needles at 1000°C for 1hr; in this reference, δ-needles were not solutionized and higher temperature ST was recommended. For higher temperatures (8N, 8Q) far above the δ-solvus, grain growth and disruption of the oriented, columnar grain structure occurs for both 1hr and 4hr treatments. Only the 1120°C for 2hrs ST (8M) was able to completely solutionize δ-needles without incurring grain growth. The result of case 8M is particularly interesting when compared to HIP results; an 1120°C, 100MPa, 2hr HIP cycle also avoided significant grain growth (in a sample without intragranular δ-needles). Grain growth in HIP was only seen in the 1120°C, 100MPa, 2hr HIP cycle (which also included δ-needles), which is the same temperature grain growth was observed at during ST. This comparison suggests that ST or HIP at 1120°C can be performed without consideration for the prior phase structure (presence or absence of δ-needles) and maintain the original grain structure.

Table 24. Results and nomenclature of ST test matrix (Build labels correspond to heat treatments of the starting material from Build 8A from §VIII.4).

Time	1020°C	1120°C	1200°C
1 hr	(8P) δ-needles remain Possible RX nucleation	-	(8Q) Near complete Solution Large grain growth
2 hr	-	(8M) Complete Solution Early stage RX/grain growth	-
4 hr	-	-	(8N) Complete Solution Large grain growth

Though LOM identified regions of partial grain growth or RX in Figure 115(8M), these regions were not identified during EBSD in Figure 116(b, e). Since grain growth or RX was notably sparse in sample 8M, it is not surprising that EBSD of a sample area of ~1000x1000um did not identify these anomalous grains. Further analysis of other regions using EBSD should be done to identify the orientation of these anomalous grains in this sample. Though no grain growth was noted in sample 8P, SEM analysis suggests possible RX nucleation sites or early stage grain growth occur near δ-needles and possibly carbides (Figure 117).

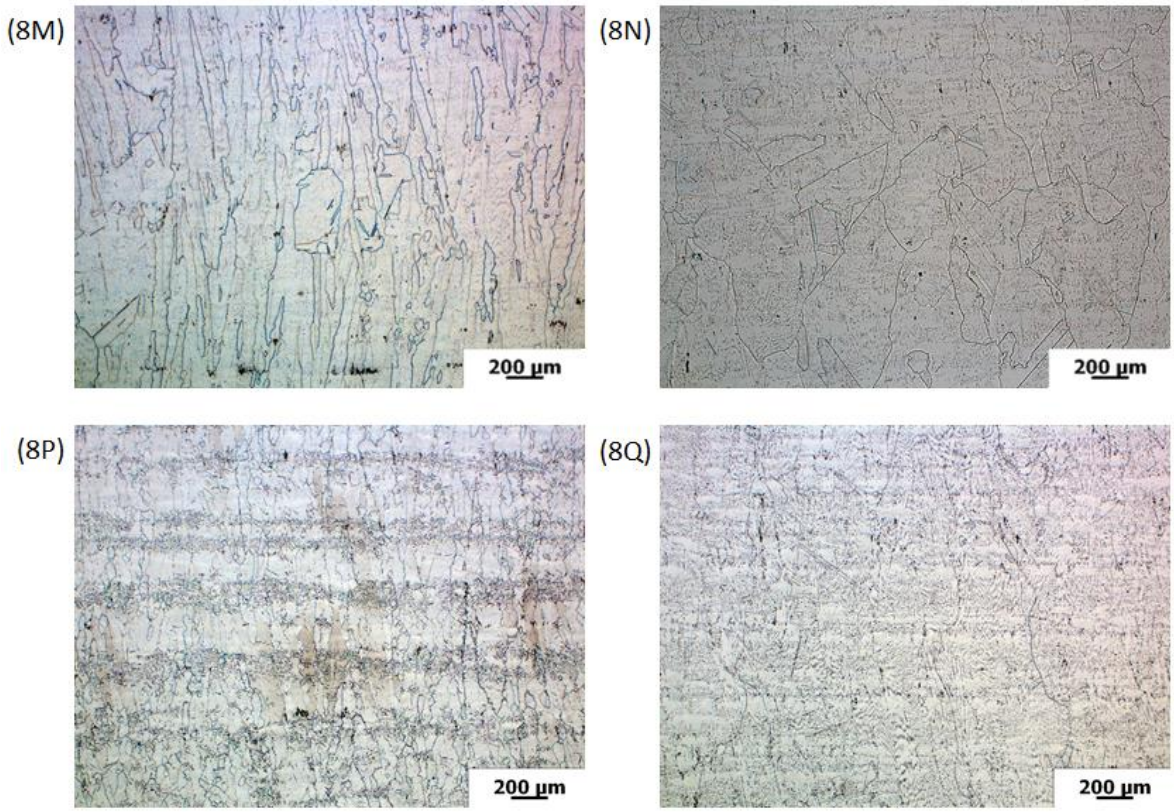

Figure 115. LOM of the XZ plane shows (8M) complete δ-needle solution and minor grain growth or RX, (8N) significant grain growth, (8P) incomplete solution of δ-needles, and (8Q) significant grain growth.

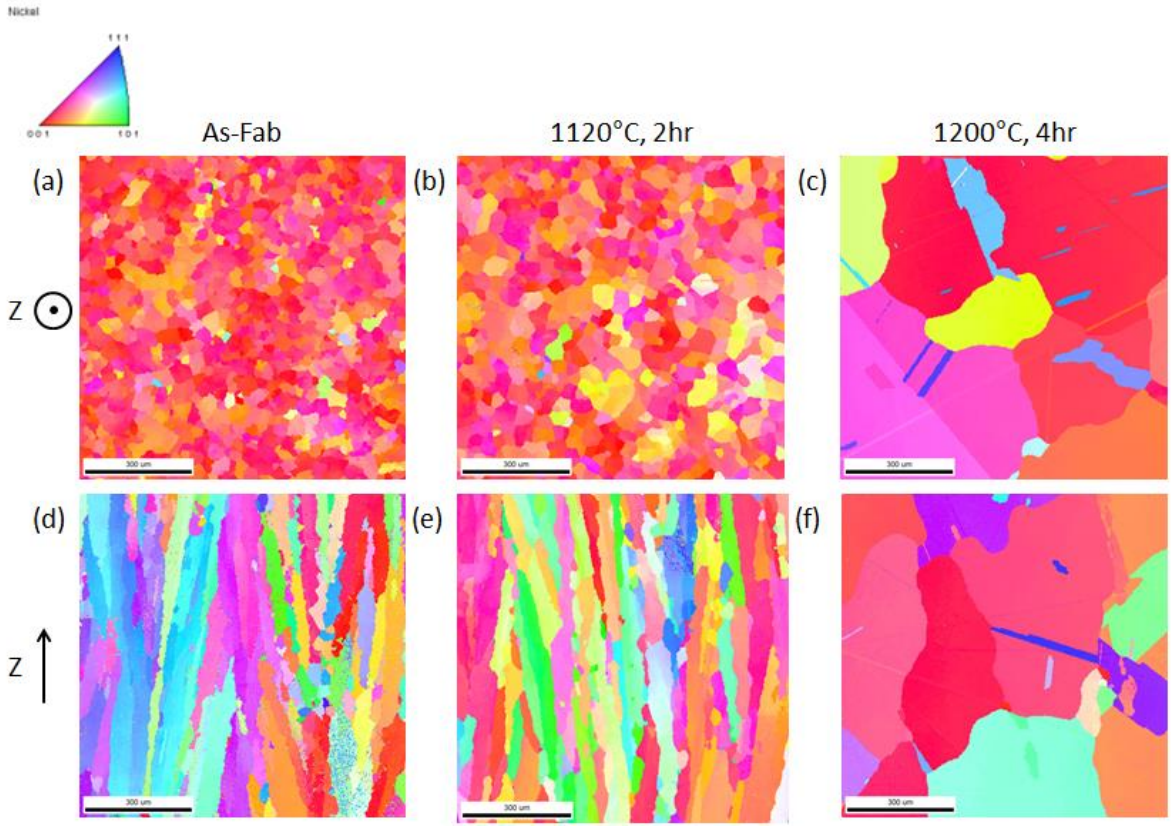

Figure 116. EBSD results of the ST matrix show significant grain growth in the 1200°C, 4hr case but do not show significant difference in grain orientation in the 1120°C, 2hr case. The As-Fabricated sample is from the bottom of Build 8A from §VIII.4.

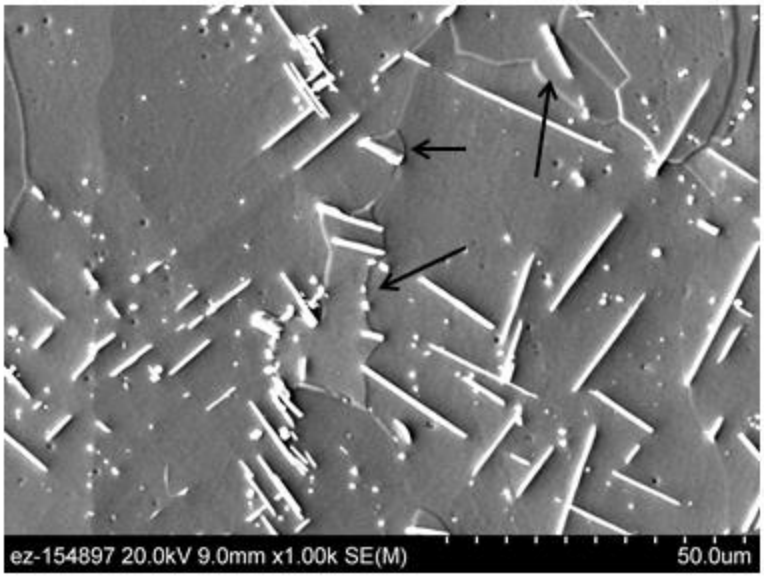

Figure 117. SEM image of ST IN718 at 1020°C for 1hr (8P). Potential RX nucleation sites or early stage growing grains are identified with arrows.

VII.2.4 Grain Growth during ST

The complete replacement of oriented, columnar grains in the as-fabricated material with large, non-columnar grains is of particular interest for study of grain growth mechanisms in IN718. Based on previous work and the work presented herein, it is not apparent why rapid, large grain growth occurs at 1200°C for EBM IN718; there must be a mechanism driving this growth. The most likely mechanisms are (1) discontinuous grain growth due to the dissolution of GB-pinning δ-phase and (2) RX causing the formation of new high angle GBs with high mobility.

Discontinuous grain growth (rapid grain growth above a certain annealing temperature) is promoted by the presence of low angle grain boundaries (<10°), precipitates, and strong texture. [298] Discontinuous grain growth has been noted in wrought IN718 above 1040°C.

[219] It is asserted in this previous study that grains become unpinned when δ-phase dissolves and re-pinned by carbides at higher temperature.

Large columnar grains (without disrupted orientation or columnar grain structure) may occur in some cases, as was observed during the *in situ* heat treatment analyzed in the previous chapter on microstructure (§VI.3.4). In this case, it was not clear if solidification kinetics or grain growth was responsible for the resulting structure. Definitive growth or coarsening of the columnar grains did occur during ST at 1120°C for 2hr as observed in Figure 116(b) compared to the as-fabricated material. The average grain size grew from 55.5um in the as-fabricated condition to 59.6um after ST, as measured from column diameter in the XY plane. The area fraction of various grain size bins is plotted in Figure 118, which shows the loss of area fraction of small grains and increase in area fraction for larger grain sizes (though the as-fabricated sample shows a larger area fraction at one particular bin). These cases point to potential differences in grain growth in EBM IN718 at different temperatures.

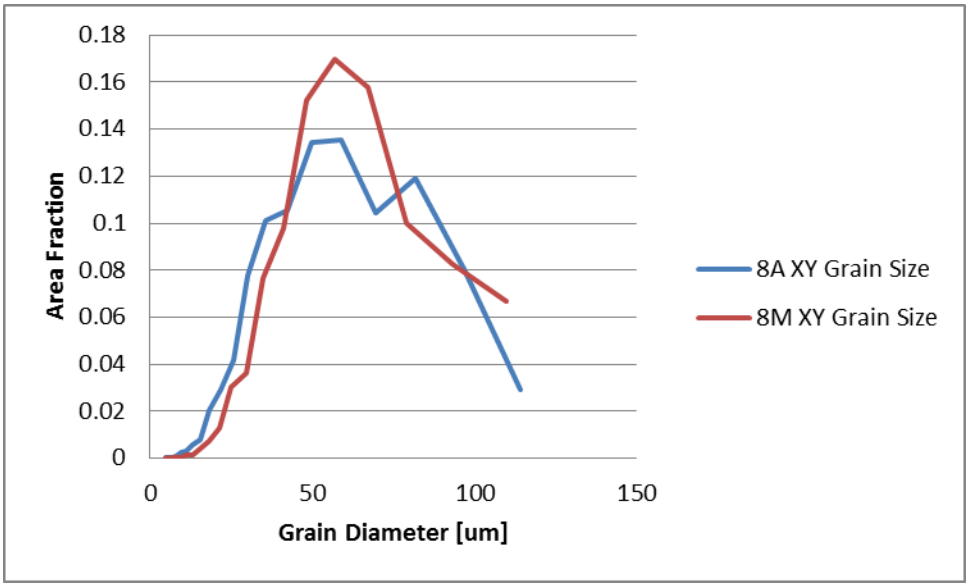

Figure 118. Area fraction of various grain diameter bin sizes for (8A) as-fabricated and (8M) ST at 1120°C for 2hr material.

A recrystallization (RX) mechanism could cause formation of small grains. If the grains had high angle GBs (high GB mobility), then they would have the potential for growth. However, for RX sites to grow, grains must have both a high local misorientation (high angle) and size advantage. [218] The presence of larger, columnar grains means that it is unclear how a RX site would be able to achieve a size advantage to promote growth. RX also requires a source of dislocations. Potential sources of dislocations and RX mechanisms are considered in §VII.2.8.

VII.2.5 Twin Boundaries

The formation of twin boundaries is a common feature of the reported HIP and ST samples with grain growth. Such twin boundaries formed during heat treatment are typically termed "annealing twins". Annealing twins in pure Nickel have been observed to increase in average density during RX and decrease in average density during grain growth. [299] So, the formation of annealing twins in EBM IN718 in interesting to note and may offer insight in future analysis of grain growth in the system.

In FCC materials, twin boundaries must have a 60° rotation around the <111> axes and secondary twins have a 38.9° rotation around the <110> axes. [300] Both coherent and incoherent twin boundaries must meet this rotation requirement. Coherent twin boundaries must also be have alignment of <111> planes on both sides of the boundary. This condition for coherency was created to overcome the 2D nature of EBSD. OIM analysis of EBSD data was used to identify boundaries in the XY plane of sample 8N (Figure 119), which shows both primary and secondary twin boundaries. Having identified twin boundaries, it is important to note whether the boundaries are coherent or incoherent. OIM analysis software was used to apply both conditions for coherency. Resulting coherent twin boundaries were then removed to compare unique grain maps including and excluding coherent annealing twins (Figure 120). By removing coherent twins, the grain size can be

noted more clearly; grain size in sample 8N is very large (>300um in diameter) for most grains.

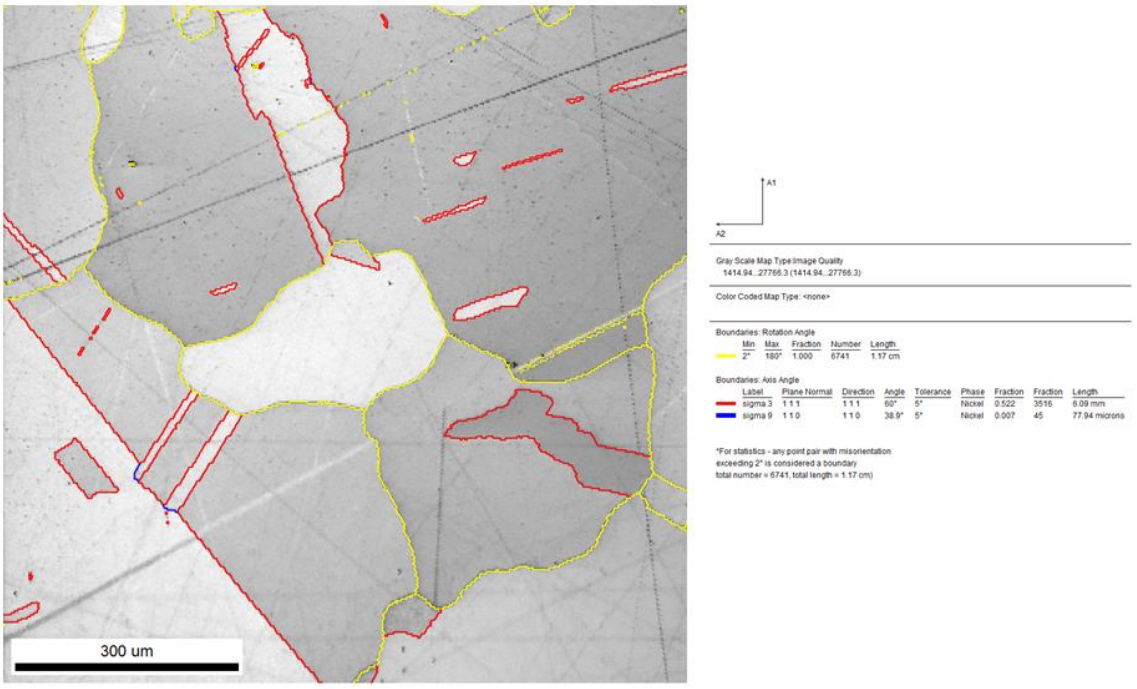

Figure 119. Grain boundaries (yellow), primary twin boundaries (red), and secondary twin boundaries (blue) are identified in the XY plane of sample 8N.

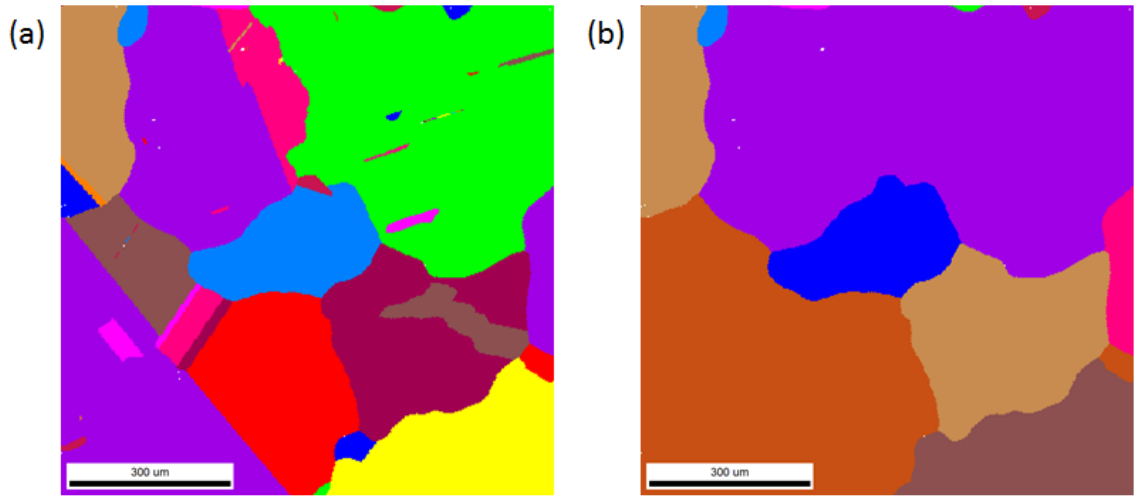

Figure 120. OIM analysis of EBSD data from the XY plane of sample 8N was used to map (a) unique grains including annealing twins and (b) unique grain excluding coherent twins.

VII.2.6 Hardness

A comparison of Vickers hardness in as-fabricated material and solution treated material (Table 25) allows for baseline values of hardness to be compared. There is a minor loss of hardness associated with the large grains as seen in the solution treated samples. This could also be due to ripening of carbides, reducing the effect of solid solution strengthening of Nb, or just creating larger carbides at the expense of smaller ones.

Table 25. Measured hardness of as-fabricated and solution treated material.

Sample	Condition	Average Hardness [HV]	Min. [HV]	Max. [HV]
8A BOT XZ	As-Fabricated	332.8±19.4	312	368
8M-9-1 XZ	ST, 1120°C for 2hr	200.0±7.0	193	212
8N-12-1 XZ	ST, 1200°C for 4hr	183.8±5.3	179	197

VII.2.7 Carbide Coarsening

SEM shows (Figure 121) that the solidification structure of carbides remains as columnar precipitate arrays in the build direction in samples without grain growth, whereas the carbide distribution is more isotropic in the case with grain growth. It appears in Figure 121 that there are regions devoid of carbides in the high temperature ST case, but upon further inspection of representative XY planes (Figure 122), it becomes clear that carbides have been removed during metallography (these carbide "holes" are distinctly different from solidification porosity in size and contrast, Figure 123). By analyzing images for the XY plane in ImageJ, carbides can be grouped into histograms bins based on calculated diameters (carbides assumed to be circular/spherical). This analysis underestimates the number and fraction of large carbides present in the high temperature ST (8M), but still shows carbide coarsening compared to 8N (Figure 124). With higher homogenization temperature in forgings, carbides have been observed to grow in size due to Ostwald Ripening and also became more dispersed than clustered. [229] The growth of carbides is an undesirable effect of the ST, that may result in permanent coarsening of carbides; since the carbides cannot be effectively solution treated, growth of carbides during post-processing should be limited.

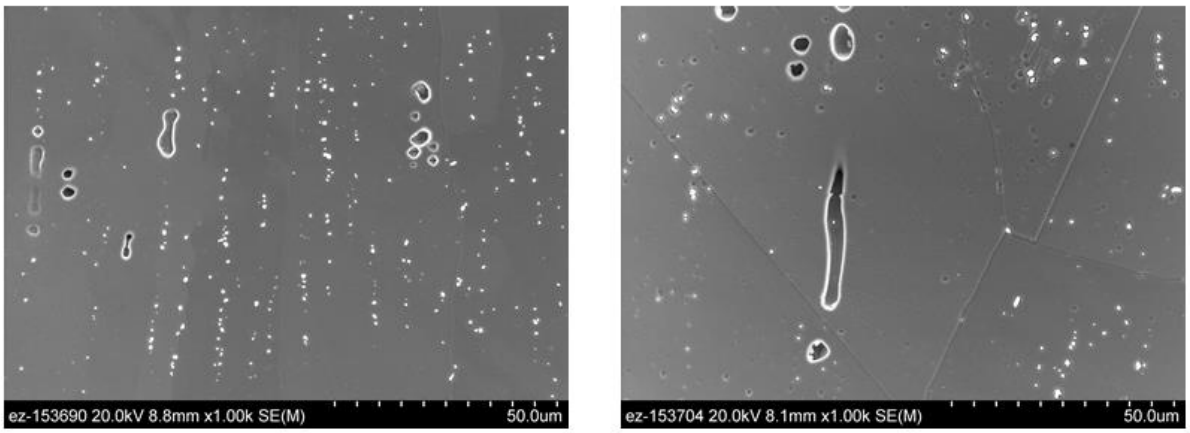

Figure 121. SEM of the XZ plane of (Left) ST at 1120°C for 2hr and (Right) ST at 1200°C for 4hr shows that carbides remain in a columnar structure in the build direction in the lower temperature/time case but exist in a more isotropic distribution in the higher temperature/time case with significant grain growth.

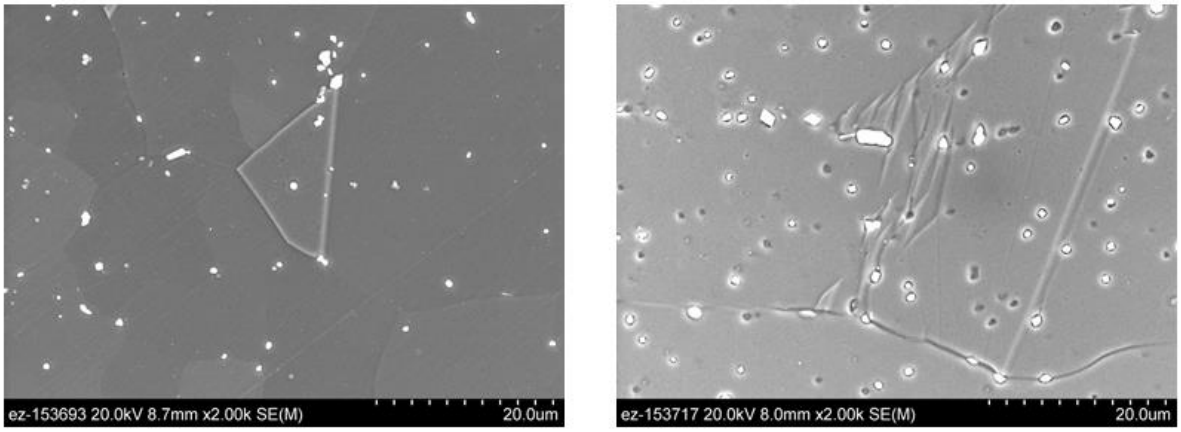

Figure 122. SEM of the XY plane of (Left) ST at 1120°C for 2hr and (Right) ST at 1200°C for 4hr shows that significant numbers of carbides have fallen out of the higher temperature ST sample during metallography, which complicates analysis.

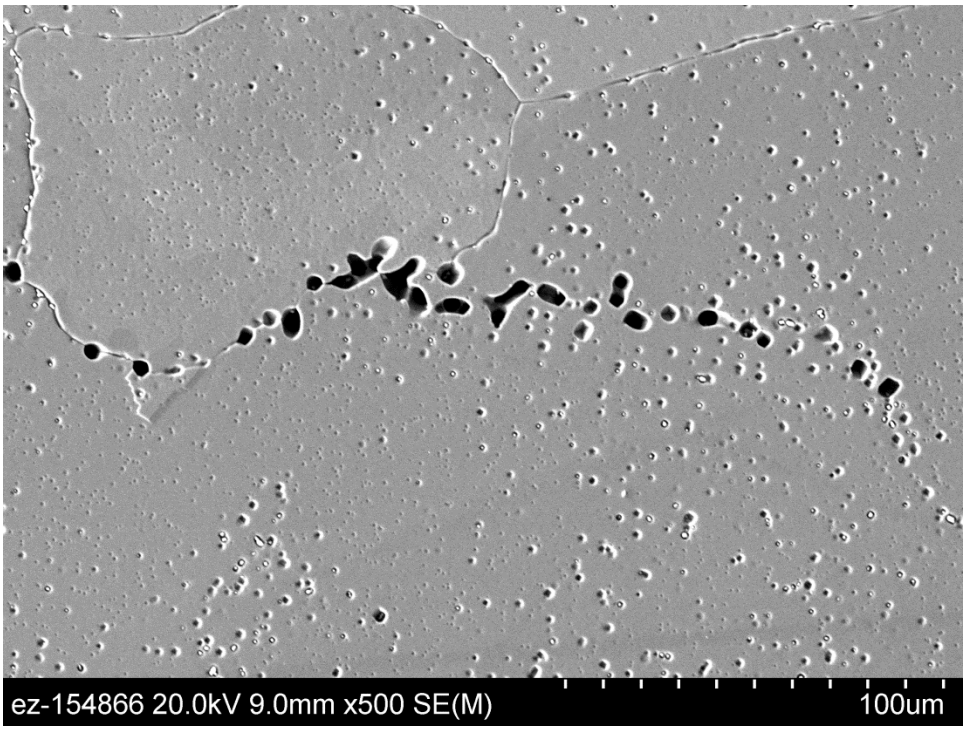

Figure 123. SEM of the XY plane of 8Q shows persistence of solidification porosity after ST (aligned in the center of the image) and the smaller carbide "holes" where large, coarsened carbides have fallen out of the sample during metallography.

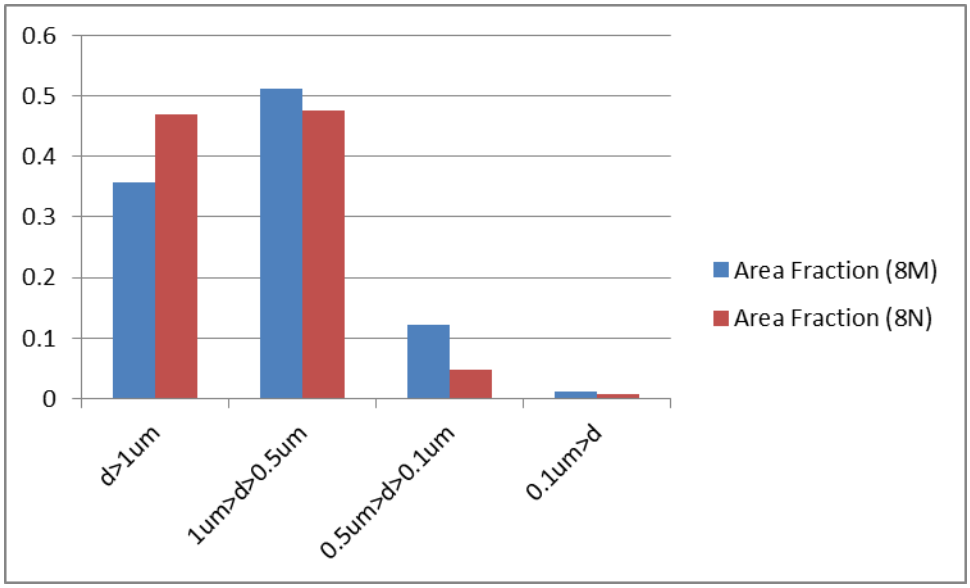

Figure 124. By grouping carbides into a histogram, the increase in area fraction of large carbides (>1um) in the high temperature ST (1200°C for 4hr) becomes apparent. Carbides are assumed to be circular and are grouped according to a calculated diameter.

VII.2.8 Possible RX Mechanisms

The potential for RX as a mechanism to precede grain growth at high temperatures should be considered. In the cases with large grain growth, all samples had δ-needles and received a high temperature ST or HIP. If RX were to occur in the material, there would have to be a source of dislocations to act as a driving force for RX. Potential sources are explored in this section.

Strain energy from closure of pores during HIP can lead to RX; RX in TiAl during HIP was noted to occur due to strain energy as driving force realized by pore closure. [301] In HIP cases studied herein, there was neither pore closure nor RX. Other previously reported cases saw both closure of porosity and grain growth. [102] Though this appears to leave open the possibility of pore closure causing RX, the results of ST also show grain growth

(and no closure of porosity). There would therefore have to be some other primary mechanism for RX of EBM IN718.

Two possible mechanisms are presented for the static RX of an initially overaged, columnar structure of IN718 with significant amounts of intragranular δ-needles as shown in Figure 125(a). There needs to be a source of dislocations to induce static PSN. Both potential mechanisms rely on the assumption that there are plentiful amounts of dislocations present in the as-fabricated structure generated during precipitation and growth of the intragranular δ-phase. Stacking faults within γ'' particles have been noted as a potential mode of the nucleation of intragranular δ-phase. Additionally, "a fairly large number of dislocations were generated in the austenite matrix during δ-phase precipitation." The generation of dislocations could provide positive feedback to promote more stacking fault formation in γ'' particles, causing more δ-phase nucleation. [197] Depending on the number of dislocations generated in the matrix due to the nucleation and growth of intragranular δ-phase, this could be a plausible source of the dislocations necessary to cause RX with PSN reducing the amount of dislocations necessary.

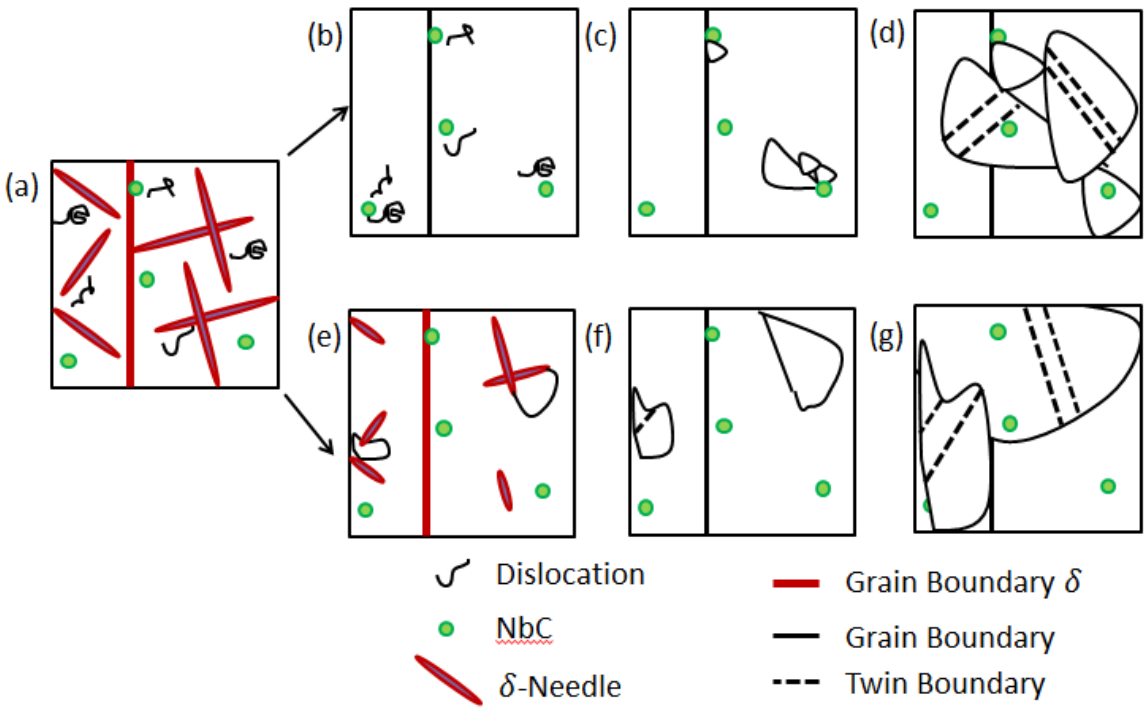

Figure 125. Possible mechanisms for RX during heat treatment of (a) overaged IN718 with columnar grain structure include (b-d) the Carbide PSN mechanism and the (e-g) Needle PSN mechanism.

The first potential mechanism, termed "Carbide PSN" in this paper, shows the initial complete dissolution of δ-phase in Figure 125(b), during which dislocations interact with the strain fields of carbides (which are not dissolved during the ST). The strain fields of the NbC particles reduces the barrier to nucleate new grains via PSN, which form near carbides in Figure 125(c). These grains then grow in Figure 125(d), disrupting the prior columnar grains.

The second potential mechanism, termed "Needle PSN", begins with dislocations interacting via PSN near dissolving δ-needles. The δ-needles still have a large misfit, which produces a local strain field. As the δ-needles dissolve, the precipitate-matrix misfit is replaced by nucleation sites of new grains as shown in Figure 125(e). As the δ-needles are

completely solutioned, the edge of the nucleated grain that is coincident with the needle may form a straight GB or twin boundary as shown in Figure 125(f). The grains in this step have also coarsened. This coarsening continues quickly in Figure 125(g), as the nucleated grains have high angle GBs with respect to the original columnar grains.

The Carbide PSN mechanism would agree with previously literature that has noted preferential RX near NbC. [223] NbC is present throughout the microstructure, and is near some potential nucleation sites in Figure 117.. The Needle PSN mechanism, however, may have been observed in the early stages in Figure 117. In this SEM image, what appear to be small RX grains are present near δ-needles, without preference for presence of NbC (though it is present in some clusters). If these are indeed RX nucleation sites, then it is apparent that the complete dissolution of δ-phase is not required for the initiation of RX (though it is likely necessary to allow RX grains to grow to the sizes observed in this paper). Regardless of the exact mechanism, it is possible for PSN to be the only nucleation mechanism to initiate RX [302].

Previous work on dynamic RX during high temperature tensile testing has identified PSN near δ-phase particles as a mechanism for nucleation, in addition to nucleation at GBs. [224, 225] The reason for this is the formation of dislocation tangles (Figure 126) at δ-needles in deformed material. This work shows that introduced dislocations from deformation can interact via PSN due to δ-phase in IN718. The results by these authors appear to be the first identification of this mechanism in IN718.

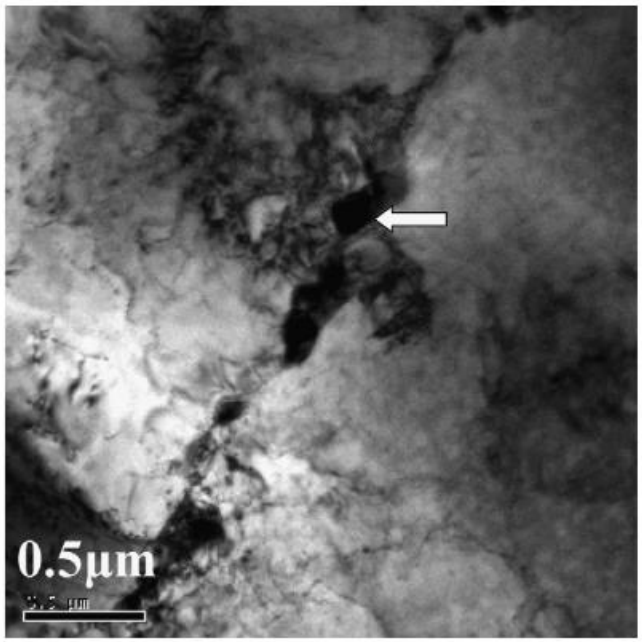

Figure 126. TEM showing dislocations near δ-phase in previous work that noted PSN assisted dynamic RX in IN718. [224]

VII.3 Summary of Post-Processing of EBM IN718

Through analysis of HIP, ST, and STA post-processing treatments on EBM IN718, many conclusions can be drawn:

- HIP processing at lower temperatures and times than standard (1120°C, 100MPa, 4hr) do not fully close shrinkage porosity
- A ST of 1120°C for 2hr was found to dissolve δ-needles without incurring significant amounts grain growth
- Since HIP (1120°C, 100MPa, 2hr) of samples without δ-needles and ST (1120°C, 2hr) of samples with δ-needles neither saw grain growth, it appears that this ST may be used on all as-fabricated microstructures

- Longer and higher temperature ST (1200°C for 4 hr) can result in grain growth and carbide coarsening

The results of the work presented herein identify the need for additional work on post-processing of EBM IN718. Further work should analyze the use of the 1120°C, 2hr ST on material without δ-needles to confirm that the procedure can be used on all as-fabricated EBM IN718 without occurrence of significant grain growth. Additionally, tighter optimization test matrices could determine a more effective ST. Further work should be done to understand the stability of the columnar grain structure and the conditions under which grain growth may occur.

Most importantly, the results of post-processing herein demonstrate that EBM IN718 can be solution treated without incurring significant grain growth. This is significant because it means that engineered grain orientations can be preserved during post-processing to achieve the desired precipitate structure. This means that grain formation and phase formation can be decoupled in EBM IN718.

CHAPTER VIII

MECHANICAL TESTING OF AS-FABRICATED EBM INCONEL 718

Microstructure, thermal history, and process conditions all impact the ultimate measure of performance for IN718: mechanical properties. IN718 is used as a high temperature alloy because it maintains mechanical strength for elevated operating temperatures. Due to these typical uses, fatigue and creep tests are common benchmarks for IN718 performance. It is often easier and faster to perform tensile testing during process development, so tensile testing was used as a means to evaluate the mechanical properties of as-fabricated material from different powder batches (GA, RA, PREP, PA), cool down rates (fast, cool, *in situ* HT), scan strategies (90 degree vs 18 degree rotations), layer thicknesses, orientation, and hold time/temperature. This tensile testing is an important tool to understanding the mechanical performance and differences between the many as-fabricated structures that were produced.

VIII.1 Relationship between Processing, Microstructure, & Mechanical Properties

All of the topics discussed in the previous chapters up to this point (microstructure, process parameters, thermal history, etc.) directly relate to the mechanical properties of a material. The impact of processing directly impacts the microstructure of the material as summarized in Figure 127 (diagram created to explain processing-microstructure-property relationships). The microstructure, in turn, impacts the mechanical properties of the material. If there are too many process defects, an EBM build may fail. Build failures include both builds that do not complete processing of all layers and completed builds that are rejected from use. It is also worth noting that post-processing behavior ultimately impacts mechanical properties as well. The remainder of this chapter will explore the resulting tensile properties measured from various build conditions.

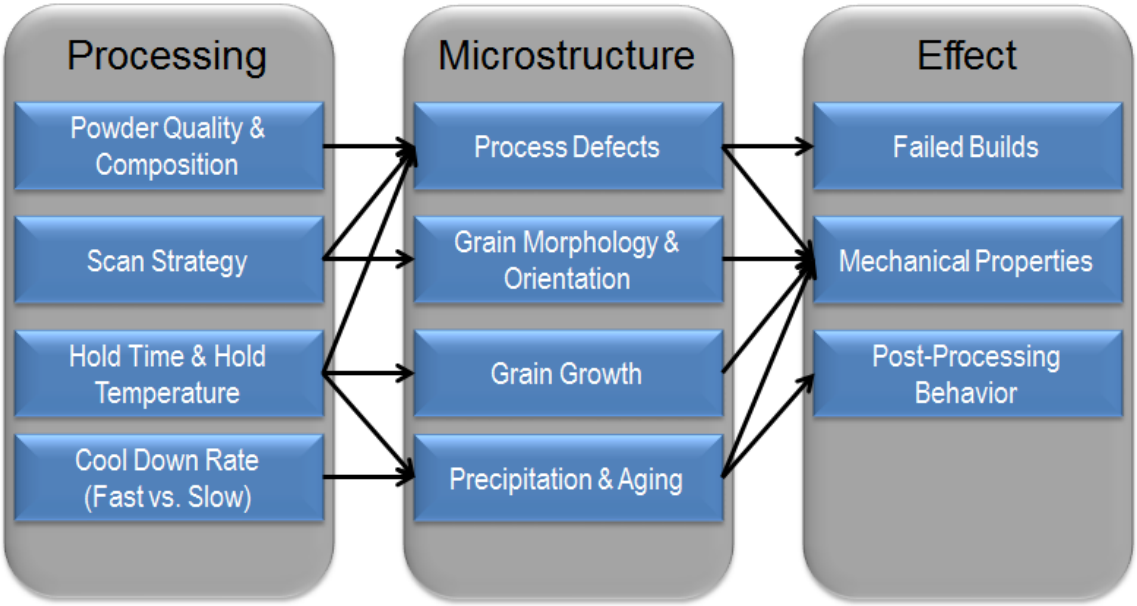

Figure 127. Flow diagram showing the relationship of processing, microstructure, and impact on the final material for EBM.

VIII.2 Influence of Powder Production Method

Previous work attempted to explore the influence of powder type on EBM IN718 production. [20] Powder types were analyzed from gas atomization (GA), rotary atomization (RA), and plasma rotating electrode process (PREP) production techniques. An additional powder type, plasma atomization (PA), was used in some of the follow-up cases presented in this chapter. It was found the PREP powder eliminated the presence of spherical, gas induced porosity from final parts. Other powder types (GA, RA) had porosity inclusions in the powder from atomization (Figure 128) that were translated into the built parts (Figure 129). There was no observed improvement in tensile properties by using PREP powder, but it was noted that the impact of such porosities could be more apparent in fatigue or creep testing. It should be noted that solidification porosities can be highly heterogeneous within

a sample (as discussed in the previous chapter on microstructure). In the threshold analysis of GA vs. PREP powder, it is not entirely possible to separate the contributions of small gas porosities from those of small solidification porosities. Such analysis is highly subjective, due identification of gas pores being made entirely by morphology (spherical shape). It is also known that powder may degrade with use in EBM (Figure 130). Recent work on EBM Ti-6Al-4V powder recyclability has shown that oxygen content increases and Al/V content decreases with powder use. [303] Despite small changes in composition, no negative effects on properties were measured. In fact, it was observed by Tang et al. that YS and UTS both increased with powder use time. Taken together, it appears that powder recycling of IN718 should be possible, though the impact of IN718 powder use in EBM should be the subject of further investigation.

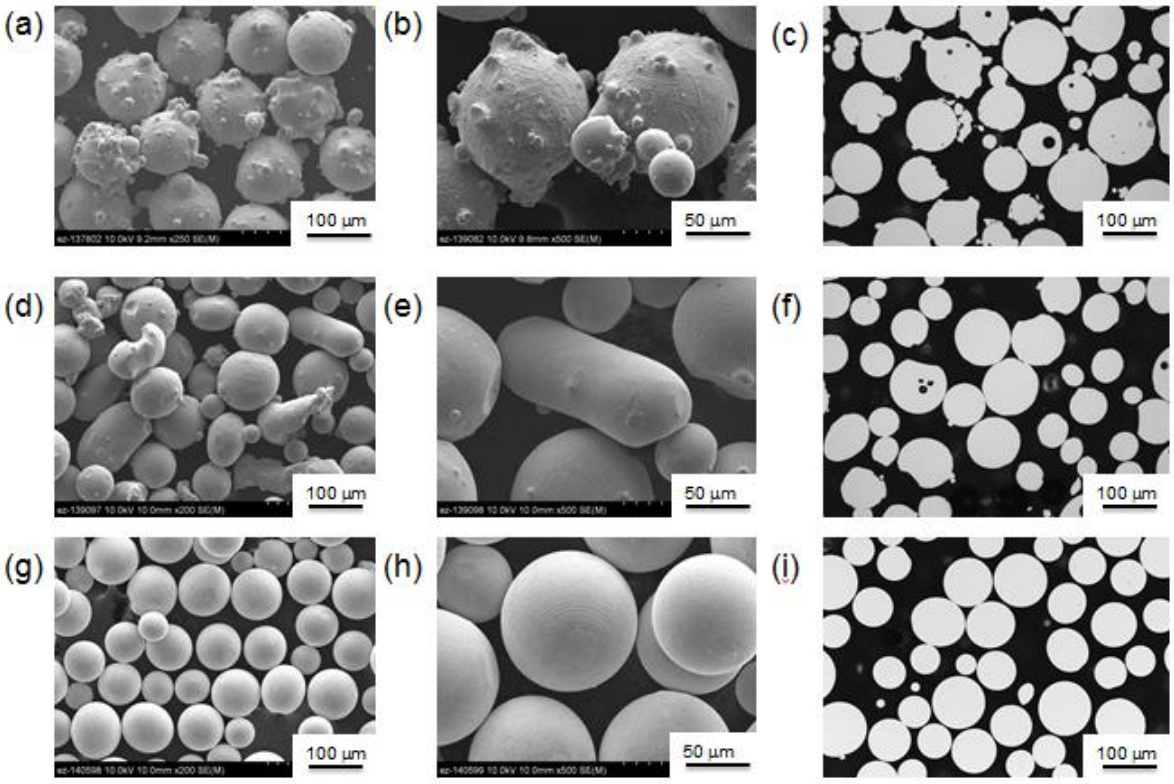

Figure 128. Comparison of powder quality before use: (a) SEM 250x of GA, (b) SEM 500x of GA, (c) LOM of GA, (d) SEM 200x of RA, (e) SEM 500x of RA, (f) LOM of RA, (g) SEM 200x of PREP, (h) SEM 500x of PREP, (i) LOM of PREP. [20]

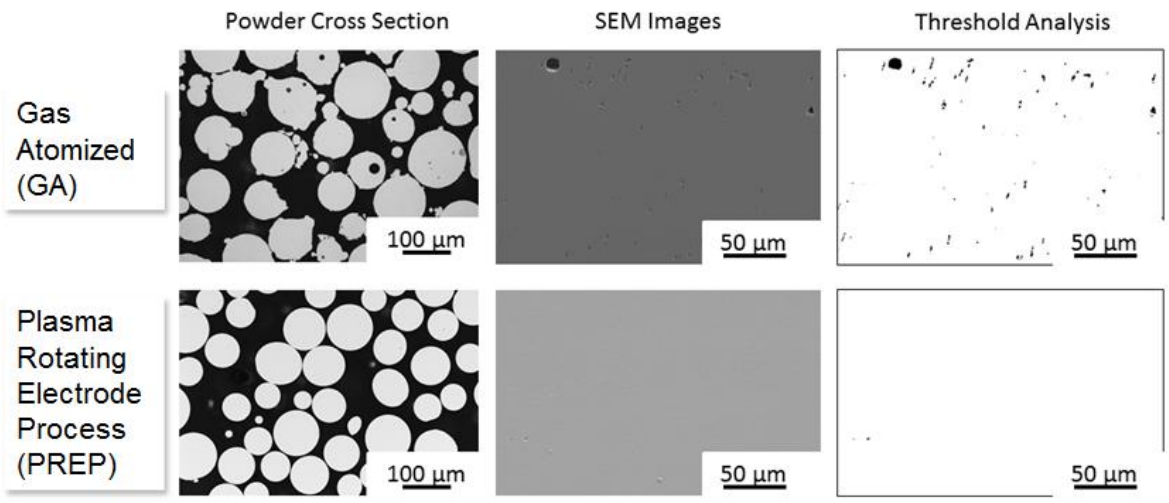

Figure 129. Threshold analysis shows greatly reduced porosity from PREP samples compared to GA samples.

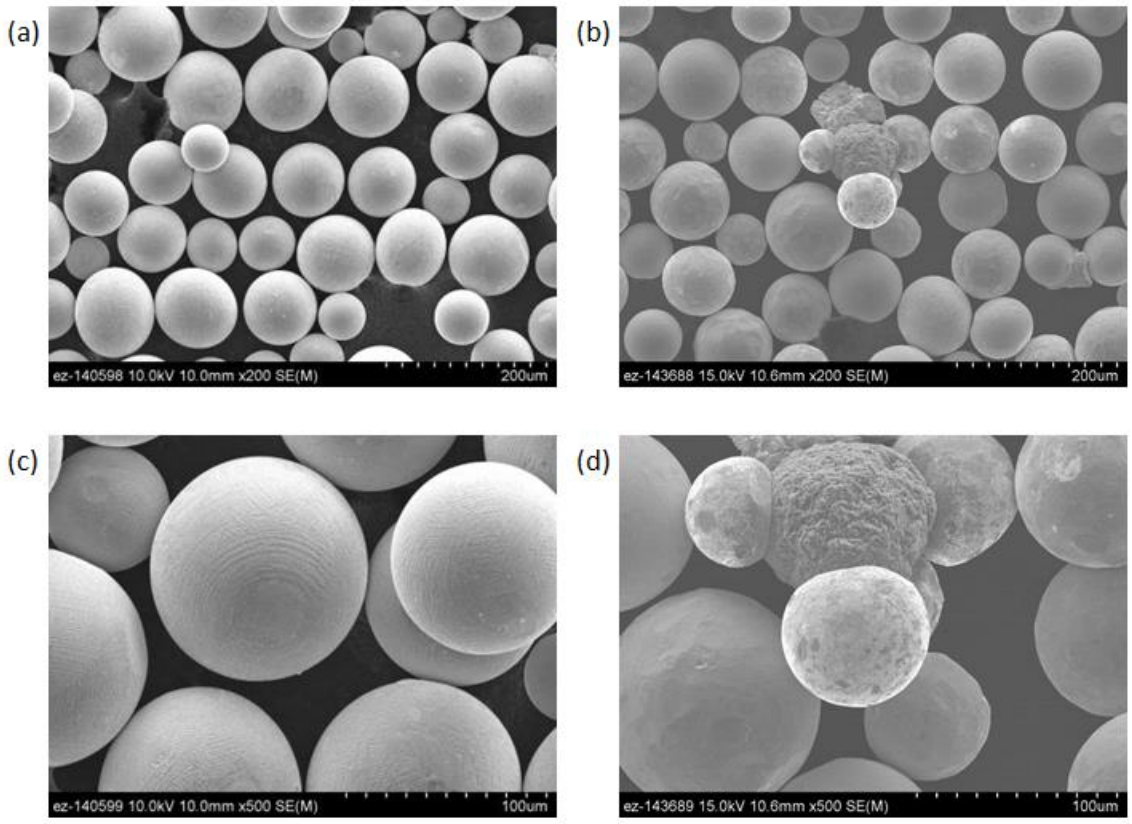

Figure 130. (a) New PREP powder at 200X, (b) used PREP powder after ~420 hours at 200X, (c) New PREP powder at 500X, and (d) used PREP powder after ~420 hours at 500X. [20]

VIII.3 Experimental Procedures

The Standard ASTM E8/E8M for round specimens was considered, within geometrical guidelines for small samples. [304] The gauge diameter was 2.54mm (0.1in) and the grip diameter was 7.62mm (0.3in), with total length up to 80mm (3.15in) depending on material constraints to accommodate space for an extensometer. Some small lathe marks were noted on the samples after failure, which could have influenced results. Reported values of elongation are taken from global strain measurement, without accounting for change in cross section at the end of the gauge length. This means that the elongation values

reported are conservative estimates and maybe systematically underreported. 2-6 samples per case were run. The samples were tested on the equipment pictured in Figure 131.

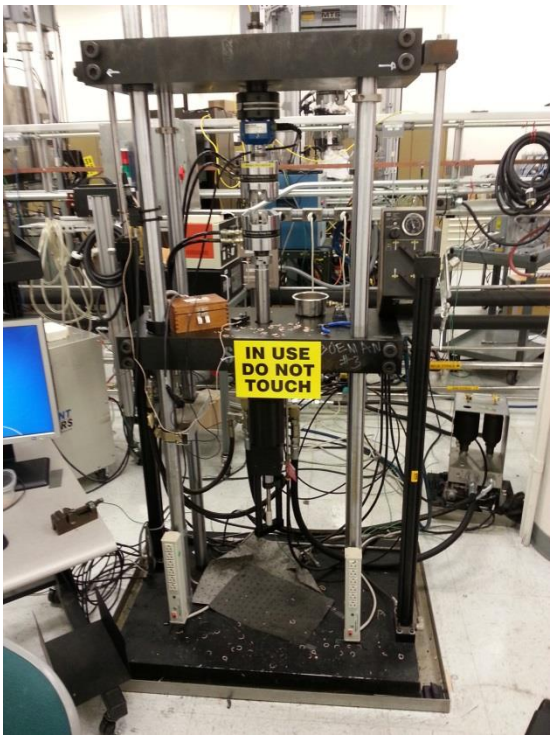

Figure 131. The equipment used at ORNL to perform tensile testing.

VIII.4 Tensile Results & Analysis

Tensile results of various EBM IN718 cases and references are reported in Table 26. The yield strength (YS), ultimate tensile strength (UTS), elongation, and elastic modulus (E) are presented. The YS was measured as the 0.2% offset standard, as is typically used in metals to account for a continuous transition between the elastic and plastic regions. Values of YS and E were calculated from in the elastic region data taken from extensometer readings. UTS and elongation were taken from global measurements. In addition to previously reported cases [20], follow-up data has been added to answer remaining questions about tensile properties in as-fabricated material. The remainder of this chapter will seek to analyze these results.

The sample numbering scheme used in this chapter does not necessarily match the sample numbering scheme used in a previous chapter to discuss log file analysis. Some builds overlap in the numbering scheme, so the corresponding build number from the log file analysis section is given in parentheses where applicable. Otherwise the identifier “A” designates as-fabricated samples. The identifier “B” designates that STA thermal post-processing was performed on the sample prior to testing.

Table 26. Tensile results for as-fabricated EBM IN718.

Build #	Powder	Orientation, Software Version	Cooling Rate	YS [MPa]	UTS [MPa]	Elongation [%]	E [GPa]
1A (#3)	GA	Horizontal - 50 um, v3.2	Fast	590±40	942±61	34.3±2.6	152±9.8
2A (#2)	GA	Horizontal - 50 um, v3.2	Slow	869±32	1108±50	22.1±1.8	150±1.7
3A	GA	Vertical - 50 um, v3.2	Fast	887±16	1003±21	5.4±1.7	121±15.3
4A (#1)	RA	Horizontal - 70 um, v3.2	Slow	957±30	1142±41	19.5±4.6	134±17.6
5A	RA	Horizontal - 50 um, v3.2	Slow	974±20	1186±34	20.1±1.3	151±11.7
6A	GA	Vertical - 50 um, v3.2	Fast	822±12	1082±10	19.6±0.7	152±0.9
7A (#4)	PREP	Horizontal - 50 um, v4.1	Fast	967±28	1186±19	20.0±1.4	180±10.5
8A	PREP	Vertical - 50 um, v4.1	Fast	632±88	1069±44	16.8±2.4	132±5.6
10A	PREP	Horizontal - 75 um, v4.1	Fast	861±21	1117±24	19.2±0.8	143±3.6
13A	PREP	Horizontal - 50 um, v4.1	Slow	939±11	1136±23	21.3±3.8	175±12.4
14A	PA	Horizontal - 75 um, v4.1	Fast	612±16	975±16	25.0±0.8	147±3.3
15A (#6)	PA	Vertical – 75um, v4.1	Fast	895±20	1145±8	12.1±2.8	131±5.0
15A (#6)	PA	Horizontal – 75um, v4.1	Fast	901±27	1120±27	12.4±3.3	164±9.1
16A (#7)	PA	Horizontal – 75um, v4.1	Fast	568±5	818±43	16.9±2.9	90±4.8
20A	PA	Vertical – 75um, v4.1	Fast	926±20	1139±24	15.7±4.3	-

(Table 26 Continued)

Build #	Powder	Orientation, Software Version	Cooling Rate	YS [MPa]	UTS [MPa]	Elongation [%]	E [GPa]
ASTM F42 [92]	-	Horizontal, Stress Relieved	-	635	980	27	-
ASTM F42 [92]	-	Vertical, Stress Relieved	-	600	920	27	-
Unocic 2014 [102]	RA	Vertical (EBM)	NR	669	1207	21	NR
Bampton 2013 [101]	NR	Vertical (EBM)	NR	689.4759	776.809514	3.8	NR
Strondl 2011 [104]	PREP	Horizontal (EBM)	NR	822 ± 25	1060 ± 26	22	NR
Strondl 2011 [104]	PREP	Vertical (EBM)	NR	744 ± 44	929 ± 20	5.5	NR
Zhao 2008 [35]	GA	NR, as-deposited (LRF)	N/A	590	845	11	NR
Amato 2012 [29]	NR	Horizontal, Stress relieved (SLM)	N/A	830	1120	25	NR
Wang 2012 [216]	GA	NR, 20um layer thickness (SLM)	N/A	889-907	1137-1148	19.2-25.9	204

VIII.4.1 Influence of Thermal History

One of the most pronounced effects on tensile properties of EBM IN718 is thermal history. [20, 86] The temperature at which a part holds during layer melting (hold temperature) and

the length of time the process holds at that temperature (hold time) have been found to impact the precipitation of δ-needles, which require special attention during post-processing. Additionally, the cool down rate has been noted to influence the amount of *in situ* aging that a build receives (Figure 132). This chapter explores a series of comparisons of thermal histories to better explain tensile testing results.

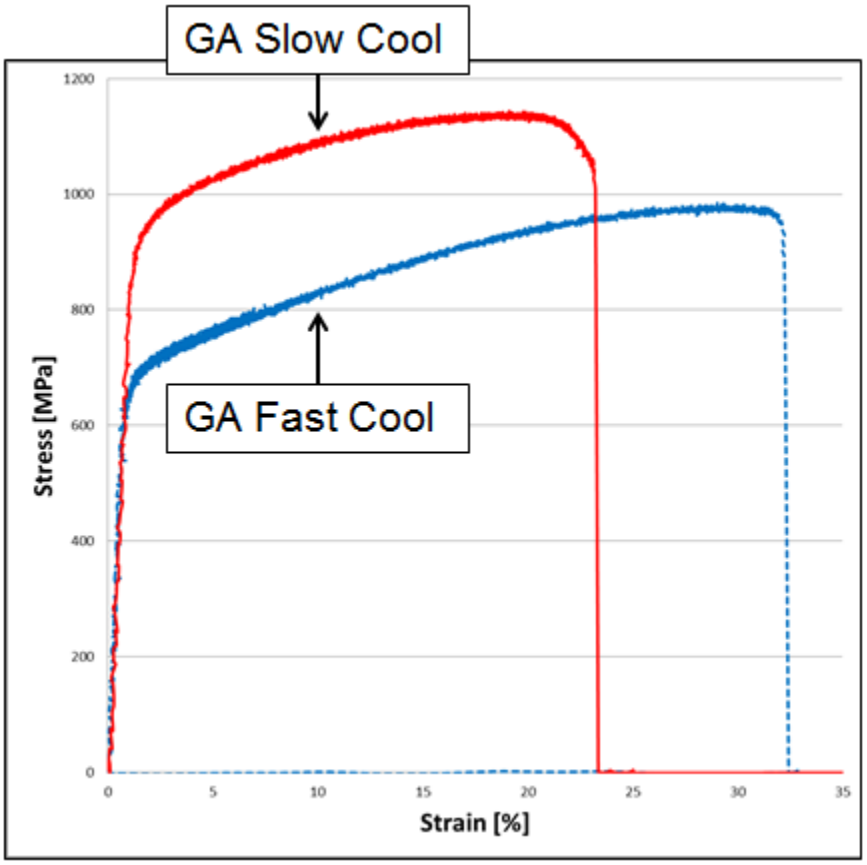

Figure 132. Representative stress-strain tests show the age hardening effect of cool down.

VIII.4.2 Effect of Process Speed

Build 16A had the lowest average layer time during processing but also shows low YS and UTS without a corresponding increase in elongation. This poor performance could be due to larger amounts of solidification or process induced porosity (Figure 133). Alternatively, the melt pool geometry could have been altered by changes in process parameters to optimize for speed. The microstructure was absent of δ-needles, and had the typical features of an underaged build. Thermal post-processing of this sample batch is needed to determine if the resulting tensile properties were due to precipitation or porosity. While 16A had the fastest mass deposition rate for those builds analyzed (0.299 kg/hr), the second highest deposition rate was 15A (0.275 kg/hr). Sample 15A exhibited significantly higher UTS/YS than 16A, with little reduction in elongation. The speed of deposition alone cannot explain the poor performance of 16A.

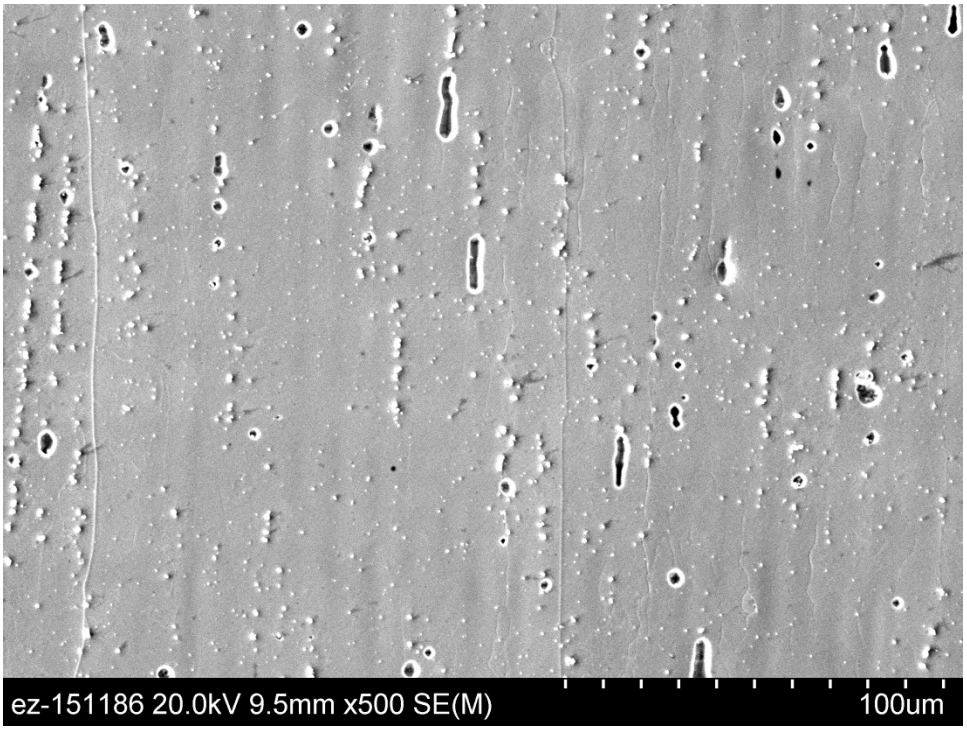

Figure 133. Etched SEM microstructure in the XZ plane of 16A shows aligned carbides and shrinkage porosity in the build direction.

VIII.4.3 Comparison to ASTM Standards

The majority of as-fabricated builds easily meets the ASTM F42 requirements [92] for YS/UTS, but do not come close to the elongation requirement of 27%. Since EBM does not require stress relief (it does not have the large residual stress build-up that LM parts do), meeting the requirement for "stress relieved" parts should not be necessary, since the elongations are set with a system bias towards LM machines. A more general standard would either lower this elongation or set an EBM specific standard to accommodate that values of slightly aged EBM IN718; EBM parts age *in situ*, and should always be expected to have a higher UTS/YS and lower elongation compared to stress relieved (and presumably solution treated) material. Builds 7A and 5A both have the highest UTS/YS with >20%

elongation. Both of these samples used 50um layer thickness, though powder type, software version, and process time/temperature were all variable between samples.

VIII.4.4 Horizontal vs. Vertical Orientation

Build #6 shows the best comparison of vertical to horizontal samples; the vertical and horizontal samples were taken from the same build, so they share the same thermal history (except for potential axial variation, which is addressed in §VIII.4.7). There is no statistically significant difference in UTS, YS, or elongation. It is important to note the significant variation in elastic modulus; since the material is highly oriented in the build direction, it can be expected that the elastic modulus will be different in that direction. Elastic modulus variation is well known for oriented, directionally solidified material. [242] Based on data for IN738 LC, it is expected that the elastic modulus in the solidification direction should be lower than perpendicular to the solidification direction. This effect is seen in the EBM IN718 results presented here; the vertical elastic modulus is less than the horizontal modulus.

VIII.4.5 Layer Thickness

Comparison of 7A and 10A shows lower YS and UTS in 10A, with no statistical difference in elongation. This may suggest that larger layer thickness is detrimental to tensile properties, but thermal history must be taken into account (Figure 134). Build 10A processed at ~1000°C, which has supported low UTS/YS and high elongation when paired with a fast cool down (1A). This is not observed in 10A; 10A shows a higher UTS/YS and lower elongation that was associated with some aging seen from slow cool down (2A). The difference between 10A and 1A may be attributed to significant variation in aging during fast cool, difference in powder type (GA vs. PREP), difference in layer thickness, or difference in scan strategy (3.2 vs. 4.1). Additionally, the short build time means less time at temperature for

homogenization of the as-solidified structure. This could have an impact as well, for the short build time in 10A. Further experiments are needed to answer these questions.

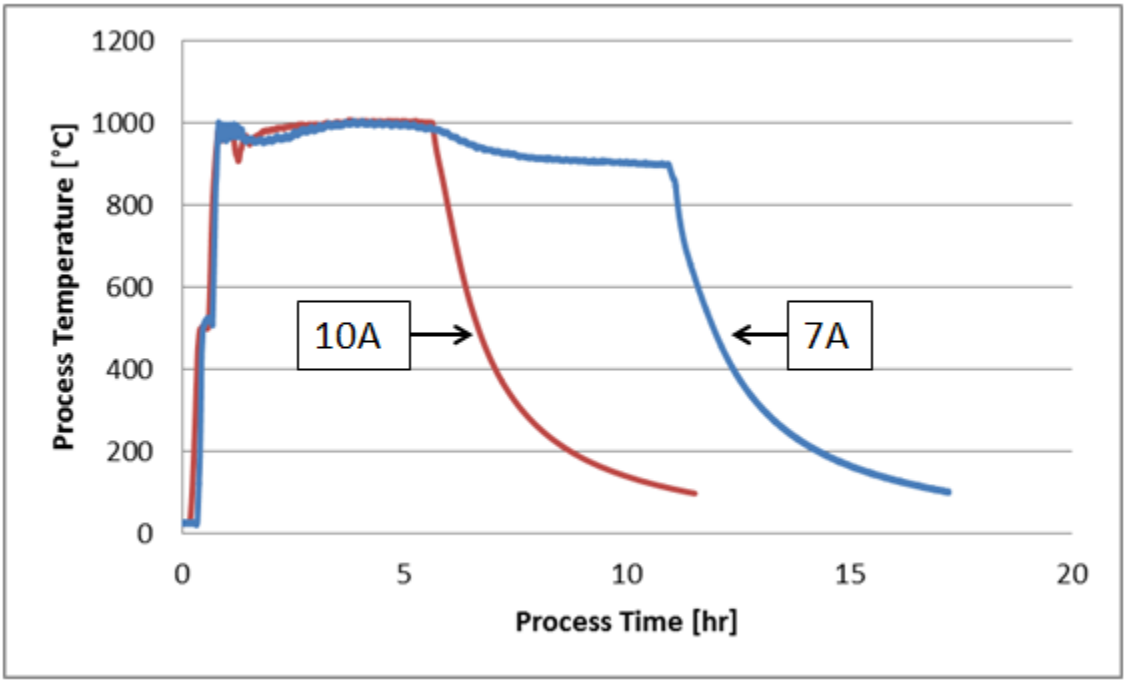

Figure 134. Thermal histories for Builds 7A and 10A shows the speed of the 75um layer thickness with parameters optimized for build speed (Build 10A).

VIII.4.6 Comparison to Previously Reported Results

Vertical as-fabricated samples showed significant improvement in UTS, YS, and elongation compared to previously reported EBM values by Strondl et al. and Bampton et al. Vertical YS in 15A was an improvement over results by Unocic et al., but UTS and elongation were lower. This comparison is of underaged material (15A) to material with significant quantities of δ-needles (Unocic et al.). Sample 20A showed similar results to 15A in the

vertical direction. The average horizontal tensile results for 20A are not presented in tabular format, as there was notable axial variation (§VIII.4.7).

When compared to SLM results by Amato et al. (stress relieved) and Wang et al. (reported as as-fabricated, but values appear to be stress relieved), EBM as-fabricated results reported herein have comparable values of YS, UTS, and elongation. Compared to as-deposited, powder-fed DED samples by Zhao et al., the YS, UTS, and elongation in as-fabricated EBM are higher. Stress relied of the DED material would likely improve the DED results similarly, as was done the reported SLM cases. Regardless of the process (EBM, SLM, DED), thermal post-processing is necessary to obtained peak-aged material (or *in situ* heat treatment in the case of EBM). The comparison of results between platforms will be extended to post-processed material.

VIII.4.7 Axial Variation

Based on previous results, it was determined that horizontal and vertical tensile samples needed to be taken from the same build in order to more accurately compare results. So, horizontal samples were machined out of blocks and vertical samples were machined out of vertical cylinders from the Verification Build geometry (see previous chapter for geometry description). The results of these tensile tests are summarized as a function of build height (z-position) in Figure 135 for sample 15A. There is no table variation in UTS, YS, or elastic modulus. Elongation fluctuates significantly, but the reasons for this fluctuation are not known. Given the sinusoidal shape, no clear correlation with build height exists. Localized porosities in the gauge section of some builds may have been a contributing factor, as solidification shrinkage porosity was present in this build. Elongation in metals has been previously noted to show more response to porosities than UTS or YS. [130] In another case (20A), tensile testing in the horizontal direction did show improvement in UTS, YS, and elongation with increasing distance from the build substrate (Figure 136). The samples with less time in the machine had better tensile properties. The variation in tensile performance

suggests an axial aging or precipitation effect in 20A that was not observed in 15A. Unfortunately, in-depth microstructure analysis along z-axis of 20A was not done, but is necessary to determine the reason for variation in tensile results. Despite not having microstructure analysis of 20A, the thermal history difference compared to 15A can still be considered.

The thermal histories of 15A and 20A show significant differences in process time and temperature (Figure 137). This data suggests that the rate of cooling at the substrate during the melt stage is potentially more important than the process temperature range; both builds have similar process temperature ranges, but 20A does not recover to the 1000°C process window and remains at a lower temperature for the rest of processing. Based on analyses of other builds, it is likely that 20A entered into the temperature range of δ-needle precipitation, which has been noted to negatively impact tensile properties in other samples (Strondl et al., 8A). Follow-up microscopy is hypothesized to show axial variation in δ-needle precipitation.

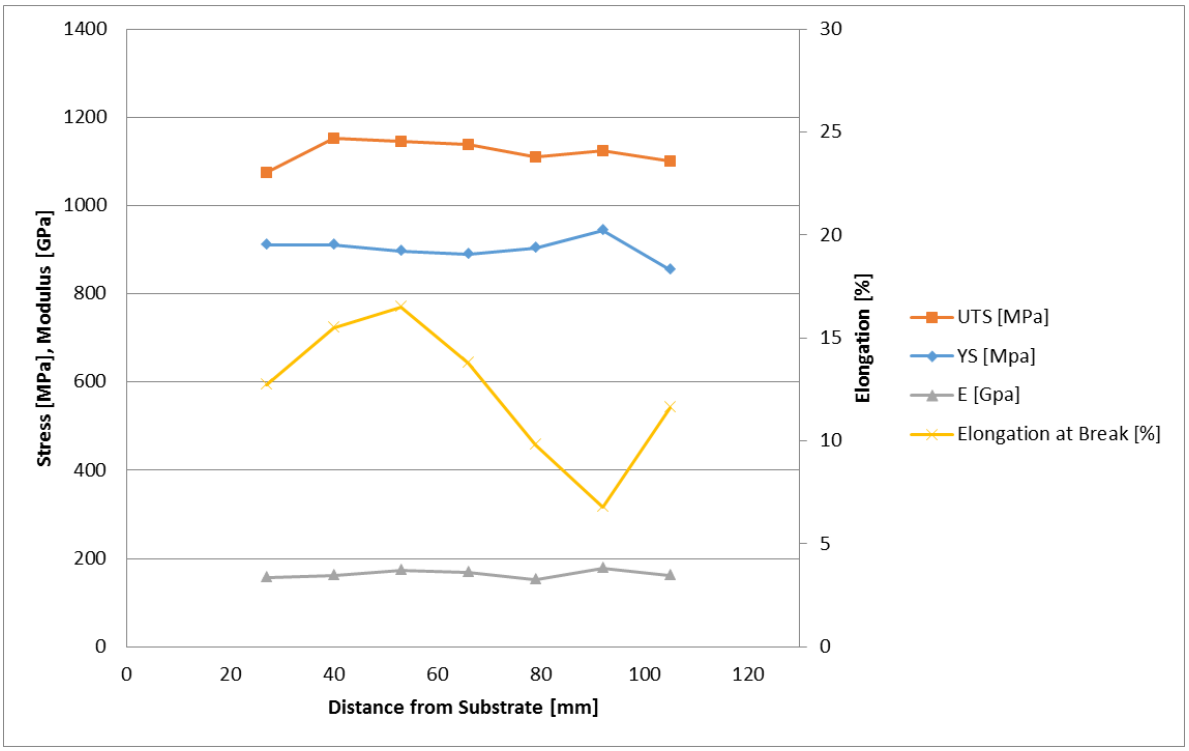

Figure 135. Tensile results of horizontal samples from 15A tested at various z-heights show little variation in UTS, YS, or elastic modulus with sample height.

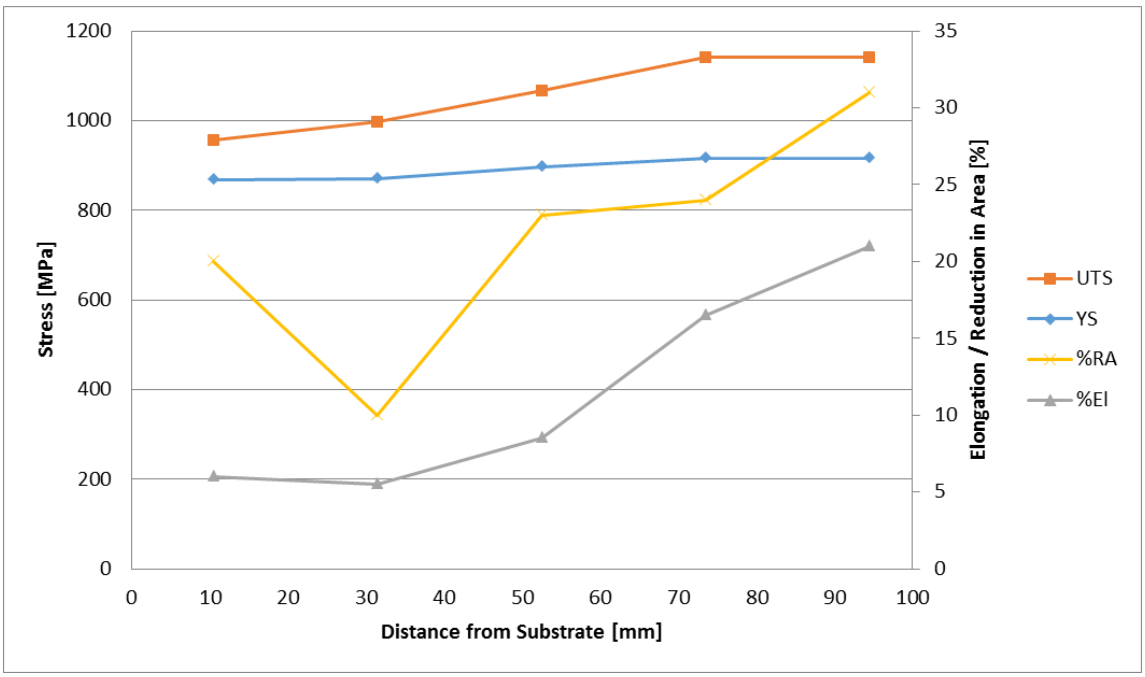

Figure 136. Tensile results of horizontal samples from 20A tested at various z-heights show improvement in UTS, YS, and elongation for material closer to the top of the part.

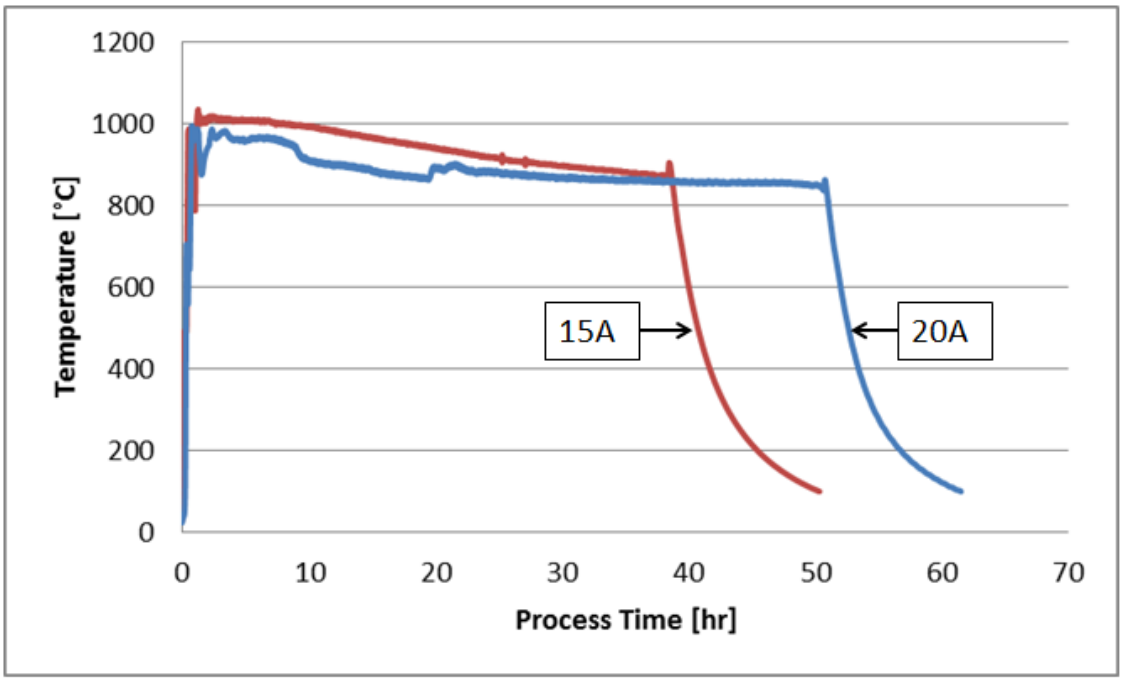

Figure 137. Comparison of the thermal histories for Verification Builds 15A and 20A shows that 20A had lower hold temperature and longer hold time than did 15A.

VIII.4.8 Hold Time

The length of hold time may not impact tensile properties, if the hold temperature it ~1000°C. Stress-strain response (Figure 138) shows similar UTS, YS, and elongation between cases that both used the vacuum, slow cool. Melting temperatures for both cases were ~1000°C, though the 13A case took ~4hr longer to process (Figure 139). This is further evidence to support the use of cool down to control mechanical properties. These observed results imply that holding near the δ-solvus (which is also higher than the γ'' and γ' solvus temperatures) may prevent or delay phase formation, rendering mechanical properties dependent on the amount of aging during cool down. So, if the impact of hold time is not

seen for samples processed near ~1000°C, then the process temperature range is important to define.

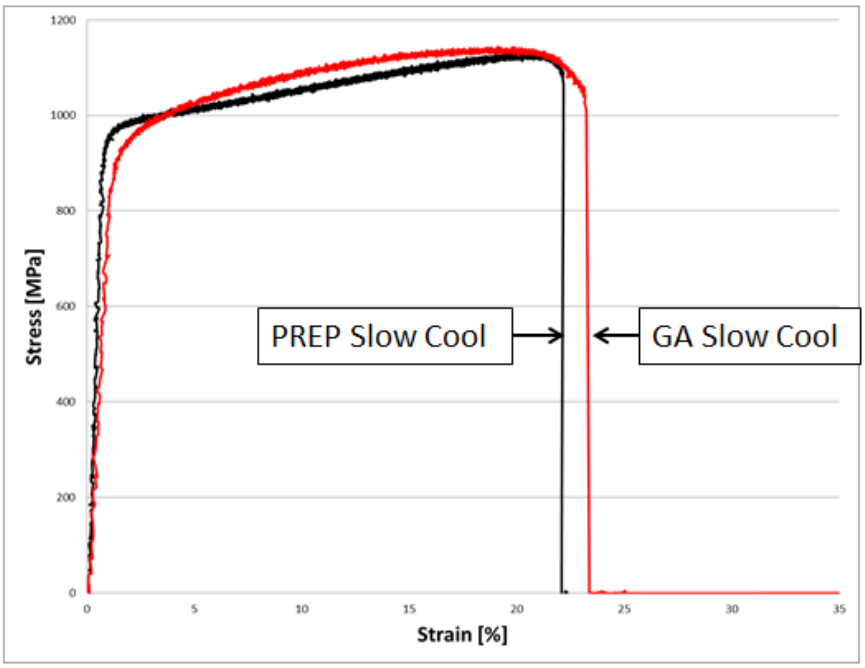

Figure 138. Stress vs. strain response for representative tensile samples for the PREP slow cool (13A) and GA slow cool (Build #2) cases shows limited variation in YS, UTS, and elongation.

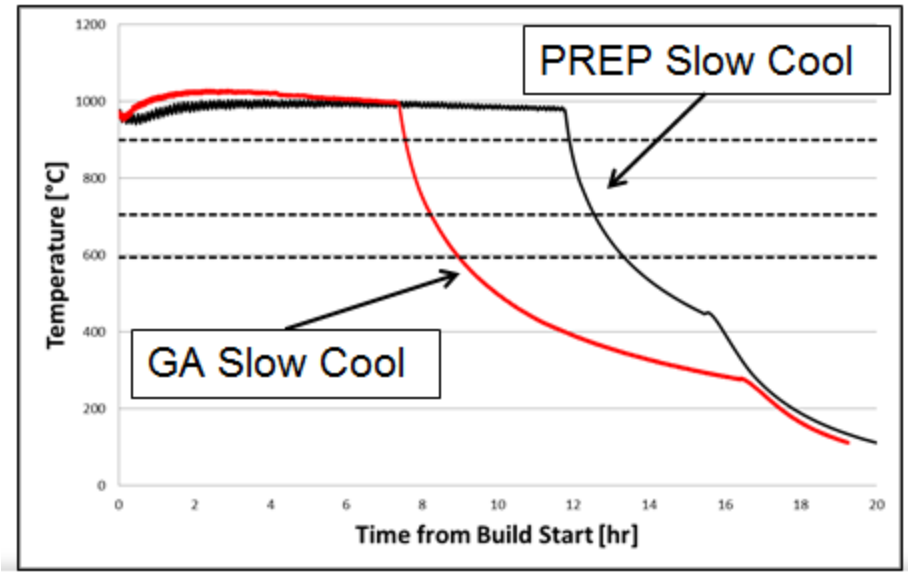

Figure 139. The thermal histories of the PREP slow cool (13A) and GA slow cool (Build #2) cases show an increased hold time for 13A. The hold temperature for both builds remains ~1000°C.

VIII.5 Heat Treated Tensile Results & Analysis

Tensile tests were also run on heat treated material. A standard solution treat and aging (STA) procedure was used; solution treatment at 980°C for 1hr and aging at 720°C for 8hr and 620°C for 10hr was used. The results are presented in Table 27. The results show no statistical difference in YS, UTS, elongation, and elastic modulus for samples produced using the X-Y Tensile geometry for horizontal samples. Notably, the variation in hardening seen between the fast and slow cool builds (Build #2 and Build #3) has been eliminated during the STA process. The results also show increase in UTS/YS and decrease in elongation when compared to the as-fabricated material for all cases in Figure 140. The reduction in variation in tensile properties is shown by comparing representative as-fabricated tensile results to STA results in Figure 141.

Table 27. Tensile test results for standard heat treatment of EBM IN718.

Build #	Powder	Orientation	Cooling Rate	YS [MPa]	UTS [MPa]	Elongation [%]	E [GPa]
1B (#3)	GA	Horizontal - 50um	Fast	1070±11	1260±8	13.4±0.5	165±9.4
2B (#2)	GA	Horizontal - 50um	Slow	1067±1	1245±5	12.5±0.8	159±0.4
7B (#4)	PREP	Horizontal - 50um	Fast	1111±2	1254±1	13.6±0.1	159±2.6
8B	PREP	Vertical - 50um	Fast	942±43	1287±5	13.2±1.6	131±3.3
14B	PA	Horizontal - 75um	Fast	1082±4	1257±9	13.1±0.4	163±4.2
ASTM F42 [92]	-	Horizontal, STA	-	940	1240	12	N/A
ASTM F42 [92]	-	Vertical, STA	-	920	1240	12	N/A
ASM [134]	Wrought Bar	-	-	1190	1430	21	-
ASM [134]	Wrought Sheet	-	-	1050	1280	22	-
Strondl 2011 [104]	PREP	HIP+STA+Age (X-Y), EBM	NR	1154±46	1238±22	7	NR
Strondl 2011 [104]	PREP	HIP+STA+Age (Z), EBM	NR	1187±27	1232±16	1.1	NR
Wang 2012 [216]	GA	STA (NR), SLM	N/A	1102-1161	1280-1358	10-22	201

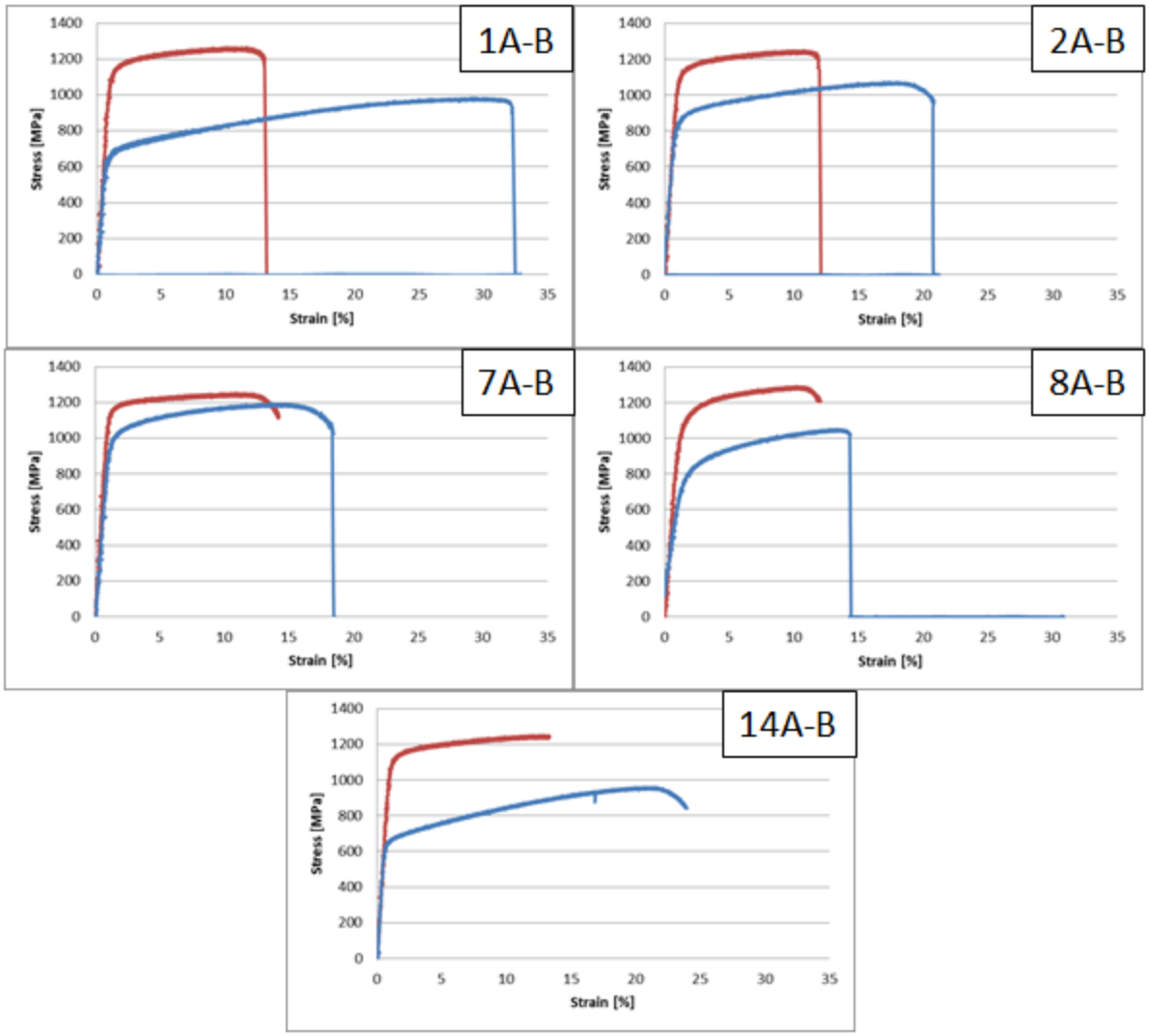

Figure 140. Representative stress-strain response shows STA results in higher UTS/YS and lower elongation for all cases tested. Each plot is a direct comparison between the as-fabricated and STA material from the same batch.

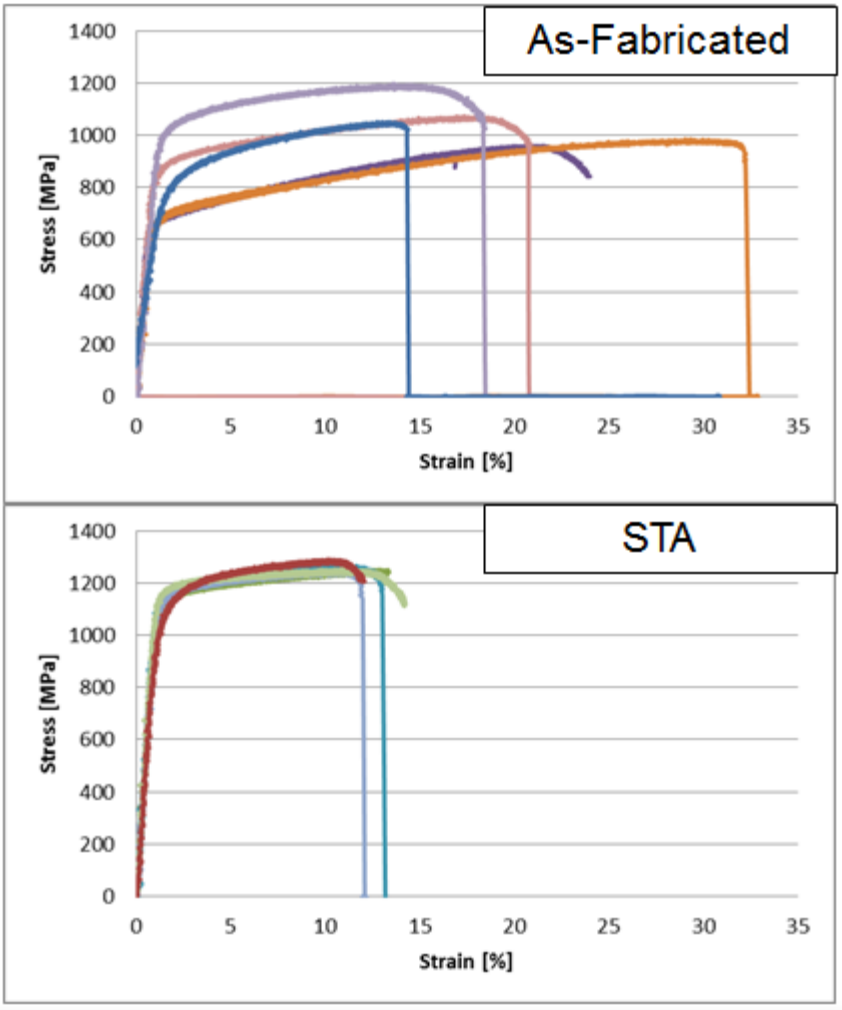

Figure 141. (Top) Representative tensile tests across samples 1, 2, 7, 8, 14 and (Bottom) representative STA tensile results of the same samples.

The vertical sample showed similar elongation, lower YS, lower elastic modulus, and higher UTS. The exact mechanism for the difference is not known, though it was observed (in a previous chapter on post-processing) that δ-needles present in the as-fabricated vertical sample were not solutionized by the 980°C solution treatment which is below the δ-solvus. This significant difference in microstructure may be responsible for the observed variation

in tensile properties. Further studies on the effect of large volume fractions of δ-phase on tensile properties of IN718 would be necessary to confirm this.

The tensile results of heat treatment material meet and exceed ASTM F42 requirements [92] for UTS, YS, and elongation of STA PBF IN718. The as-fabricated UTS/YS nearly meet stress relieved requirements (Figure 142) and exceed the standard after STA. Similarly, elongation of as-fabricated EBM IN718 nearly meets the standard (Figure 143) for stress relieved powder bed fusion material and exceeds the standard after STA.

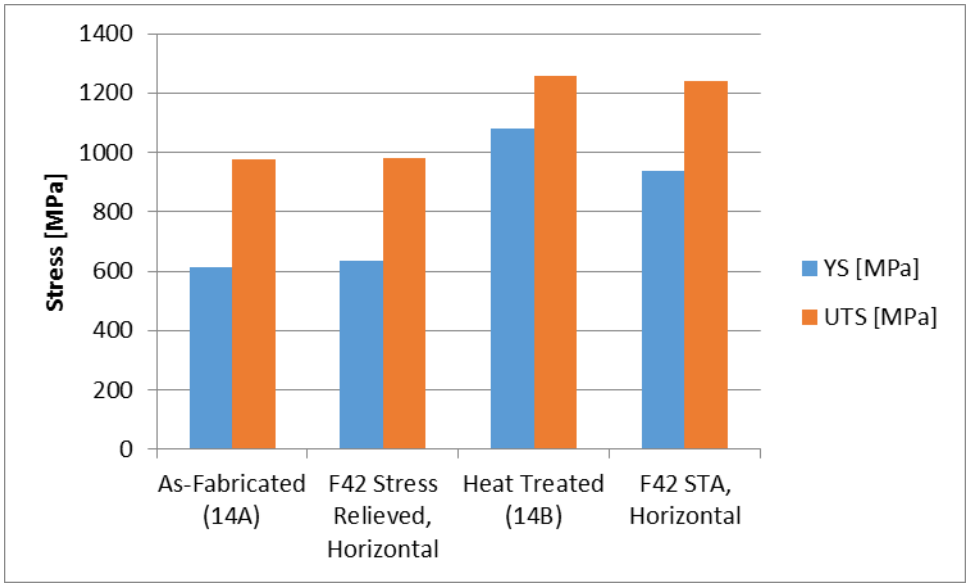

Figure 142. Results of YS and UTS show that as-fabricated EBM material nearly meets the ASTM standard for stress relieved IN718 from powder bed fusion and that, after heat treatment, EBM STA material exceeds the standard for UTS/YS.

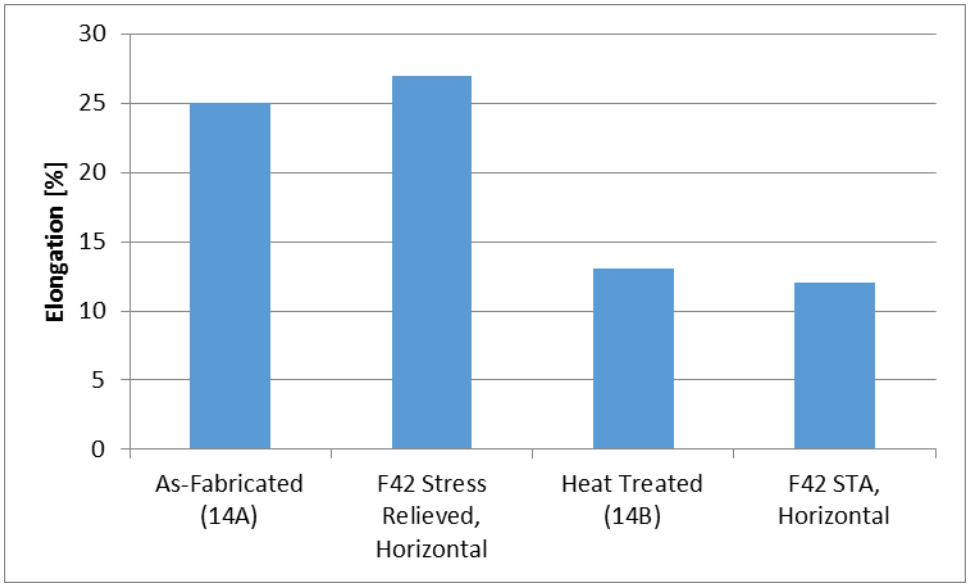

Figure 143. As-fabricated EBM IN718 nearly meets the ASTM standard for elongation for stress relieved powder bed fusion material and exceeds the standard for elongation after STA.

The heat treated tensile results show significant improvement in elongation compare to previously reported values for EBM by Strondl et al., but similar values of UTS and lower YS. The properties of the heat treated EBM IN718 by Strondl et al. was noted to have poor performance due to the continued presence of δ-phase needles, which were also present in sample 8B (which underperform other samples without δ-needles) in the data herein. This improvement to a more ductile material may improve fatigue and creep life, also leading to less catastrophic failure. The STA EBM tensile tests reported here are comparable to the lower end of the ranges for UTS, YS, and elongation reported for STA LM material by Wang et al.

VIII.6 Conclusions on Mechanical Properties

Through the study of tensile properties, some important conclusions can be made:

- As-fabricated EBM material nearly meets the ASTM standard for YS, UTS, and elongation for stress relieved powder bed fusion IN718, though the standard is clearly defined for LM processes
- STA EBM material meets and exceeds the ASTM standard for YS, UTS, and elongation set for STA IN718 for powder bed fusion
- STA achieves nearly uniform properties in samples without δ-needles
- The tensile properties of wrought bar are better than EBM IN718 in terms of YS, UTS and elongation, though the properties of wrought sheet are similar to EBM IN718
- STA improves the UTS and YS of as-fabricated material at the expense of elongation (classic age hardening)
- The formation of δ-needles in the microstructure appears to negatively impact tensile properties, which is in agreement with early results by Strondl et al. [104]
- The effect of hold time appears less important than the effect of hold temperature on tensile properties
- Builds held near ~1000°C typically prevent significant quantities of δ-phase from forming, with the resulting tensile properties mostly determined by aging during cool down

For samples without significant formations of δ-needles, it was observed in this chapter that STA tensile results were statistically equivalent despite previous differences in as-fabricated properties due to layer thickness, processing strategy (software), or powder type. If techniques explored in the previous chapter on post-processing are used on samples with δ-needles, variation in mechanical properties due to differences in processing technique should be reduced compared to the results in this chapter (sample 8B had lower tensile

properties than other STA samples without δ-needles). No literature exists on tensile properties that include volume fractions of δ-phase greater than 1.38%, so future work should explore the effect of larger volume fractions and the change in deformation mechanisms. [240] Further testing is needed to explore the fatigue and creep properties of both the as-fabricated material and the post-processed material.

CHAPTER IX

CONCLUSIONS & RECOMMENDATIONS

The preceding chapters of this work have introduced metal Additive Manufacturing, introduced IN718 metallurgy, analyzed the effect of process parameters, reported common features in as-fabricated IN718 microstructure, demonstrated a novel, controlled *in situ* heat treatment, explored recrystallization and aging during post-processing, and examined the tensile properties of as-fabricated and post-processed material. Taken together, this work addresses the challenges associated with process development and achieving desired mechanical problems. Ultimately, this work supports material property and process improvement in producing parts for end-use (Figure 144). A brief summary of each major topic is presented here.

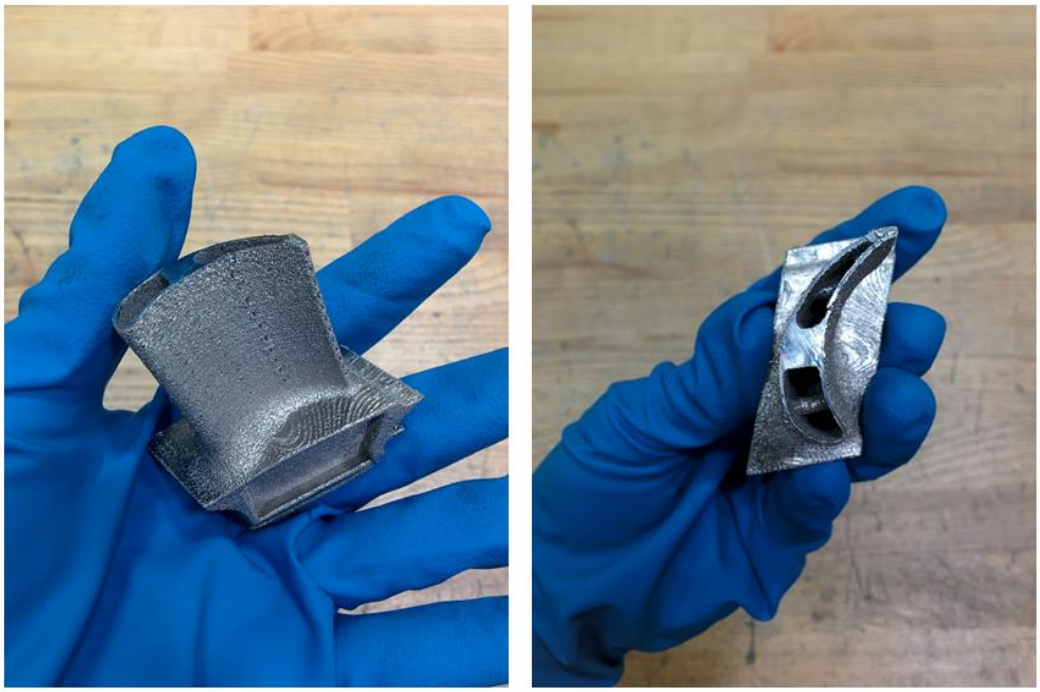

Figure 144. (Left) Turbine blade made of IN718 using EBM at ORNL with (Right) internal features exposed by cutting through the sample cross-section. (Credit: W. Sames)

IX.1 Process Parameters & Hardware/Software

The EBM process has a more complex process controls on beam power and speed than LM processes, which were defined in detail herein. It was shown that some swelling defects can be explained by analyzing local variations in applied energy (Figure 145). Additionally, layer time was shown to be highly dependent on part geometry and the angle of rectilinear infill of the snaking melt scan strategy. Analyzing the current vs. time profile for a single layer was shown to be an effective technique for understanding the ultimate impact of process parameters on applied energy. Builds that maximized the current used during melting also maximized beam speed, which reduced individual layer time. Layer thickness was shown to impact overall build time (increasing or decreasing the number of layers required to be melted in a part), but did not necessarily impact individual layer time in the cases studied. The IN718 EBM process was compared to the Ti-6Al-4V EBM process, which shows that the IN718 operates at much higher temperatures. Build time for IN718 can be longer when the same layer thickness is used, but the standard 75um layer thickness process for IN718 is fast than the standard 50um layer thickness process for Ti-6Al-4V. While IN718 is slower on volumetric deposition rate than Ti-6Al-4V, both materials have similar ranges of mass deposition rate.

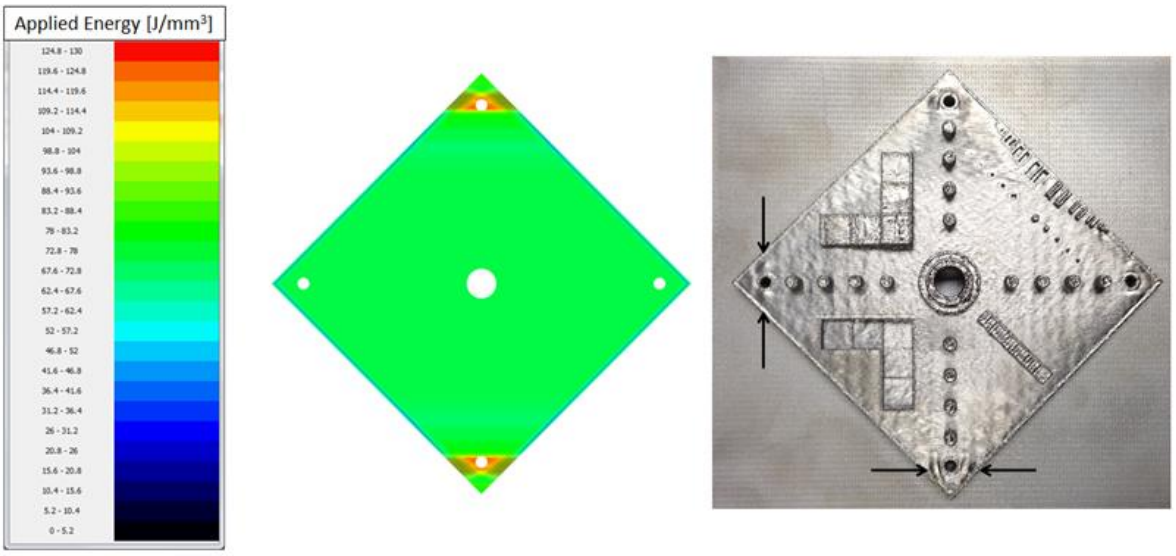

Figure 145. Analysis of process parameters shows that (Left) increases in local applied energy can lead to (Right) swelling in EBM parts (IN625 pictured).

IX.2 As-Fabricated Microstructure

The as-fabricated microstructure of EBM IN718 was shown to have two major possibilities: underaged or "overaged". Both structures show oriented columnar grains, networks of small precipitates, columnar architectures of carbides, and shrinkage porosity. The "overaged" material also has the additional growth of intragranular δ-phase needles. The formation temperature range of the δ-needles is characteristic of direct precipitation from a supersaturated matrix, so the structure is not likely from the actual overaging transition of $\gamma'' \rightarrow \delta$. The presence or absence of these δ-needles is very significant during thermal post-processing. The formation of δ-needles was shown to be related to process temperature (Figure 146).

Additionally, material near the top of a build was shown to have a much different structure that included clusters of precipitates and shrinkage pores aligned at interdendritic regions. This top region is limited to the top 30-35um from the surface of a build, and may be considered as close to “as-solidified” as can be observed in EBM material. The bulk microstructure is significantly different due to an effective *in situ* homogenization from holding at a high processing temperature (~1000°C).

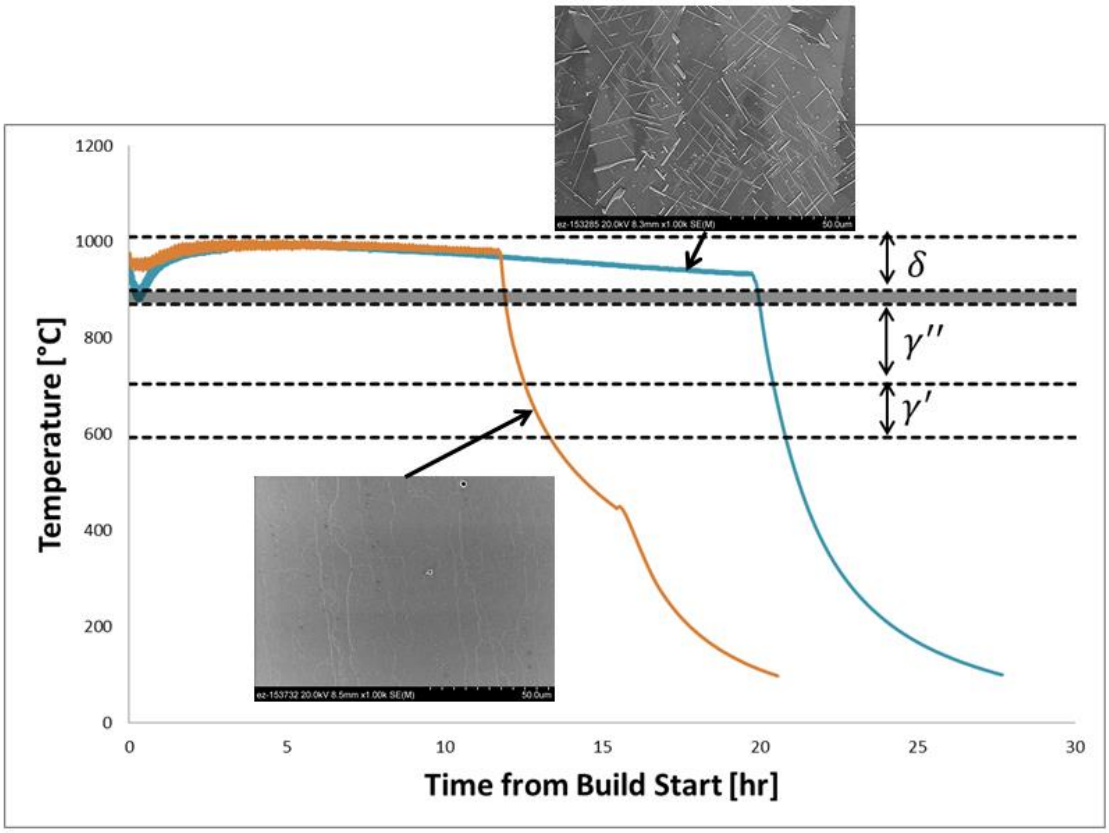

Figure 146. The formation of intragranular δ-phase needles typically happens in samples where build temperature falls below the temperature for direct δ-phase precipitation from the matrix (~960°C).

IX.3 *In Situ* Heat Treatment

In situ aging occurs naturally during cool down but can also be controlled through a novel process that was demonstrated herein. For material processed near 1000°C without intragranular δ-needles, cool down was shown to be the primary aging mechanism. Precipitate sizes grow and the morphologies of matrix phases change with increasing cool down time. An age hardening response was shown between using a vacuum (slow) cool and a helium-injection (fast) cool, with the slow cool case showing hardening. A novel, controlled cool down approach (*in situ* HT) was designed to mimic a standard solution treatment and aging process. The ISHT achieved hardness values at or above those of peak-aged material (Figure 147).

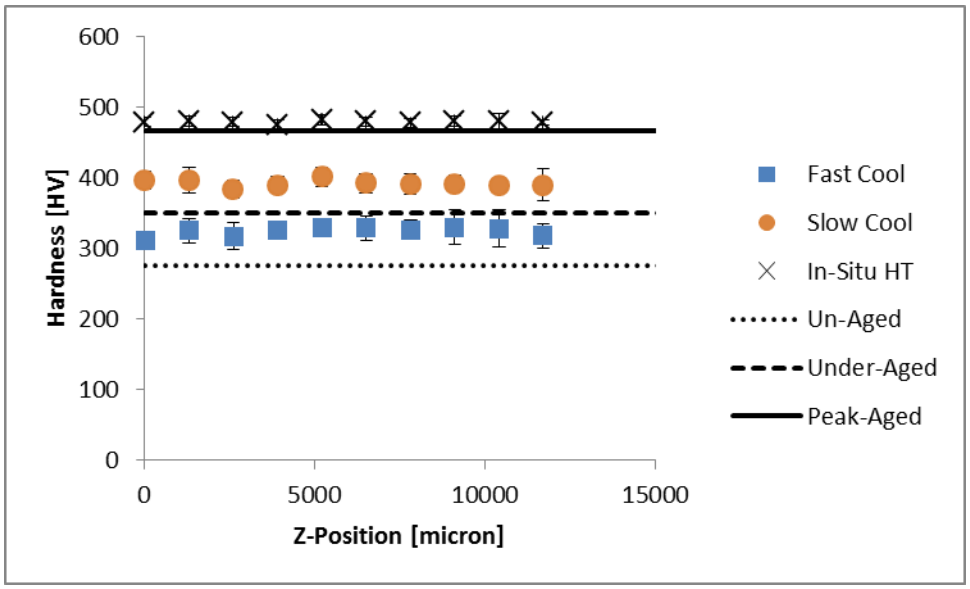

Figure 147. Cool down procedure was shown to effect significant changes in hardness.

IX.4 Post-Processing

Variation in post-processing results was shown to relate to the as-fabricated microstructure, with the presence of absence of δ-needles being the defining feature. High temperature (1200°C) solution treatment (ST) and hot isostatic pressing (HIP) of samples with δ-needles present experienced large amounts of grain growth (Figure 148) that transformed the oriented, columnar grain structure into large, misoriented grains with annealing twins present. A low temperature (1020°C, 1hr) ST was observed to not fully dissolve δ-needles. A medium temperature (1100°C, 2hr) ST was found to completely dissolve δ-needles, without disrupting the oriented, columnar grain structure (only small regions of grains were noted to be anomalous). This ST is considered an "optimized" ST, where dissolution of prior phases is balanced with grain growth. The origins of grain growth in EBM material were considered, with both classic, discontinuous grain growth and growth of recrystallized grains presented as possible explanations. Heavy grain texture and pinning of grain boundaries (GBs) both promote discontinuous grain growth (grain growth that has a rapid increase in the rate of growth at a certain temperature). EBM material is not worked, not deformed, and has low amounts of residual stress; so the only possible source of dislocations for RX could be from generation of dislocations from the growth of δ-needles (which are known to generate dislocations during growth due to misfit with the matrix). The optimized ST shows that the as-fabricated grain structure and orientation can be maintained throughout processing, if desired (this means that engineered grain structures can be maintained during post-processing).

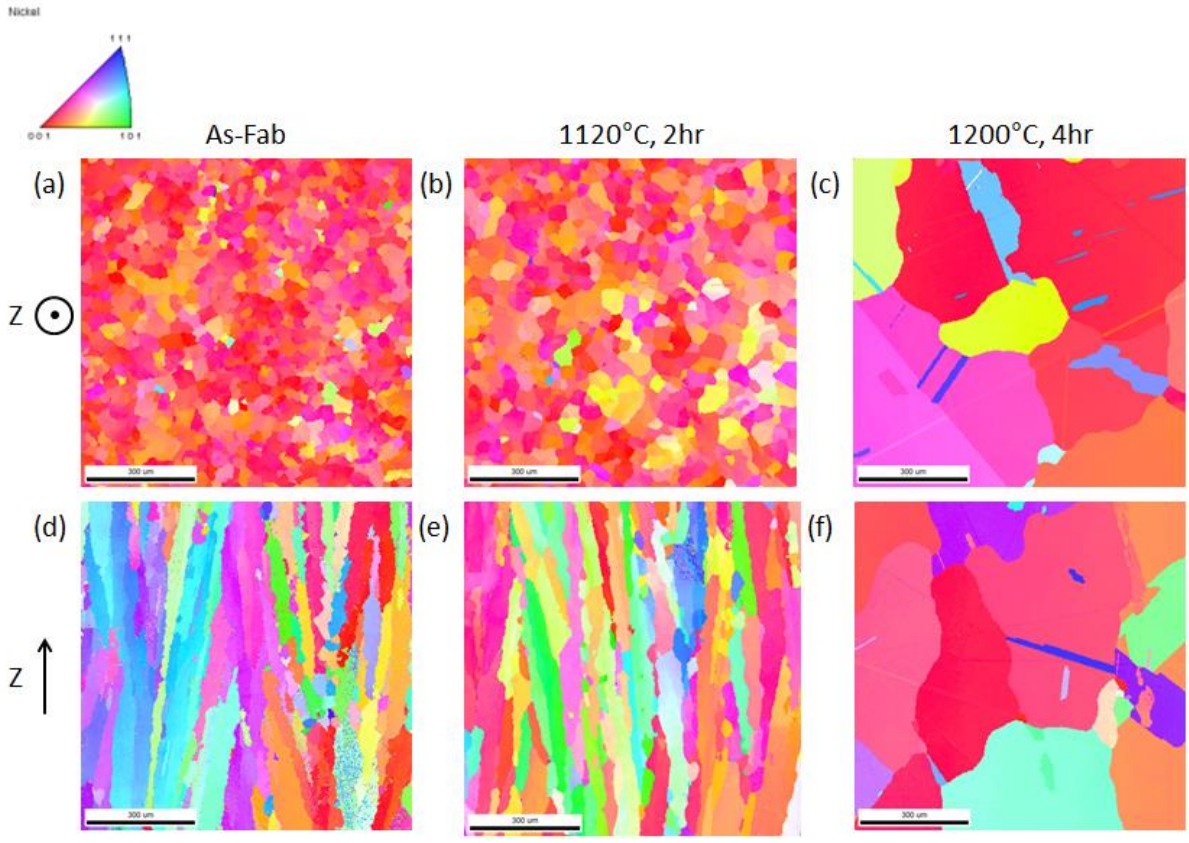

Figure 148. An (b, e) optimized solution treatment can be used to dissolve δ-needles without incurring significant grain growth as seen at (c,f) higher temperatures.

IX.5 Mechanical Properties

The tensile properties of EBM IN718 were shown to have some variance based on microstructure, have reduced variability upon STA, and meet ASTM standards. Differences in build orientation (horizontal vs. vertical), part size, and build temperature were all shown to be important to as-fabricated tensile properties. For most cases, STA eliminated these differences and resulted in consistent tensile properties (YS, UTS, and elongation). The presence of intragranular, δ-phase needles was shown to impact tensile properties in both as-fabricated and STA samples (when not fully solutionized). Though ASTM standard F3055-

14 on powder bed fusion of IN718 shows bias towards LM parts (stress-relief is not typically performed on EBM material), EBM nearly meets the requirements of YS, UTS, and elongation without any thermal post-processing. STA EBM IN718 exceeds the F3055-14 standard for YS, UTS, and elongation of STA material.

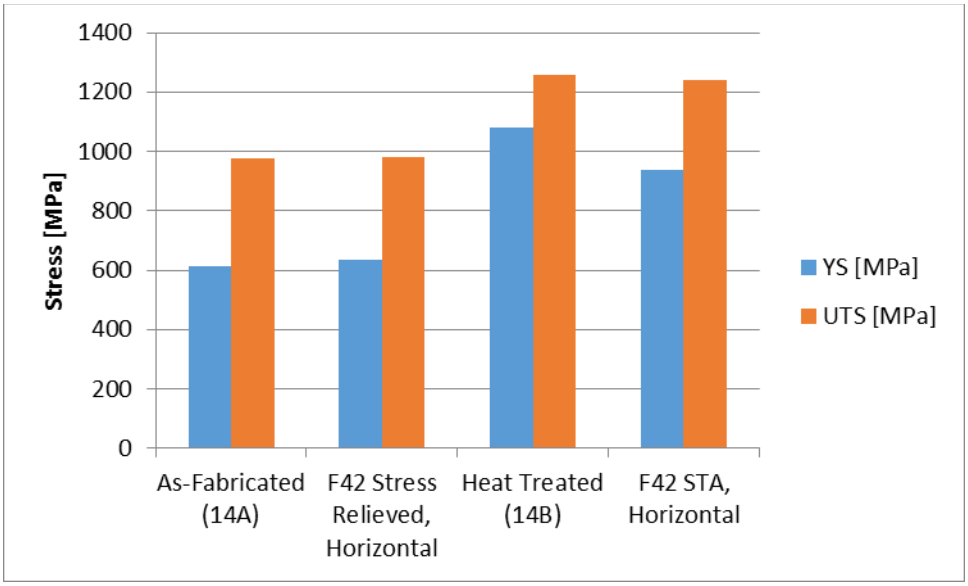

Figure 149. EBM IN718 nearly meets ASTM F3055 standards by the F42 committee for stress relieved material directly from the machine. Heat treated EBM IN718 exceeds the F3055 standards for YS, UTS, and elongation.

IX.6 Future Work

The results presented herein identify the need for future work in both EBM processing and IN718 metallurgy. Specifically, the following recommendations are made regarding future research directions:

- The EBM process speed can be increased through process parameter design choices, and work should be done to significantly increase the process speed
- Demonstrate mechanical post-processing for EBM IN718 by removing powder under a wide range of sintering conditions and machining or polishing a wide range of surface finishes
- *In situ* aging can be controlled to change as-fabricated material properties by using a controlled cool down, but process control changes are needed to reduce the amount of powder-oversintering that occurs
- Proposed mechanisms for grain growth or RX in unstressed EBM IN718 should be explored in detail using *in situ* SEM annealing, modeling, or other techniques
- Use of the optimized solution treatment presented herein should be explored on material without δ-needles to explore universal application of the treatment
- Further material development for the EBM process should be done to continue to expand the range of materials offered by the process

REFERENCES

[1] W. J. Sames, F. A. List, S. Pannala, R. R. Dehoff, and S. S. Babu, "The Metallurgy and Processing Science of Metal Additive Manufacturing," *International Materials Reviews,* 2015 (Invited, Internal Review).

[2] C. R. Deckard, "Part generation by layer-wise selective laser sintering," M.S., Univeristy of Texas - Austin, Austin, TX, 1986.

[3] A. Lou and C. Grosvenor. (2012, 4/11/2014). *Selective Laser Sintering, Birth of an Industry*. Available: http://www.me.utexas.edu/news/2012/0712_sls_history.php

[4] C. R. Deckard, "Selective Laser Sintering," Ph.D., Univeristy of Texas - Austin, Austin, TX, 1988.

[5] D. L. Bourell, H. L. Marcus, J. W. Barlow, and J. J. Beaman, "Selective laser sintering of metals and ceramics," *International Journal of Powder Metallurgy,* vol. 28, pp. 369-381, 1992.

[6] H. L. Marcus, D. L. Bourell, J. J. Beaman, A. Manthiram, J. W. Barlow, and R. H. Crawford, "Challenges in Laser Processed Solid Freeform Fabrication," presented at the TMS-AIME Fall Meeting, Pittsburgh, PA, United states, 1993.

[7] C. R. Deckard, "Method and apparatus for producing parts by selective sintering," PCT Patent WO1988002677 A2, 1986.

[8] M. J. Cima, J. S. Haggerty, E. M. Sachs, and P. A. Williams, "Three-dimensional printing techniques," U.S. Patent US5204055 A, 1989.

[9] EOS-GmbH. (April 16, 2014). *History*. Available: http://www.eos.info/about_eos/history

[10] Sandia-National-Laboratories. (1997). *Creating a complex metal part in a day is goal of commercial consortium*. Available: http://www.sandia.gov/media/lens.htm

[11] D. White, "Ultrasonic object consolidation," U.S. Patent US6519500 B1, 1999.

[12] L.-E. Andersson and M. Larsson, "Device and arrangment for producing a three-dimensional object," U.S. Patent US 7537722 B2, 2000.

[13] Arcam-AB. (April 16, 2014). *Arcam History*. Available: http://www.arcam.com/company/about-arcam/history/

[14] F. P. Jeantette, D. M. Keicher, J. A. Romero, and L. P. Schanwald, "Method and system for producing complex-shape objects," U.S. Patent US 6046426 A, 1996.

[15] K. Skiba, E. J. Hirst, and A. Sachdev. (2014). *Obama formally annouces Chicago as site for digital manufacturing lab*. Available: http://articles.chicagotribune.com/2014-02-26/site/ct-digital-lab-obama-0226-biz-20140226_1_president-barack-obama-institutes-advanced-manufacturing-partnership

[16] ASTM-International, "Standard Terminology for Additive Manufacturing Technologies," vol. F2792-12a, ed. West Conshohocken, PA: ASTM International, 2012.

[17] J. P. Kruth, X. Wang, T. Laoui, and L. Froyen, "Lasers and materials in selective laser sintering," *Assembly Automation,* vol. 23, pp. 357-371, 2003.

[18] custompartnet.com. (2015). *Direct Metal Laser Sintering*. Available: http://www.custompartnet.com/wu/direct-metal-laser-sintering

[19] Arcam-AB. (2015). *EBM Hardware*. Available: http://www.arcam.com/technology/electron-beam-melting/hardware/

[20] W. J. Sames, F. Medina, W. H. Peter, S. S. Babu, and R. R. Dehoff, "Effect of Process Control and Powder Quality on Inconel 718 Produced Using Electron Beam Melting," in *Superalloy 718 and Derivatives*, Pittsburgh, PA, 2014.

[21] Sciaky. (2014). *Additive Manufacturing*. Available: http://www.sciaky.com/additive_manufacturing.html

[22] R. P. Mudge and N. R. Wald, "Laser Engineered Net Shaping Advances Additive Manufacturing and Repair," *Welding Journal,* vol. 86, pp. 44-48, 01// 2007.

[23] M. L. Griffith, D. L. Keicher, J. T. Romero, J. E. Smugeresky, C. L. Atwood, L. D. Harwell*, et al.*, "Laser Engineered Net Shaping (LENSTM) for the fabrication of metallic components," in *Proceedings of the 1996 ASME International Mechanical Engineering Congress and Exposition, November 17, 1996 - November 22, 1996*, Atlanta, GA, USA, 1996, pp. 175-176.

[24] J. E. Matz and T. W. Eagar, "Carbide Formation in Alloy 718 during Electron-Beam Solid Freeform Fabrication," *Metallurgical and Materials Transactions A,* vol. 33A, pp. 2559-2567, 2002.

[25] B. Baufeld, E. Brandl, and O. van der Biest, "Wire based additive layer manufacturing: Comparison of microstructure and mechanical properties of Ti–6Al–4V components

fabricated by laser-beam deposition and shaped metal deposition," *Journal of Materials Processing Technology,* vol. 211, pp. 1146-1158, 6/1/ 2011.

[26] J. Xiong and G. Zhang, "Adaptive control of deposited height in GMAW-based layer additive manufacturing," *Journal of Materials Processing Technology,* vol. 214, pp. 962-968, 4// 2014.

[27] L. E. Murr, S. M. Gaytan, D. A. Ramirez, E. Martinez, J. Hernandez, K. N. Amato*, et al.*, "Metal Fabrication by Additive Manufacturing Using Laser and Electron Beam Melting Technologies," *Journal of Materials Science & Technology,* vol. 28, pp. 1-14, 1// 2012.

[28] F. A. List, R. R. Dehoff, L. E. Lowe, and W. J. Sames, "Properties of Inconel 625 mesh structures grown by electron beam additive manufacturing," *Materials Science and Engineering: A,* vol. 615, pp. 191-197, 10/6/ 2014.

[29] K. N. Amato, S. M. Gaytan, L. E. Murr, E. Martinez, P. W. Shindo, J. Hernandez*, et al.*, "Microstructures and mechanical behavior of Inconel 718 fabricated by selective laser melting," *Acta Materiala,* vol. 60, pp. 2229-2239, 2012.

[30] P. A. Kobryn, E. H. Moore, and S. L. Semiatin, "The effect of laser power and traverse speed on microstructure, porosity, and build height in laser-deposited Ti-6Al-4V," *Scripta Materialia,* vol. 43, pp. 299-305, 7/28/ 2000.

[31] S. Stecker, K. W. Lachenberg, H. Wang, and R. C. Salo, "Advanced Electron Beam Free Form Fabrication Methods & Technology," in *AWS Welding Show*, Atlanta, GA, 2006, pp. 35-46.

[32] K. A. Mumtaz and N. Hopkinson, "Selective Laser Melting of thin wall parts using pulse shaping," *Journal of Materials Processing Technology,* vol. 210, pp. 279-287, 1/19/ 2010.

[33] B. Ferrar, L. Mullen, E. Jones, R. Stamp, and C. J. Sutcliffe, "Gas flow effects on selective laser melting (SLM) manufacturing performance," *Journal of Materials Processing Technology,* vol. 212, pp. 355-364, 2// 2012.

[34] A. Santomaso, P. Lazzaro, and P. Canu, "Powder flowability and density ratios: the impact of granules packing," *Chemical Engineering Science,* vol. 58, pp. 2857-2874, 7// 2003.

[35] X. Zhao, J. Chen, X. Lin, and W. Huang, "Study on microstructure and mechanical properties of laser rapid forming Inconel 718," *Materials Science and Engineering A,* vol. 478, pp. 119-124, 2008.

[36] H. Qi, M. Azer, and A. Ritter, "Studies of Standard Heat Treatment Effects on Microstructure and Mechanical Properties of Laser Net Shape Manufactured INCONEL 718," *Metallurgical and Materials Transactions A,* vol. 40A, pp. 2410-2422, 2009.

[37] ASTM-International, "Standard Test Methods for Flow Rate of Metal Powders Using the Hall Flowmeter Funnel," vol. B213-13, ed. West Conshohocken, PA: ASTM International, 2013.

[38] ASTM-International, "Standard Test Method for Apparent Density of Free-Flowing Metal Powders Using the Hall Flowmeter Funnel," vol. B212-13, ed. West Conshohocken, PA: ASTM International, 2013.

[39] AP&C. (2014). *Designed for Additive Manufacturing*. Available: http://advancedpowders.com/our-plasma-atomized-powders/designed-for-additive-manufacturing/

[40] S. Zekovic, R. Dwivedi, and R. Kovacevic, "Numerical simulation and experimental investigation of gas–powder flow from radially symmetrical nozzles in laser-based direct metal deposition," *International Journal of Machine Tools and Manufacture,* vol. 47, pp. 112-123, 1// 2007.

[41] J. Karlsson, A. Snis, H. Engqvist, and J. Lausmaa, "Characterization and comparison of materials produced by Electron Beam Melting (EBM) of two different Ti–6Al–4V powder fractions," *Journal of Materials Processing Technology,* vol. 213, pp. 2109-2118, 12// 2013.

[42] H. Tan, F. Zhang, R. Wen, J. Chen, and W. Huang, "Experiment study of powder flow feed behavior of laser solid forming," *Optics and Lasers in Engineering,* vol. 50, pp. 391-398, 3// 2012.

[43] D. D. Gu, W. Meiners, K. Wissenbach, and R. Poprawe, "Laser additive manufacturing of metallic components: materials, processes and mechanisms," *International Materials Reviews,* vol. 57, pp. 133-64, 05/ 2012.

[44] V. I. Murav'ev, R. F. Krupskii, R. A. Fizulakov, and P. G. Demyshev, "Effect of the quality of filler wire on the formation of pores in welding of titanium alloys," *Welding International,* vol. 22, pp. 853-858, 2008.

[45] W. U. H. Syed, A. J. Pinkerton, and L. Li, "Combining wire and coaxial powder feeding in laser direct metal deposition for rapid prototyping," *Applied Surface Science,* vol. 252, pp. 4803-4808, 4/30/ 2006.

[46] A. F. H. Kaplan and J. Powell, "Spatter in laser welding," *Journal of Laser Applications,* vol. 23, pp. -, 2011.

[47] E. C. Santos, M. Shiomi, K. Osakada, and T. Laoui, "Rapid manufacturing of metal components by laser forming," *International Journal of Machine Tools and Manufacture,* vol. 46, pp. 1459-1468, 10// 2006.

[48] S. Li, G. Chen, S. Katayama, and Y. Zhang, "Relationship between spatter formation and dynamic molten pool during high-power deep-penetration laser welding," *Applied Surface Science,* vol. 303, pp. 481-488, 6/1/ 2014.

[49] T. R. Mahale, "Electron Beam Melting of Advanced Materials and Structures," Ph.D., North Carolina State University, 2009.

[50] C. Eschey, S. Lutzmann, and M. F. Zaeh, "Examination of the powder spreading effect in Electron Beam Melting (EBM)," in *Solid Freeform Fabrication Symposium*, Austin, TX, 2009, pp. 308-319.

[51] M. Kahnert, S. Lutzmann, and M. F. Zaeh, "Layer Formations in Electron Beam Sintering," in *Solid Freeform Fabrication Symposium*, Austin, TX, 2007.

[52] C. Korner, A. Bauereiss, and E. Attar, "Fundamental consolidation mechanisms during selective beam melting of powders," *Modelling Simul. Mater. Sci. Eng.,* vol. 21, p. 18, 2013.

[53] T. Vilaro, C. Colin, and J. D. Bartout, "As-Fabricated and Heat-Treated Microstructures of the Ti-6Al-4V Alloy Processed by Selective Laser Melting," *Metallurgical and Materials Transactions A,* vol. 42, pp. 3190-3199, 2011/10/01 2011.

[54] W. Frazier, "Metal Additive Manufacturing: A Review," *Journal of Materials Engineering and Performance,* pp. 1-12, 2014/04/08 2014.

[55] M. Svensson, "Ti6Al4V manufactured with Electron Beam Melting (EBM): Mechanical and Chemical Properties," in *Aeromat 2009*, Dayton, OH, 2009.

[56] L. N. Carter, M. M. Attallah, and R. C. Reed, "Laser Powder Bed Fabrication of Nickel-Base Superalloys: Influence of Parameters; Characterisation, Quantification and Mitigation of Cracking," in *Superalloys 2012*, ed: John Wiley & Sons, Inc., 2012, pp. 577-586.

[57] K. Kempen, L. Thijs, B. Vrancken, S. Buls, J. Van Humbeeck, and J.-P. Kruth, "Producing, Crack-Free, High Density M2 HSS Parts by Selective Laser Melting: Pre-Heating the Baseplate," in *Solid Freeform Fabrication Symposium*, Austin, TX, 2013.

[58] A. Hussein, L. Hao, C. Yan, R. Everson, and P. Young, "Advanced lattice support structures for metal additive manufacturing," *Journal of Materials Processing Technology,* vol. 213, pp. 1019-1026, 7// 2013.

[59] J. P. Kruth, L. Froyen, J. Van Vaerenbergh, P. Mercelis, M. Rombouts, and B. Lauwers, "Selective laser melting of iron-based powder," *Journal of Materials Processing Technology,* vol. 149, pp. 616-622, 6/10/ 2004.

[60] M. F. Zäh and S. Lutzmann, "Modelling and simulation of electron beam melting," *Production Engineering,* vol. 4, pp. 15-23, 2010/02/01 2010.

[61] A. Bauereiß, T. Scharowsky, and C. Körner, "Defect generation and propagation mechanism during additive manufacturing by selective beam melting," *Journal of Materials Processing Technology,* vol. 214, pp. 2522-2528, 11// 2014.

[62] C. Körner, E. Attar, and P. Heinl, "Mesoscopic simulation of selective beam melting processes," *Journal of Materials Processing Technology,* vol. 211, pp. 978-987, 6/1/ 2011.

[63] A. Wu, M. M. LeBlanc, M. Kumar, G. F. Gallegos, D. W. Brown, and W. E. King, "Effect of Laser Scanning Pattern and Build Direction in Additive Manufacturing on Anisotropy, Porosity and Residual Stress," in *2014 TMS Annual Meeting & Exhibition*, San Diego, CA, 2014.

[64] P. Prabhakar, W. J. Sames, R. Dehoff, and S. S. Babu, "Computational Modeling of Residual Stress Formation during the Electron Beam Melting Process for Inconel 718," *Additive Manufacturing,* 2015.

[65] P. Mercelis and J.-P. Kruth, "Residual stresses in selective laser sintering and selective laser melting," *Rapid Prototyping Journal,* vol. 12, pp. 254-265, 2006.

[66] T. Gnäupel-Herold, J. Slotwinski, and S. Moylan, "Neutron measurements of stresses in a test artifact produced by laser-based additive manufacturing," *AIP Conference Proceedings,* vol. 1581, pp. 1205-1212, 2014.

[67] P. Rangaswamy, T. M. Holden, R. B. Rogge, and M. L. Griffith, "Residual stresses in components formed by the laser-engineered net shaping (LENS&reg) process," *Journal of Strain Analysis for Engineering Design,* vol. 38, pp. 519-527, 2003.

[68] L. M. Sochalski-Kolbus, E. A. Payzant, P. A. Cornwell, T. R. Watkins, S. S. Babu, R. R. Dehoff*, et al.*, "Comparison of Residual Stresses in Inconel 718 Simple Parts Made by Electron Beam Melting and Direct Laser Metal Sintering," *Metallurgical and Materials Transactions A,* vol. 46, pp. 1419-1432, 2015/03/01 2015.

[69] C. A. Brice and W. H. Hofmeister, "Determination of bulk residual stresses in electron beam additive-manufactured aluminum," *Metallurgical and Materials Transactions A: Physical Metallurgy and Materials Science,* vol. 44, pp. 5147-5153, 2013.

[70] J. Ding, P. Colegrove, J. Mehnen, S. Ganguly, P. M. Sequeira Almeida, F. Wang*, et al.*, "Thermo-mechanical analysis of Wire and Arc Additive Layer Manufacturing process on large multi-layer parts," *Computational Materials Science,* vol. 50, pp. 3315-3322, 12// 2011.

[71] A. S. Wu, D. W. Brown, M. Kumar, G. F. Gallegos, and W. E. King, "An Experimental Investigation into Additive Manufacturing-Induced Residual Stresses in 316L Stainless Steel," *Metallurgical and Materials Transactions A,* vol. 45, pp. 6260-6270, 2014/12/01 2014.

[72] S. Suresh and A. E. Giannakopoulos, "A new method for estimating residual stresses by instrumented sharp indentation," *Acta Materialia,* vol. 46, pp. 5755-5767, 10/9/ 1998.

[73] B. Song, S. Dong, Q. Liu, H. Liao, and C. Coddet, "Vacuum heat treatment of iron parts produced by selective laser melting: Microstructure, residual stress and tensile behavior," *Materials & Design,* vol. 54, pp. 727-733, 2// 2014.

[74] M. B. Prime, "Cross-Sectional Mapping of Residual Stresses by Measuring the Surface Contour After a Cut," *Journal of Engineering Materials and Technology,* vol. 123, pp. 162-168, 2001.

[75] T. Watkins, H. Bilheux, A. Ke, A. Payzant, R. Dehoff, C. Duty, *et al.*, "Neutron Characterization for Additive Manufacturing," *Advanced Materials & Processes,* vol. 171, pp. 23-27, 2013.

[76] R. J. Moat, A. J. Pinkerton, L. Li, P. J. Withers, and M. Preuss, "Residual stresses in laser direct metal deposited Waspaloy," *Materials Science and Engineering: A,* vol. 528, pp. 2288-2298, 3/15/ 2011.

[77] M. Zaeh and G. Branner, "Investigations on residual stresses and deformations in selective laser melting," *Production Engineering,* vol. 4, pp. 35-45, 2010/02/01 2010.

[78] ReaLizer. (2015). *Selective Laser Melting: Visions become Reality*. Available: http://www.realizer.com/en/wp-content/themes/realizer/Brochure.pdf

[79] S. S. Al-Bermani, " An investigation into microstructure and microstructural control of additive layer manufactured Ti-6Al-4V by electron beam melting," Ph.D., University of Sheffield, Sheffield, UK, 2011.

[80] D. Dye, O. Hunziker, and R. C. Reed, "Numerical analysis of the weldability of superalloys," *Acta Materialia,* vol. 49, pp. 683-697, 2/23/ 2001.

[81] H. Gu, H. Gong, D. Pal, K. Rafi, T. Starr, and B. Stucker, "Influences of Energy Density on Porosity and Microstructure of Selective Laser Melted 17-4PH Stainless Steel," in *Solid Freeform Fabrication Symposium*, Austin, TX, 2013.

[82] J. D. Hunt, "Steady state columnar and equiaxed growth of dendrites and eutectic," *Materials Science and Engineering,* vol. 65, pp. 75-83, 7// 1984.

[83] L. Nastac, J. J. Valencia, M. L. Tims, and F. R. Dax, "Advances in the Solidification on IN718 and RS5 Alloys," in *Superalloys 718, 625, 706, and Various Derivatives*, 2001, pp. 103-112.

[84] C. Körner, H. Helmer, A. Bauereiß, and R. F. Singer, "Tailoring the grain structure of IN718 during selective electron beam melting," in *EUROSUPERALLOYS*, 2014.

[85] J. Gockel and J. Beuth, "Understanding Ti-6Al-4V Microstructure Control in Additive Manufacturing via Process Maps," in *Solid Freeform Fabrication Symposium*, Austin, TX, 2013.

[86] W. J. Sames, K. A. Unocic, R. R. Dehoff, T. Lolla, and S. S. Babu, "Thermal Effects on Microstructural Heterogeneity of Inconel 718 Materials Fabricated by Electron Beam Melting " *Journal of Materials Research,* vol. 29, pp. 1920-1930, 2014.

[87] N. Shen and K. Chou, *Thermal Modeling of Electron Beam Additive Manufacturing Process: Powder Sintering Effects*, 2012.

[88] L. N. Carter, C. Martin, P. J. Withers, and M. M. Attallah, "The influence of the laser scan strategy on grain structure and cracking behaviour in SLM powder-bed fabricated nickel superalloy," *Journal of Alloys and Compounds,* vol. 615, pp. 338-347, 12/5/ 2014.

[89] K. T. Makiewicz, "Development of Simultaneous Transformation Kinetics Microstructure Model with Application to Laser Metal Deposited Ti-6Al-4V and Alloy 718," ed: Ohio State University, 2013.

[90] K. Zeng, D. Pal, and B. Stucker, "A review of thermal analysis methods in Laser Sintering and Selective Laser Melting," in *Solid Freeform Fabrication Symposium*, Austin, TX, 2012.

[91] P. A. Kobryn and S. L. Semiatin, "Mechanical Properties of Laser-Deposited Ti-6Al-4V," in *Solid Freeform Fabrication Proceedings*, ed. Austin, TX, 2001.

[92] ASTM-International, "Standard Specfication for Additive Manufacturing Nickel Alloy (UNS N07718) with Powder Bed Fusion," vol. F3055-14, ed. West Conshohocken, PA: ASTM International, 2014.

[93] ASTM-International, "Standard Specification for Additive Manufacturing Titanium-6 Aluminum-4 Vanadium ELI (Extra Low Interstitial) with Powder Bed Fusion," vol. F3001-14, ed. West Conshohocken, PA: ASTM International, 2014.

[94] "Nickel-Base Superalloys," in *Heat Treater's Guide: Practices and Procedures for Nonferrous Alloys*, ed: ASM International, 1996, pp. 41-58.

[95] E. Brandl and D. Greitemeier, "Microstructure of additive layer manufactured Ti–6Al–4V after exceptional post heat treatments," *Materials Letters,* vol. 81, pp. 84-87, 8/15/ 2012.

[96] E. Brandl, A. Schoberth, and C. Leyens, "Morphology, microstructure, and hardness of titanium (Ti-6Al-4V) blocks deposited by wire-feed additive layer manufacturing (ALM)," *Materials Science and Engineering: A,* vol. 532, pp. 295-307, 1/15/ 2012.

[97] J. Cao, F. Liu, X. Lin, C. Huang, J. Chen, and W. Huang, "Effect of overlap rate on recrystallization behaviors of Laser Solid Formed Inconel 718 superalloy," *Optics & Laser Technology,* vol. 45, pp. 228-235, 2013.

[98] P. L. Blackwell, "The mechanical and microstructural characteristics of laser-deposited IN718," *Journal of Materials Processing Technology,* vol. 170, pp. 240-246, 12/14/ 2005.

[99] L. Facchini, E. Magalini, P. Robotti, and A. Molinari, "Microstructure and mechanical properties of Ti-6Al-4V produced by electron beam melting of pre-alloyed powders," *Rapid Prototyping Journal,* vol. 15, pp. 171-178, 2009.

[100] L. E. Murr, E. Martinez, S. M. Gaytan, D. A. Ramirez, B. I. Machado, P. W. Shindo*, et al.*, "Microstructural Architecture, Microstructures, and Mechanical Properties for a Nickel-Base Superalloy Fabricated by Electron Beam Melting," *Metallurgical and Materials Transactions A,* vol. 42, pp. 3491-3508, 2011/11/01 2011.

[101] C. Bampton, J. Wooten, and B. Hayes, "Additive Manufactuing by Electron Beam Melting (EBM) of Alloy 718," in *Material Science & Technology*, Montreal, Canada, 2013.

[102] K. A. Unocic, L. M. Kolbus, R. R. Dehoff, S. N. Dryepondt, and B. A. Pint, "High-Temperature Performance of N07718 Processed by Additive Manufacturing," in *NACE Corrosion 2014*, San Antonio, TX, 2014.

[103] A. Strondl, S. Milenkovic, A. Schneider, U. Klement, and G. Frommeyer, "Effect of Processing on Microstructure and Physical Properties of Three Nickel-Based Superalloys with Different Hardening Mechanisms," *Advanced Engineering Materials,* vol. 14, pp. 427-438, 2012.

[104] A. Strondl, M. Palm, J. Gnauk, and G. Frommeyer, "Microstructure and mechanical properties of nickel based superalloy IN718 produced by rapid prototyping with electron beam melting (EBM)," *Materials Science and Technology,* vol. 27, pp. 876-883, 2011.

[105] E. Łyczkowska, P. Szymczyk, B. Dybała, and E. Chlebus, "Chemical polishing of scaffolds made of Ti–6Al–7Nb alloy by additive manufacturing," *Archives of Civil and Mechanical Engineering*.

[106] R. Dehoff, C. Duty, W. Peter, Y. Yamamoto, C. Wei, C. Blue*, et al.*, "Case Study: Additive Manufacturing of Aerospace Brackets," *Advanced Materials & Processes,* vol. 171, pp. 19-22, 2013.

[107] A. Lasemi, D. Xue, and P. Gu, "Recent development in CNC machining of freeform surfaces: A state-of-the-art review," *Computer-Aided Design,* vol. 42, pp. 641-654, 7// 2010.

[108] K. P. Karunakaran, S. Suryakumar, V. Pushpa, and S. Akula, "Low cost integration of additive and subtractive processes for hybrid layered manufacturing," *Robotics and Computer-Integrated Manufacturing,* vol. 26, pp. 490-499, 10// 2010.

[109] J. Jones, P. McNutt, R. Tosi, C. Perry, and D. Wimpenny, "Remanufacture of turbine blades by laser cladding, machining and in-process scanning in a single machine," in *Solid Freeform Fabrication Symposium*, Austin, TX, 2012.

[110] O. Grong, *Metallurgical Modeling of Welding*, 2nd Edition ed.: The Institute of Materials, 1997.

[111] S. A. David and J. M. Vitek, "Correlation between solidification parameters and weld microstructures," *International Materials Reviews,* vol. 34, pp. 213-245, 1989.

[112] S. S. Al-Bermani, M. L. Blackmore, W. Zhang, and I. Todd, "The Origin of Microstructural Diversity, Texture, and Mechanical Properties in Electron Beam Melted Ti-6Al-4V," *Metallurgical and Materials Transactions A,* vol. 41A, pp. 3422-3434, 2010.

[113] P. Edwards and M. Ramulu, "Fatigue performance evaluation of selective laser melted Ti–6Al–4V," *Materials Science and Engineering: A,* vol. 598, pp. 327-337, 3/26/ 2014.

[114] J. Yu, M. Rombouts, G. Maes, and F. Motmans, "Material Properties of Ti6Al4V Parts Produced by Laser Metal Deposition," *Physics Procedia,* vol. 39, pp. 416-424, // 2012.

[115] E. Amsterdam and G. A. Kool, "High Cycle Fatigue of Laser Beam Deposited Ti-6Al-4V and Inconel 718," in *ICAF 2009, Bridging the Gap between Theory and Operational Practice*, M. J. Bos, Ed., ed: Springer Netherlands, 2009, pp. 1261-1274.

[116] Z. Wang, K. Guan, M. Gao, X. Li, X. Chen, and X. Zeng, "The microstructure and mechanical properties of deposited-IN718 by selective laser melting," *Journal of Alloys and Compounds,* vol. 513, pp. 518-523, 2012.

[117] L. P. Parimi, M. M. Attallah, J. C. Gebelin, and R. C. Reed, "Direct Laser Fabrication of Inconel 718," in *Superalloys 2012: 12th International Symposium on Superalloys*, 2012, pp. 511-519.

[118] A. A. Antonysamy, J. Meyer, and P. B. Prangnell, "Effect of build geometry on the β-grain structure and texture in additive manufacture of Ti6Al4V by selective electron beam melting," *Materials Characterization,* vol. 84, pp. 153-168, 10// 2013.

[119] L. Thijs, K. Kempen, J.-P. Kruth, and J. Van Humbeeck, "Fine-structured aluminium products with controllable texture by selective laser melting of pre-alloyed AlSi10Mg powder," *Acta Materialia,* vol. 61, pp. 1809-1819, 3// 2013.

[120] Y. Tian, D. McAllister, H. Colijn, M. Mills, D. Farson, M. Nordin*, et al.*, "Rationalization of Microstructure Heterogeneity in INCONEL 718 Builds Made by the Direct Laser Additive Manufacturing Process," *Metallurgical and Materials Transactions A,* vol. 45, pp. 4470-4483, 2014/09/01 2014.

[121] J. Mireles, C. Terrazas, F. Medina, and R. Wicker, "Automatic Feedback Control in Electron Beam Melting Using Infrared Tomography," in *Solid Freefrom Fabrication Symposium*, Austin, TX, 2013.

[122] L. Thijs, M. L. Montero Sistiaga, R. Wauthle, Q. Xie, J.-P. Kruth, and J. Van Humbeeck, "Strong morphological and crystallographic texture and resulting yield strength anisotropy in selective laser melted tantalum," *Acta Materialia,* vol. 61, pp. 4657-4668, 7// 2013.

[123] R. R. Dehoff, M. M. Kirka, F. A. List, K. A. Unocic, and W. J. Sames, "Crystallographic Texture Engineering Through Novel Melt Strategies via Electron Beam Processing: Inconel 718," *Materials Science & Technology,* 2015 (In Press).

[124] H. E. Helmer, C. Körner, and R. F. Singer, "Additive manufacturing of nickel-based superalloy Inconel 718 by selective electron beam melting: Processing window and microstructure," *Journal of Materials Research,* vol. 29, pp. 1987-1996, 2014.

[125] S. Mitzner, S. Liu, M. Domack, and R. Hafley, "Grain Refinement of Freeform Fabricated Ti-6Al-4V Alloy Using Beam/Arc Modulation," in *Solid Freeform Fabrication Symposium*, Austin, TX, 2012.

[126] R. R. Dehoff, M. M. Kirka, W. J. Sames, H. Bilheux, A. S. Tremsin, L. E. Lowe*, et al.*, "Site Specific Control of Crystallographic Grain Orientation Through Electron Beam Additive Manufacturing," *Materials Science & Technology,* 2015 (In Press).

[127] L. Thijs, F. Verhaeghe, T. Craeghs, J. V. Humbeeck, and J.-P. Kruth, "A study of the microstructural evolution during selective laser melting of Ti–6Al–4V," *Acta Materialia,* vol. 58, pp. 3303-3312, 5// 2010.

[128] D. A. Ramirez, L. E. Murr, E. Martinez, D. H. Hernandez, J. L. Martinez, B. I. Machado*, et al.*, "Novel precipitate–microstructural architecture developed in the fabrication of solid copper components by additive manufacturing using electron beam melting," *Acta Materialia,* vol. 59, pp. 4088-4099, 6// 2011.

[129] J. F. Rudy and E. J. Rupert, "EFFECTS OF POROSITY ON MECHANICAL PROPERTIES OF ALUMINUM WELDS," *Welding Journal,* vol. 49, pp. 322s-336s, 1970.

[130] R. F. Ashton, R. P. Wesley, and C. R. Dixon, "The Effect of Porosity on 5086-H116 Aluminum Alloy Welds," *Welding Journal,* pp. 95-98, 1975.

[131] H. K. Rafi, T. Starr, and B. Stucker, "A comparison of the tensile, fatigue, and fracture behavior of Ti–6Al–4V and 15-5 PH stainless steel parts made by selective laser melting," *The International Journal of Advanced Manufacturing Technology,* vol. 69, pp. 1299-1309, 2013/11/01 2013.

[132] N. Hrabe and T. Quinn, "Effects of processing on microstructure and mechanical properties of a titanium alloy (Ti–6Al–4V) fabricated using electron beam melting (EBM), Part 2: Energy input, orientation, and location," *Materials Science and Engineering: A,* vol. 573, pp. 271-277, 6/20/ 2013.

[133] G. K. Lewis and E. Schlienger, "Practical considerations and capabilities for laser assisted direct metal deposition," *Materials & Design,* vol. 21, pp. 417-423, 8/1/ 2000.

[134] M. Bauccio, *ASM Metals Reference Book, Third Edition*. Materials Park, OH: ASM International, 1993.

[135] J. E. Northwood, "Improving Turbine Blade Performance by Solidification Control," *Metallurgia,* vol. 46, pp. 437-439, 441, 442, 2011-11-10 1979.

[136] ASTM-International, "Standard Specification for Additive Manufacturing Nickel Alloy (UNS N06625) with Powder Bed Fusion," vol. F3056-14, ed. West Conshohocken, PA: ASTM International, 2014.

[137] N. Hrabe, R. Kircher, and T. Quinn, "Effects of Processing on Microstructure and Mechanical Properties of Ti-6Al-4V Fabricated Using Electron Beam Melting (EBM): Orientation and Location," in *Solid Freefrom Fabrication Symposium*, Austin, TX, 2012.

[138] N. Hrabe and T. Quinn, "Effects of processing on microstructure and mechanical properties of a titanium alloy (Ti–6Al–4V) fabricated using electron beam melting (EBM), part 1: Distance from build plate and part size," *Materials Science and Engineering: A,* vol. 573, pp. 264-270, 6/20/ 2013.

[139] D. Pal, N. Patil, and B. Stucker, "Prediction of mechanical properties of Electron Beam Melted Ti6Al4V parts using dislocation density based crystal plasticity framework," in *Solid Freeform Fabrication Symposium*, Austin, TX, 2012.

[140] H. Brodin, O. Andersson, and S. Johansson, "Mechanical testing of a selective laser melted superalloy," in *13th International Conference on Fracture*, Beijing, China, 2013.

[141] ExOne. (2013). *ExOne-Rapid Growth of Additive Manufacturing (AM) Disrupts Traditional Manufacturing Process*. Available: http://additivemanufacturing.com/2013/06/06/exone-rapid-growth-of-additive-manufacturing-am-disrupts-traditional-manufacturing-process/

[142] S. Rengers. (2012). *Electron Beam Melting [EBM] vs. Direct Metal Laser Sintering [DMLS]*. Available: http://www.midwestsampe.org/content/files/events/dpmworkshop2012/Rengers%20EBM%20vs%20DMLS.pdf

[143] RepRapPro. (2014). *RepRapPro Tricolour Mendel specifications*. Available: https://reprappro.com/shop/reprap-kits/tricolour-mendel/

[144] Renishaw. (2015). *About AM250*. Available: http://www.renishaw.com/en/am250-laser-melting-metal-3d-printing-machine--15253

[145] (2013). *Building the Future: Assessing 3D Printing's Opportunities and Challenges*. Available: https://portal.luxresearchinc.com/research/report_excerpt/13277

[146] A. R. Thryft. (2013). *Report: 3D Printing Will (Eventually) Transform Manufacturing*. Available: http://www.designnews.com/author.asp?doc_id=262205

[147] E. Atzeni and A. Salmi, "Economics of additive manufacturing for end-usable metal parts," *The International Journal of Advanced Manufacturing Technology,* vol. 62, pp. 1147-1155, 2012/10/01 2012.

[148] A. Koptyug, L.-E. Rannar, M. Backstrom, S. F. Franzen, and P. Derand, "Additive Manufacturing Technology Applications Targeting Practical Surgery," *International Journal of Life Science and Medical Research,* vol. 3, pp. 15-24, 2013.

[149] Z. Bi, M. P. Paranthaman, P. A. Menchhofer, R. R. Dehoff, C. A. Bridges, M. Chi*, et al.*, "Self-organized amorphous TiO2 nanotube arrays on porous Ti foam for rechargeable lithium and sodium ion batteries," *Journal of Power Sources,* vol. 222, pp. 461-466, 1/15/ 2013.

[150] L. J. Love, B. Richardson, R. Lind, R. R. Dehoff, B. Peter, L. Lowe*, et al.*, "Freeform Fluidics," in *Mechanical Engineering - CIME*, 2013.

[151] T. Catts. (2013). *GE Turns to 3D Printing for Plane Parts*. Available: http://www.businessweek.com/articles/2013-11-27/general-electric-turns-to-3d-printers-for-plane-parts

[152] 3ders. (2014). *GE reveals breakthrough in 3D printing super light-weight metal blades for jet engine*. Available: http://www.3ders.org/articles/20140818-ge-reveals-breakthrough-in-3d-printing-super-light-weight-metal-blades-for-jet-engine.html

[153] M. Gäumann, C. Bezençon, P. Canalis, and W. Kurz, "Single-crystal laser deposition of superalloys: processing–microstructure maps," *Acta Materialia,* vol. 49, pp. 1051-1062, 4/2/ 2001.

[154] L. Rickenbacher, A. Spierings, and K. Wegener, "An integrated cost-model for selective laser melting (SLM)," *Rapid Prototyping Journal,* vol. 19, pp. 208-214, 2013.

[155] S. Merkt, C. Hinke, H. Schleifenbaum, and H. Voswinckel, "Integrative Technology Evaluation Model (ITEM) for Selective Laser Melting (SLM)," *Advanced Materials Research,* vol. 337, pp. 274-280, 2011.

[156] S. S. Babu, L. J. Love, W. H. Peter, and R. R. Dehoff, "Additive Manufacturing: The Future of Manufacturing in a Flat World: Challenges and Path Forward," 2014 (in progress).

[157] D. W. Rosen. (2014). *Additive Manufacturing Process Overview*. Available: http://pages.wilsoncenter.org/rs/woodrowwilson/images/AMprocesses_DRosen1014_site.pdf

[158] K. Maxey. (2014). *ExOne M-Flex Production Metal 3D Printer*. Available: http://www.engineering.com/3DPrinting/3DPrintingArticles/ArticleID/7618/ExOne-M-Flex-Production-Metal-3D-Printer.aspx

[159] M. Dahlbom. (2013). *Arcam AB, A Very Promising 3D Printer Company*. Available: http://seekingalpha.com/article/1316271-arcam-ab-a-very-promising-3d-printer-company

[160] G. Nelson. (2013). *NAMII Open House Shows Potential of 3-D Printing*. Available: http://businessjournaldaily.com/awards-events/namii-open-house-shows-potential-3-d-printing-2013-10-4

[161] L. P. Vigna, "Additive Manufacturing - 3D Printing Emerging Technologies," ed, 2012.

[162] C. G. McCracken, C. Motchenbacher, and D. P. Barbis, "Review of Titanium-Powder-Production Methods," *International Journal of Powder Metallurgy,* vol. 46, pp. 19-26, 2010.

[163] X. Wu, "A review of laser fabrication of metallic engineering components and of materials," *Materials Science and Technology,* vol. 23, pp. 631-640, 2007.

[164] (2014, 2014/05/03) Additive Manufacturing: Heavy Metal. *The Economist*.

[165] NIST, "Measurement Science Roadmap for Metal-Based Additive Manufacturing," National Institute for Standards and Technology 2013.

[166] PCC. (2014). *A Look Inside the Future of Metals*. Available: http://www.specialmetals.com/files/SMC-Overview-2014.pdf

[167] A. Lingenfelter, "Welding of Inconel Alloy 718: A Historical Overview," in *Superalloy 718 - Metallurgy and Applications*, 1969, pp. 673-683.

[168] D. F. Paulonis and J. J. Schirra, "Alloy 718 at Pratt & Whitney - Historical Perspective and Future Challenges," in *Superalloys 718, 625, 706 and Various Derivatives*, 2001, pp. 13-23.

[169] T. Baldridge, G. Poling, E. Foroozmehr, R. Kovacevic, T. Metz, V. Kadekar*, et al.*, "Laser cladding of Inconel 690 on Inconel 600 superalloy for corrosion protection in nuclear applications," *Optics and Lasers in Engineering,* vol. 51, pp. 180-184, 2013.

[170] H. X. Hu, Y. G. Zheng, and C. P. Qun, "Comparison of Inconel 625 and Inconel 600 in resistance to cavitation erosion and jet impingement erosion," *Nuclear Engineering and Design,* vol. 240, pp. 2721-2730, 2010.

[171] A. F. Rowcliffe, L. K. Mansur, D. T. Hoelzer, and R. K. Nanstad, "Perspectives on radiation effects in nickel-base alloys for applications in advanced reactors," *Journal of Nuclear Materials,* vol. 392, pp. 341-352, 7/15/ 2009.

[172] T. M. Pollock and S. Tin, "Nickel-Based Superalloys for Advanced Turbine Engines: Chemistry, Microstructure, and Properties," *Journal of Propulsion and Power,* vol. 22, pp. 361-374, 2006.

[173] J. F. Radavich, "The Physical Metallurgy of Cast and Wrought Alloy 718," in *Superalloy 718 - Metallurgy and Applications*, TMS, 1989.

[174] G. P. Sabol and R. Stickler, "Microstructure of Nickel-Based Superalloys," *physica status solidi (b),* vol. 35, pp. 11-52, 1969.

[175] Special-Metals. (2007). *Inconel Alloy 718*. Available: http://www.specialmetals.com/documents/Inconel%20alloy%20718.pdf

[176] ASTM-International, "Standard Specification for Precipitation-Hardening Nickel Alloy (UNS N07718) Plate, Sheet, and Strip for High-Temperature Service," vol. B670-07, ed. West Conshohocken, PA: ASTM International, 2013.

[177] R. C. Reed, *The Superalloys: Fundamentals and Applications*: Cambridge University Press, 2006.

[178] S. T. Wlodek and R. D. Field, "The Effects of Long Time Exposure on Alloy 718," in *Superalloys*, 1994, pp. 659-670.

[179] M. Dehmas, J. Lacaze, A. Niang, and B. Viguier, "TEM Study of High-Temperature Precipitation of Delta Phase in Inconel 718 Alloy," *Advances in Materials Science and Engineering,* vol. 2011, 2011.

[180] S. Bourguignon, P. Martin, and Y. Honnorat, "Segregation of Defects in Wrought Alloy 718," in *Superalloys 718, 625 and Various Derivatives*, 1991.

[181] W. D. Cao, R. L. Kennedy, and M. P. Willis, "Differential Thermal Analysis (DTA) Study of the Homogenization Process in Alloy 718," in *Superalloys 718, 625, and Various Derivatives*, 1991, pp. 147-160.

[182] J. R. Davis, *ASM Specialty Handbook: Heat-Resistant Materials*: ASM International, 1997.

[183] D. L. Sponseller, "Differential Thermal Analysis of Nickel-Base Superalloys," in *Superalloys*, 1996.

[184] H. S. Choi and J. Choi, "Precipitation in Inconel 718 Alloy," *Journal of the Korean Nuclear Society,* vol. 4, pp. 203-213, 1972.

[185] J. de Jaeger, D. Solas, T. Baudin, O. Fandeur, J.-H. Schmitt, and C. Rey, "Inconel 718 Single and Multipass Modelling of Hot Forging," in *Superalloys*, 2012.

[186] T. Fang, S. J. Kennedy, L. Quan, and T. J. Hicks, "The structure and paramagnetism of Ni3Nb," *Journal of Physics: Condensed Matter,* vol. 4, pp. 2405-2414, 1992.

[187] T. Alam, M. Chaturvedi, S. P. Ringer, and J. M. Cairney, "Precipitation and clustering in the early stages of ageing in Inconel 718," *Materials Science and Engineering: A,* vol. 527, pp. 7770-7774, 11/15/ 2010.

[188] R. Cozar and A. Pineau, "Morphology of y' and y" precipitates and thermal stability of inconel 718 type alloys," *Metallurgical Transactions,* vol. 4, pp. 47-59, 1973/01/01 1973.

[189] C. Slama and M. Abdellaoui, "Structural characterization of the aged Inconel 718," *Journal of Alloys and Compounds,* vol. 306, pp. 277-284, 6/23/ 2000.

[190] M. Gao and R. P. Wei, "Grain boundary γ" precipitation and niobium segregation in inconel 718," *Scripta Metallurgica et Materialia,* vol. 32, pp. 987-990, 4/1/ 1995.

[191] M. Gao and R. P. Wei, "GRAIN BOUNDARY NIOBIUM CARBIDES IN INCONEL 718," *Scripta Materialia,* vol. 37, pp. 1843-1849, 12/15/ 1997.

[192] J. He, S. Fukyyama, and K. Yokogawa, "γ" precipitate in Inconel 718," *Journal of Materials Science and Technology,* vol. 10, pp. 293-303, 1994.

[193] M. C. Chaturvedi and Y.-f. Han, "STRENGTHENING MECHANISMS IN INCONEL 718 SUPERALLOY," *Metal science,* vol. 17, pp. 145-149, 1983.

[194] K. Hiroto, "Microstructure-Property Relationship in Advanced Ni-Based Superalloys," ed, 2012.

[195] I. Kirman and D. H. Warrington, "The precipitation of Ni3Nb phases in a Ni−Fe−Cr−Nb alloy," *Metallurgical Transactions,* vol. 1, pp. 2667-2675, 1970/10/01 1970.

[196] V. Beaubois, J. Huez, S. Coste, O. Brucelle, and J. Lacaze, "Short term precipitation kinetics of delta phase in strain free Inconel* 718 alloy," *Materials Science and Technology,* vol. 20, pp. 1019-1026, 2004/08/01 2004.

[197] M. Sundararaman, P. Mukhopadhyay, and S. Banerjee, "Precipitation of the δ-Ni3Nb phase in two nickel base superalloys," *Metallurgical Transactions A,* vol. 19, pp. 453-465, 1988/03/01 1988.

[198] C. Slama, C. Servant, and G. Cizeron, "Aging of the Inconel 718 alloy between 500 and 750 °C," *Journal of Materials Research,* vol. 12, pp. 2298-2316, 1997.

[199] G. D. Smith and S. J. PAtel, "The Role of Niobium in Wrought Precipitation-Hardened Nickel-Base Alloys," in *Superalloys 718, 625, 706 and Derivatives* 2005, pp. 135-154.

[200] E. Nembach and G. Neite, "Precipitation Hardening of Superalloys by Ordered γ'-Particles," *Progress in Materials Science,* vol. 29, pp. 177-319, 1985.

[201] D. Srinivasan, "Effect of long-time exposure on the evolution of minor phases in Alloy 718," *Materials Science and Engineering: A,* vol. 364, pp. 27-34, 1/15/ 2004.

[202] E. J. Pickering, H. Mathur, A. Bhowmik, O. M. D. M. Messé, J. S. Barnard, M. C. Hardy*, et al.*, "Grain-boundary precipitation in Allvac 718Plus," *Acta Materialia,* vol. 60, pp. 2757-2769, 4// 2012.

[203] N. Zhou, D. C. Lv, H. L. Zhang, D. McAllister, F. Zhang, M. J. Mills*, et al.*, "Computer simulation of phase transformation and plastic deformation in IN718 superalloy: Microstructural evolution during precipitation," *Acta Materialia,* vol. 65, pp. 270-286, 2/15/ 2014.

[204] Y. Huang and T. Langdon, "The evolution of delta-phase in a superplastic Inconel 718 alloy," *Journal of Materials Science,* vol. 42, pp. 421-427, 2007/01/01 2007.

[205] D. Cai, P. Nie, J. Shan, W. Liu, Y. Gao, and M. Yao, "Precipitation and residual stress relaxation kinetics in shot-peened inconel 718," *Journal of Materials Engineering and Performance,* vol. 15, pp. 614-617, 2006.

[206] X.-p. Wei, W.-j. Zheng, Z.-g. Song, T. Lei, Q.-l. Yong, and Q.-c. Xie, "Strain-induced Precipitation Behavior of δ Phase in Inconel 718 Alloy," *Journal of Iron and Steel Research, International,* vol. 21, pp. 375-381, 3// 2014.

[207] R. Trivedi and W. Kurz, "Dendritic growth," *International Materials Reviews,* vol. 39, pp. 49-74, 1994/01/01 1994.

[208] W. J. Boettinger, S. R. Coriell, A. L. Greer, A. Karma, W. Kurz, M. Rappaz*, et al.*, "Solidification microstructures: recent developments, future directions," *Acta Materialia,* vol. 48, pp. 43-70, 1/1/ 2000.

[209] T. Antonsson and H. Fredriksson, "The effect of cooling rate on the solidification of INCONEL 718," *Metallurgical and Materials Transactions B,* vol. 36, pp. 85-96, 2005/02/01 2005.

[210] G. A. Knorovsky, M. J. Cieslak, T. J. Headley, A. D. Romig, and W. F. Hammetter, "INCONEL 718: A solidification diagram," *Metallurgical Transactions A,* vol. 20, pp. 2149-2158, 1989/10/01 1989.

[211] A. Mitchell, "The Precipitation of Primary Carbides in IN718 and Its Relation to Solidification Conditions," in *Superalloys 718, 625, 706 and Derivatives*, 2005, pp. 299-310.

[212] J. L. Albarrán, B. Campillo, R. Pérez, L. Martínez, and J. A. Juárez-Islas, "Some preliminary results on the microstructure and mechanical properties of rapidly solidified nickel-based superalloys," *Scripta Metallurgica et Materialia,* vol. 25, pp. 1611-1616, 7// 1991.

[213] A. Mitchell, A. J. Schmalz, C. Schvezov, and S. L. Cockcroft, "The Precipitation of Primary Carbides in Alloy 718," in *Superalloys 718, 625, 706 and Various Derivatives*, 1994, pp. 65-78.

[214] A. Mitchell and T. Wang, "Solidification and Precipitation in IN718," in *Superalloys 718, 625, 706 and Various Derivatives*, 2001, pp. 81-90.

[215] L. Wang, L. Liu, H. Wu, J. Dong, and M. Zhang, "Effects of superheat on the microsegregation and fluid flow tendency during directional solidification of superalloy In718," *Chemical Engineering Communications,* vol. 197, pp. 1586-1596, 2010.

[216] L. Wang, L. Liu, J. X. Dong, and X. S. Xie, "Effects of solidification rate on segregation and fluid flow tendency in mushy zone of directionally solidified superalloy Inconel 718," *Materials Science and Technology,* vol. 28, pp. 1349-1355, 2012.

[217] F. J. Humphreys and M. Hatherly, "Introduction," in *Recrystallization and Related Annealing Phenomena (Second Edition)*, F. J. H. Hatherly, Ed., ed Oxford: Elsevier, 2004, pp. 1-10.

[218] R. D. Doherty, D. A. Hughes, F. J. Humphreys, J. J. Jonas, D. J. Jensen, M. E. Kassner*, et al.*, "Current issues in recrystallization: a review," *Materials Science and Engineering: A,* vol. 238, pp. 219-274, 11/15/ 1997.

[219] S. Azadian, L.-Y. Wei, and R. Warren, "Delta phase precipitation in Inconel 718," *Materials Characterization,* vol. 53, pp. 7-16, 9// 2004.

[220] M. C. Mataya and D. K. Matlock, "Effects of Multiple Reductions on Grain Refinement During Hot Working of Alloy 718," in *Superalloy 718 - Metallurgy and Applications*, 1989.

[221] X. Liang, R. Zhang, Y. Yang, and Y. Han, "An Investigation of the Homogenization and Deformation of Alloy 718 Ingots," in *Superalloys 718, 625, 706 and Various Derivatives*, 1994, pp. 947-956.

[222] R. G. Thompson, B. Radhakrishnan, and D. E. Mayo, "Intergranular Liquid Formation, Distribution, and Cracking," in *Superalloy 718 - Metallurgy and Applications*, 1989, pp. 437-455.

[223] DiConza, P.J., R. R. Biederman, and R. P. Singh, "Homogenization and Thermomechanical Processing of Cast Alloy 718," in *Superalloys 718, 625, and Various Derivatives*, 1991, pp. 161-171.

[224] Y. Wang, W. Z. Shao, L. Zhen, C. Yang, and X. M. Zhang, "Tensile deformation behavior of superalloy 718 at elevated temperatures," *Journal of Alloys and Compounds,* vol. 471, pp. 331-335, 3/5/ 2009.

[225] Y. Wang, L. Zhen, W. Z. Shao, L. Yang, and X. M. Zhang, "Hot working characteristics and dynamic recrystallization of delta-processed superalloy 718," *Journal of Alloys and Compounds,* vol. 474, pp. 341-346, 4/17/ 2009.

[226] R. Watson, M. Preuss, J. Q. Fonseca, T. Witulski, and G. Terlinde, "The Effect of Strain and Temperature on Static Recrystallization During Solution Heat Treatment After Hot Deformation of Alloy 718," in *Superalloy 718 and Derivatives*, Pittsburgh, PA, 2014, pp. 781-792.

[227] R. P. Singh, J. M. Hyzak, T. E. Howson, and R. R. Biederman, "Recrystallization Behavior of Cold Rolled Alloy 718," in *Superalloys 718, 625, and Various Derivatives*, 1991, pp. 205-215.

[228] B. Marty, J. Y. Guedou, P. Gergaud, and J. L. Lebrun, "Recrystallization and Work-Hardening Prediction During Forging Process of Inconel 718," in *Superalloy 718, 625, 706 and Various Derivatives*, 1997, pp. 331-342.

[229] J. M. Poole, K. R. Stultz, and J. M. Manning, "The Effect of Ingot Homogenization Practice on the Properties of Wrought Alloy 718 and Structure," in *Superalloy 718 - Metallurgy and Applications*, 1989, pp. 219-228.

[230] S. H. Chang, S. C. Lee, T. P. Tang, and H. H. Ho, "Evaluation of HIP pressure on Inconel 718 superalloy," *International Journal of Cast Metals Research,* vol. 19, pp. 181-187, 2006.

[231] S. H. Chang, S. C. Lee, T. P. Tang, and H. H. Ho, "Effects of temperature of HIP process on characteristics of Inconel 718 superalloy," *International Journal of Cast Metals Research,* vol. 19, pp. 175-180, 2006.

[232] J. J. Schirra, "Effect of Heat Treatment Variations on the Hardness and Mechanical Properties of Wrought Inconel 718," in *Superalloys 718, 625, 706 and Various Derivatives*, 1997, pp. 431-438.

[233] A. Baldan, "Review Progress in Ostwald ripening theories and their applications to nickel-base superalloys Part I: Ostwald ripening theories," *Journal of Materials Science,* vol. 37, pp. 2171-2202, 2002/06/01 2002.

[234] I. M. Lifshitz and V. V. Slyozov, "The kinetics of precipitation from supersaturated solid solutions," *Journal of Physics and Chemistry of Solids,* vol. 19, pp. 35-50, 4// 1961.

[235] Y.-f. Han, P. Deb, and M. C. Chaturvedi, "Coarsening behaviour of γ''- and γ'-particles in Inconel alloy 718," *Metal Science,* vol. 16, pp. 555-562, 1982/12/01 1982.

[236] W. D. Cao and R. L. Kennedy, "pretreatment in solution so that portion of the grain boundary precipitates is dissolved, then heating, cooling and aging, to develop a microstructure that imparts heat resistance, tensile strength and ductility," ed, 2007.

[237] G. A. Rao, M. Kumar, M. Srinivas, and D. S. Sarma, "Effect of standard heat treatment on the microstructure and mechanical properties of hot isostatically pressed superalloy inconel 718," *Materials Science and Engineering: A,* vol. 355, pp. 114-125, 8/25/ 2003.

[238] G. A. Rao, M. Srinivas, and D. S. Sarma, "Influence of modified processing on structure and properties of hot isostatically pressed superalloy Inconel 718," *Materials Science and Engineering: A,* vol. 418, pp. 282-291, 2/25/ 2006.

[239] G. A. Rao, M. Srinivas, and D. S. Sarma, "Effect of oxygen content of powder on microstructure and mechanical properties of hot isostatically pressed superalloy Inconel 718," *Materials Science and Engineering: A,* vol. 435–436, pp. 84-99, 11/5/ 2006.

[240] L. C. M. Valle, L. S. Araújo, S. B. Gabriel, J. Dille, and L. H. De Almeida, "The Effect of d Phase on the Mechanical Properties of an Inconel 718 Superalloy," *Journal of Materials Engineering and Performance,* vol. 22, pp. 1512-1518, 2013.

[241] J. J. Schirra and D. V. Viens, "Metallurgical Factors Influencing the Machinability of Inconel 718," in *Superalloys 718, 625, 706 and Various Derivatives*, 1994, pp. 827-838.

[242] W. Hermann, H. G. Sockel, J. Han, and A. Bertram, "Elastic Properties and Determination of Elastic Constants of Nickel-Base Superalloys by a Free-Free Beam Technique," in *Superalloys*, 1996, pp. 229-238.

[243] R. N. Yellakara and Z. Wang, "A three-dimensional dislocation dynamics study of the effects of grain size and shape on strengthening behavior of fcc Cu," *Computational Materials Science,* vol. 87, pp. 253-259, 5// 2014.

[244] B. Geddes, H. Leon, and X. Huang, *Superalloys: Alloying and Performance*: ASM International, 2010.

[245] J. J. Schirra, R. H. Caless, and R. W. Hatala, "The Effect of the Laves Phase on the Mechanical Properties of Wrought and Cast + HIP Inconel 718," in *Superalloys*, 1991, pp. 375-388.

[246] D. Cai, W. Zhang, P. Nie, W. Liu, and M. Yao, "Dissolution kinetics of δ phase and its influence on the notch sensitivity of Inconel 718," *Materials Characterization,* vol. 58, pp. 220-225, 3// 2007.

[247] C. M. Kuo, Y. T. Yang, H. Y. Bor, C. N. Wei, and C. C. Tai, "Aging effects on the microstructure and creep behavior of Inconel 718 superalloy," *Materials Science and Engineering: A,* vol. 510–511, pp. 289-294, 6/15/ 2009.

[248] L. Renhof, C. Krempaszky, E. Werner, and M. Stockinger, "Analysis of microstructural properties of IN 718 after high speed forging," in *Superalloys 718, 625, 706 and Derivatives*, 2005, pp. 261-270.

[249] N. El-Bagoury, T. Matsuba, K. Yamamoto, H. Miyahara, and K. Ogi, "Influence of heat treatment on the distribution of Ni 2Nb and microsegregation in cast inconel 718 alloy," *Materials Transactions,* vol. 46, pp. 2478-2483, 2005.

[250] G. K. Bouse and M. R. Behrendt, "Mechanical Properties of Microcast-X Alloy 718 Fine Grain Investment Castings," in *Superalloy 718 - Metallurgy and Applications*, 1989, pp. 319-328.

[251] G. K. Bouse and J. R. Mihalisin, "Metallurgy of Investment Cast Superalloy Components," in *Superalloys, Supercomposites and Superceramics*, ed: Academic Press, 1989, pp. 99-148.

[252] J. Hou, B. J. Wicks, and R. A. Antoniou, "An investigation of fatigue failures of turbine blades in a gas turbine engine by mechanical analysis," *Engineering Failure Analysis,* vol. 9, pp. 201-211, 4// 2002.

[253] R. Viswanathan and W. Bakker, "Materials for ultrasupercritical coal power plants—Turbine materials: Part II," *Journal of Materials Engineering and Performance,* vol. 10, pp. 96-101, 2001/02/01 2001.

[254] NDT-Education-Resource-Center, "Materials/Processes: Mechanical Properties," ed: Iowa State University, 2015.

[255] B. Pieraggi and J. F. Uginet, "Fatigue and Creep Properties in Relation with Alloy 718 Microstructure," in *Superalloys 718, 625, 706 and Various Derivatives*, 1994, pp. 535-544.

[256] D. Gopikrishna, S. N. Jha, and L. N. Dash, "Influence of Microstructure on Fatigue Properties of Alloy 718," in *Superalloys 718, 625, 706, and Various Derivatives*, 1997, pp. 567-573.

[257] A. Thomas, M. El-Wahabi, J. M. Cabrera, and J. M. Prado, "High temperature deformation of Inconel 718," *Journal of Materials Processing Technology,* vol. 177, pp. 469-472, 7/3/ 2006.

[258] C. A. Borg, R. W. Hatala, and J. J. Schirra, "Characterization of Vacuum Die Cast Inconel 718 and Derivatives (PWA 1472/PWA 1473)," in *Superalloys 718, 625, 706 and Various Derivatives*, 2001, pp. 627-636.

[259] G. D. Janaki Ram, A. Venugopal Reddy, K. Prasad Rao, G. M. Reddy, and J. K. Sarin Sundar, "Microstructure and tensile properties of Inconel 718 pulsed Nd-YAG laser welds," *Journal of Materials Processing Technology,* vol. 167, pp. 73-82, 8/25/ 2005.

[260] G. Madhusudhana Reddy, C. V. Srinivasa Murthy, N. Viswanathan, and K. Prasad Rao, "Effects of electron beam oscillation techniques on solidification behaviour and stress rupture properties of Inconel 718 welds," *Science and Technology of Welding and Joining,* vol. 12, pp. 106-114, 2007.

[261] J. Andersson, G. P. Sjöberg, L. Viskari, and M. C. Chaturvedi, "Effect of solution heat treatments on superalloys Part 1 - Alloy 718," *Materials Science and Technology,* vol. 28, pp. 609-619, 2012.

[262] S. Gobbi, L. Zhang, J. Norris, K. H. Richter, and J. H. Loreau, "High powder CO2 and Nd-YAG laser welding of wrought Inconel 718," *Journal of Materials Processing Technology,* vol. 56, pp. 333-345, 1996.

[263] M. D. Rowe, "Ranking the Resistance of Wrought Superalloys to Strain-Age Cracking," *Welding Journal,* pp. 27-34, 2006.

[264] R. Vincent, "Precipitation around welds in the nickel-base superalloy, Inconel 718," *Acta Metallurgica,* vol. 33, pp. 1205-1216, 7// 1985.

[265] K. R. Vishwakarma, N. L. Richards, and M. C. Chaturvedi, "HAZ Microfissuring in EB Welded ALLVAC 718 PLUS Alloy," in *Superalloys 718, 625, 706 and Derivatives*, 2005, pp. 637-647.

[266] A. Odabaşı, N. Ünlü, G. Göller, and M. Eruslu, "A Study on Laser Beam Welding (LBW) Technique: Effect of Heat Input on the Microstructural Evolution of Superalloy Inconel 718," *Metallurgical and Materials Transactions A,* vol. 41, pp. 2357-2365, 2010/09/01 2010.

[267] A. K. A. Jawwad, M. Strangwood, and C. L. Davis, "Microstructural modification in full penetration and partial penetration electron beam welds in inconel-718 (IN-718) and its effect on fatigue crack initiation," *Metallurgical and Materials Transactions A: Physical Metallurgy and Materials Science,* vol. 36, pp. 1237-1247, 2005.

[268] USPTO. (2014). *Chapter 0900: Prior Art, Classification, and Search*. Available: http://www.uspto.gov/web/offices/pac/mpep/s901.html

[269] R. Larson, "Method and device for producing three-dimensional bodies," U.S. Patent US5786562 A, 1993.

[270] M. Larsson and M. Larsson, "Arrangement for the production of a three-dimensional product " U.S. Patent US 7540738 B2, 2002.

[271] M. Larsson, "Arrangement and method for production of a three dimensional object " U.S. Patent US 7454262 B2, 2002.

[272] M. Larsson, "Arrangement and method for producing a three-dimensional product " U.S. Patent US 7713454 B2 2002.

[273] G. Wallgren, U. Ackelid, and M. Svensson, "Systems, apparatus, and methods to feed and distribute powder used to produce three-dimensional objects " U.S. Patent US 7871551 B2, 2005.

[274] M. Larsson and A. Snis, "Method and device for producing three-dimensional objects " U.S. Patent US 8187521 B2, 2006.

[275] U. Ackelid and G. Wallgren, "Apparatus for producing a three-dimensional object " U.S. Patent US 8308466 B2, 2009.

[276] L. Loewgren, "Safety protection method and apparatus for additive manufacturing device " U.S. Patent US 8570534 B1 2012.

[277] U. Ljungblad and M. Svensson, "Method and apparatus for generating electron beams " U.S. Patent US 20130300286 A1 2012.

[278] U. Ljungblad, "Method and apparatus for producing three-dimensional objects " U.S. Patent US 20120100031 A1, 2009.

[279] L. Lowgren and M. Wildheim, "Vacuum chamber with inspection device," PCT Patent WO 2014090510 A1, 2012.

[280] U. Ackelid, "Apparatus and method for producing a three-dimensional object " U.S. Patent US 20120223059 A1, 2007.

[281] E. Rodriguez, "Development of a thermal imaging feedback control system in electron beam melting," ed: ETD Collection for University of Texas, El Paso., 2013.

[282] E. Rodriguez, F. Medina, D. Espalin, C. Terrazas, D. Muse, C. Henry*, et al.*, "Integration of a Thermal Imaging Feedback Control System in Electron Beam Melting," in *Solid Freeform Fabrication Symposium*, Austin, TX, 2012.

[283] R. B. Dinwiddie, R. R. Dehoff, P. D. Lloyd, L. E. Lowe, and J. B. Ulrich, "Thermographic In-Situ Process Monitoring of the Electron Beam Melting Technology used in Additive Manufacturing," in *Thermosense: Thermal Infrared Applications XXXV*, Baltimore, Maryland, 2013.

[284] E. W. Weisstein. (February 1, 2015). *Circle-Circle Intersection*. Available: http://mathworld.wolfram.com/Circle-CircleIntersection.html

[285] I. Elfstrom, "Process Parameters," Arcam AB 2012.

[286] S. Moylan, J. Slotwinski, A. Cooke, K. Jurrens, and M. A. Donmez, "Proposal For A Standardized Test Artifact For Additive Manufacturing Machines And Processes," in *Solid Freeform Fabrication Symposium*, Austin, TX, 2012.

[287] A. Strondl, R. Fischer, G. Frommeyer, and A. Schneider, "Investigations of MX and gamma'/gamma'' precipitates in the nickel-based superalloy 718 produced by electron beam melting," *Materials Science and Engineering A,* vol. 480, pp. 138-147, 2008.

[288] R. A. Overfelt, V. Sahai, Y. K. Ko, and J. T. Berry, "Porosity in Cast Equiaxed Alloy 718," in *Superalloys 718, 625, 706 and Various Derivatives*, 1994, pp. 189-200.

[289] R. S. Cremisio, J. F. Radavich, and H. M. Butler, "The Effect of Thermomechanical History on the Stability of Alloy 718," in *Superalloys*, 1968, pp. 597-618.

[290] J. G. Landau, "Functionally graded additive manufacturing with in situ heat treatment," U.S. Patent US 20130015609 A1, 2013.

[291] J. M. Oblak, D. F. Paulonis, and D. S. Duvall, "Coherency strengthening in Ni base alloys hardened by DO22 γ' precipitates," *Metallurgical Transactions,* vol. 5, pp. 143-153, 1974/01/01 1974.

[292] R. Chandrasekar, "Swept frequency eddy current (SFEC) measurements of Inconel 718 as a function of microstructure and residual stress," Ph.D., Iowa State University, 2013.

[293] R. Chandrasekar, C. C. H. Lo, A. M. Frishman, B. F. Larson, and N. Nakagawa, "Quantification of precipitates and their effects on the response of nickel-base superalloy to shot peening," *AIP Conference Proceedings,* vol. 1430, pp. 1437-1444, 2012.

[294] H. F. Merrick, "Effect of heat treatment on the structure and properties of extruded P/M alloy 718," *Metallurgical Transactions A,* vol. 7, pp. 505-514, 1976/04/01 1976.

[295] J. M. Eridon and R. P. Dalal, "Method for preventing recrystallization during hot isostatic pressing," U.S. Patent US 4743312 A, 1988.

[296] W. J. Sames, M. M. Kirka, K. A. Unocic, F. Medina, and R. R. Dehoff, "The Effect of Post-Processing on the Microstructure and Mechanical Properties of Inconel 718 Produced by Electron Beam Melting," in *TMS Annual Meeting & Exhibition*, Orlando, FL, 2015.

[297] J. R. Brinegar, L. F. Norris, and L. Rozenberg, "Microcast-X Fine Grain Casting - A Progress Report," presented at the Superalloys, 1984.

[298] F. J. Humphreys and M. Hatherly, "Chapter 11 - Grain Growth Following Recrystallization," in *Recrystallization and Related Annealing Phenomena (Second Edition)*, F. J. H. Hatherly, Ed., ed Oxford: Elsevier, 2004, pp. 333-378.

[299] Y. Jin, B. Lin, M. Bernacki, G. S. Rohrer, A. D. Rollett, and N. Bozzolo, "Annealing twin development during recrystallization and grain growth in pure nickel," *Materials Science and Engineering: A,* vol. 597, pp. 295-303, 3/12/ 2014.

[300] EDAX. (2015). *Measuring Grain Size in Heavily Twinned Materials*. Available: http://www.edax.com/Markets/Characterizing-of-Twins-in-OIM.aspx

[301] J. H. Jeon, A. B. Godfrey, P. A. Blenkinsop, W. Voice, and Y. D. Hahn, "Recrystallization in cast 45-2-2 XD™ titanium aluminide during hot isostatic pressing," *Materials Science and Engineering: A,* vol. 271, pp. 128-133, 11/1/ 1999.

[302] F. J. Humphreys and M. Hatherly, "Chapter 9 - Recrystallization of Two-Phase Alloys," in *Recrystallization and Related Annealing Phenomena (Second Edition)*, F. J. H. Hatherly, Ed., ed Oxford: Elsevier, 2004, pp. 285-319.

[303] H. P. Tang, M. Qian, N. Liu, X. Z. Zhang, G. Y. Yang, and J. Wang, "Effect of Powder Reuse Times on Additive Manufacturing of Ti-6Al-4V by Selective Electron Beam Melting," *JOM,* pp. 1-9, 2015/02/05 2015.

[304] ASTM-International, "Standard Testing Methods for Tension Testing of Metallic Materials," vol. E8/E8M-11, ed. West Conshohocken, PA: ASTM International, 2012.